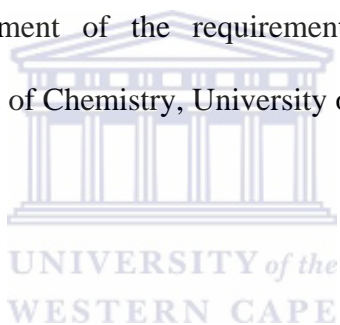**SYNTHESIS OF SULPHONATED AND TRANSITION METAL OXIDE DOPED POLYMERIC NANOCOMPOSITES FOR APPLICATION IN DESIGN OF SUPERCAPACITORS.**

Njagi Njomo

A thesis submitted in fulfilment of the requirements for the degree of Doctor Philosophiae in the Department of Chemistry, University of the Western Cape.

UNIVERSITY *of the*
WESTERN CAPE

Supervisors: Prof. Emmanuel I. Iwuoha, University of the Western Cape.

Prof. Kenneth I. Ozoemena, Council for Scientific and Industrial Research.

November 15, 2011

Key words

Sol gel method

Transition mixed metal oxides nanoparticles

Sulphonated polyaniline nanocomposites

Electrochemical cell

Electrochemical double layer capacitor

Scanning electrochemical microscopy

Cyclic voltammetry

Specific capacitance

Specific energy

Specific power

Abstract

To meet a fast-growing market demand for next generation portable electronic devices with higher performance and increased device functionalities, efficient electrical energy devices with substantially higher energy, power densities and faster recharge times such as supercapacitors are needed. The overall aim of this thesis was to synthesize nanostructured sulphonated polyaniline and transition metal single, binary and ternary mixed oxide doped nanocomposites with electro-conductive properties. These nanocomposites were anchored on activated graphitic carbon and used in design of asymmetric supercapacitors. Tantalum(IV)oxide, tantalum(IV)oxide-nickel(II)oxide, tantalum(II)oxide-manganese(III)oxide, tantalum(II)oxide-nickel(II)oxide-manganese(II,III)oxide nanoparticles were synthesised using modified sol-gel methods. These were then dispersed, individually, in acidic media through sonication and incorporated *in-situ* into the polymeric matrix during the oxidative chemical polymerization of aniline doped with poly(4-styrene sulphonic acid). These novel polymeric nanocomposites were characterised with FTIR, UV-visible, TEM, SEM, EDS, XRD to ascertain successful polymerization, doping, morphology and entrapment of the metal oxide nanoparticles. SECM approach curves and interrogation of CV revealed that these nanocomposites are conductive and electro-active. The cells showed good supercapacitor characteristics with high specific capacitances of 170.5 Fg^{-1} in TaO_2-PANi-PSSA, 166.1 Fg^{-1} in TaO_2-NiO-PANi-PSSA, 248.4 Fg^{-1} in TaO-Mn_2O_3-PANi-PSSA and 119.6 Fg^{-1} in TaO-NiO-Mn_3O_4-PANi-PSSA. Their corresponding energy

densities were calculated as 245.5 Whg^{-1}, 179.4 Whg^{-1}, 357.7 Whg^{-1} and 172.3 Whg^{-1} respectively. They also gave respective power densities of 0.50 Whg^{-1}, 0.61 Whg^{-1}, 0.57 Whg^{-1} and 0.65 Whg^{-1} and showed good coulombic efficiencies ranging between 77.97% and 83.19%. These materials are found to have a long cycle life and therefore good electrode materials for constructing supercapacitor cells.

UNIVERSITY *of the*
WESTERN CAPE

Declaration

I declare that this piece of work entitled; **Synthesis of sulphonated and transition metal oxide doped polymeric nanocomposites for application in design of supercapacitors** is my own work, that it has not been submitted before for any degree or examination in any other university, and that all the sources I have used or quoted have been indicated and acknowledged as complete references.

Njagi Njomo   November 15, 2011

Signature…………………..

Supervisors:

Prof. Emmanuel Iwuoha   Prof. Kenneth Ozoemena

Signature…………………..   Signature…………………..

Acknowledgements

Table of contents

Table of figures

List of tables

Chapter 1

General Introduction

1.1 Background information

As global demand for energy rises inexorably with growth in human population and in step with industrial growth and technological advancement, a progressive swing towards renewable energy and energy storage becomes inevitable as concern grows over usage of fossil fuel and as the world focuses its attention on global warming and resource depletion. Renewable energy is intermittent by its nature. This then necessitates the development of improved methods for storing electrical energy when it is available and retrieving it when it is needed. Without advances in electrical energy storage, important alternative forms of energy cannot be fully realized. Electrical energy can be stored using two fundamentally different methods; (i) Directly, in an electrostatic way as negative and positive electric charges on the plates of a capacitor by a non-Faradaic process and (ii) Indirectly, in batteries as potentially available chemical energy requiring Faradaic oxidation and reduction of the electro-active reagents. The advantages of such storage and eventual retrieval are two-fold: reduced greenhouse gas emissions (notably CO_2) and improved energy sustainability.

Electrostatic capacitors, unlike storage batteries, are high power but substantially low energy-density storage devices which can only store a very small amount of electric charge unless they are large. Though they have been used as energy storage elements for nearly a century, their low capacitance values have traditionally limited them to low power applications as components in analogue circuits, or at most as short-term memory

backup supplies. Recent developments in manufacturing techniques have changed this and with the ability to construct materials of high surface-area and electrodes of low resistance, combined with an understanding of the charge transfer processes that occur in the electric double-layer has made high-power electrochemical capacitors possible. We can characterize the four decades history of capacitors technology perhaps best as one of continual breakthrough development in which initial cost and power-energy density challenges have consistently led to innovations that not only meet cost concerns but open up new avenues of discovery [1-2] The practical realization of this possibility led to a new paradigm viz; the development of supercapacitors. Supercapacitors are devices able to store charges in an electrode/electrolyte interface. Also referred to as electrochemical capacitors, electrical double-layer capacitors, ultracapacitors, power capacitors, etc, supercapacitors store energy electrostatically between a solid electrode and oppositely charged electrolyte ions that migrate towards the electrode when a potential is applied. They therefore represent a new breed of technology that occupies a niche amongst other energy storage devices that was previously vacant. They have the ability to store greater amounts of energy than conventional capacitors, and are able to deliver more power than batteries.

Development of supercapacitors occupies a pivotal role in the context of electrochemical energy storage and conversion devices. Their unique combination of high power capability and good specific energy make them occupy a functional position between batteries and conventional capacitors [3-7]. This position of supercapacitors is easily visualised by means of a Ragone plot (Figure 1), a graphical representation of a device's energy and power capabilities.
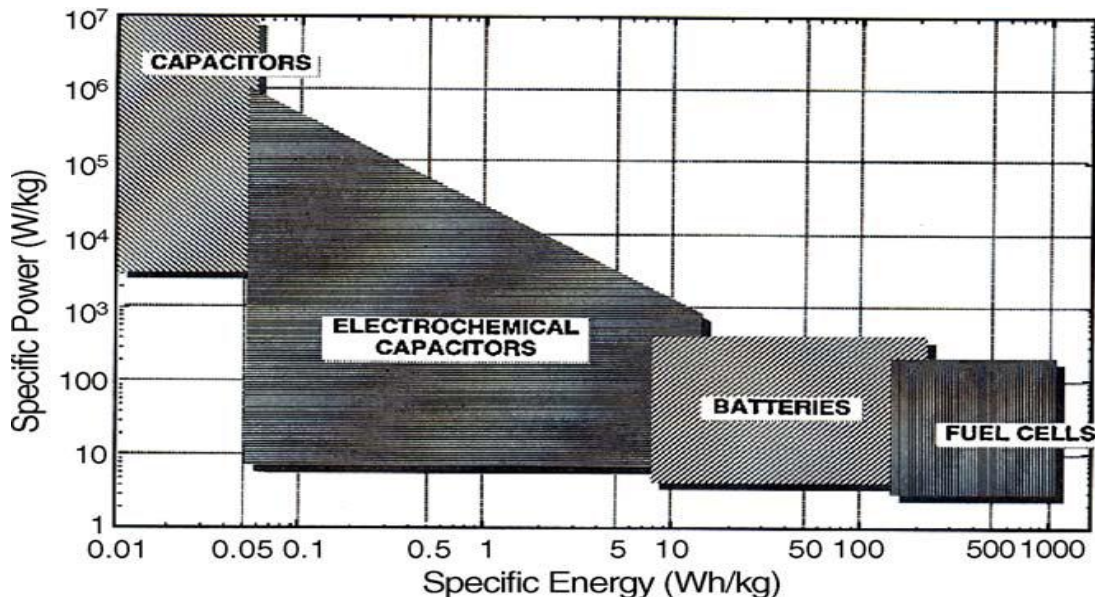
Figure 1. Sketch of Ragone plot for various energy storage and conversion devices [8].

The charge and discharge processes in a storage battery often involve irreversibility in chemical inter-conversions of the electrode materials. This limits the cycle life of storage batteries. By contrast, only an excess and a deficiency of charges on the capacitor plates have to be established on charge and the reverse on discharge without chemical changes involved. These highly reversible charge-storage processes of the supercapacitors make them to have longer cycle-lives and can rapidly be charged and discharged making capacitors to have an unlimited recyclability. This unique capacitor characteristic has generated interest in their application and has attracted worldwide research interest. They have found use in a wide, potential and growing range of applications that include mobile devices, consumer electronic devices, hybrid electric vehicles, aerospace and industrial power management and in particular in those applications where size is paramount [9-13]. According to energy storage mechanisms, supercapacitors can be divided into two types [13]; (i) electrochemical double layer capacitors (EDLC) and, (ii) the

3

pseudocapacitors (also referred to as redox supercapacitors). In the electrochemical double layer, energy storage is principally electrostatic in nature. It arises mainly from the separation of electronic and ionic charges at the interface between electrode materials and the electrolyte solution. Electric charges are stored directly across the double layer of the electrode. There is no charge transfer across the interface. The effect is true capacitance. The mechanism of surface charge generation can be enumerated as; surface dissociation, ion adsorption from solution, and crystal lattice defect. As an excess or deficiency of charge builds up on the electrode surface, ions of opposite charge build up in the electrolyte near the electrode/electrolyte interface in order to provide electro-neutrality. The thickness of the double layer depends on the concentration of the electrolyte and the size of ions. Figure 2 shows the mechanism of charge storage in an EDLC cell [14-15].
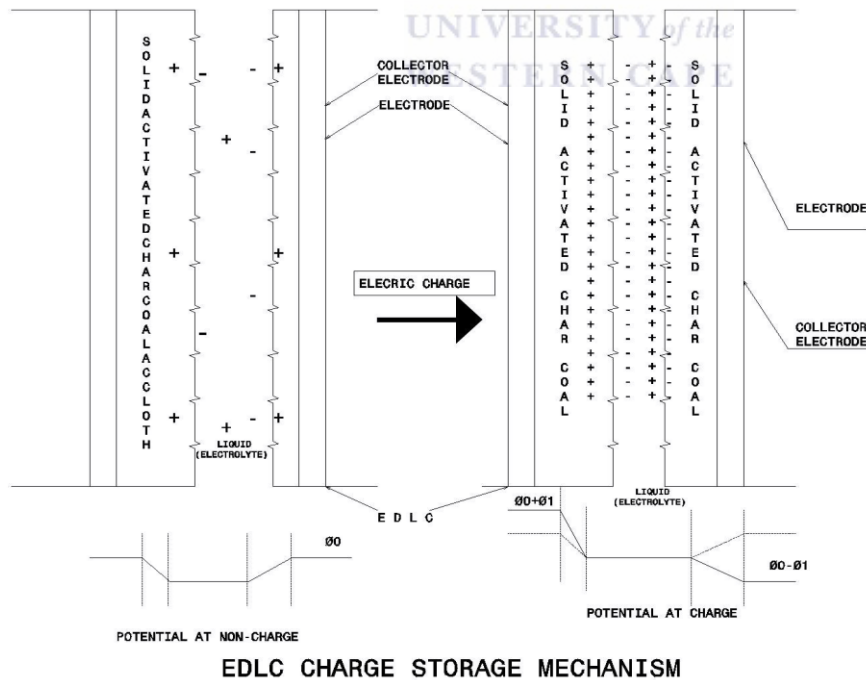
Figure 2. Charge storage mechanism of an EDLC cell under uncharged and charged conditions

In the redox supercapacitors, fast Faradaic reactions take place to an extent limited by a finite amount of active material or available surface [16]. This occurs at the electrode when the application of a potential induces Faradaic current from reactions such as (i) electrosorption which occurs when chemisorption of electron donating anion such as Cl^-, Br^-, or CNS^- takes place in a process such as $M + A^- \leftrightarrow MA^{(1-\delta)-} + \delta e^-$. (ii) redox reactions of electroactive materials when an exchange of charge across the double layer occurs rather than a static separation of charge across a finite distance resulting in oxidation-reduction indicated as $O_{ad} + ne^- \leftrightarrow R_{ed}$ [11]. The two different storage mechanisms, EDLC and pseudocapacitance, can exist for a supercapacitor system giving what is rightly referred to as Electrochemical capacitor. Normally one of the storage mechanisms dominates with the other being relatively weak.

1.2 Justification

Power demand and demand for the storage of energy in form of batteries for both portable and static electronic applications have greatly increased. The present storage systems are too costly to penetrate major new markets. Demand for higher performance and increased device functionality in electronic devices such as radio tuners, notebooks, cordless tools, cameras, mobile phones, laptops, etc. coupled with environmentally acceptable materials have raised interest in search for efficient electrochemical energy storage devices, and hence new materials whose constituents must be available in large quantities in nature, to bring the cost of device production low [17]. Next generation portable devices will require stable solid state supercapacitors with high power density, flexible and transparent to meet the various design and power needs [18-19]. In a world

5

expressing growing concerns for the environment and conservation of natural resources, a focus on development of vehicles with supercapacitor-battery power coupled systems (hybrid electric vehicles (HEVs)) has taken an accelerated pace, with the design of an automobile propulsion system currently going through a major evolution, perhaps the biggest since its invention. The center of this change focuses on electrifying the power system of the automobile. Contributing to the acceleration of HEVs is the factor of energy supplies. As the economies of developed nations are sustained and as those of developing countries mature, the automotive population is expected to be five times larger by mid-century, growing from 700 million to 2.5 billion [20-21]. With petroleum being a finite resource, two questions begs for answer. Where will the oil come from? Where will the emissions be dispersed? The automobile companies have reduced the emission of greenhouse gases, but due to the growth in the automotive population, air pollution continues to increase. The answers to these gloomy questions compel us to make every effort to build sustainable renewable energy systems. The rapid development of stand-alone renewable energy systems such as wind and solar is limited by high life cycle costs. One main contributor to the high life cycle cost is the battery which is used to store electricity generated from these intermittent systems. Energy storage is an integral part of renewable energy systems such as wind and solar due to their intermittent nature. However this very intermittent nature of their output causes the battery to operate at conditions of deep-discharged and overcharged states. Continuous exposure to rapid charge/discharge profiles degrades the battery performance and reduces its lifetime [22-24]. The reduced battery lifetimes lead to frequent replacement thereby increasing the overall life cycle costs. Also as the power demand increases the battery energy capacity

decreases and the batteries then need to be oversized for high power applications. This can be a problem for space constrained applications [22]. It can be seen from Figure 2 that supercapacitors have much higher power densities than traditional battery systems [25] making a hybrid electric model worth consideration. This configuration is mainly being considered by industry for hybrid electric and HEV applications because of the potential reduction in the size/volume of the overall energy storage system. The usage of sucapacitors also decreases the current loads on battery systems thereby potentially improving battery lifetimes. Studies have shown that a simple parallel combination of battery and supercapacitor leads to improved energy storage system performance as peak power of the energy storage system can be enhanced, internal losses reduced and discharge life of the battery be extended with the usage of supercapacitors [20-21]. It is these advantages that make it worth investigating the supercapacitor configurations in the context of building sustainable energy systems.
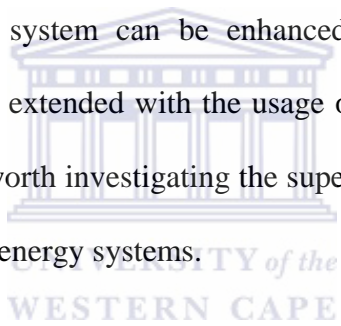
1.3 Aims and objectives of study

This research work aimed at developing cheap, environmentally friendly sulphonated and transition metal oxide doped polymeric nanocomposite electrode materials that can be applied in the design of high specific capacitance, high power and high supercapacitor devices. Different binary, ternary and quartenary nanocomposite systems were developed using different combinations of aniline, synthesized metal oxides; nickel oxide, tantalum oxide and manganese oxide with the organic dopant poly(4-styrene sulphonic acid). The specific objectives of this study were:

1   Synthesis of nanostructured transition metal oxides; nickel oxide, tantalum oxide, manganese oxide, and the mixed metal oxides; nickel oxide-tantalum oxide, tantalum

oxide-manganese oxide, and the ternary tantalum oxide-nickel oxide-manganese oxides.

2   Synthesis of nanostructured poly(4-styrene sulphonic acid) doped-polyaniline nanocomposites with *in-situ* incorporation of the tantalum oxide and the mixed metal oxides; nickel oxide-tantalum oxide, tantalum oxide-manganese oxide, and the ternary tantalum oxide-nickel oxide-manganese oxides.

3   Electrochemical and spectroscopic characterization of the sulphonated and transition metal oxide doped polyaniline nanocomposites.

4   Design of supercapacitor cells using the polymeric sulphonated and transition metal oxide doped polyaniline anchored on activated graphitic carbon.

5   Characterization of the supercapacitor cells using two electrode electrochemical cell configurations.
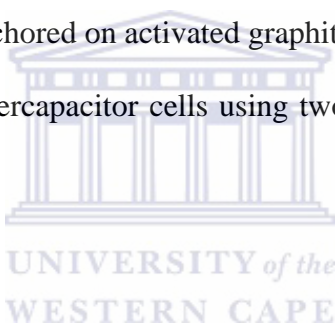
1.4 Thesis layout

Chapter 2 reviews the historical perspective of the concept of electrical energy storage at the interface between an electrolytic solution and a solid since the 1800s. It looks at the contemporary competing commercial interests of supercapacitors. An account of development of the basic theory of double layer and double layer models is reviewed. Storage of energy in a double layer is discussed. A review of suitable materials for construction of supercapacitors including carbon based, polymer based and metal oxide based plus a review of suitability of polyaniline as electrode polymer material for supercapacitors is reviewed. Chapter 3 summarizes the basic description of all the characterization techniques employed in the study while chapter 4 summarizes all the

8

procedures employed in the synthesis of metal oxide nanostructures, doping of polyaniline and *in-situ* incorporation of the metal oxides into the polymer matrix to form the desired polymeric nanocomposites. Methods of integration of nanocomposites with activated graphite, preparation of electrodes, construction and testing of asymmetric supercapacitor cells are discussed. Chapter 5 gives detailed summary of the results of synthesis of nanostructures, characterization, construction and testing of supercapacitor cells while Chapter 6 concludes the studies by arguing a strong case for supercapacitors as part of the new wave of advanced energy storage devices that will further the push towards greater energy efficiency and more sustainable alternatives.

UNIVERSITY *of the*
WESTERN CAPE

Chapter 2

Literature review

2.1 Double-layer electrical energy storage: A historical perspective

The concept of storing electrical energy in the electric double layer that is formed at the interface between an electrolytic solution and a solid has been known since the late 1800s. This concept of the double layer has been studied by chemists since the 19th century when von Helmholtz first developed and modeled [26] the double layer concept in investigations on colloidal suspensions. His work was subsequently extended to the surface of metal electrodes in the late 19th and early mid-20th centuries [27-29]. A brief historical review of the double layer is given later in the chapter.
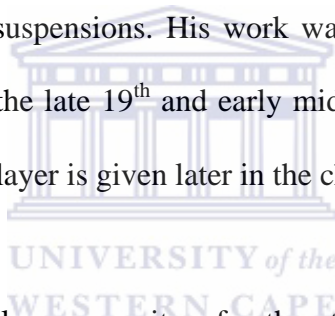
The practical use of a double-layer capacitor, for the storage of electrical charge, was demonstrated when in 1957 General Electric patented [27] an electrolytic capacitor (Figure 3). This early patent utilized crude porous carbon electrodes in an aqueous electrolyte and admits that "it is not positively known exactly what takes place when the devices are used as energy storing devices," it was believed that energy was being stored in the pores of the carbon, and it was noted that the capacitor exhibited an exceptionally high capacitance.
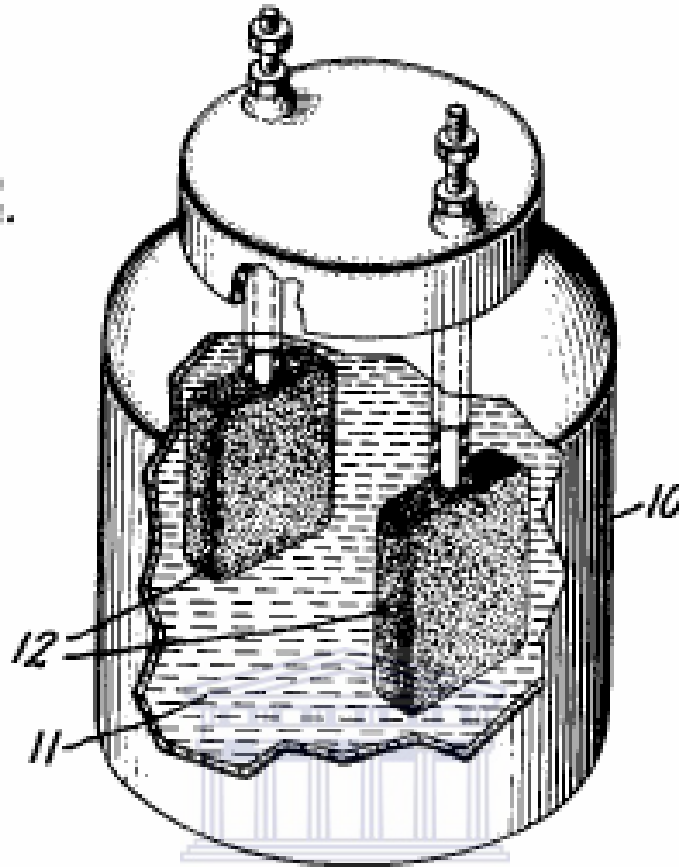
Figure 3. The capacitor patented by General Electric [27].

From the Standard Oil Company of Cleveland, Ohio (SOHIO) patent granted in 1966 [30], it was acknowledged that electrolytic capacitors actually store energy in the electrical double-layer, at the inter-phase between electrode and solution (Figure 4) with the 'double-layer' at the interface behaving like a capacitor of relatively high specific capacity."
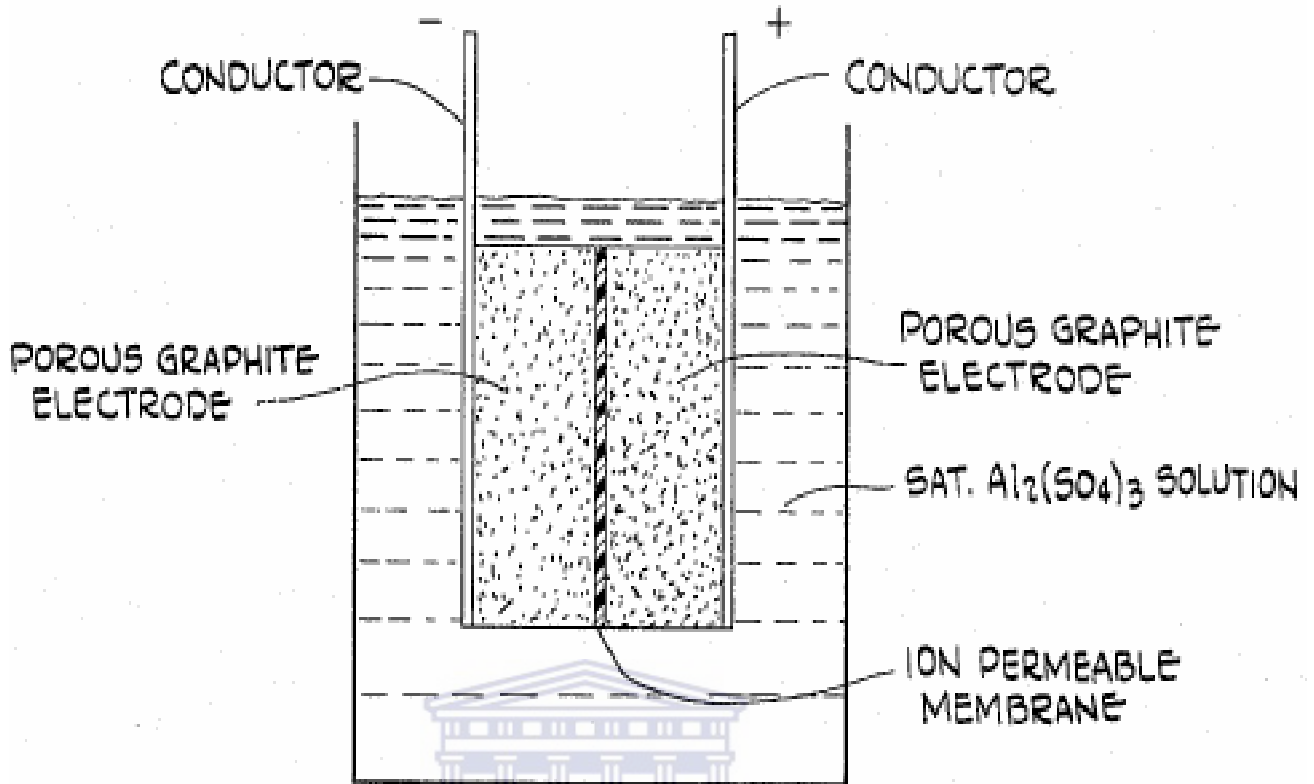
Figure 4. An electrolytic energy storage device patented by SOHIO [30].

SOHIO also originated the first commercial double-layer supercapacitors in 1970. In the year, they patented [29] [4] a disc-shaped device that consisted of carbon paste electrodes, formed by soaking porous carbon in an a non-aqueous electrolyte separated by an ion-permeable separator (Figure 5). SOHIO then licensed their technology to Nippon Electric Company (NEC) of Japan in 1971 [31], who further developed and successfully marketed double-layer supercapacitors, primarily for memory backup applications becoming the first company to produce the first commercially successful double-layer capacitors under the name "supercapacitor."
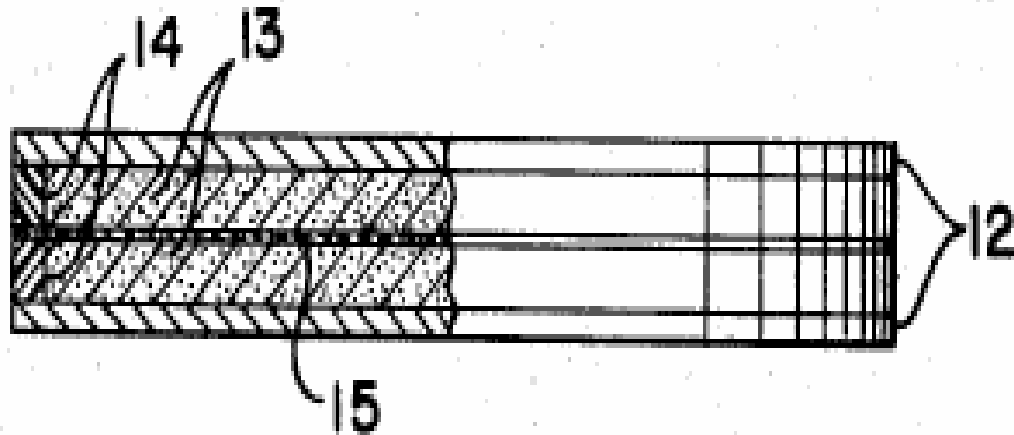
Figure 5. A capacitor patented by SOHIO [29].

By the 1980's a number of companies such as Matsushita Electric Industrial Company, simply known as Panasonic in the Western world, had developed their "Gold capacitor" intended also for use in memory backup applications [32]. By 1987 Elna corporation had begun producing their own double-layer capacitor under the name "Dynacap" [33]. Pinnacle Research Institute (PRI) developed the first high-power double-layer capacitors (PRI Ultracapacitor) incorporating metal-oxide electrodes for military applications such as laser weaponry and missile guidance systems [34]. Challenged by the PRI ultracapacitor, the United States Department of Energy (DoE) started an aggressive double-layer capacitor initiative as part of their hybrid electric vehicles program, and by 1992 the DoE Ultracapacitor Development Program was started at Maxwell Laboratories [35]. A number of commercial companies around the world currently manufacture EDLCs in a commercial capacity. NEC and Panasonic in Japan have been producing electric double layer capacitor (EDLC) components since the 1980's. In the U.S.A Epcos, Elna, AVX, and Cooper companies produce components, while Evans and Maxwell produce integrated modules that include voltage balancing circuitry. Kold Ban

International markets a supercapacitor module designed specifically for starting internal combustion engines in cold weather. Cap-XX in Australia offers a range of components, as does Ness Capacitor Co. in Korea. In Canada, Tavrima manufactures a range of modules. ESMA in Russia sells a wide variety of EDLC modules for applications in power quality, electric vehicles, and for starting internal combustion engines. Research is currently being conducted in many institutions in the interests of improving both the energy and power densities of EDLC technology.

2.2 Electrochemical techniques

Electrochemical (Electroanalytical) techniques rely on electrochemistry which is an interfacial science concerned with the interactions between chemical species and interfaces. It is the use of electricity to effect chemical processes. It deals with the measurements and understanding of electric quantities such as current, potential, and charge, and their relationship to chemical parameters [36-37]. Electrochemical processes occur at all kinds of interfaces ranging from those involving two phases such as solid-liquid, liquid-liquid, liquid-gas and solid-gas interfaces through those involving three phases such as solid-liquid-gas interfaces to those that take place at more complex interfaces such as biological membranes. All these interfaces can be harnessed for analytical measurements [37]. The reactions concerned in electrochemical processes are redox reactions which involve the oxidized and reduced forms of a species be it an ion, a molecule or a biological entity. Most of these cases correspond to the conversion of one form into another and therefore involve the transfer of electrons across the interface. The interface may be inert and thus only provide a suitable site for the reaction and a source or sink for the electrons but more often than not the interface participates in the reaction.

14

Electroanalytical techniques therefore harness the electrochemical relationship at the interface to establish a link between an electrical signal (current or voltage) and the presence of a chemical species in the vicinity of the electrode. Depending on the technique used the output signal reflects any of the following quantities: the potential difference between a working electrode and a reference electrode, the current flowing between two electrodes or its integral over time (the charge passed) or the electrical impedance of an electrochemical cell. The species of interest may be neutral or ionic while the electrode may be bare or modified with a film. This film may range from a single molecular layer to several mm thick [38]. Examples of materials used to modify electrodes include mercury for the polarographic determination of trace metals [39], conducting polymers [40], gels [41-42], polymers loaded with enzymes and redox mediators [43-46], doped polymers [45], molecular constructions tethered to the electrode surface and nanostructured materials [47-48] The electrodes may be passive as in potentiometry or active as in amperometry and impedimetry. In potentiometry the indicator electrode is in equilibrium with the analyte while in amperometry or impedimetry the working electrode drives a reduction or an oxidation. In this case the reaction at the electrode consumes species from the analyte and produces new species in the analyte; the electron involved in the electrode reaction may therefore be viewed as a reagent that can be supplied (reduction) or taken away (oxidation). In amperometry and impedimetry the other electrode, often called the counter or secondary electrode, undergoes a reverse reaction to that on the working electrode (e.g. an oxidation if the working electrode runs a reduction) and therefore also alters the composition of the analyte. A supercapacitor is an electrochemical device that operates on principles similar

to those of conventional electrostatic capacitors in the sense that it uses an electrode-solution interface that behaves similar to a capacitor. A brief review of supercapacitor interface models is undertaken.

2.3 The double layer

2.3.1Conventional capacitor

Conventional capacitor stores energy in the form of electrical charge. A typical device (Figure 6) consists of two conducting material plates separated by a dielectric.
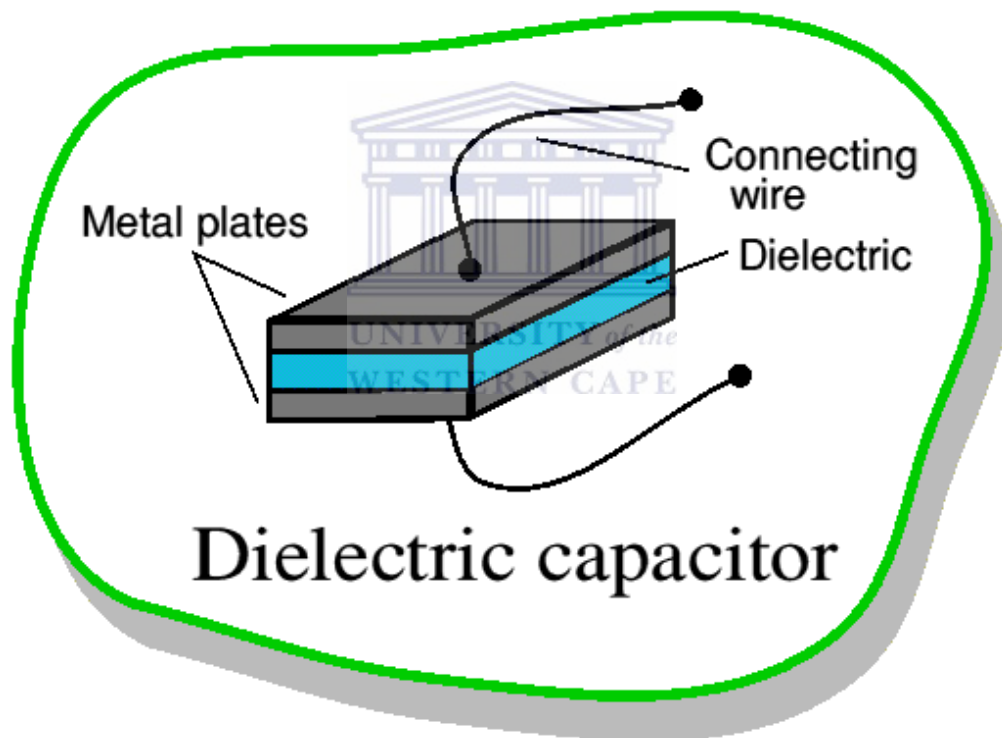
Figure 6. A conventional dielectric capacitor [49].

When an electric potential is applied across the conductors electrons begin to flow and charge accumulates on each conductor. When the potential is removed the conducting plates remain charged until they are brought into contact again, in which case the energy

16

is discharged. The amount of charge that can be stored in relation to the strength of the applied potential is known as the capacitance, and is a measure of a capacitor's energy storage capability. The charge, Q, for this capacitor is proportional to the applied voltage, V, and known capacitance, C. Thus,

$$Q = CV \hspace{6cm} 2.1$$

The capacitance is dependent on the physical characteristics of the capacitor. In parallel plate capacitors, capacitance is proportional to the surface area of each plate, S, permittivity of the dielectric material, ε, and indirectly to the dielectric thickness, d [31]. Thus,

$$C = \frac{S\varepsilon}{d} \hspace{6cm} 2.2$$

From equation 2.2, three inferences [50] can be made; (i) the larger the surface area on the plates, the larger the capacitance, (ii) The smaller the distance separating the plates, the greater the capacitance, (iii) the higher the permittivity, the higher the capacitance. Despite the substantial differences in construction and structure of parallel plate capacitors and supercapacitors, the three general inferences always apply.

Supercapacitors use an electrode-solution interface that behaves similar to a conventional capacitor shown in figure 7.
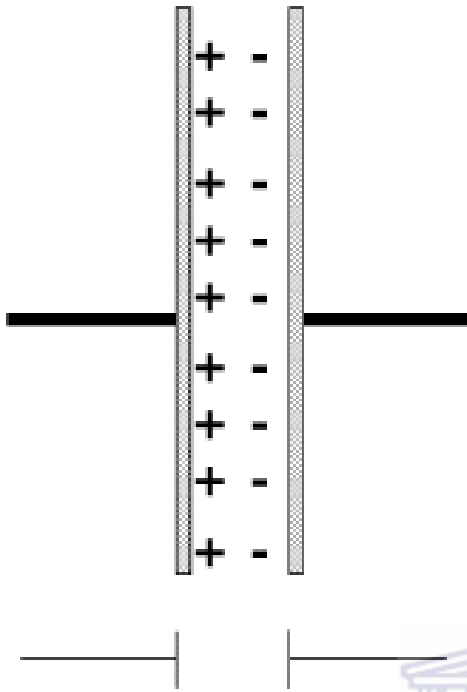
Figure 7. Schematic of a conventional capacitor

For an applied potential voltage, a charge on the electrode, q_e, and in the solution, q_s will exist. Depending on the excess or deficiency of electrons, the charge on the electrode will either be positive or negative. These electrons reside in a very thin layer on the solid surface. The solution charge is determined by the cations or anions in the vicinity of the electrode surface [51]. At all times,

$$q_e = -q_s \qquad\qquad 2.3$$

applies to one electrode surface; in actual experiments, both metal electrodes would have to be considered. However, due to coulombic interaction between the electrode and electrolyte, the situation is more complicated [51].

As stated earlier, EDLCs store electrical charge in a manner similar to a capacitor but charge does not accumulate on two conductors separated by a dielectric. Instead charge

accumulates at the interface between the surface of a conductor and an electrolytic solution (Figure 8).
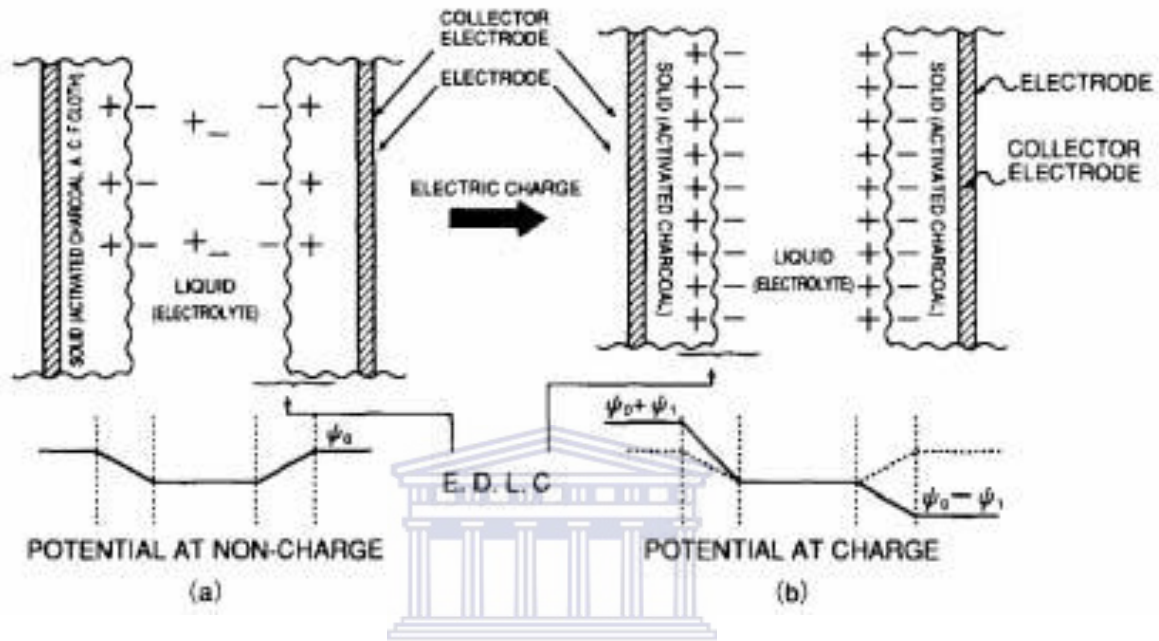
Figure 8. EDLC charge storage mechanism [52]

The accumulated charge hence forms an electric double-layer, the separation of each layer being of the order of a few Angstroms. An estimate of the capacitance can be obtained from the double-layer model.

2.3.2 Double layer interface models

The understanding of the electrical processes that occur at the boundary between a solid conductor and an electrolyte has developed gradually. Various models have been developed over the years to explain the phenomena observed by chemical scientists. The double-layer model was first proposed by Helmholtz in 1853 [26]. His double-layer idea consisted of two array monolayers of opposite charge separated by a distance of molecular order. One layer forms on the charged electrode, and the other layer is

comprised of ions in the electrolyte. In this model, the interface consisted of a layer of electrons at the surface of the electrode, and a monolayer of ions in the electrolyte (figure 9). According to the Helmholtz model the differential capacitance is given by;

$$C_\delta = \frac{\varepsilon}{4\pi\delta}$$ 2.4

Where, C_δ, the differential capacitance predicted by the Helmholtz model, is a constant value dependent only on dielectric constant, ε, and charge layer separation, δ. The model does not consider the adsorption of water molecules and counter ions.

Two flaws were found to be inherent with the Helmholtz model. First, it became apparent that the ions on the solution side of the double layer would not remain in a static compact array but be subject to the effects of thermal fluctuation according to the Boltzmann principle [2]. Second, the structure is equivalent to a parallel-plate capacitor. The relationship between the charge density, σ, and voltage drop, V, between the plates is

$$\sigma = \frac{\varepsilon^* \varepsilon_0}{\delta} V$$ 2.5

ε^* is the dielectric constant of the medium, ε_0 is the permittivity of free space and δ is the interplate spacing. If differential capacitance is defined as,

$$C_\delta = \frac{\partial \sigma}{\partial V}$$ 2.6

Then, $\frac{\partial \sigma}{\partial V} = C_\delta = \frac{\varepsilon^* \varepsilon_0}{\delta}$ 2.7

This equation predicts the differential capacitance to be constant. However, variations in the differential capacitance with potential and electrolyte concentration suggest that either

the dielectric constant of the medium or the inter-plate spacing depends on these variables [51]. Hence, a model was needed that addressed the two flaws.
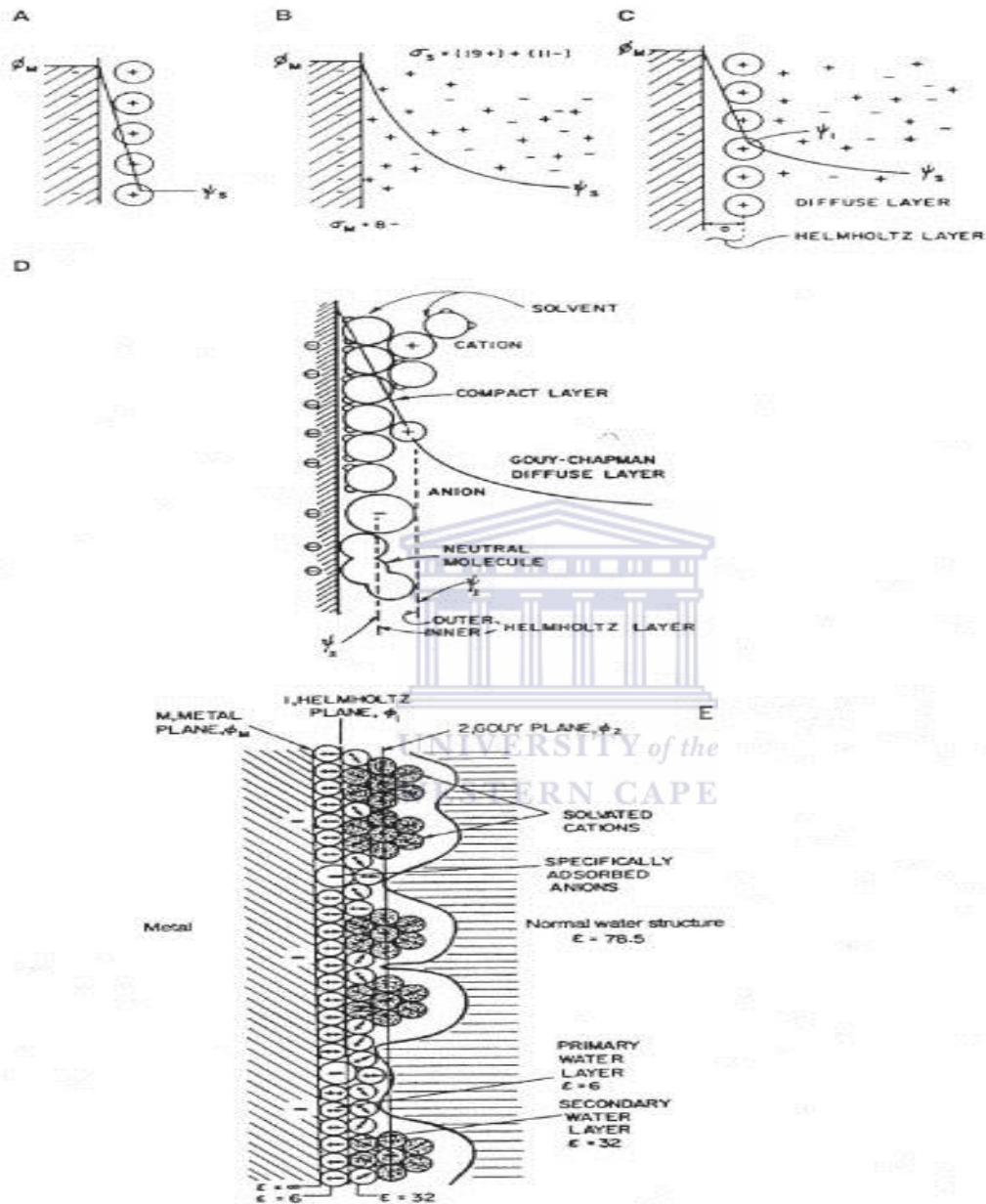
Figure 9. Models of the double layer as historically developed: a) Helmholtz model b) Gouy-Chapman model of the diffuse layer c) Stern's model, combining (a) and (b) d) Grahame's later model and e) Model of Bockris, Devanathan and Muller showing presence and orientation of solvent dipoles [53].

With the charge of the electrode confined to the surface, the same is not totally true on the solution side. At low concentrations of electrolyte, it may require a significant thickness of solution to accumulate the excess charge needed to counterbalance charge density on the metal [51]. In the early 1900's, Gouy considered observations that capacitance was not a constant and that it depended on the applied potential and the ionic concentration. To account for this behaviour Gouy proposed that thermal motion kept the ions from accumulating on the surface of the electrode, instead forming a diffuse space charge. To explain the theory, Gouy and Chapman introduced a mathematical model based on combined application of the Boltzmann's energy distribution equation and Poisson's equation. The Poisson equation was used to relate potential to charge density, and the Boltzmann equation was used to determine the distribution of ions. Ions were considered as point charges with no volume [54-55].
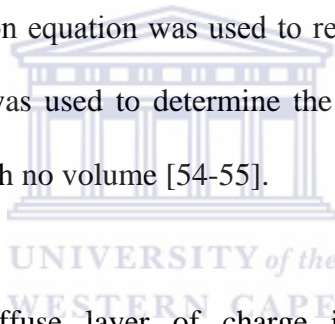
The model introduces a diffuse layer of charge in the solution. The greatest concentration of excess charge would be adjacent to the electrode, while lesser concentrations would be found at greater distances. In the Gouy-Chapman theory, the ions are not restricted with respect to the location of the solution phase. The theory considers ions as point charges that can approach the surface boundary arbitrarily close, thereby at high polarization, the effective separation distance between the solid and solution phase can decrease to zero. Thus, the model assumes the charges decay rapidly and continuously from conductive material to electrolyte without distinct layer separation, a case which is not realistic [51]. This model successfully predicts the temperature and potential effects on the capacitance and is accurate for low electrolyte

22

concentrations, i.e. low surface charge density. The serious problem with Gouy-Chapman theory is the overestimation of the double-layer capacitance. Also the model does not take into account the distorted structure by steric effect and hydration force or overlapping problem occurring in the nanopores. In 1924 Stern developed modifications to overcome the serious problems in the Gouy-Chapman model by including a compact layer as well as Gouy's diffuse layer. The compact Stern layer consisted of a layer of specifically adsorbed ions [56]. Grahame divided the Stern layer into two regions. He denoted the closest approach of the diffuse ions to the electrode surface as the outer Helmholtz plane (sometimes referred to as the Gouy plane). The layer of adsorbed ions at the electrode surface was designated as being the inner Helmholtz plane (sometimes referred to as the Gouy plane).
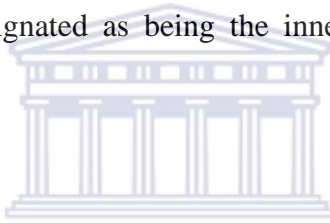
The theory argues that ions have a finite size and cannot approach the surface any closer than the ionic radius. The solution side of the double layer is thought to be made up of several "layers". The layer closest to the electrode, the inner layer, contains solvent molecules and other species which are said to be specifically absorbed. The loci for these electrical centers reside in the inner Helmholtz plane, IHP, at a distance x_1. The total charge density for this inner layer is σ^i. If the ions remained solvated, the thickness of the primary solution sheath would have to be added to the ionic radius. For solvated ions, the loci of centers reside at a distance, x_2. This layer is called the outer Helmholtz plane, OHP. The interaction of the solvated ions with the solid surface involves long range electrostatic forces and therefore, their interaction is independent of the chemical properties of the ions. These are said to be nonspecifically adsorbed. Due to thermal

agitation in the solution, the nonspecifically adsorbed ions are distributed throughout a three dimensional region called the diffuse layer. The diffuse layer extends from the OHP into the bulk of the solution. The charge density in the diffuse layer is σ^d. The total charge density on the solution side of the double layer is σ^s, which is equal to and opposite the total charge on the solid side. Thus,

$$\sigma^s = \sigma^i + \sigma^d = -\sigma^M \qquad 2.8$$

Figure 10 depicts the proposed model where anions are specifically adsorbed.

In 1924, Stern modified the Gouy-Chapman model by including a compact layer as well as Gouy's diffuse layer. The compact Stern layer consisted of a layer of specifically adsorbed ions [56]. Grahame divided the Stern layer into two regions. He denoted the closest approach of the diffuse ions to the electrode surface as the outer Helmholtz plane (this is sometimes referred to as the Gouy plane). The layer of adsorbed ions at the electrode surface was designated as being the inner Helmholtz plane
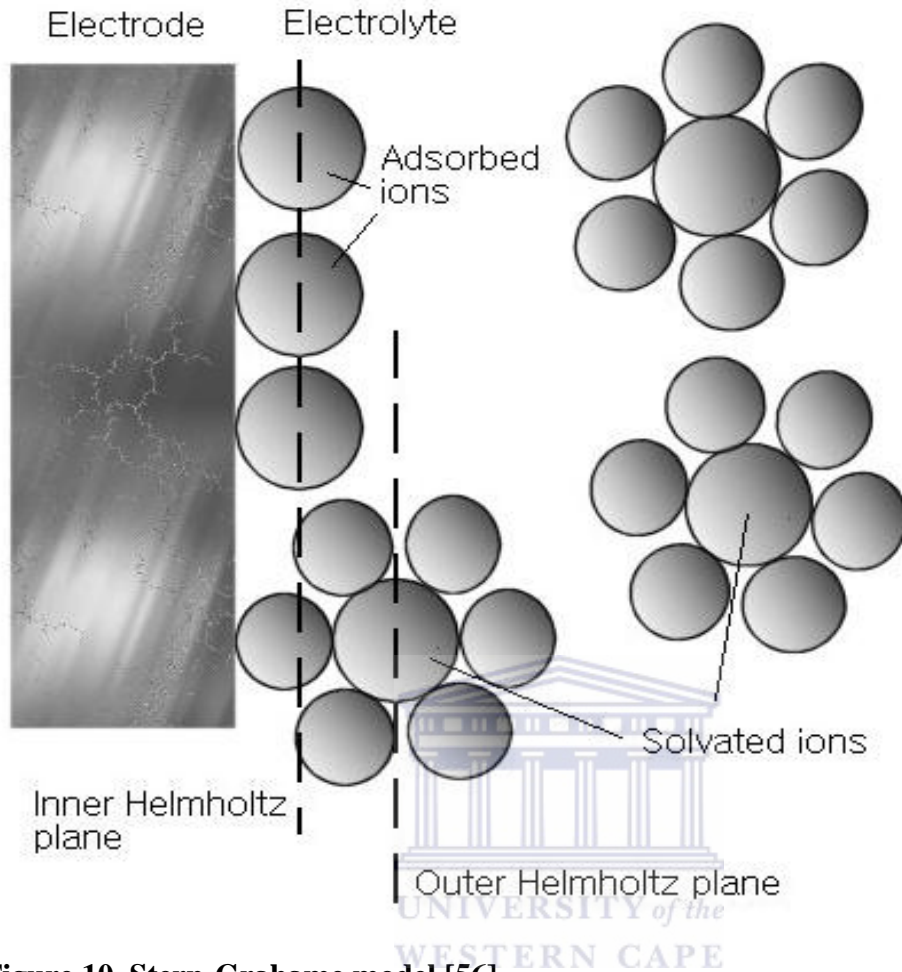
Figure 10. Stern-Grahame model [56]

The capacitance associated with the charge held at the OHP and independent of potential is C_H. The diffuse layer charge, C_D, will vary with electrolyte concentration and potential. Grahame combined the capacitance resulting from the Stern layer, C_H, and that resulting from the diffuse layer, C_D. The total capacitance, C, is then described by Equation 2.9;

$$\frac{1}{C} = \frac{1}{C_H} + \frac{1}{C_D}$$

2.9

In systems near the point of zero charge and low electrolyte concentration, one can expect C_D to vary in a V-shape fashion. At large electrolyte concentrations or large polarizations in dilute media, C_D becomes so large that the contribution to the overall

capacitance is negligible meaning that the diffuse layer effect can be ignored. Equation 2.9 becomes invalid if specific adsorption of ions occurs, however, and if this is the case, the capacitance is equated by Equation 3.0 [26].

$$\frac{1}{C} = \frac{1}{C_H} + \frac{1}{C_D}(1 + \frac{\partial \sigma_A}{\partial \sigma})$$ 3.0

σ is charge density on the electrode, and σ_A is the surface charge of the adsorbed ions. However, this model does not take into account the adsorption of water molecules and other adsorbed ions.

In 1963 Bockris, Devanathan and Muller proposed a model (Figure 11) that included the action of the solvent [56]. They suggested that a layer of water was present within the inner Helmholtz plane at the surface of the electrode. The dipoles of these molecules would have a fixed alignment because of the charge in the electrode. Some of the water molecules would be displaced by specifically adsorbed ions. Other layers of water would follow the first, but the dipoles in these layers would not be as fixed as those in the first layer. However, this modern model still cannot be used to elucidate the situation inside the nanopores and to predict the complications associated with nanopores such as ion pairing and limited mobility. More accurate models are needed to better understand the double layer structure. Despite the theoretical difference between EDLC and pseudocapacitance, often both contribute to the actual capacitance of a supercapacitor. Calculation of the capacitance of the supercapacitor is more difficult due to the complex phenomena occurring near the pores and the pseudocapacitance involved [57].
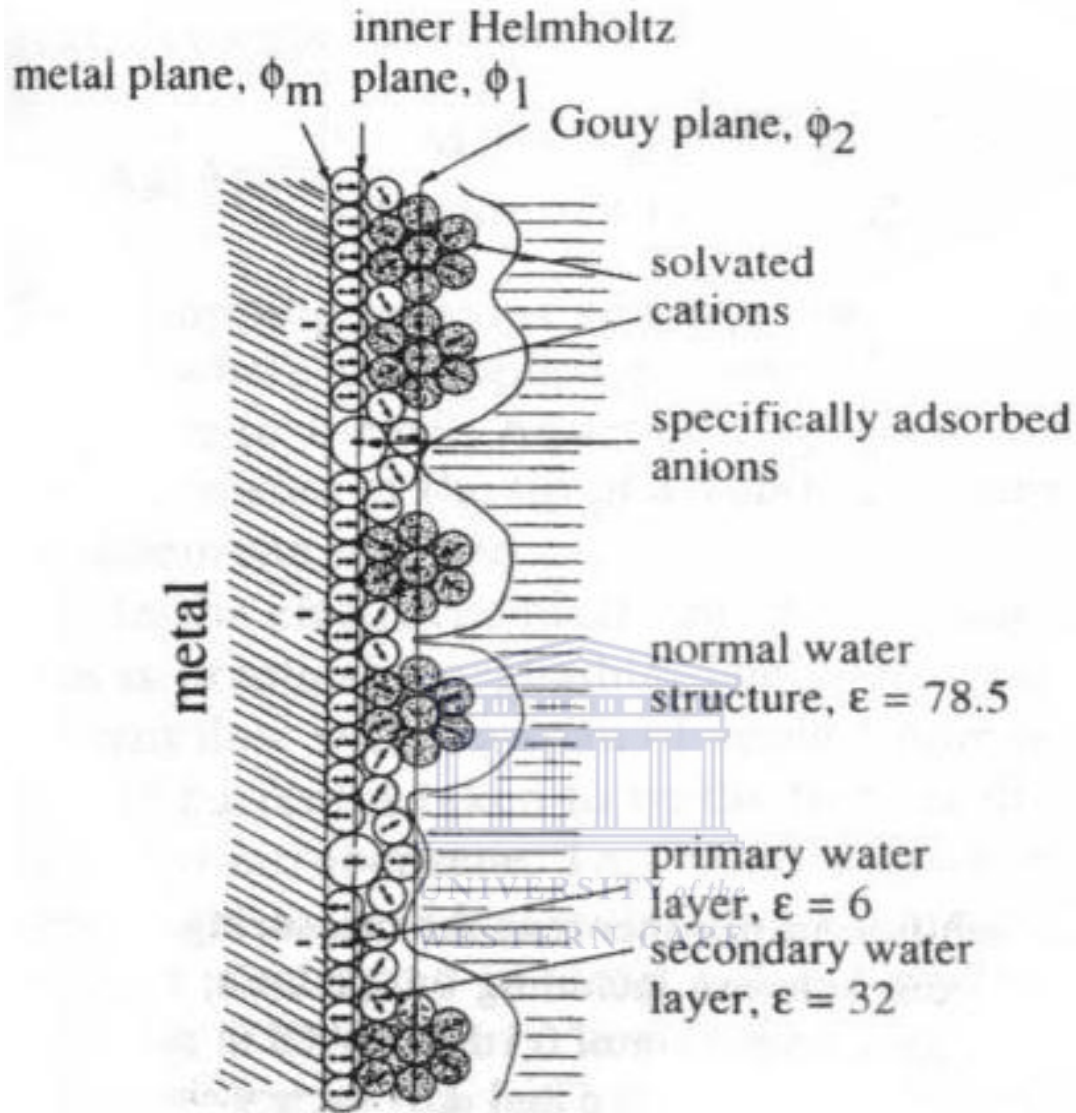
Figure 11. A double layer model including layers of solvent [56]

2.3.3 Construction of a conventional supercapacitor

In the construction of a conventional supercapacitor, two electrodes are immersed in an electrolyte, with an ion permeable separator located between the electrodes (figure 12).
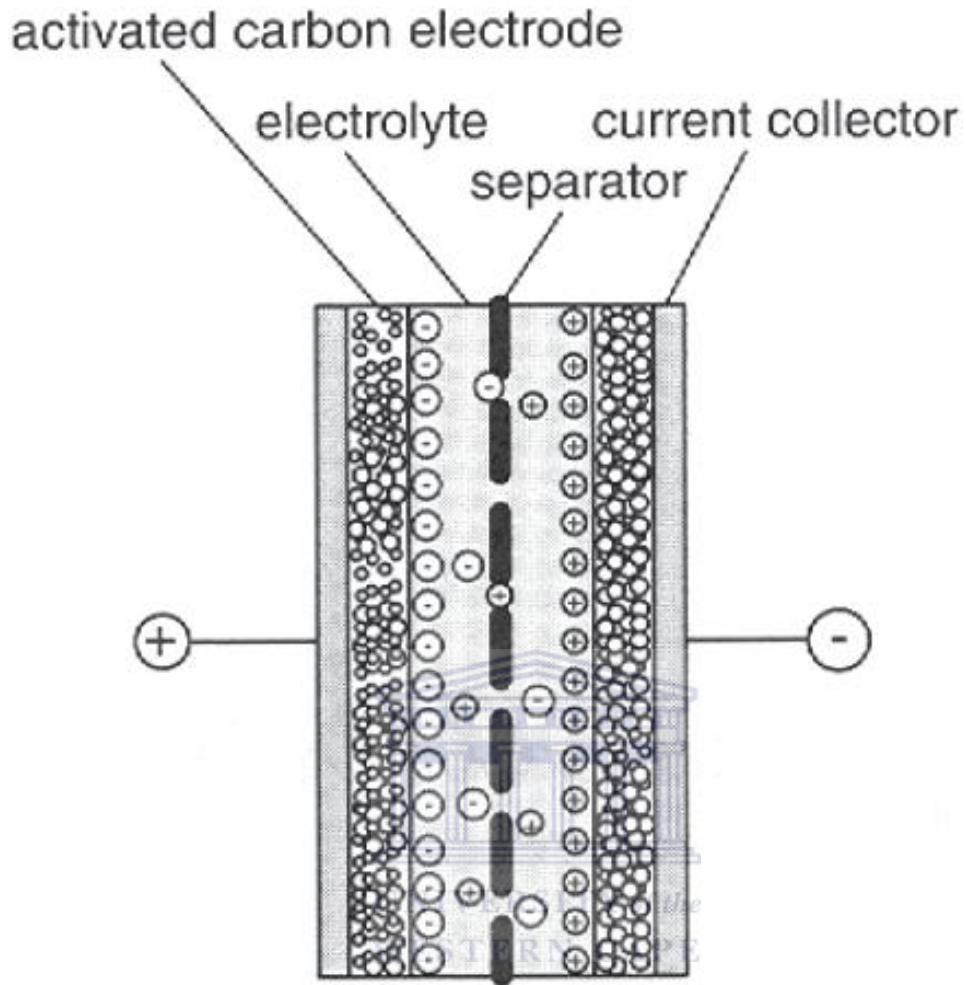
Figure 12. Representation of an electrochemical double layer capacitor, in its charged state [58].

Each electrode–electrolyte interface represents a capacitor so that the complete cell can be considered as two capacitors in series. For a symmetrical capacitor i.e. one with similar electrodes, the overall cell capacitance is determined by the series equivalent circuit. Thus,

$$\frac{1}{C_{cell}} = \frac{1}{C_1} + \frac{1}{C_2} \qquad\qquad 3.1$$

2.4 Electrode materials for supercapacitors

The development of supercapacitors seeks to develop optimal electrode materials able to provide a high and efficient accumulation of electrical energy with a simultaneous long durability. There are three main categories for supercapacitor electrode materials. These are; (i) carbon based, (ii) transition metal oxides and (iii) conductive polymer materials. The salient features of these different classes of materials are discussed in this brief review.

2.2.1 Carbon based electrode materials

The main factors that dictate the selection of carbon for many electrochemical applications are its accessibility, low cost, easy processability, as well as different forms that are attainable (powder, fibers, foams, fabrics, composites, foils, mats, monoliths) and adaptable porosity with various surface functionality [59]. Carbon electrodes are well polarizable, chemically stable in different solutions (acidic, basic, aprotic) and in a wide range of temperatures. The amphoteric character of carbons, both electron donor/acceptor, and with the possibility of simultaneous presence of acidic/basic surface groups, allows the electrochemical properties of materials based on carbon to be extensively used. The properties of carbon materials are strongly affected by the preparation method. Hence, the selection of the synthesis route, type of precursor, heating, atmosphere and temperature of pyrolysis allows to control the final product but also to design carbons for a demanded practical target. Different carbon materials including active carbons, aerogels, xerogels, nanotubes, etc, have been already tested for supercapacitors. Generally, highly developed surface area, which is characteristic for microporous carbons, is necessary for formation of electrical double layer but presence of

mesopores are crucial if a high propagation of charge is demanded [6, 58]. Of the forms of carbon, applications of carbon nanotubes as electrode materials for supercapacitors have ignited significant worldwide investigation on their microscopic and macroscopic porous structures and electrochemical behavior.

CNTs are remarkable nanostructure tubes of carbon that resemble rolled up graphene sheets. The tubes may be single tubes, known as single walled carbon nanotubes (SWCNT), or comprised of two or more nested concentric tubes, known as multi-walled carbon nanotubes (MWCNT). The diameter of a SWCNT is typically on the order of 1 nm, whereas that of a MWCNT depends on the number of concentric tubes, and ranges from several nanometers up to approximately 100 nm. The specific surface area of a MWCNT is inversely proportional to its diameter, and varies from <100 m^2 g^{-1} for relatively thick MWCNT to >1000 m^2 g^{-1} for SWCNT. The unique properties of high surface area, high electrical conductivity, good chemical stability and significant mechanical strength have promoted major research efforts aimed at finding practical applications for these materials. They have been evaluated as electrodes for supercapacitors, batteries and sensors [60-63]. Composites of carbon nanotubes and polyaniline (PANi) have been found to exhibit superior characteristics than pure PANi or pure CNTs. They show much higher specific capacitance, specific energy and specific power and excellent long cyclic stability [64-65]. The uniform dispersion of CNTs adheres strongly to the PANi matrix by the formation of a charge transfer complex rather than the weak van der Waals interactions between them. This maybe due to the fact that CNTs are a good electron acceptor and aniline is a fairly good electron donor. This complex with strong interactions leads to charge stabilization and effectively promote the

protonation of PANi. This may then serve as condensation nuclei to increase the propensity for the polymer to coat on the tubes to form the composite. This improves dispersion of SWCTs into the PANi matrix and results in enhanced electric conductivity [66-67]. In their investigation of capacitance of CNT/polymer composite and their configurations, Frackowiak *et al* [68] showed that a 20 wt % of CNTs in a PANi/CNT electrodes is sufficient to ensure a good permeability for the electrolyte and hence a high electrochemical performance. They also showed that capacitance values of polymer/CNTs are strongly dependent on cell configuration. This has been shown to be the case by other workers [69]. In their study of the influence of microstructure on the supercapacitive behaviour of PANi/SWCT composites, Gupta *et al* [64] has shown that the specific capacitance of PANi/CNT composite is strongly influenced by their microstructure with the microstructure itself depending on the wt % of PANi deposited. They found that morphologies of the PANi/SWCNT composites were found to vary with the diameter of PANi.

Of a comparable mechanical strength to that of carbon nanotubes is graphene, the perfectly flat monolayer of sp^2-carbon-atom tightly packed into a two dimensional honeycomb lattice (Fig. 13) [70-71]. When individual graphene sheets where isolated from mechanically cleaved graphite, they were found to exhibit unusual electronic properties arising from the confinement of electrons in two dimensions [71]. Graphene is a giant macromolecule that conducts both electricity and heat well in two dimensions with individual graphene sheets having a theoretical specific surface area more than double that of the finely divided activated carbon and a mechanical strength comparable

31

only to that of carbon nanotubes which can be considered as graphene with a twist. It is a two-dimensional (2D) building material for carbon materials of all other dimensionalities (Fig 13) [71-72]. It can be wrapped up into zero dimensional fullerene, rolled into one-dimensional carbon nanotubes (CNTs) or stacked into three-dimensional graphite [70], meaning that the sheets can thus be modified by engineering their shape, size, and chemical structure.
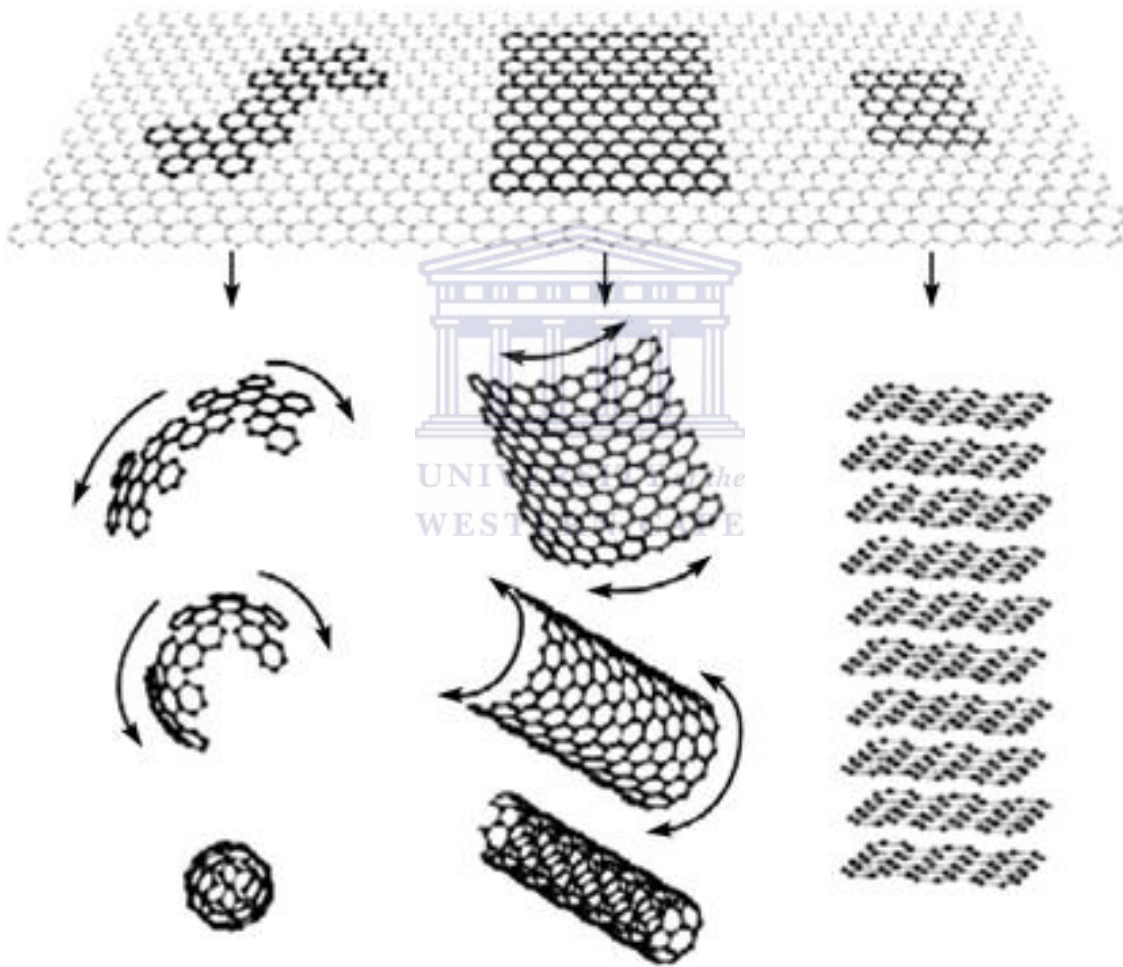
Figure 13. Graphene: Mother of all graphitic forms [70-71]

The single-layer graphene is a zero band gap semiconductor or semimetal and exhibits

fascinating properties such as a perfect ballistic effect, a room-temperature fractional quantum Hall effect and an ambipolar electric field effect [73]. Based on these excellent performances coupled with its low production cost in large quantities, makes graphene commercially attractive and a promisingly useful material as atomically thin yet robust components for nano-electronic and nano-electromechanical device applications in the fields of energy storage, biomedicine, information transmission and in nanocomposite materials as well as in nanoscale building blocks for new materials. The production cost of graphene sheets in large quantities is much lower than that of carbon nanotubes making it commercially attractive as atomically thin yet robust components for nanoelectronic and nanoelectromechanical devices and as nanoscale building blocks for new materials [74].
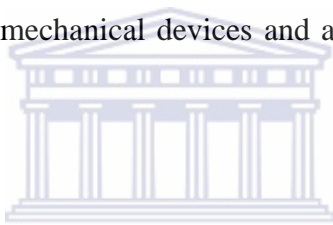
2.2.2 Conducting Polymers

Conducting polymers are organic polymers that conduct electricity. For many years, all carbon based polymers were rigidly regarded as insulators, extensively utilized by the electronics industry as inactive packaging and insulating materials because of their insulating property. The idea that plastics could be made to conduct electricity would have been considered to be absurd. This narrow perspective rapidly changed with the discovery in 1960 of intrinsically conducting polymers (ICPs), commonly known as synthetic metals. These are organic polymers that possess the electrical, electronic, magnetic and optical properties of a metal while retaining the mechanical properties, commonly associated with a conventional polymer. This class of polymers is inherently conducting in nature due to the presence of a conjugated π-electron system in their structure. ICPs have a low energy optical transition, low ionization potential and a high

electron affinity [75]. The unique electronic properties of the conjugated polymers are derived from the presence of π-electrons, the wave functions of which are delocalized over a long portion of the polymer chain when the molecular structure of the backbone is planar. It is therefore necessary that there are no large torsion angles at the bonds, which would decrease the delocalization of the π-electrons system. The essential properties of the delocalized π-electrons system, which differentiate a typical conjugated polymer from a conventional polymer with σ-bonds are: (a) the electronic (π) band gap (Eg) is relatively small at between 1 to 3.5 eV with corresponding low excitation and semi-conducting behaviour; (b) the polymer molecules can be easily oxidized or reduced, usually through charge transfer with atomic or molecular dopant species, to produce conducting polymers; (c) net charge mobility in the conducting state are large enough so that high electrical conductivities are realized, and (d) presence of quasi − particles, which, under certain conditions, may move relatively freely through the material [76]
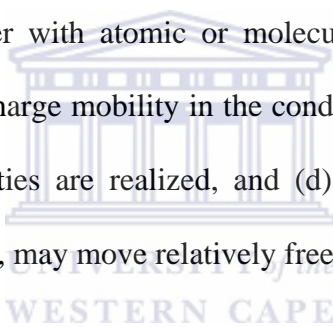
A high level of conductivity (near metallic) can be achieved in ICPs through oxidation–reduction as well as doping with a suitable dopant [75]. The first ICP to be discovered was polyacetylene, synthesized by Shirakawa *et al* [77]. They found that the conductivity of polyacetylene could be increased by several orders of magnitude through chemical doping and in reality it can be converted from an insulator to a metal like conductor. This discovery heralded the dawn of a new era of conducting polymers. Following the study other, polymers such as polypyrrole, polythiophene, polyaniline, poly(phenylene vinylene), and poly(p-phenylene), as well as their derivatives, have been synthesized and reported. Since Shirakawa, interest in ICPs has developed through three stages:

34

(i) An initial interest motivated by their unique properties and practical possibilities;

(ii) A decline in interest owing to difficulties in processing and poor mechanical properties;

(iii) Renewed interest following the discovery of solution and melt processibility of Pani in the early 1990s [78].

ICPs can generally be divided into four primary types of electrically active polymer systems based on their degrees of conductivity [79]. First, composites in which an insulating polymer matrix is filled with a particulate or fibrous conductive fillers such as a carbon or a metal to impart high conductivity are the most widely used conducting polymeric systems with wide applications in interconnections, printed circuit boards, encapsulations, heat sinks, conducting adhesives, electromagnetic interference (EMI) shielding, electrostatic discharge (ESD), and aerospace engineering. Second, ionically conducting polymers which have their application in the battery industry, the origin of their electrical conductivity is a result of the movement of ions present in the system. An example of such a polymer is polyethylene oxide, in which lithium ions are mobile. The third group is the redox polymers in which the system contains immobilized redox centers (electroactive centers) which are not necessarily in contact with one another, but can conduct charge by electron transfer from one center to another through "hopping" mechanism. During conduction, electrons tunnel from one redox center to another through an insulating barrier. The systems need to have a large number of redox centers to increase the probability of such tunneling. The last group is the conjugated polymers. These polymers consist of alternating single and double bonds, creating an extended π-

network. The movement of electrons within this π-framework is the source of conductivity. A dopant is required to increase the level of conductivity for this type of polymers.

Valence electrons in traditional polymers such as polyethylene are bound in sp^3 hybridized covalent bonds. Such sigma-bonding electrons have low mobility and do not contribute to the electrical conductivity of the material. The situation is completely different in conjugated materials. The extended π -systems of conjugated polymer are highly susceptible to chemical or electrochemical oxidation or reduction. These alter the electrical and optical properties of the polymer, and by controlling this oxidation and reduction, it is possible to precisely control these properties. Since these reactions are often reversible, it is possible to systematically control the electrical and optical properties with a great deal of precision. It is even possible to switch from a conducting state to an insulating state. Conducting polymers have backbones of continous sp^2 hybridized carbon centers. One valence electron on each center resides in a p_z orbital, which is orthogonal to the other three sigma-bonds. The electrons in these delocalized orbitals have high mobility, when the material is doped by oxidation, which removes some of these delocalized electrons. Thus the p-orbitals form a band, and the electrons within this band become mobile when it is partially emptied. In principle, these same materials can be doped by reduction, which adds electrons to an otherwise unfilled band. Conductive organic polymers associated with protic solvents may also be "self-doped" as the solvent abstract electrons from the polymer.

The field of conducting polymers has witnessed an explosive growth in recent years with electrically conducting conjugated polymers such as polyaniline, polythiophene, polypyrrole and polyacetylene as well as their derivatives receiving considerable attention because of their remarkable properties and numerous application potentials in such multidisciplinary areas as electrical, electronics, thermoelectric, electrochemical, electromagnetic, electromechanical, electro-luminescence, electro-rheological, chemical, membrane, and sensors [80-84].

However, applications of such polymers still remain limited because most of them show lower level of conductivity compared to metals. Also one of the main difficulties in the control of the structure-properties relationship is their infusibility and poor solubility in available solvents such that most of them cannot be characterized in solution. This has been improved through doping. Also the presence of various substituent groups on the monomer unit increases solubility but can decrease the conductivity [85]. Methods of preparation, chemical constitution and doping can influence the physical and chemical properties of polyaniline.

Polyaniline (PANi) is a typical phenylene based polymer having a chemically flexible -NH- group in the polymer chain flanked by phenyl ring on either side with its physicochemical properties being strongly related to the proportion of aryl amine and quinone imine units present. PANi represents a class of macromolecules whose electrical conductivity can be varied from an insulator to a conductor by the redox process. This

polymer can achieve its highly conductive state either through the protonation of the imine nitrogens or through the oxidation of amine nitrogens. For example the conducting state of PANi can be obtained in its 50% oxidized emeraldine state in aqueous acids like HCl and the resulting material is a p-type semiconductor. PANi possesses two voltammetric redox pairs including three stable oxidation states, with the half-oxidized state (emeraldine) being highly conductive in its protonated state. With the extent of doping, polyaniline can have four different oxidation states [80]; Leucomeraldine base (LEB), Emeraldine (EB), Emeraldine salt (ES) and Pernigraniline (PNB). Oxidative doping of the leucomeraldine base or protonic acid doping of the emeraldine base material produces the conducting emeraldine salt. Existence of different oxidation states of PANi makes it useful as an electrode material in electrochemical capacitors [86-89].

A partial oxidation of PANi usually leads to the reorganization of bonds, resulting in an increase in electronic conductivity. In the conducting state, there are regions that are three-dimensionally ordered in which the conducting electrons are three-dimensionally delocalized and regions where the polymer is strongly disordered, in which conduction electrons diffuse through one-dimensional polymer chains that are nearly electrochemically isolated. One dimensional localization in these nearly isolated chains lead to decrease in conductivity with decrease in temperature.

Chapter 3

Experimental: Analytical Techniques

3.1 Scanning Electrochemical Microscopy

3.1.1 Operational Principles

Scanning electrochemical microscopy (SECM) is a technique capable of probing surface reactivity of materials at microscopic scales. In SECM current flows through a very small mobile electrode tip called an ultramicroelectrode (UME) near a conductive, semiconductive, or insulating substrate immersed in a solution containing an electroactive species, the redox mediator. The current is used either amperometrically (or potentiometrically) to interrogate the activity and/or topography of an interface on a localized scale at a substrate as the tip is moved near the substrate surface [90-95]. The UME is fabricated as a conductive disk of metal or carbon in an insulating sheath of glass or polymer. Many different types of UMEs have been fabricated, e.g., microband electrodes, cylindrical electrodes, microrings, disk-shaped, and hemispherical electrodes. The disk geometry is preferred for SECM tips. UMEs offer important advantages for electroanalytical applications including greatly diminished ohmic potential drop in solution and double-layer charging current, the ability to reach a steady state in seconds or milliseconds, and a small size allowing one to do experiments in microscopic domains. The precise positioning capabilities, which make high spatial resolution possible, give the SECM an important edge over other electrochemical techniques employing UMEs. A basic operation of SECM involves means of moving the tip with a resolution down to the Angstrom unit region by means of piezoelectric elements or stepping motors driving

differential springs. A bipotentiostat controls the potentials of the tip and/or the substrate versus the reference electrode and measures the tip and substrate currents. The SECM instrument is often mounted on a vibration-free optical table to isolate it from environmental vibrations. This is especially important for high resolution and low-current measurements. The tip can be moved normal to the surface (the z- direction) to probe the diffusion layer, or the tip can be scanned at constant z across the surface (the x and y directions). The tip and substrate are part of an electrochemical cell that usually also contains other (e.g., auxiliary and reference) electrodes. The substrate may also be biased and serve as the second working electrode.
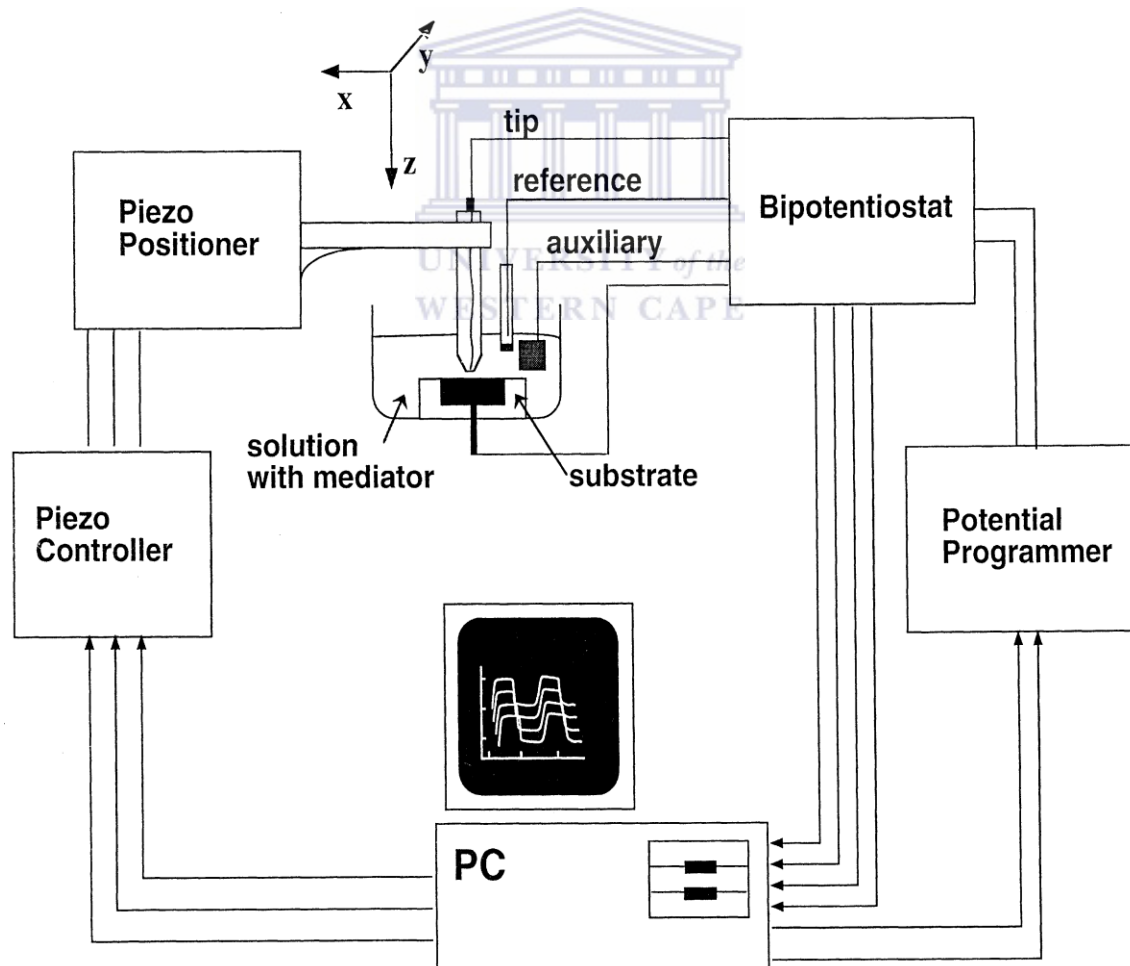
Figure 14. Block diagram of the SECM apparatus [1].

The electrode reaction at the tip gives rise to a tip current that is affected by the substrate. This tip current is controlled by electrochemical reactions at the tip electrode and sample substrate and is a function of the tip/substrate distance and the conductivity and chemical nature of the sample substrate. The measurement of tip current can thus provide the information about sample topography and its electrical and chemical properties. Several SECM modes of operation can be realized. These include feedback mode [90-91], generation/collection (G/C) mode [93], penetration mode [95] and ion transfer feedback mode [96-97]. In this work, the feedback mode was used. This mode offers a simple technique of characterizing the surface conductivity of the polymeric nanocomposite substrate.

3.1.2 Construction of carbon paste electrode (CPE)

The increasing application of chemically modified carbon paste electrodes [98-99] for electroanalytical measurements has received considerable attention for electroanalytical measurements. The operation mechanism of such chemically modified carbon paste electrodes depends on the properties of the modifier materials used to promote selectivity and sensitivity towards the target species. In this work, carbon paste electrodes were fabricated for use as SECM sample substrate. The modified carbon paste electrode were prepared by mixing already prepared metal oxides or their sulphonated polymer nanocomposites anchored on activated graphitic carbon powder with paraffin binder in the ratio of 2 gm to 1 mL. This mixture was mixed in a mortar for at least 20 min to produce the final semi-dry/wet paste. The carbon paste was packed into an electrode body consisting of fabricated Teflon holes of 3 mm deep by 3 mm diameter fitted with copper

41

rod which serves as an external electric contact. Appropriate packing was achieved by pressing and polishing the electrode surface against a perfectly polished smooth Teflon sheet to produce a very smooth electrode surface. The electrode was then fitted into a μ-Tricell.

3.1.3 μ-Tricell cell unit configuration.

The 15 μM diameter UME is cleaned by first polishing it on wet 1 μM alumina-oxide (Al_2O_3) size particle polishing powder followed by 0.5 and lastly 0.03 μM Al_2O_3 powder all placed on alumina pads Buehler (Illinois, USA) aligned on a glass substrate. It was then rinsed with ultra-pure distilled de-ionised water and sonicated in ethanol and ultra-pure water for 10 minutes each. The modified CPE was fitted into the tricell making sure that it was water tight. The cell was then mounted onto the leveled black base of the SECM making sure that its window faces the direction of the VCAM camera. It is then leveled using the bubble-leveling device and Allen-key screw and after the UME is held in position using the SECM probe clamp, the four electrodes (counter electrode, reference electrode, UME as working electrode and CPE the sample substrate) then connected in place. The cell was then filled with 0.1M potassium chloride containing 0.005M potassium ferricyanide mediator solution. The feedback approach curve and potential area map experiments were then performed using the SECM model 370 in SECM mode.

3.2 Fourier Transform Infra-red spectroscopy (FTIR)

3.2.1 Basic principles

Fourier Transform-Infrared Spectroscopy (FTIR) [100-104] is a mechanically simple, fast non-destructive analytical technique used to determine qualitative and quantitative

features of IR-active molecules in organic or inorganic solid, liquid or gas samples. It's a precise measurement method which requires no external calibration and can be used to identify an unknown material, to determine the quality or consistency of a sample and the amount of components in a mixture when a material is irradiated with infrared radiation. Absorbed IR radiation usually excites molecules into a higher vibrational state and the wavelength of light absorbed by a particular molecule is a function of the energy difference between the at-rest and excited vibrational states. The wavelengths that are absorbed by the sample are characteristic of its molecular structure [101]. Fourier Transform Infrared (FT-IR) spectrometry was developed in order to overcome the limitations encountered with analytical dispersive instruments. The main difficulty with dispersive instruments was the slow scanning process. A method for measuring all of the infrared frequencies simultaneously, rather than individually, was needed. A solution was developed which employed a very simple optical device called an interferometer. The interferometer produces a unique type of signal which has all of the infrared frequencies "encoded" into it. The signal can be measured very quickly, usually on the order of one second or so. Thus, the time element per sample is reduced to a matter of a few seconds rather than several minutes. Most interferometers employ a beamsplitter which takes the incoming infrared beam and divides it into two optical beams. One beam reflects off of a flat mirror which is fixed in place. The other beam reflects off of a flat mirror which is on a mechanism which allows this mirror to move a very short distance (typically a few millimeters) away from the beamsplitter. The two beams reflect off of their respective mirrors and are recombined when they meet back at the beamsplitter. Because the path that one beam travels is a fixed length and the other is constantly changing as its mirror

43

moves, the signal which exits the interferometer is the result of these two beams interfering with each other. The resulting signal is called an interferogram which has the unique property that every data point (a function of the moving mirror position) which makes up the signal has information about every infrared frequency which comes from the source. This means that as the interferogram is measured, all frequencies are being measured simultaneously. Thus, the use of the interferometer results in extremely fast measurements. Because the analyst requires a frequency spectrum (a plot of the intensity at each individual frequency) in order to make identification, the measured interferogram signal can not be interpreted directly. A means of "decoding" the individual frequencies is required. This can be accomplished via a well-known mathematical technique called the Fourier transformation. This transformation is performed by the computer which then presents the user with the desired spectral information for analysis [102]. The normal instrumental process [100-104] includes the IR source which emits infrared energy from a glowing black-body source.
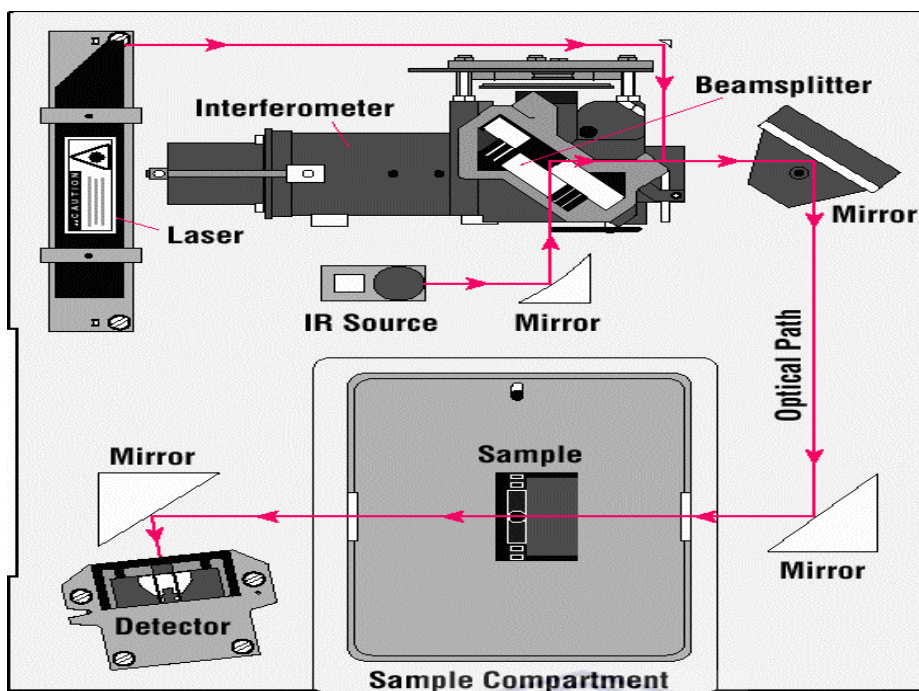
Figure 15. A simple FTIR spectrometer layout [104]
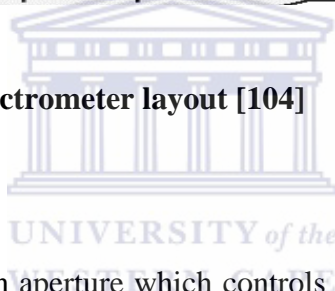
The IR beam passes through an aperture which controls the amount of energy presented to the sample (and, ultimately, to the detector). It enters the interferometer where the "spectral encoding" takes place and the resulting interferogram signal then exits the interferometer. A laser beam is superimposed to provide a reference for the instrument operation. The beam enters the sample compartment where it is transmitted through or reflected off of the surface of the sample, depending on the type of analysis being accomplished. This is where specific frequencies of energy, which are uniquely characteristic of the sample, are absorbed. The beam finally passes to the detector for final measurement. The detectors used are specially designed to measure the special interferogram signal. The measured signal is digitized and sent to the computer where the Fourier transformation takes place. The final FTIR spectrum is then presented to the user

45

as plots of intensity versus wavenumber for interpretation and any further manipulation. Because there needs to be a relative scale for the absorption intensity, a background spectrum must also be measured. This is normally a measurement with no sample in the beam. This can be compared to the measurement with the sample in the beam to determine the percent transmittance resulting in a spectrum which has all of the instrumental characteristics removed. Thus, all spectral features which are present are strictly due to the sample. A single background measurement can be used for many sample measurements because this spectrum is characteristic of the instrument itself. To identify the material being analyzed, the unknown IR absorption spectrum is compared with standard spectra in computer databases or with a spectrum obtained from a known material. Spectrum matches identify the polymer or other constituent(s) in the sample. Absorption bands in the range of 4000 - 1500 wavenumbers are typically due to functional groups (e.g., -OH, C=O, N-H, CH3, etc.). The region from 1500 - 400 wavenumbers is referred to as the fingerprint region. Absorption bands in this region are generally due to intramolecular phenomena and are highly specific to each material. The specificity of these bands allows computerized data searches within reference libraries to identify a material.

3.3 Scanning Electron Microscopy (SEM)

3.3.1 Basic operational principle

SEM is a microscopic technique that uses a focused beam of high-energy electrons to systematically scan across the surface of a solid specimen generating a variety of signals at the surface through the electron-sample interactions revealing information about the sample including external morphology (texture), chemical composition, and crystalline

46

structure and orientation of materials making up the sample. A 2-dimensional image is generated that displays spatial variations in these properties.

An electron gun generates the beam which is accelerated by a high voltage and formed into a fine probe by electromagnetic lenses. The electron-optical column, through which the beam passes, is held under high vacuum to allow a free path for the electrons to pass through as well as to prevent high voltage discharge. The first lens, the condenser lens, causes the beam to converge and pass through a focal point just above a condenser aperture. The intensity of the electron beam when it strikes the specimen, and hence the brightness of the image signal is primarily determined by the condenser lens, in conjunction with the chosen accelerating voltage. The beam diverges again below the condenser aperture and is brought into focus at the specimen through the demagnification of a final lens, the objective lens which determines the diameter of the spot size of the electron beam at the specimen, which in turn determines the specimen resolution [105-106]. All SEM instruments are built around an electron column (see figure 16), which produces a stable electron beam, controls beam current, beam size and beam shape.
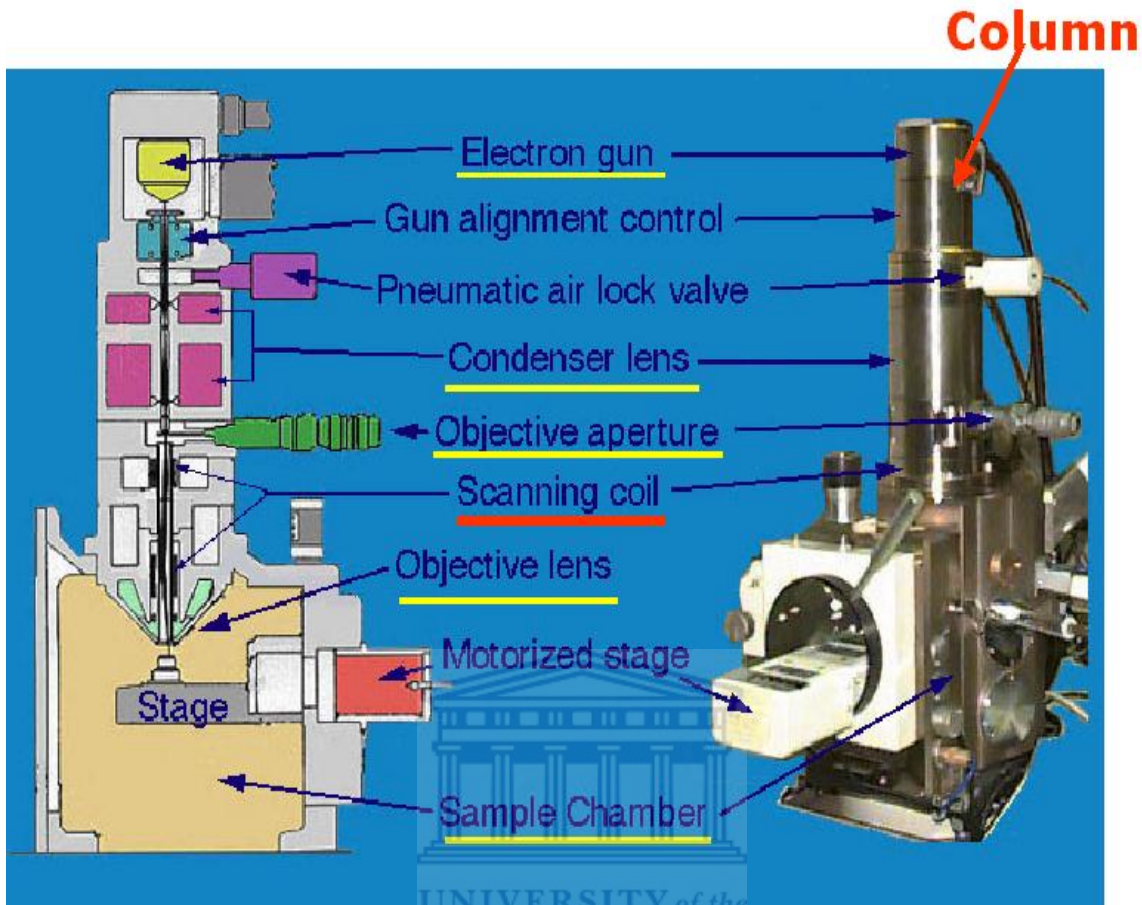
Figure 16. Schematic of a SEM [107]

The degree to which a specimen can be magnified is not the only consideration in microscopy. A far more important factor to consider is its resolution. The limit of resolution is the smallest separation at which two points can be seen as distinct entities. As the resolution improves, the images of the objects tend to separate until they can be independently visualized. This ability of the instrument to resolve fine structure is limited by the diameter of the probe, and the number of electrons contained within the beam. The image is effectively made up of lines of image points, each point being the size of the beam probe. If a structure is smaller than the probe, it is not resolved. If however, the probe is too small in relation to the area being imaged, it misses out on several smaller

regions on the specimen thereby forming a poor quality image. There is a finite relationship between magnification and the optimum probe size to obtain the derived signal level, and it varies from specimen to specimen. The relationship between resolution and wavelength is given by Abbe's equation;

$$d = \frac{0.612\lambda}{n\sin\theta}$$
3.1

where d is the resolution, λ the wavelength of the energy source, n the refractive index of the medium through which the energy source travels, and θ the aperture angle. Abbe's equation signifies the mathematical limit of resolution for an optical system.

Accelerated electrons in a SEM carry significant amounts of kinetic energy which is dissipated as a variety of signals produced by electron-sample interactions when the incident electrons are decelerated in the solid sample [107]. These signals include secondary electrons (that produce SEM images), diffracted backscattered electrons (that are used to determine crystal structures and orientations of minerals), photons (characteristic X-rays that are used for elemental analysis and continuum X-rays), visible light, and heat. Secondary electrons and backscattered electrons are commonly used for imaging samples: secondary electrons are most valuable for showing morphology and topography on samples and backscattered electrons are most valuable for illustrating contrasts in composition in multiphase samples (i.e. for rapid phase discrimination). X-ray generation is produced by inelastic collisions of the incident electrons with electrons in discrete orbitals (shells) of atoms in the sample. As the excited electrons return to lower energy states, they yield X-rays that are of a fixed wavelength (that is related to the difference in energy levels of electrons in different shells for a given element). This is

49

especially useful in qualitative determination of chemical compositions using Energy-Dispersive X-Ray Spectroscopy (EDS).

3.3.2 Energy-Dispersive X-Ray Spectroscopy (EDS)

Energy Dispersive X-ray Spectroscopy (EDX or EDS), is a technique based on the collection and energy dispersion of X-rays created when high energy electrons bombard a sample. EDS systems [108-110] are typically integrated into either a TEM or SEM. Either way, the two techniques are often used together. Interaction of an electron beam in the TEM/SEM with a sample target produces a variety of emissions, including X-rays. An energy-dispersive (EDS) detector is used to separate the characteristic X-rays of different elements into an energy spectrum in order to determine the abundance of specific elements. EDS can be used to find the chemical composition of materials down to a spot size of a few microns, and to create element composition maps over a much broader raster area. Together, these capabilities provide fundamental compositional information for a wide variety of materials.

3.4 X-ray diffraction (XRD) Spectroscopy

3.4.1 Basic theory

A crystal lattice is a regular three-dimensional distribution (cubic, rhombic, etc.) of atoms in space. These are arranged so that they form a series of parallel planes separated from one another by a distance d, which varies according to the nature of the material. For any crystal, planes exist in a number of different orientations - each with its own specific d-spacing. Detailed information about the crystal nature of a material can be revealed using X-ray diffraction (XRD) technique. This is a versatile, non-

destructive technique used to reveal detailed information about the chemical composition and crystallographic structure of natural and manufactured materials.

The basic instrumental measurement geometry is depicted in figures 17 and 18 [111]. The sample should preferably exhibit a plane or flattened surface. The angle of both the incoming and the exiting beam is θ with respect to the specimen surface. The diffraction pattern is collected by varying the incidence angle of the incoming x-ray beam by θ and the scattering angle by 2θ while measuring the scattered intensity I as a function of 2θ. Two angles have thus to be varied during a θ/2θ scan. Various types of powder diffractometers are in use. For one set of instruments the x-ray source remains fixed while the sample is rotated around θ and the detector moves by 2θ. For other systems the sample is fixed while both the x-ray source and the detector rotate by θ simultaneously, but clockwise and anticlockwise, respectively. The rotations are performed by a so-called goniometer, which is the central part of a diffractometer. A goniometer of a powder diffractometer (Fig. 17 and 18) comprises at least two circles or – equally – two axes of rotation.
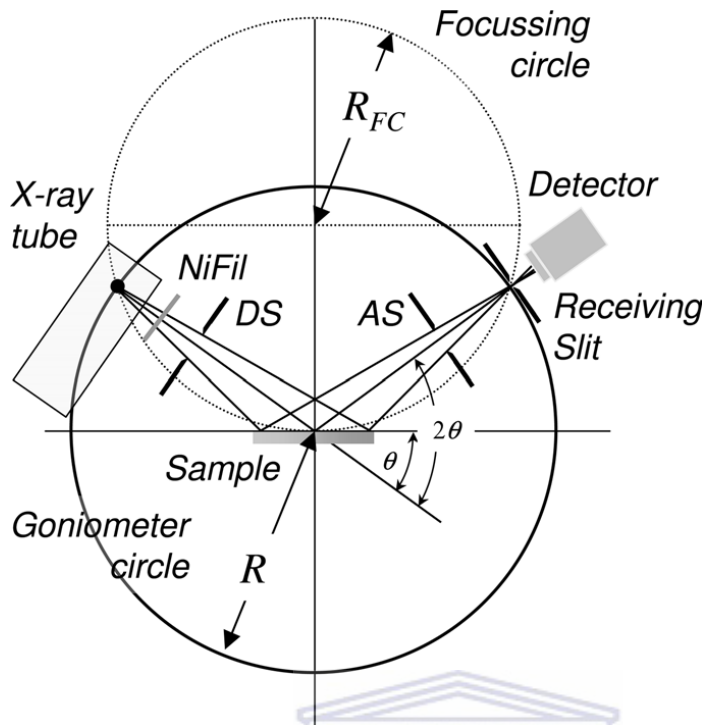
Figure 17. Schematic representation of θ/2θ diffraction in Bragg–Brentano geometry [111].
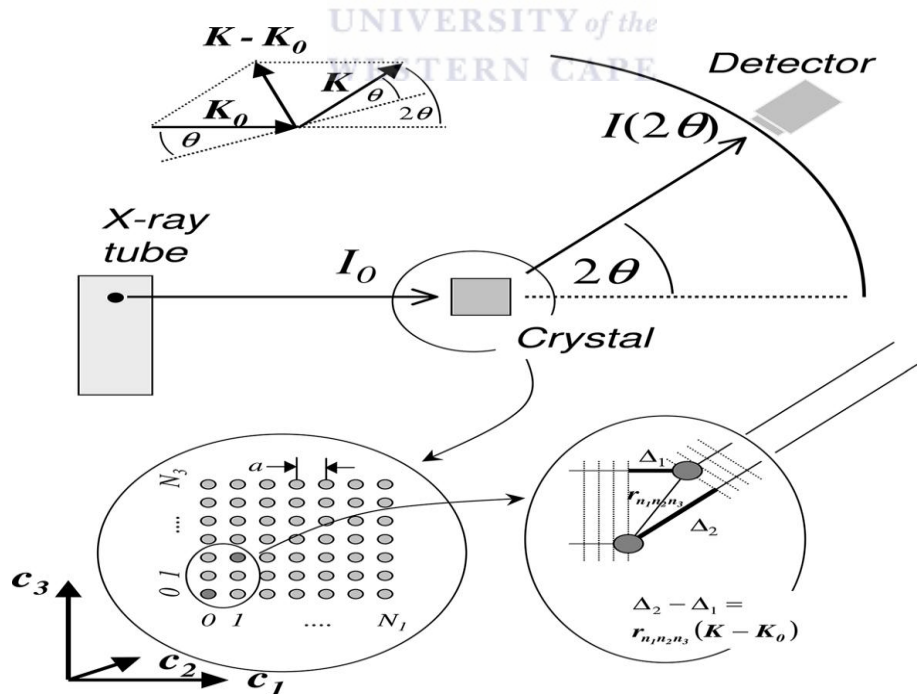
Figure 18. Scattering of x-rays by a Crystallite of simple cubic structure [111].

The high degree of order and periodicity in a crystal can be envisioned by selecting sets of crystallographic lattice planes that are occupied by the atoms comprising the crystal. The planes are all parallel to each other and intersect the axes of the crystallographic unit cell. Any set of lattice planes is indexed by an integer triple indicated by the Miller indices. The distance between two adjacent planes is given by the interplanar spacing d_{hkl} with the indices specifying the Miller indices of the appropriate lattice planes. To observe maximum intensity in the diffraction pattern, Bragg's equation has to be obeyed. The equation is called Bragg equation and was applied by W.H. Bragg and W.L. Bragg [112] in 1913 to describe the position of x-ray scattering peaks in angular space.

Bragg's equation, $2d_{hkl}\sin\theta_B = \lambda$ (3.2)

By varying the angle *theta*, the Bragg's Law conditions are satisfied by different *d*-spacings in polycrystalline materials. Plotting the angular positions and intensities of the resultant diffracted peaks of radiation produces an emission spectrum characteristic of the sample comprising a continuous part, called Bremsstrahlung, and some discrete lines indicative of the chemical elements of the target material. Where a mixture of different phases is present, the resultant diffractogram is formed by addition of the individual patterns. Based on the principle of X-ray diffraction, a wealth of structural, physical and chemical information about the material investigated can be obtained. A host of application techniques for various material classes is available, each revealing its own specific details of the sample studied.

53

3.5 Electrochemical impedance spectroscopy

3.5.1 Basic operational principle

EIS is a technique which involves the application of a sinusoidal electrochemical pertubation (potential or current) to a sample that covers a wide range of frequencies. This multi-frequency excitation allows the measurement of several electrochemical reactions that take place at different rates and the measurement of the capacitance of an electrode.

Electrochemical impedance spectroscopy has been utilized to characterize impedance parameters of supercapacitor electrode materials. Important among these parameters are charge transfer resistance, electrical double layer capacitance, and diffusion resistances. Resistances to transport can be thought of in terms of an electrical circuit, where flow is inhibited by impedances. The definition of impedance, as used in EIS, is given by;

$$Z = \frac{V_0 \sin(\omega t)}{I_0 \sin(\omega t + \phi)} = Z_0 \frac{\sin(\omega t)}{\sin(\omega t + \phi)} \qquad 3.3$$

The Current (Io) and f (phase shift) can be measured as a function of an applied pertubation AC signal (Vo), allowing the determination of impedance, Z [113]. By applying this signal over a spectrum of frequency, the magnitudes of various resistances and capacitances can be determined via an equivalent circuit model.

The two primary regions of resistance in most supercapacitor electrode are at the electrode-electrolyte interfaces and in the bulk electrolyte. The resistances in these regions are typically termed charge transfer resistance and solution resistance, respectively. Another common name for the solution resistance can be ohmic resistance. This resistance can be used to determine conductivity and diffusion of a charged species through the electrolyte. Charge transfer resistance yields important information about

exchange current and electrode polarization [51]. In addition to the resistances in these regions, Electrochemical Double Layers (EDL) form between a charged electrode and surrounding electrolyte. Accumulation of counter-ions near the electrodes gives rise to an electrochemical capacitance at the solid-liquid interface. However, the capacitive behavior is usually not ideal and this non-ideality is attributed to such factors as non-uniform reaction rates on the electrode surface and electrode surface roughness [114]. EDL capacitance is exhibited by phase shift of the signal when performing EIS. EIS measurements allow the study of phenomena happening at the electrodes and within the solid-solution region. Specific parameters related to mass transfer, charge transfer and reaction kinetics can be evaluated using the technique and EIS has been demonstrated to provide insight regarding the total internal resistance of an electrode material.
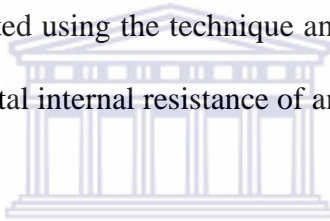
Bode plots and Nyquist plots are both popular forms of displaying EIS results. The Bode plot simply displays impedance and phase shift as functions of frequency. Such information is useful for estimating electrode parameters, considering that behavior in the Bode plots can be associated with either resistive or capacitive elements. In general, impedance at very low phase shift (near 0) is associated with resistances such as charge transfer and ohmic resistances. These low phase shift regions often occur at very high and very low frequencies. In the mid-frequency range (1000 Hz to 1 Hz, for example), impedance responses are often dominated by high phase shift. This generally indicates capacitive behavior [113].

Chapter 4

Experimental: Synthesis of nanostructured materials

4.1 Synthesis of metal oxide nanoparticles

4.1.1 Introduction

Nanoparticles are defined as particulate dispersions or solid particles with a size in the range of 10-100 nm [115]. They are larger than individual atoms and molecules but are smaller than bulk solid. Hence, they obey neither absolute quantum chemistry nor laws of classical physics and have properties that differ markedly from those expected of atoms and molecules or those of bulk solid. Two major phenomenon are responsible for these differences; first the high dispersity of nanocrystalline systems. As the size of a crystal is reduced, the number of atoms at the surface of the crystal compared to the number of atoms in the crystal itself increases. Also, the spacing of the electronic levels and the band gap increases with decreasing particle size. As such, properties which are usually determined by the molecular structure of the bulk lattice become increasingly dominated by the defect structure of the surface resulting in a state of matter representing a transition state between bulk solids and individual atoms. The second phenomenon occurs noticeably only in metals and semiconductors. It is called size quantisation and arises because the size of a nanoparticle is comparable to the de Broglie wavelength of its charge carriers (*i.e.* electrons and holes). Due to the spatial confinement of the charge carriers, the edge of the valence and conduction bands split into discrete, quantized, electronic levels. These electronic levels are similar to those in atoms and molecules. Because of these phenomenon differences, nanoparticles display unique mechanical, optical, electrical, and magnetic properties that differ radically from the corresponding bulk material.

Synthesis methods for nanoparticles are typically grouped into two categories: "top-down" and "bottom-up". The first involves division of a massive solid into smaller portions. This approach may involve milling or attrition, chemical methods, and volatilization of a solid followed by condensation of the volatilized components. This is also referred to as the physical method, a process in which coarse particles are ground to nanoscale particles. Ball-milling requires high mechanical energy which results in straining the particles and in contamination by the material of which the ball mill is made.

The second, "bottom-up", method of nanoparticle fabrication involves condensation of atoms or molecular entities in a gas phase or in solution. The latter approach is far more popular in the synthesis of nanoparticles [116]. Chemical techniques provide for the mixing at the atomic or molecular level, allowing for the production of highly homogeneous materials. Nanoparticles can be synthesized chemically through electrochemical methods [117], hydrothermal techniques [118], chemical vapor deposition [119], sol-gel methods, etc. This work explores the use of sol-gel techniques in the synthesis of binary and ternary mixed metal oxide systems containing tantalum, manganese and nickel. The aim is to obtain a very fine inter-dispersion of the metal oxides and possibly the formation of mixed oxide phases and study the synergetic effects between different pure or mixed oxide phases, which can contribute to the pseudocapacitor activity and even more when they are incorporated to a sulphonated polyaniline nanocomposite.

4.1.2 The sol-gel synthesis

To obtain metal oxides as nanoscale materials with well defined shape, size, and composition, soft-chemistry routes, and in particular sol–gel procedures, offer advantages

such as the possibility of obtaining metastable materials, achieving superior purity and compositional homogeneity of the products at moderate temperatures with simple laboratory equipment, and influencing the particle morphology during the chemical transformation of the molecular precursor to the final oxidic network [120]. Sol-gel processes have been extensively investigated by solid-state chemists for the preparations of metal oxides for decades [121-126]. The process is convenient for its simple procedures, requiring little more than standard solution chemistry. The initial aim in the sol-gel technique is to produce a sol, which is a suspension of solid colloidal particles in a liquid. The colloidal particles may or may not have the chemical composition of the desired end-product. The particles, through van der Waals attraction, eventually connect to form a gel, a 3-dimensional solid network having high porosity and high specific surface area. The gel can simply be dried and ground if a nanoscale powder is the aim. The wet sol may be deposited onto a substrate and then allowed to gel if a thin film is desired. The gel may be heated to induce chemical phase changes, or to densify a thin film or ceramic structure. Sol-gel chemistry is used mainly to produce metal oxides through reactive metal precursors which includes metallic salts M_mX_n and alkoxides $M(OR)_n$, (M is a metal, X is an anion, R is an alkyl group). Metal oxides can be synthesized directly in the initial chemical reaction, or a metal hydroxide may form which can be heated to yield the oxide.

4.1.3 Apparatus and reagents

Analytical grades nickel acetate tetrahydrate [$Ni(OAc)_2.4H_2O$], polyvinyl pyrrolidone (PVP), potassium hydroxide (KOH), citric acid, hydrochloric acid (HCl, 98%), ammonium persulphate (APS, $(NH_4)_2S_2O_8$, 98%), nickel nitrate hexahydrate, sulphuric acid, tantalum ethoxide, absolute ethanol, glacial acetic acid. All chemicals were purchased from Sigma-

58

Aldrich (Cape Town, South Africa). They were used as received without further purification except aniline. Aniline was purified by distillation. The distilled aniline was purged with argon gas and then stored in a freezer at a temperature of below $0\ ^0C$. Falcon tubes, centrifuging machine, vacuum furnace, box furnace. Cyclic voltammetric experiments were carried using a BAS100W integrated and automated electrochemical work station from Bio Analytical Systems, Lafayette, USA. The voltammograms were recorded with a computer interfaced to the BAS 100W electrochemical workstation. Chronopotentiometric measurements were carried out using VoltaLab PGZ 402 from Radiometer Analytical (Lyon, France) and recorded on a computer interfaced with the VoltaLab PGZ 402 work station. A 10 mL electrochemical cell with a conventional three electrode set up was used. The electrodes were: (i) glassy carbon working electrode from BAS either bare or modified with nickel oxide (ii) platinum wire, from Sigma Aldrich, acted as a counter electrode and (iii) Ag/AgCl (3 M KCl) from BAS was the reference electrode. Transmission electron microscopy (TEM) and energy dispersive X-ray spectroscopic analysis of the nickel oxide mounted on a carbon membrane supported on a copper coated or grid was done using a Tecnai G2 F20X-Twin MAT 200 kV Field Emission Transmission Electron Microscope from FEI (Eindhoven, Netherlands. The TEM and EDX specimens were prepared by dispersing an arbitrary amount of solid in ethanol by ultrasonic treatment. A few drops were poured onto a porous carbon membrane or on a copper grid, and then dried in ambient temperature.

4.2 Synthesis of nickel oxide, manganese oxide and tantalum oxide nanostructures

4.2.1 Introduction

Nickel oxide (NiO) has been investigated as a promising material that can be used as battery cathodes, catalysts, gas sensors, supercapacitors electrode materials, electrochromic films, and in magnetic materials [127-131]. Because of the volume effect, the quantum size effect, and the surface effect, nanocrystalline NiO may possess many improved properties than those of bulk NiO particles. The particle nanostructural properties (particle size, distribution, and morphology) are closely related to the preparation techniques. Various methods on the preparation of NiO nanostructures have been reported. Wu et al [132] synthesized NiO nanoparticles of different shapes by four different methods using different amines and surfactants. His study showed that by altering the concentration and composition of solvents, different morphologies having variant diameters, shape, and distribution can be achieved. Tiwari and Rajeev [133] prepared NiO nanoparticles of different sizes by sol–gel method using nickel nitrate as precursor. Microemulsion route has been employed to prepare NiO nanoparticles by using cationic surfactant by Han et al [134]. Li et al [135] obtained NiO nanoparticles via thermal decomposition using ethanol as solvent. Wu and Hsieh [136] prepared NiO nanoparticles by a chemical precipitation method. Dharmaraj et al [137] obtained NiO nanoparticles using nickel acetate as precursor. An et al [138] synthesized NiO nanocrystals using nickel chloride hydrate as nickel source.

The low cost, environmentally friendly and potentially useful manganese (IV) oxide for pseudocapacitor applications have been prepared by various synthetic methods starting from such precursor materials as carbonyls [139], manganese acetylacetonate [140], acetate [141],

or formate [142] in trioctylamine, with oleic acid as a stabilizing agent and manganese cupferronate complexes or fatty acid salts in high boiling solvents [143-144].

Tantalum oxide nanoparticles are of considerable interest in optical and optoelectronic technology [145] especially as an ion conductor for applications in electro-optical devices such as chromogenic glazing in windows and large scale information displays [146-147]. It has been used commercially by Donnelly Corp (Holland, MI) in electrochromic mirror devices for vehicle applications [145]. Because of its high protonic conductivity, tantalum oxide is a candidate for inorganic type solid electrolyte in electrochromic devices [148]. Tantalum oxide has been used commercially by Donnelly Corp. (Holland, MI) in electrochromic mirror devices for vehicle applications [149]. Tantalum oxide films have been prepared by conventional techniques, such as reactive evaporation [150], reactive sputtering [151], pulsed-laser assisted deposition [129], and chemical vapor deposition [152]. In this work, sol-gel method was used to synthesis tantalum oxide nanoparticles

The fabrication of nanomaterials emphasis not only size, the geometry, and chemical homogeneity, but also the simplicity and practicability of synthesis techniques. When developing a synthesis method for generation of nanostructures, the most important issue that one needs to consider is the simultaneous control over composition, dimensions, morphology, and monodispersivity. In this work, two simple surfactant assisted sol-gel approaches to the synthesis of NiO and MnO_2 nanostructures, and a non-aqueous alkoxide based sol-gel for the synthesis of tantalum oxide nanostructures were adopted.

4.2.2 Experimental

4.2.2.1 Synthesis and characterization of nickel oxide nanoparticles

Two surfactant assisted synthetic routes were followed to synthesize nickel oxide nanostructures; an aqueous and a non-aqueous route. In the aqueous synthesis, 1.0 gm of nickel acetate tetrahydrate, $Ni(OAc)_2.4H_2O$, and 2.0 gm of polyvinyl pyrrolidone (PVP) was dissolved in 100.0 mL distilled de-ionised water at room temperature. The solution was stirred thoroughly for one hour using a magnetic stirrer. A solution of 1M potassium hydroxide (KOH) was prepared in distilled de-ionised water. The KOH solution was added dropwise slowly to the solution of $Ni(OAc)_2.4H_2O$ and PVP till the pH reaches 12.0. This was stirred for one hour using a magnetic stirrer. The resultant light green fine suspension was centrifuged for 20 minutes at 6000 rpm. After the supernatant was discarded, the resulting precipitate was washed three times with a lot of water and 3 times with ethanol. It was dried at 50 °C for 12 hours under vacuum. The drying temperature was increased to 80°C and dried for a further 6 hours. The dried solid was calcined for 3 hours in a box furnace at 350 °C. In the non-aqueous synthesis, 2.5 gm of nickel nitrate hexahydrate and 3.8 gm citric acid were dissolved in 50 mL of ethanol with thorough stirring with a magnetic stirrer until a clear mixed solution was formed. The solution was kept at 120 °C in an oven until the alcohol entirely evaporates and a green barmy paste formed. The paste was placed in a large crucible and calcined at 750 °C for 8 hours in air.

4.2.2.2 Synthesis of manganese oxide nanoparticles

The synthetic route for the synthesis of manganese oxide nanoparticles was adopted from the route for the aqueous surfactant assisted synthesis of nickel oxide. In the method, manganese acetate tetrahydrate was used instead of nickel acetate tetrahydrate.

4.2.2.3 Synthesis of tantalum oxide nanoparticles

508 µL of tantalum ethoxide was mixed with 2.532 mL of absolute ethanol in a 50 mL bottle and stirred for 30 minutes. 191 µL of glacial acetic acid was slowly added with slow stirring. The content was stirred for 2 hours to form a white gel. The gel was transferred to 50 mL falcon tubes and centrifuged for 15 minutes at 6000 rpm. It was washed with absolute ethanol by adding the ethanol to the residual, mechanically shaking and centrifuging again and discarding the supernatant. The residual is dried in vacuum furnace at 45 °C for 12 hours then 120 °C for 4 hours. They are then annealed at 350 °C in a box furnace for 3 hours.

4.2.2.4 Synthesis of the binary and ternary mixed metal oxides nanoparticles.

To synthesize tantalum and nickel mixed oxides nanoparticles, 508 µL of tantalum ethoxide was mixed with 2.532 mL of absolute ethanol in a 50 mL bottle and stirred for 30 minutes. Simultaneously 1.0 gm of nickel acetate tetrahydrate, $Ni(OAc)_2.4H_2O$, and 2.0 gm of polyvinyl pyrrolidone (PVP) were dissolved in 50.0 mL of absolute ethanol and the mixture stirred for 30 minutes at room temperature. The tantalum ethoxide and nickel acetate tetrahydrate solutions were mixed together in a 200 mL bottle with thorough stirring for one hour using a magnetic stirrer. A solution of 1M potassium hydroxide (KOH) was prepared in distilled de-ionised water. The KOH solution was added dropwise slowly to the reaction

mixture of tantalum ethoxide, Ni(OAc)$_2$.4H$_2$O and PVP till the pH reached 11. Stirring was continued for one hour. The resultant product was filtered using sunction pump and the residual washed three times with a lot of water and 3 times with ethanol. It was dried at 50 °C for 12 hours under vacuum. The drying temperature was increased to 80°C and dried for a further 6 hours. The dried solid was calcined for 3 hours in a box furnace at 350 °C. For the synthesis of tantalum and manganese mixed metal oxide oxides, the experiment was repeated using manganese acetate tetrahydrate instead of nickel acetate tetrahydrate. Similarly for the ternary tantalum, nickel and manganese mixed oxides, the experiment was repeated by dissolving equal masses of nickel and manganese acetate tetrahydrate in 100 mL of absolute ethanol.
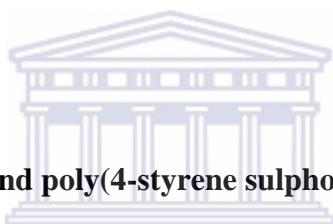
4.2.2.5 Synthesis of polyaniline and poly(4-styrene sulphonic acid) doped polyaniline

PANi and PSSA-doped PANi were synthesized by chemical oxidation of their respective monomers. In a 200 mL bottle, 2 mL aniline was dissolved in a 100 mL solution of 2 M HCl in distilled water. The solution was stirred for 30 minutes at room temperature using a magnetic stirrer (500 rpm). The mixture was then transferred in ice-bath kept at 0-5 ºC and stirred for a further 30 minutes. Thereafter, 1.165 g of ammonium per sulphate (APS) was added to the solution to initiate polymerization. The resultant mixture was stirred for another 3 hours. The product was left standing for 4 hours in ice-bath. 25 mL of absolute ethanol (99.9%) was added. The mixture was left standing for 48 hours at room temperature. Two distinct layers of a solid that settled at the bottom and a supernatant liquid formed. The upper liquid layer was slowly decanted and discarded. The residual was washed thoroughly with large amount of ultra-pure distilled de-ionized water by mechanical shaking,

centrifuging the mixture for 15 minutes at 6000 rpm and discarding the upper solution layer. The washing was done three times and lastly repeated with ethanol. The product was dried at 45 ºC for four hours under vacuum then at 78 ºC for 12 hours. To dope polyaniline with poly-(4-styrene sulphonic acid), the experiment was repeated by adding 4.5 mL of the dopant (PSSA) and 2 mL of aniline to the 100 mL of 2M HCl solution.

4.2.2.6 Synthesis of sulphonated polyaniline and metal oxide polymeric nanocomposites

The synthesis of the polymeric nanocomposites was done by ultrasonic dispersion and polymerization of aniline. 0.225 g of tantalum oxide was weighed and added to 100 mL of 2M HCl in a 200 mL bottle to which 4.5 mL of poly-(4-styrene sulphonic acid) was added. The mixture was sonicated for 30 minutes and then transferred to an ice-bath maintained at between 0-5 ºC. 2 mL of aniline and 1.165 g of ammonium persulphate were added to the mixture and stirred for 1 hour using a magnetic stirrer. The mixture was left standing for 4 hours in ice-bath and then out of the bath for 48 hours. Two distinct layers of a solid that settled at the bottom and a supernatant liquid formed. The upper liquid layer was slowly decanted and discarded. The residual was washed thoroughly by adding a large amount of ultra-pure distilled de-ionized water, mechanically shaking, centrifuging the mixture for 15 minutes at 6000 rpm and discarding the upper solution layer. The washing was done three times and lastly repeated with ethanol. The product was dried at 45 ºC for four hours under vacuum then at 78 ºC for 12 hours. For the PANi-tantalum oxide-nickel oxide-PSSA, PANi-tantalum oxide-manganese oxide-PSSA and PANi-tantalum oxide-nickel oxide-manganese oxide-PSSA nanocomposites, experiments was repeated by using 0.225 g of the respective metal oxide mixture.

4.3 Preparation of supercapacitor electrode materials and fabrication of electrodes

A unit cell experimental setup was used to test the performance of electrochemical materials, i.e. an electrochemical unit cell with two electrodes and a separator sandwiched between the two. A single electrode can also be used. A unit cell is used to simulate a real supercapacitor and can give information of practical performance. It is structurally similar to a supercapacitor product while a single electrode can provide detailed electrochemical information about electrode materials excluding effects of cell structure. Normally, a single electrode is tested in a "three-electrode cell" in which the electrode material acts as the "working" electrode and the potential of the electrode is measured relative to a reference electrode. The cell is completed by a counter electrode.

4.3.1 Preparation of electrode materials

The electrode materials used in the experiments for fabrication of electrodes consisted of 90% wt active material and 10% wt PTFE bidder. The active material consisted of chemically synthesized; (i) TaO_2-PANi-PSSA, (ii) TaO_2-NiO-PANi-PSSA (iii) TaO-Mn_2O_3-PANi-PSSA and (iv) TaO-NiO-Mn_3O_4-PANi-PSSA. All of these materials were integrated with activated graphite. The bidder used in each material was 10% wt polytetrafluoroethylene (PTFE) (Aldrich, solution form of 60% PTFE in H_2O). Samples were made on a 0.3 g basis.

4.3.2 Oxidative pre-treatment of graphitic carbon

Oxidative pre-treatment [40] of graphitic carbon was undertaken to functionalise the graphite. The following protocol was observed. 5.0 g of graphitic carbon was weighed and sonicated for 7 hours in a mixture of 150 mL conc. HNO_3 and 50 mL conc. H_2SO_4

(acid ratio = 3:1). The mixture was left standing overnight. Two layers were formed with the solid settling at the bottom and a supernatant liquid forming at the top. The supernatant liquid was decanted slowly. The oxidized graphite residual was extensively washed with de-ionised water by adding 50 mL of water in a plastic bottle, mechanically shaking the mixture and centrifuging at 6000 revolutions per minute (rpm) for 15 minutes using a centrifuging machine model EBA 21 Hettich ZENTRIFUGEN. This washing was repeated until the washings ran neutral at pH 7. The sample was dried under vacuum overnight at a temperature of 55 °C prior to use.

4.3.3 Integration of the nanocomposites with activated graphite.

0.5 g of the composite, 0.5 g of activated graphitic carbon and 1.0 g of the surfactant hexadecylcetyltrimethylammonium bromide (CTAB) were weighed and added to a glass bottle to give a 1:1:2 mass/mass/mass ratio respectively. 100 mL of water was added and the content was placed in a silicone oil bath and the temperature was adjusted to 80 °C. The content was stirred for 48 hours in a closed system using magnetic stirring. The mixture was vacuum filtered and repeatedly washed with distilled de-ionised water five times to get rid of the surfactant. The solid was dried under vacuum overnight at 45 °C.

4.3.4   Preparation of electrode

For each of the active materials, 0.225 g of the material was measured and 42 uL of PTFE were measured and dispersed in 3 mL isopropyl alcohol in a 30 mL beaker by ultrasonic shaking for 30 minutes to form homogeneous mixed slurry. The beaker and its content is placed on top of a hot plate at the lowest setting and constantly stirred with a cellulose rod to evaporate the solvent and further mix the components to form dough. Once the isopropyl alcohol has almost completely evaporated, the dough is transferred to

a flat glass plate and using a Teflon rod, rolled into a thin mm thick film. The prepared film was put into an oven and baked at 100 ^{o}C in a vacuum oven for 24 hours during which time the remaining isopropyl alcohol and/or moisture in the film completely evaporated. The large piece of film was cut into small pieces of about 1 cm^2. The mass of each piece to be used is weighed and recorded for specific capacitance calculations.

4.3.5 Construction of a single electrode

A single electrode was assembled with three parts; electrode material, nickel mesh current collector and copper wire. The electrode was assembled by cutting the nickel mesh current collector into a 1 cm $\times$ 4 cm rectangular shape. It was then cleaned mechanically shaking it in 1 M H_2SO_4 and washed with deionised water. Dried in oven and weighed. The piece of material wafer was placed on the nickel mesh and the two folded in between an aluminium foil and then sandwiched between two stainless steel blocks whose surface is well polished for pressing the wafer onto the nickel mesh. A pressure of 20 MPa was applied and kept for 5 min to enhance the contact between the electrode material wafer and the current collector. The electrode was then weighed and the difference in mass was used as the active mass of the electrode. The copper wire was tightly held onto the current collector using seal tape for external circuit connection. This acted as the cathode in the cell construction. The anode electrode was made similarly save for the active material. The active material for anode electrode was activated carbon. The two were used to make asymmetric supercapacitor cell. The procedure was repeated for each nanocomposite.

4.3.6 Fabrication of two-electrode supercapacitor cell and testing its performance.

The cell was fabricated and tested using the BST8-3 eight-channel battery testing machine in a two-electrode cell system. A supercapacitor cell was made by holding together the two single electrodes (cathode and anode) with a porous and electronically non-conductive separator (polypropylene film) placed between them to form the cell configuration. This two-electrode cell was then tested using the **BST8-3** eight-channel battery testing machine in a two-electrode cell system for cycling and potentiostatic-galvanostatic charge/discharge.

Chapter 5

Results and discussion

5.1 Introduction

This chapter presents the characterization results of the chemically synthesized poly(styrene sulphonic acid (PSSA) and transition metal oxide doped polyaniline nanocomposites. This includes the use of the techniques TEM, HRTEM, SEM, XRD, UV-Visible, FTIR, SNIFTIR, CV, EIS and SECM. These techniques are used to basically interrogate the morphological and spectroscopic properties, elemental composition, electrochemical and kinetic parameters of the composites. Results of design and characterization of supercapacitor cells are finally discussed.

5.2 Synthesis of nickel oxide nanoparticles

Figure 19 shows a TEM image of nickel oxide nanoparticles. These were identified as nickel oxide by EDX (fig 20) analysis. The image reveals a large number of dispersed nanoparticles with a uniform average particle size of 7 nm.
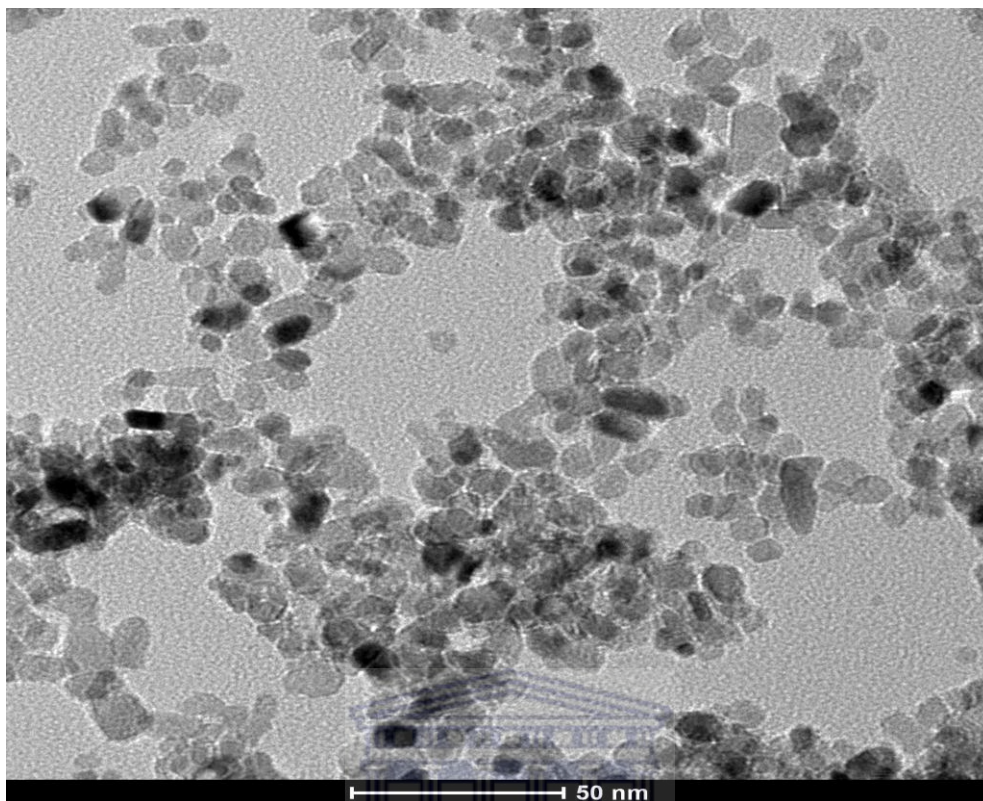
Figure 19. TEM picture of nickel oxide nanoparticles.

The EDX spectrum of the nanoparticles illustrated in figure 20 shows pronounced peaks of nickel and oxygen and confirms the identity of the nanoparticles. The carbon peaks in the EDX spectrum originated from the carbon membrane used to support the samples for TEM observations.
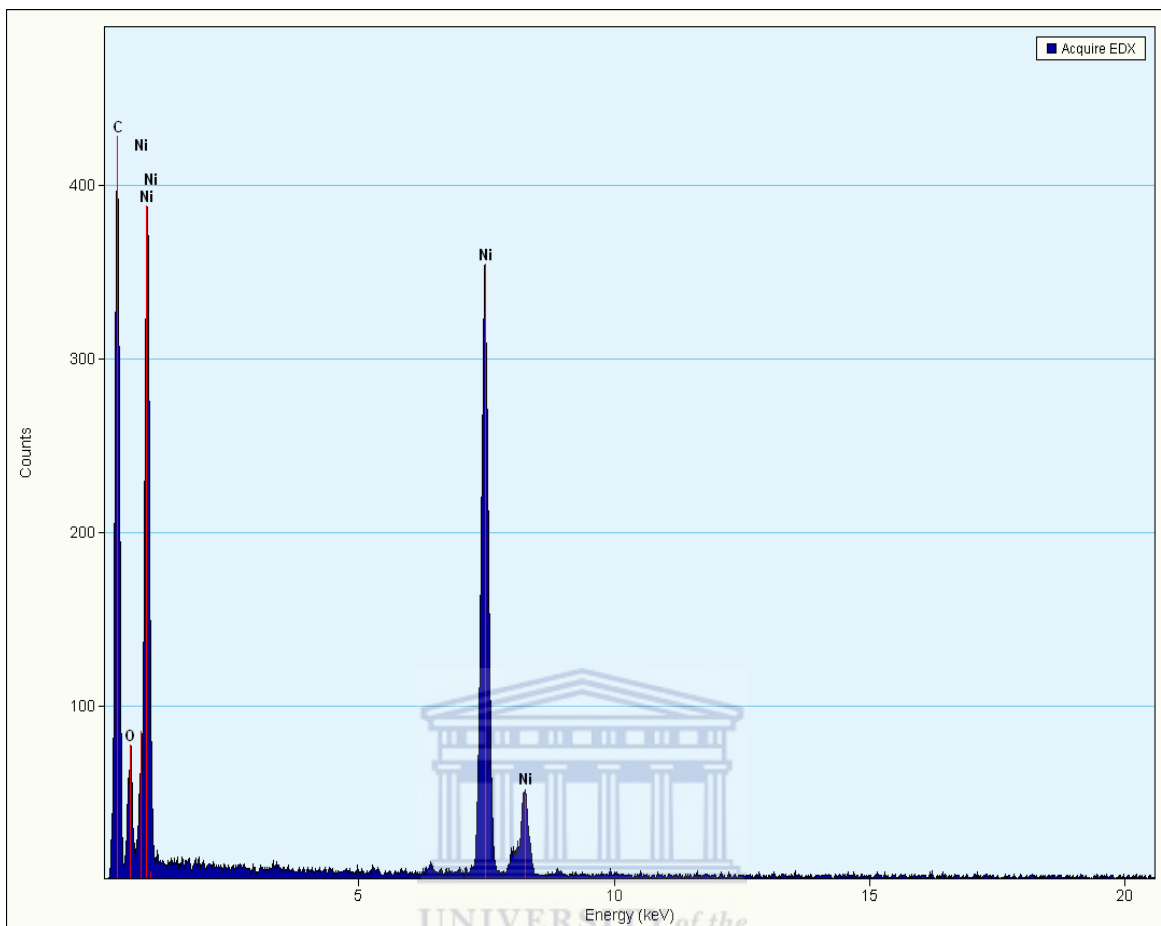
Figure 20. EDX spectrum of nickel oxide nanoparticles

The synthesis of nickel oxide nanoparticles used a surfactant (polyvinyl pyrrolidone) assisted protocol. The use of the surfactant played a role in the formation of well dispersed nanoparticles. Particle formation is a complex process and a surfactant not only provides a favourable site for the growth of the particulate assemblies, but it also influences the formation process including nucleation, growth, coagulation and flocculation [153-154]. Polyvinyl pyrrolidone nucleates by forming co-ordinate bonds with nickel ion in the composite mixture. This controls particle aggregation and led to the formation of size homogeneous and well dispersed nickel oxide during calcinations in the air.

The XRD pattern of NiO nanoparticles is given in figure 21. The nature, position and existence of strong and sharp diffraction peaks at 2-Theta values corresponding to (111) (200) and (220) crystal planes indicate the formation of phase pure cubic nickel oxide (the bunsenite structure). The nickel oxide formed in this synthesis was black in colour. The characteristics of nickel oxide formed in sol gel synthesis depend largely on the crystallite nanosize and distribution besides the synthesis route and prevailing experimental conditions, e.g. nickel oxide can be pale apple green or jet black depending up on the stoichiometry. While the green corresponds to the composition NiO and is an insulator, the black material has a deficiency of Ni^{2+} ions represented as $Ni_{0.98}O_{1.00}$ and behaves as a p-type conductor [155].
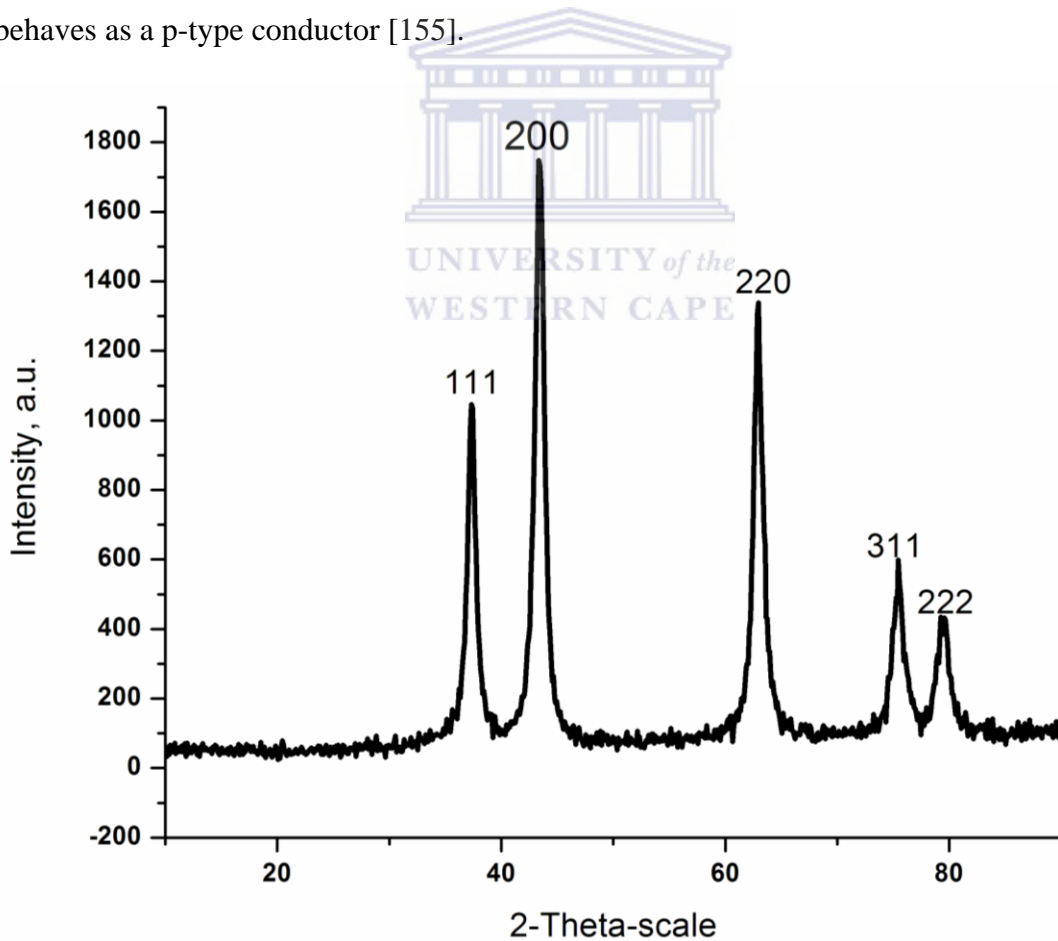
Figure 21. XRD of NiO nanoparticles

From the XRD spectra, all the detectable peaks are consistent with those of NiO phase. The XRD pattern of the PVP precursor residues is a broad peak from 10° to 30° [156]. However, there is no broad peak that is observed within this 2-Theta range. This means that the PVP decomposes completely on heating the precursor at 350 °C for 3 hours. This fact is supported by an analysis of the FTIR spectra of the calcinations product (see figure 22).
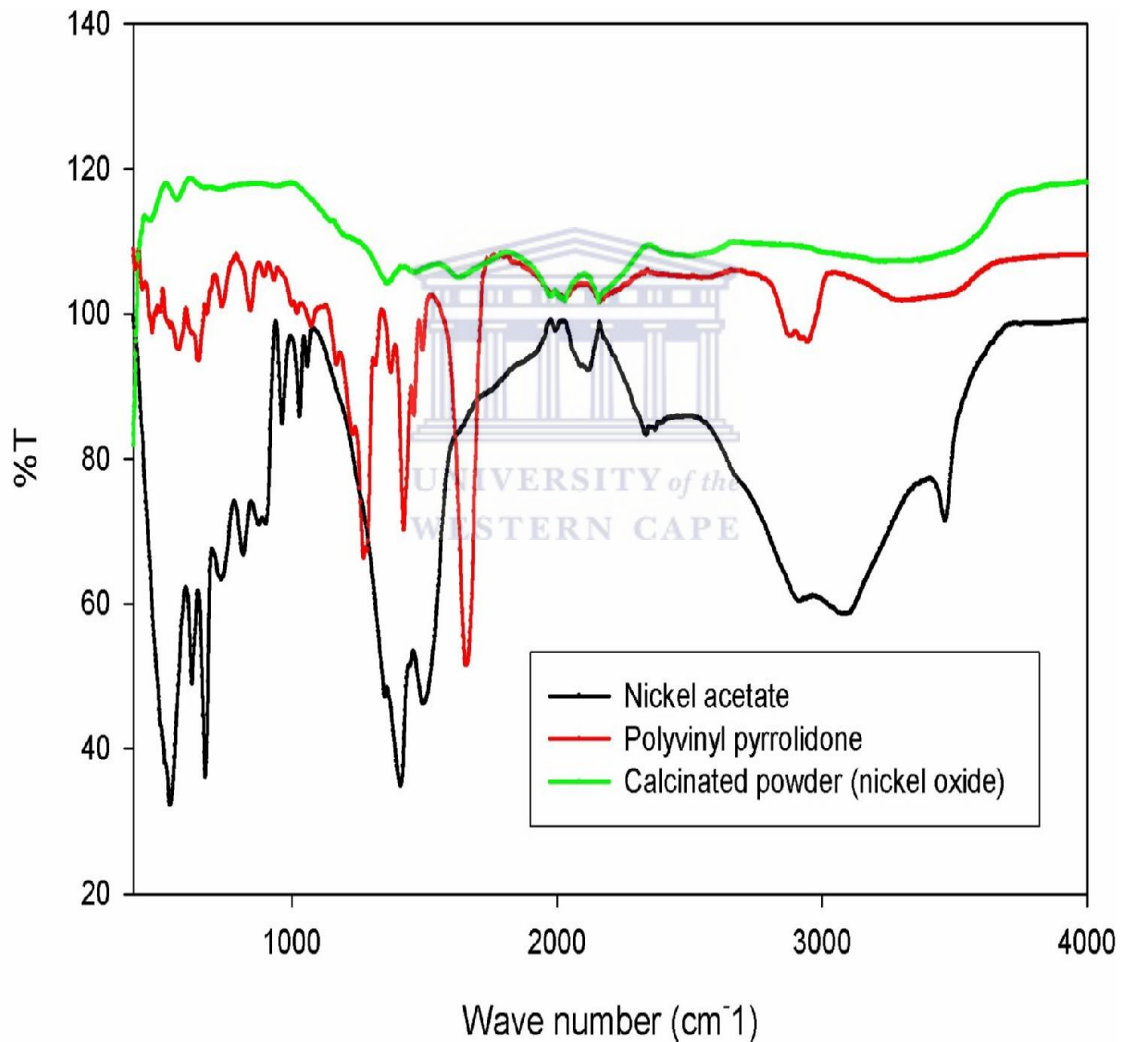
Figure 22. FTIR of precursors and calcined nickel oxide

The precursor materials for synthesis of the nanoparticles were thermally decomposed and got eliminated as gases during calcination. The spectrum of nickel acetate/PVA precursor showed strong absorption peaks in the region below 1800 cm^{-1} which are absent in the calcination product confirming complete removal. A peak around 450 cm^{-1} for calcined powder arising from Ni-O stretching has been reported by other researchers [137]. Figure 23 is a characteristic cyclic voltammetric (CV) curve profile for the NiO nanostructure sample showing a pair of redox peak which can be attributed to transitions in the oxidation states of nickel. The presence of a redox pair means that the material can contribute to pseudocapacitance when used in a composite form to construct supercapacitors.
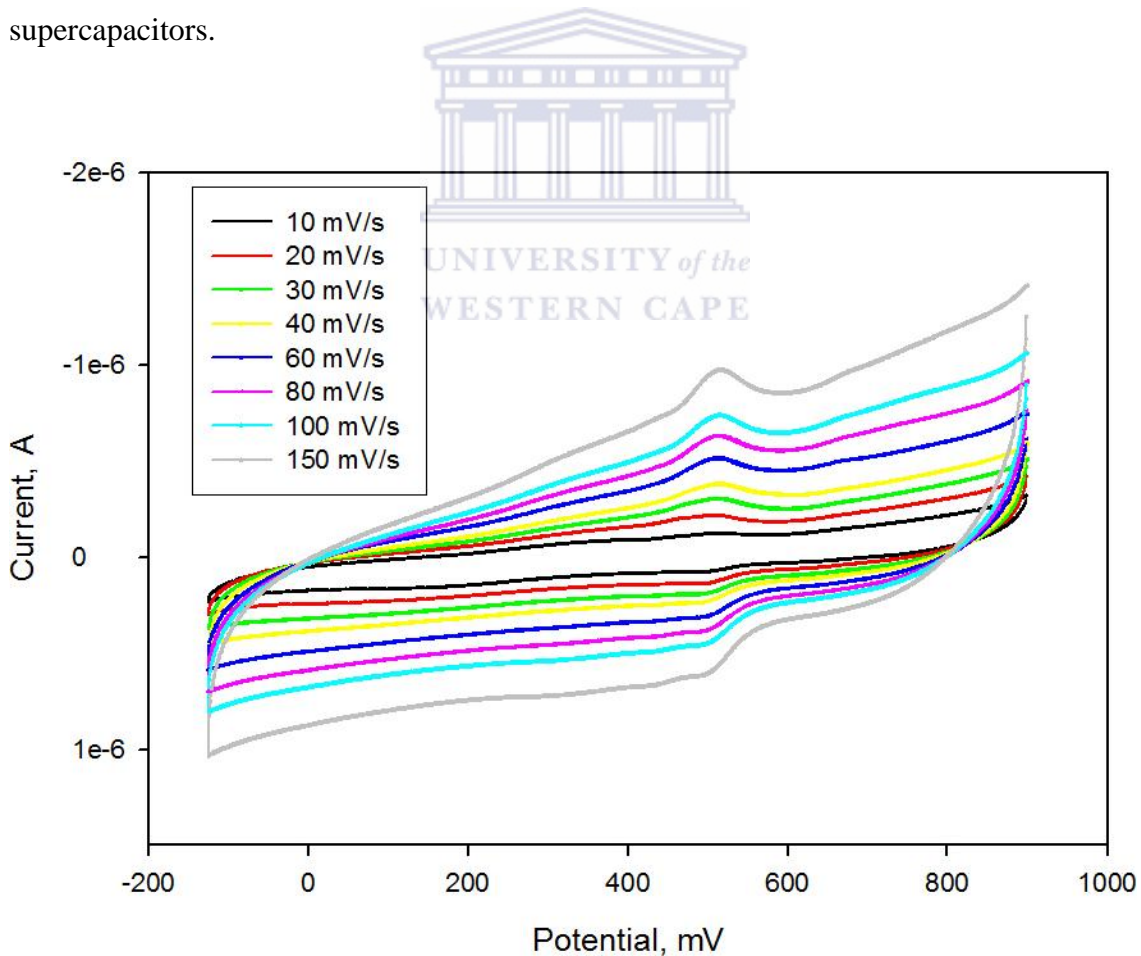
Figure 23. Cyclic voltammetry of nickel oxide nanoparticles

5.3 Synthesis of manganese oxide nanoparticles

The protocol for the synthesis of manganese oxide nanoparticles was similar to that of the synthesis of nickel oxide nanoparticles save for the source of manganese ion and some citric acid that was added.

The growth of the nanorods may follow a vapour-solid phase mechanism [157]. Acting as a ligand, citric acid, (3-carboxy-3-hydroxypentanedioic acid), hold Mn^{2+} particles in a chelate. Mn particles are formed first during the sol-gel derived products according to equation 5.1;

$$9Mn(NO_3)_2.6H_2O_{(l)} + 2C_6H_8O_7.H_2O_{(s)} \rightarrow 9Mn_{(g)} + 12CO_{2(g)} + 18NO_{2(g)} + 64H_2O_{(l)} \qquad (5.1)$$
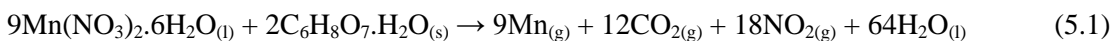
These Mn particles were formed in different sizes. The small-sized particles were first evaporated into the atmosphere. These then reacted with oxygen to form a complex network of Mn_3O_4 nanowires of varied lateral sizes via the vapour-solid mechanism with longitudinal lengths that ranges from nanoscale to microscale.

From the EDX spectra in figure 24, the elemental composition of the nanorods is found to be Mn and O.
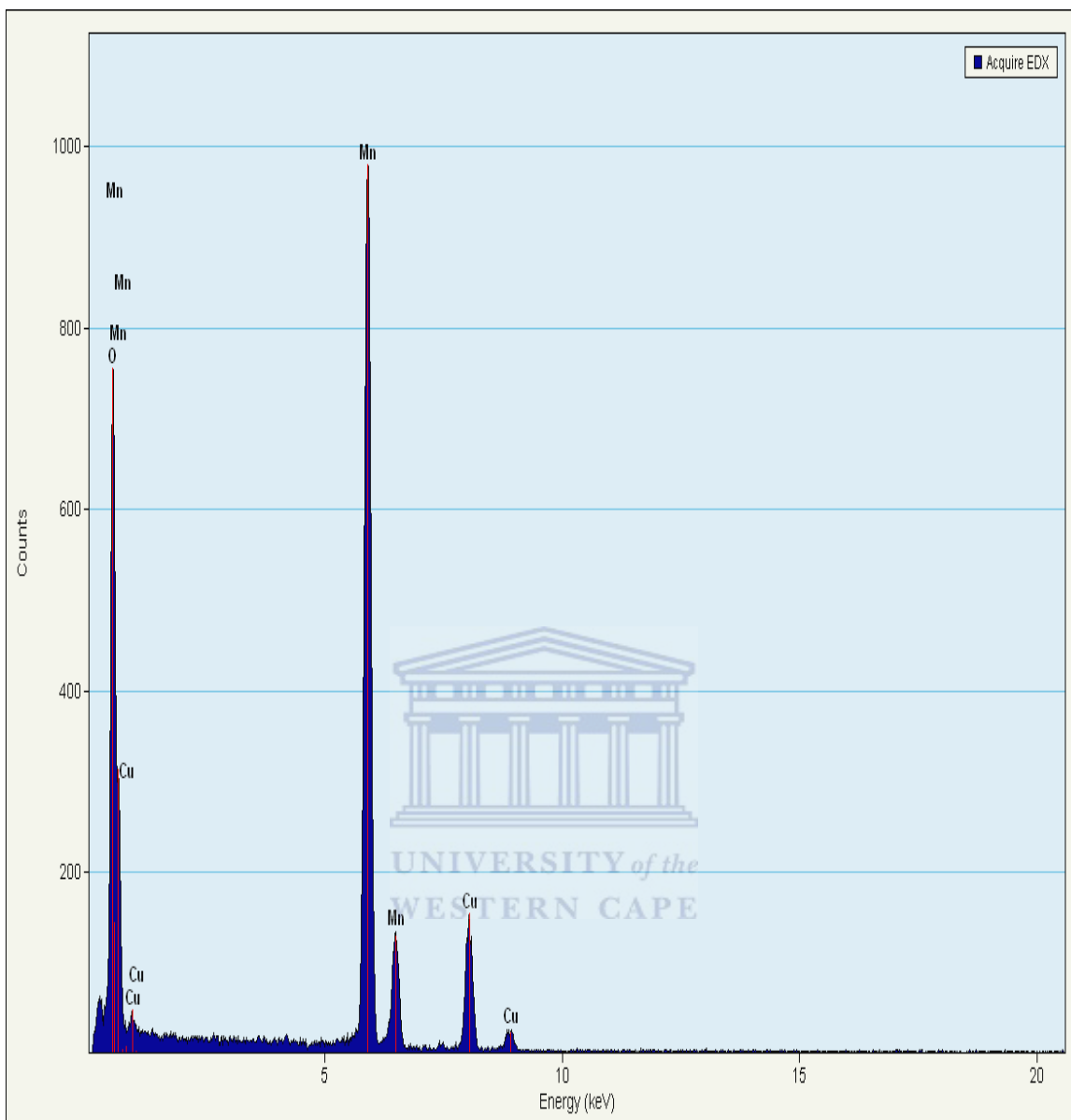
Figure 24. EDX spectrum of Mn₃O₄

The entire XRD diffraction pattern of the sample is shown in figure 25. All the strong and sharp diffraction peaks are consistent with the Joint Committee on Powder Diffraction Standards (JCPDS) card file no. 24-0734 which are indexed to the tetragonal phase of hausmanite, Mn_3O_4, confirming that the bright brown materials of the samples formed as

the calcination product in the present study and consistent with those of other workers, were basically permanganese trioxide, Mn_3O_4 [158-159].
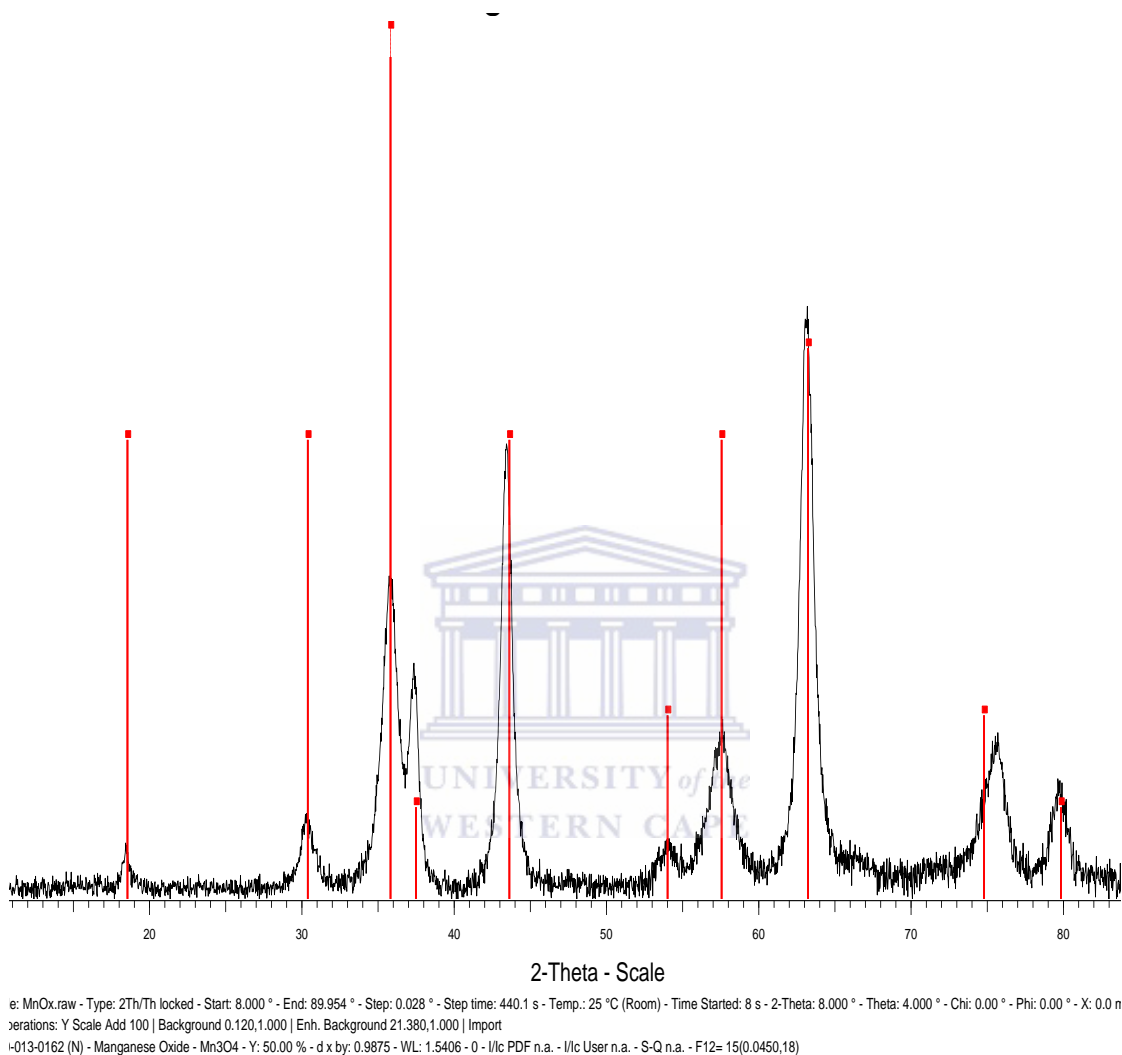
Figure 25. XRD of Mn_3O_4

Mn_3O_4, manganese (II, III) oxide, has a spinel structure, also known by the mineral name Hausmanite. In the compound, Mn^{2+} occupies tetrahedral positions and Mn^{3+} occupies the corresponding octahedral sites. The general formula of the compound is $(Mn^{2+})(Mn^{3+})_2O_4$. These manganese oxides present several oxidation states (+2, +3, +4

and +7). As such it is redox active and presents several redox peacks as is shown in figure 26.
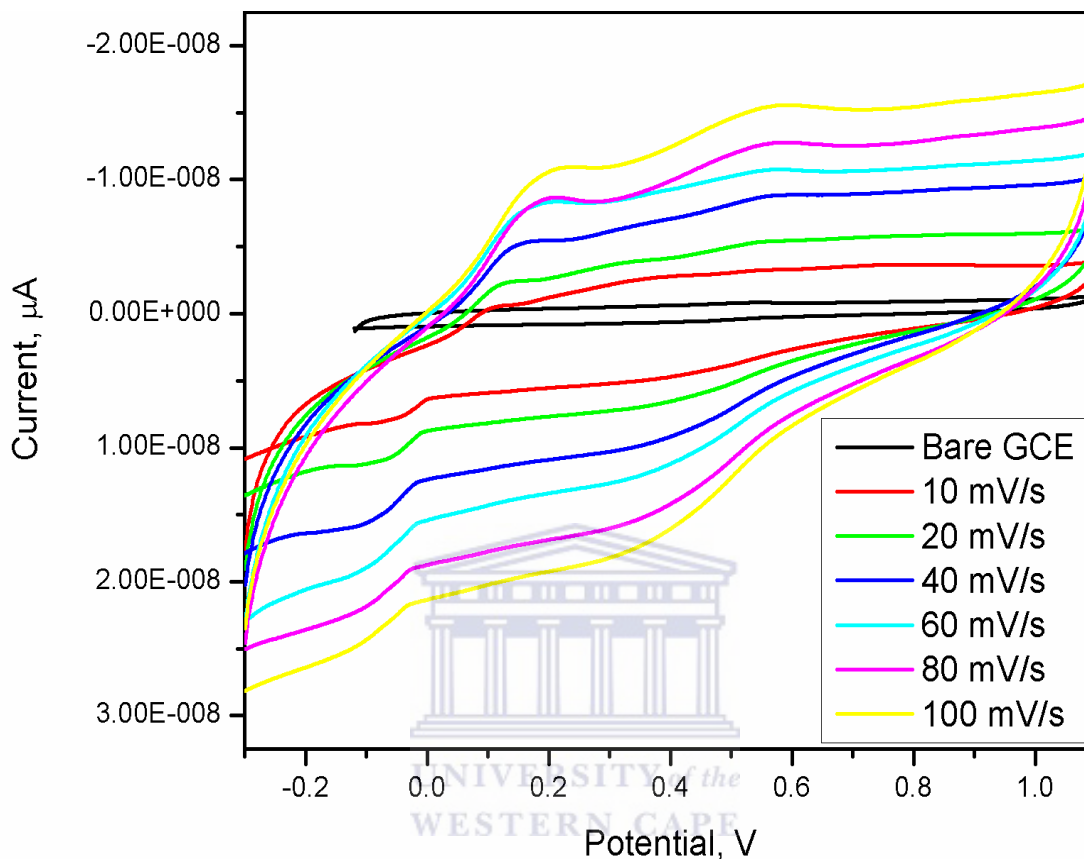
Figure 26. CV of Mn₃O₄ in 1 M H₂SO₄

From its redox characteristics, Mn_3O_4 would thus offer strong contribution to pseudocapacitance. Also, hausmanite (Mn_3O_4) is of interest in many industrial and technological applications. It is widely used as reactive catalysts, raw material of humidity sensors, the cathode oxides of Li-ion secondary batteries and soft magnetic materials. The Bulk Mn_3O_4 materials have also been well studied from a theoretical point of view due to its special electronic configuration and distorted spinel structure. Mn_3O_4 is known to have the normal spinel structure with tetragonal distortion elongated along the c-axis due to Jahn-Teller effect on the Mn^{3+} ion [160]. In this work, Mn_3O_4 was used to

form binary and ternary composites with tantalum oxides. These oxides were then used to form polymeric nanocomposites with sulphonated polyaniline. The materials were then used to fabricate electrodes for supercapacitor applications. It is expected that Mn_3O_4 will contribute to an enhanced pseudocapacitance since it displays multiple redox activities as the multi-scan cyclic voltammetric characterization shown in figure 26 shows.

5.5 Synthesis of tantalum oxide

Figure 27 is a TEM micrograph of the product formed through the alkoxide-based sol-gel synthetic route. Its corresponding EDX spectra shown in figure 28 verified Ta and O as the elemental constituents of the calcination product.
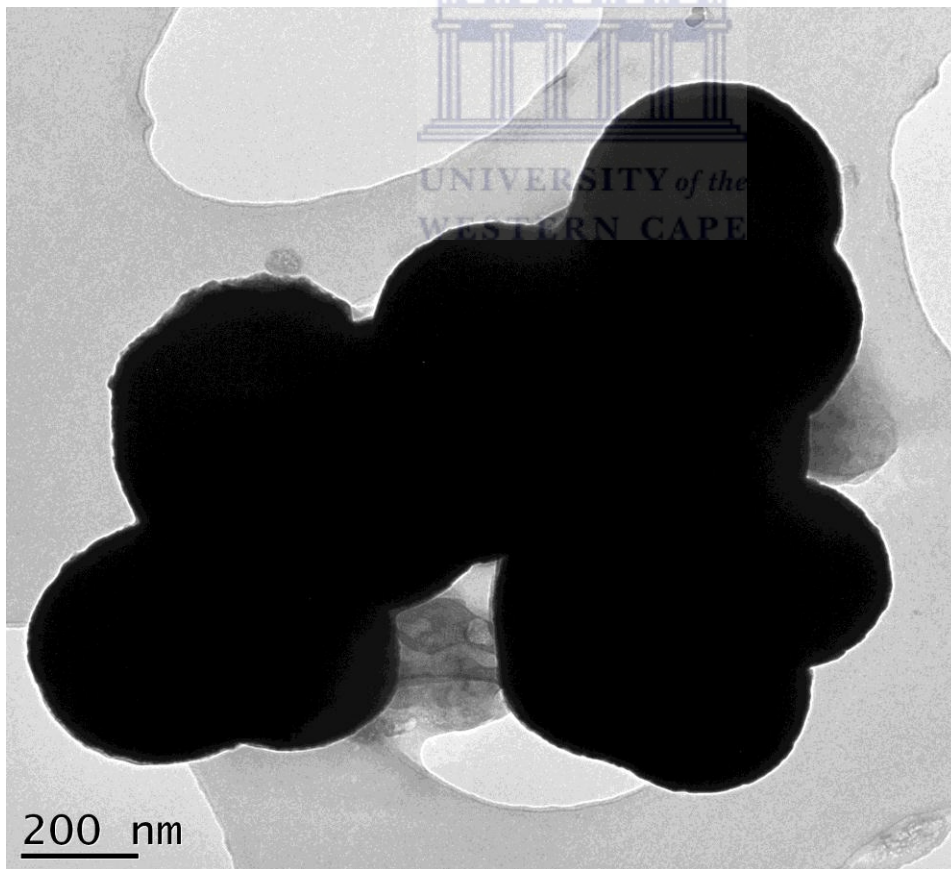
Figure 27. TEM of tantalum dioxide nanoparticles

Fig. 28 is the XRD pattern of the sample. The diffraction signals, matched with signals from the database, confirm the formation of agglomerated and amorphous tantalum (IV) oxide (TaO_2) phase. The sol-gel chemistry in the synthesis of nanoparticles is quite complex due to the large number of reaction parameters that have to be strictly controlled such as hydrolysis and condensation, nature of the metal oxide precursors, pH, temperature, method of mixing, rate of oxidation, the nature and concentration of anions, etc, in order to provide good reproducibility of the synthesis protocol. A fundamental problem of sol-gel chemistry is that the as-synthesized precipitates are generally amorphous and the required control of their post-synthetic annealing step to induce crystallization process is a challenge that prevents any subtle control over crystal size and shape. This constitutes a major challenge in case of nanoparticle synthesis and could explain the aggregation and the amorphous nature of the TaO_2 nanoparticles observed in this work.
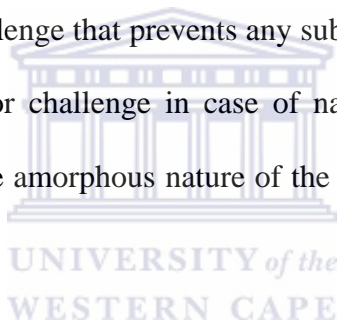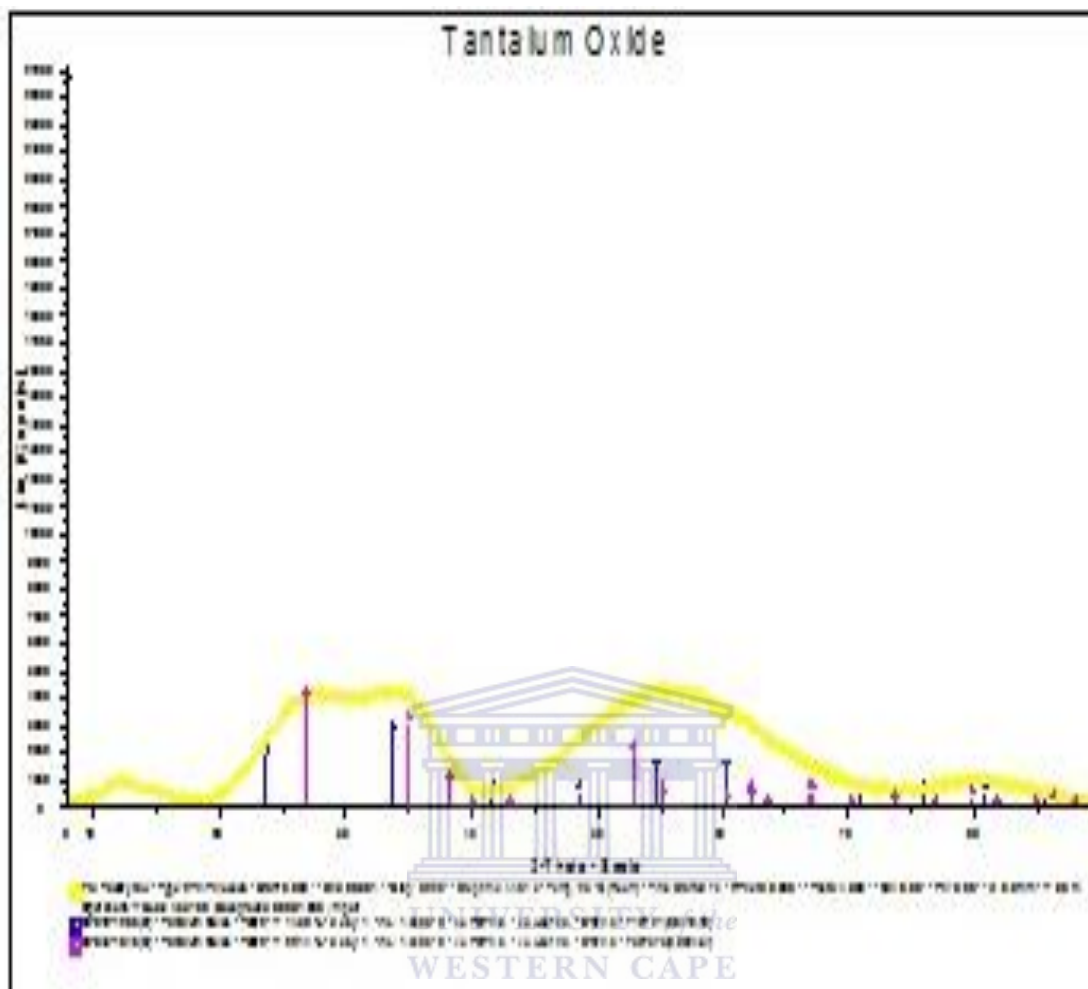
Figure 28. XRD of TaO₂

5.6 Synthesis of transition metal mixed oxides

The synthesis of the mixed binary and ternary oxides was performed using tantalum alkoxide, nickel and manganese acetates as the inorganic precursors at a pH of 11 adjusted using sodium hydroxide solution. All the organics were removed during calcination at temperatures of 350 °C as was observed during the synthesis of NiO nanoparticles. The HRTEM and STEM images of the binary tantalum oxide-nickel oxide are shown in Fig. 29 (a) and (b) respectively. The HRTEM image shows a dispersed

material spread on holy carbon support whose elemental chemical composition as derived from the corresponding EDX analysis shown in figure 30 is Ta and Ni and O. The sample was also scanned using STEM and a spot EDX analysis done (see figures 31 (a), (b), (c)) at three randomly spotted regions to confirm the elemental composition and distribution of the dispersed nanoparticles. The XRD spectra (shown in figure 32) analysis identified the TaO_2-NiO to be the polycrystallite phases present.
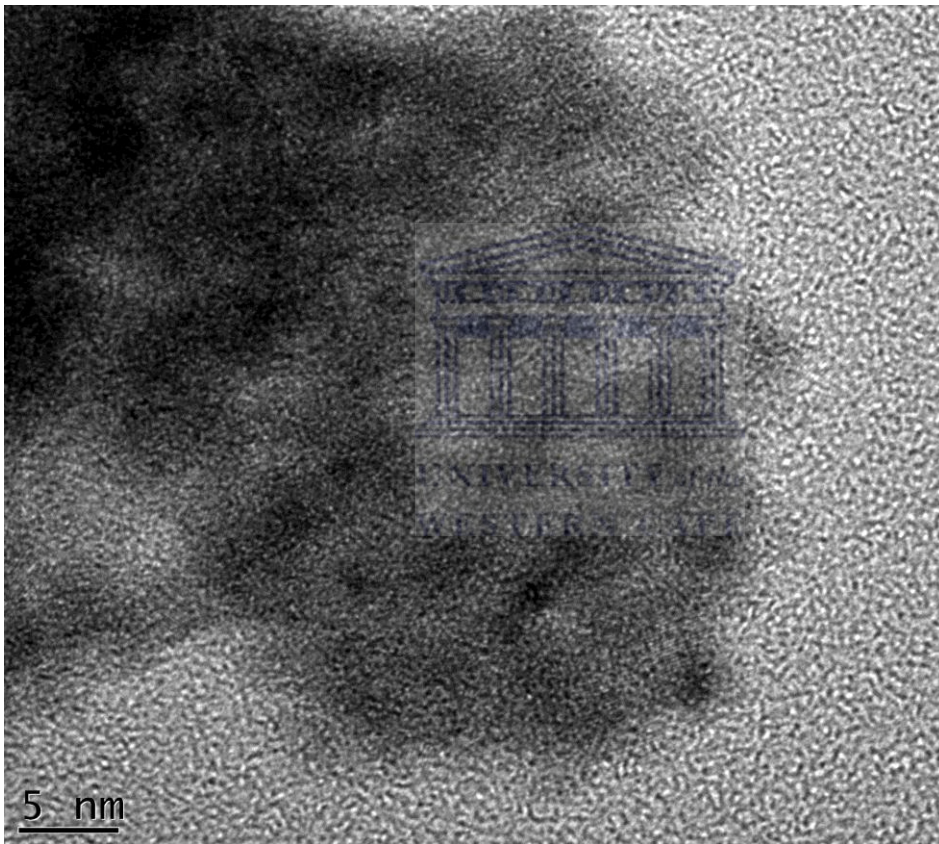
(a)
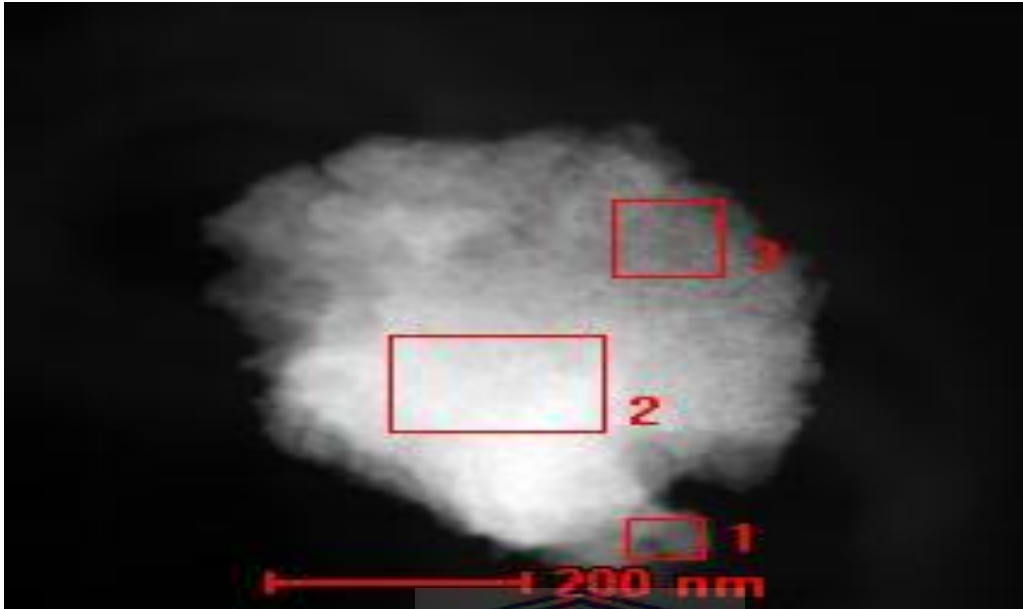
(b)

Figure 29. HRTEM (a) and STEM (b) of TaO$_2$-NiO
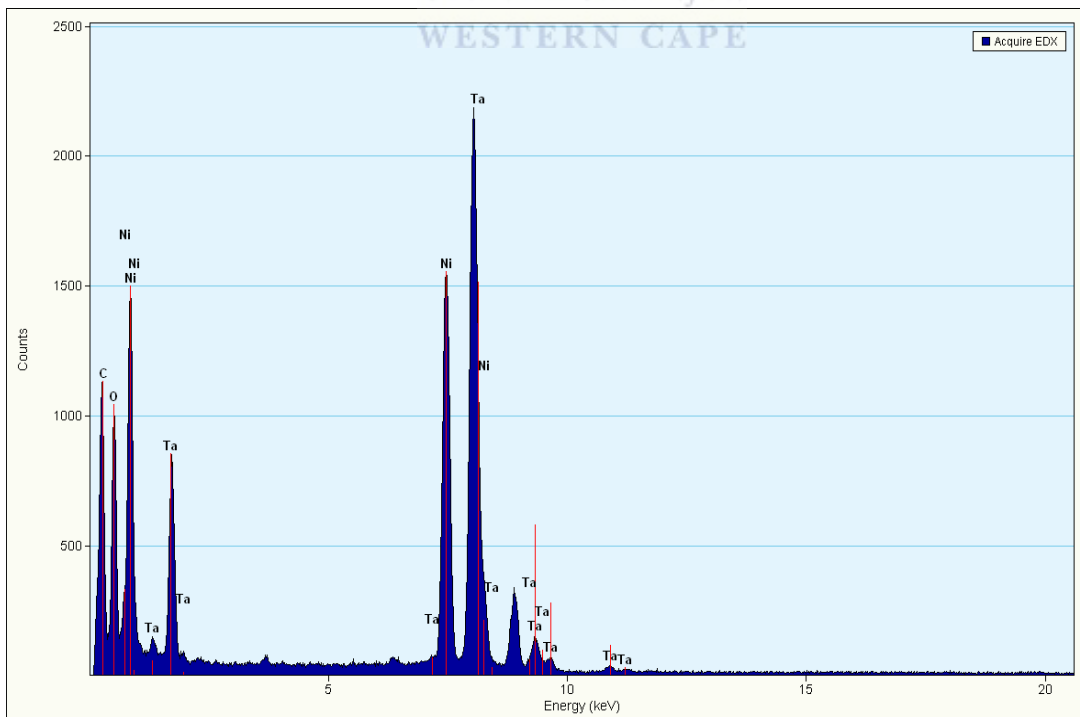
Figure 30. EDX of TaO$_2$-NiO on HRTEM sample

(a)

(b)

(c)
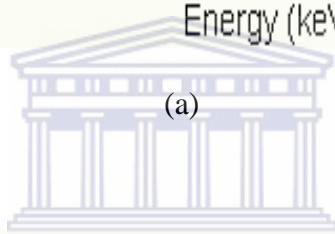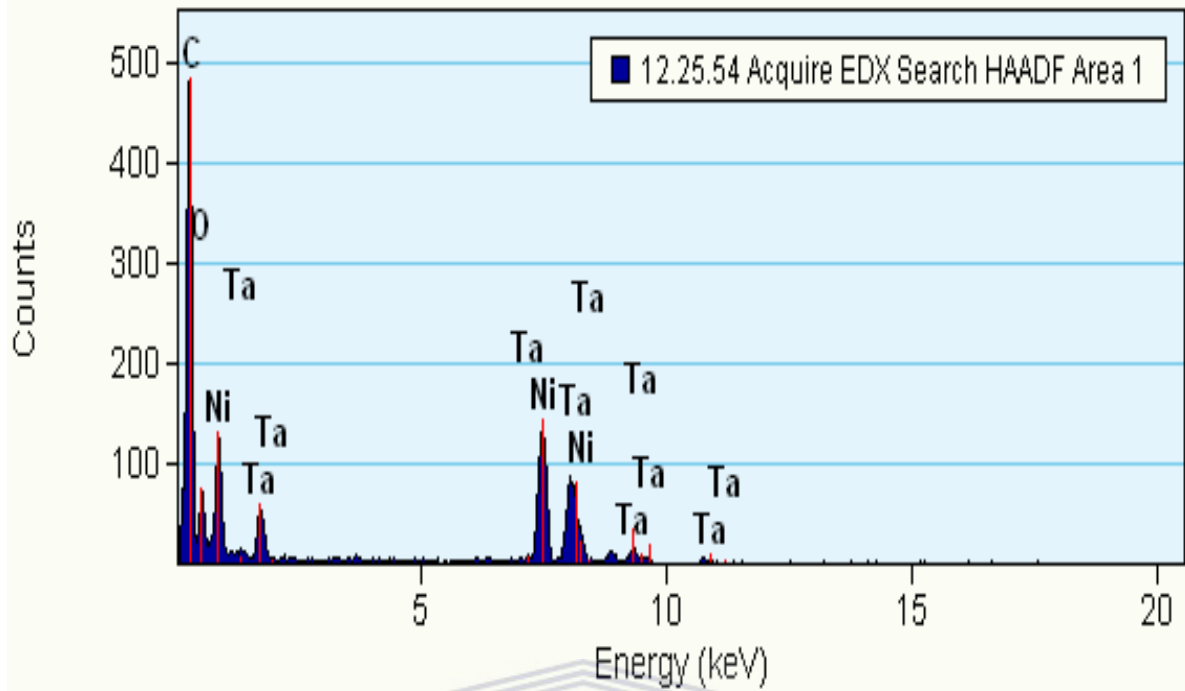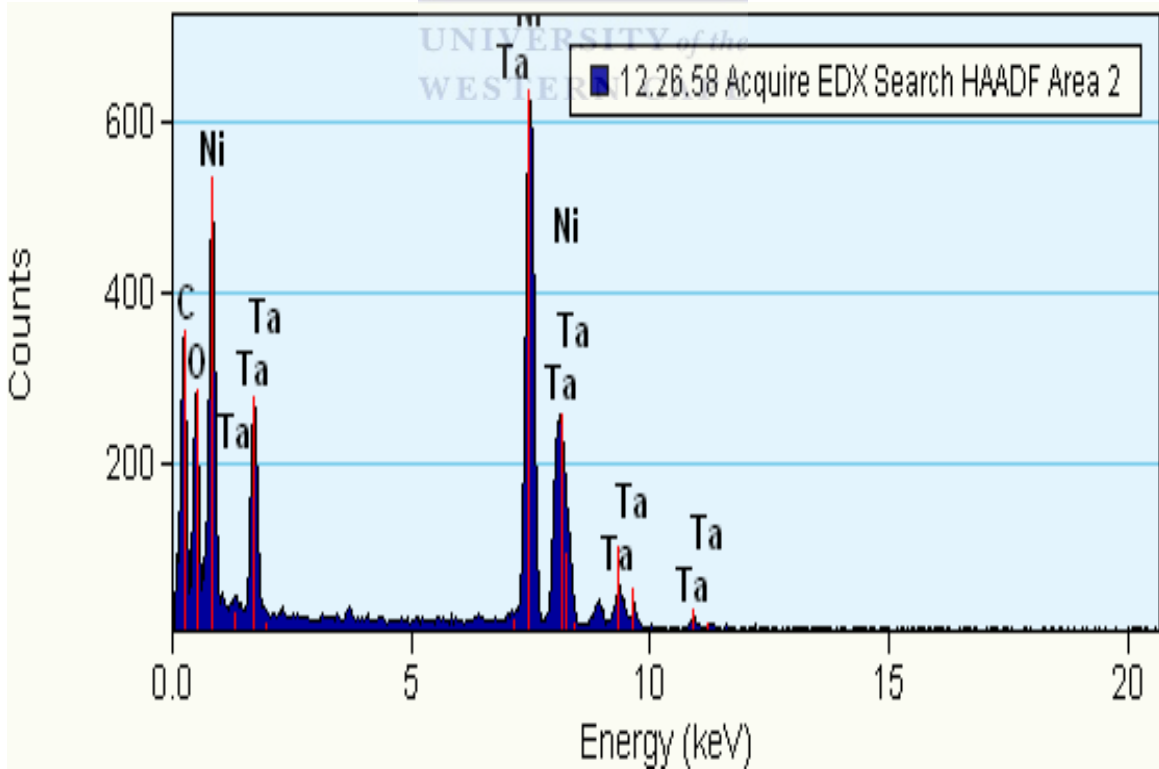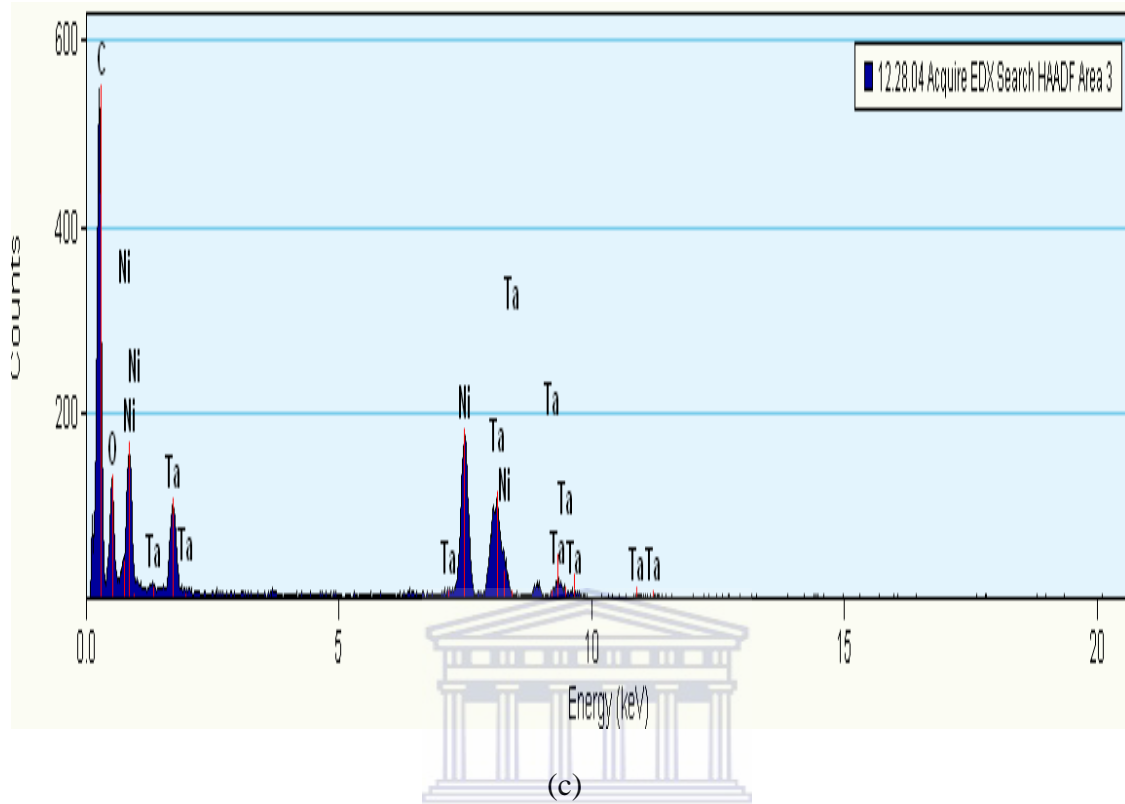
Figure 31. EDX of (a) spot 1, (b) spot 2 and (c) spot 3 of STEM

2-Theta - Scale

e: NiO-TaO.raw - Type: 2Th/Th locked - Start: 8.000 ° - End: 89.981 ° - Step: 0.028 ° - Step time: 440.1 s - Temp.: 25 ℃ (Room) - Time Started: 7 s - 2-Theta: 8.000 ° - Theta: 4.000 ° - Chi: 0.00 ° - Phi: 0.00 ° - X: 0.

perations: Y Scale Add 100 | Background 0.174,1.000 | Import

-044-1159 (*) - Nickel Oxide - NiO - Y: 16.67 % - d x by: 1. - WL: 1.5406 - 0 - I/Ic PDF n.a. - I/Ic User n.a. - S-Q n.a. - F15=130(0.0061,19)

-019-1296 (D) - Tantalum Oxide - TaO2 - Y: 14.58 % - d x by: 1. - WL: 1.5406 - 0 - I/Ic PDF n.a. - I/Ic User n.a. - S-Q n.a. - F10= 21(0.0470,10)

Figure 32. XRD spectrum of TaO₂-NiO

HRTEM was performed to analyze the surface structure of the sample obtained in the synthesis of the binary tantalum oxide-manganese oxide nanoparticles. Figure 33 (a) and (b) shows the micrographs recorded at different resolutions for the sample, coupled with the EDX analysis whose results are shown in figure 34. The micrographs show clumps of agglomerated nanocystalline structures with weakly defined atomic fridges. The chemical constituents of the samples are found to be Ta, Mn and O. These are shown to be of the TaO-Mn_2O_3 crystal phase by the XRD in figure 35.
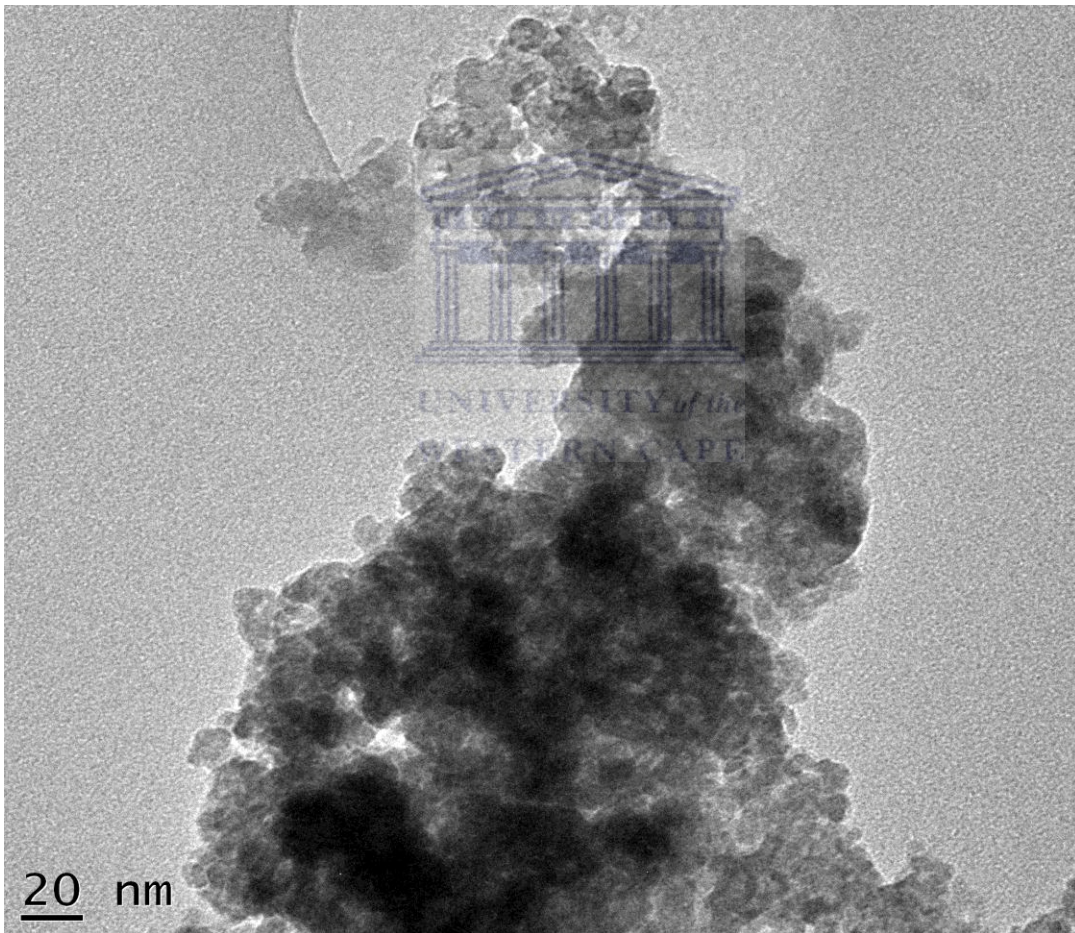
(a)

(b)

Figure 33. HRTEM of TaO-Mn₂O₃ at a magnification of (a) x 64K and (b) x 530K
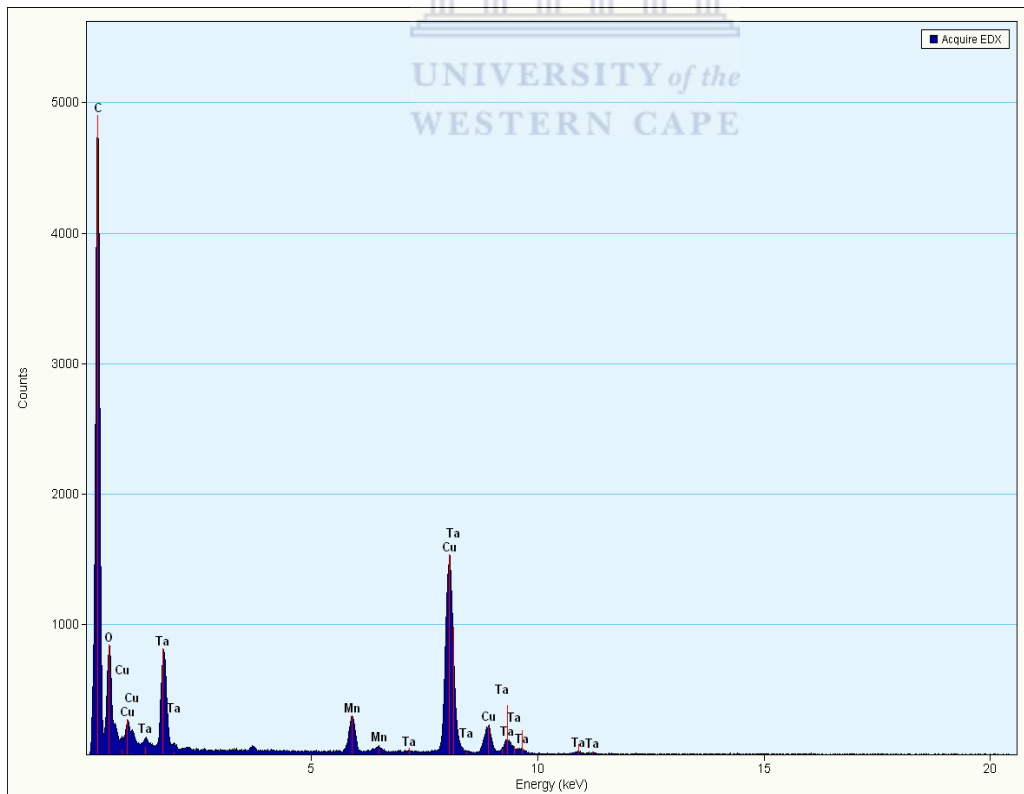
Figure 34. EDX of TaO-Mn₂O₃

2-Theta - Scale

e: MnxOx-TaxOy.raw - Type: 2Th/Th locked - Start: 12.000 ° - End: 90.027 ° - Step: 0.096 ° - Step time: 880. s - Temp.: 25 °C (Room) - Time Started: 8 s - 2-Theta: 12.000 ° - Theta: 6.000 ° - Chi: 0.00 ° - Phi: 0.00 °
erations: Background 0.081,1.000 | Import
-037-0117 (*) - Tantalum Oxide - Ta0.97O2 - Y: 6.86 % - d x by: 1. - WL: 1.5406 - 0 - I/Ic PDF n.a. - I/Ic User n.a. - S-Q n.a. - F12= 61(0.0116,17)
-024-0508 (C) - Bixbyite-O, syn - Mn2O3 - Y: 15.99 % - d x by: 1. - WL: 1.5406 - 0 - I/Ic PDF n.a. - I/Ic User n.a. - S-Q n.a. - F30= 23(0.0047,284)

Figure 35. XRD of TaO-Mn$_2$O$_3$

A TEM image of the surfactant assisted synthetic product of a novel ternary tantalum oxide-nickel oxide-manganese oxide mixed oxide is shown in Figure 36 (a) with its high resolution TEM micrograph (figure 36 (b)) showing clearly defined atomic fringes, a sign that the material is polycrystalline. The images clearly show that TEM can only provide a rough estimate of the particle size and that the oxides aggregate into poly-dispersed clusters. The elemental composition of the material done by EDX whose spectra is shown in figure 37, shows that the material is made up of Ta, Ni, Mn and O, with the XRD (see figure 38) confirming the existence of the TaO-NiO-Mn$_3$O$_4$ crystallite mixed phases.

89
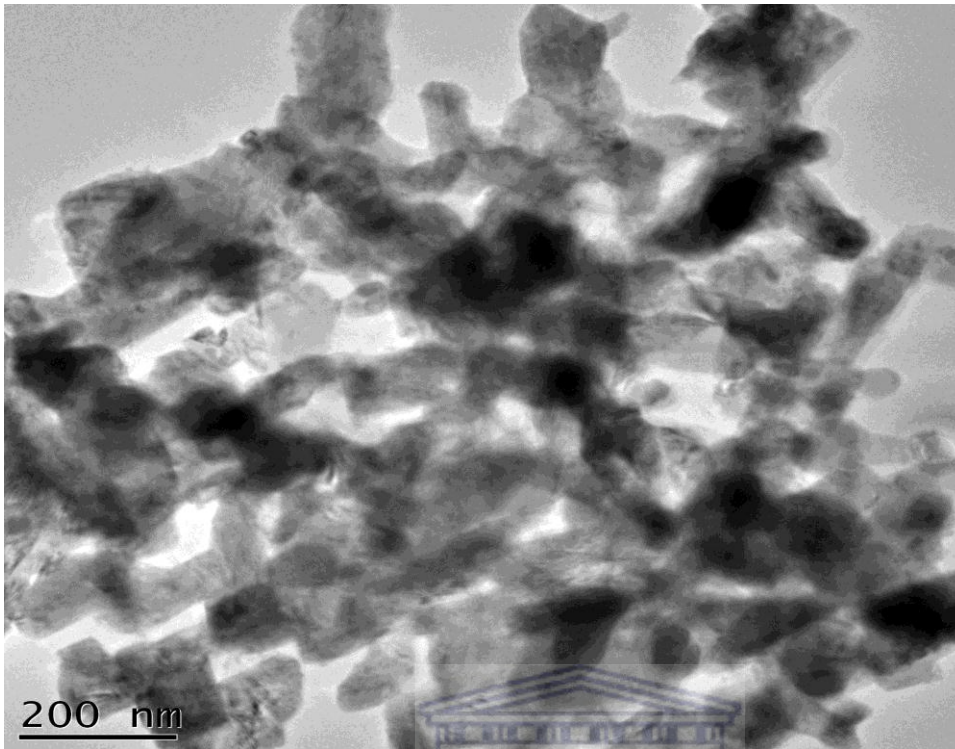
(a)
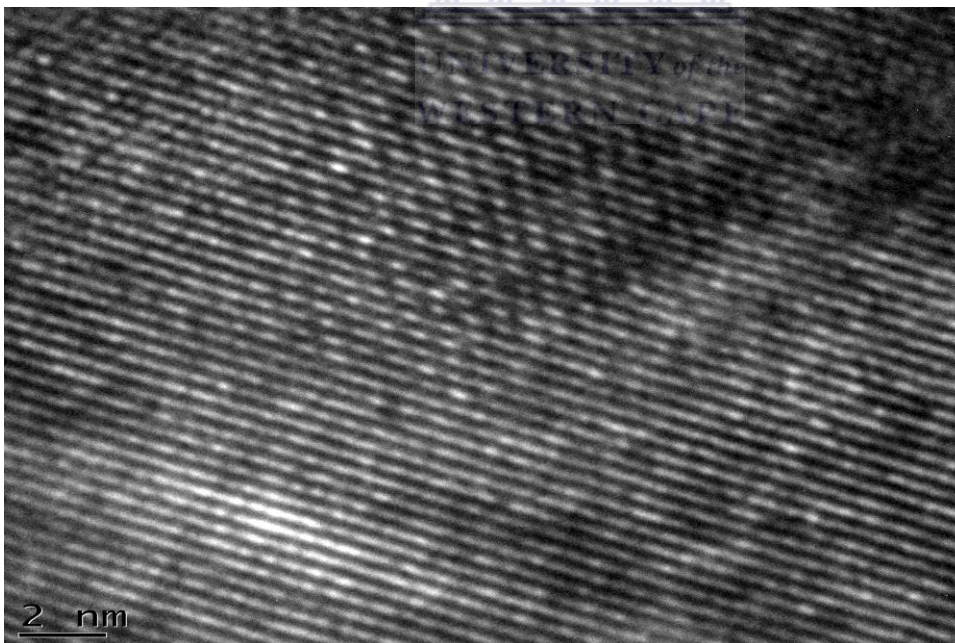
(b)

Figure 36. HRTEM of TaO-NiO-Mn$_3$O$_4$ at a magnification of (a) x 39K and (b) x 530K
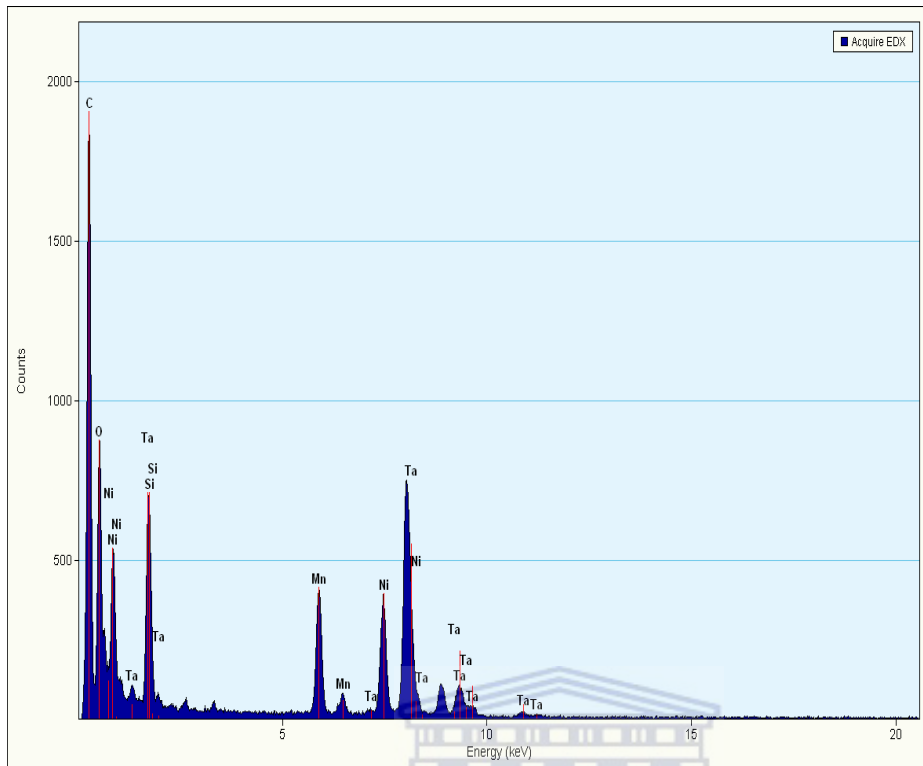
Figure 37. EDX of TaO-NiO-Mn₃O₄
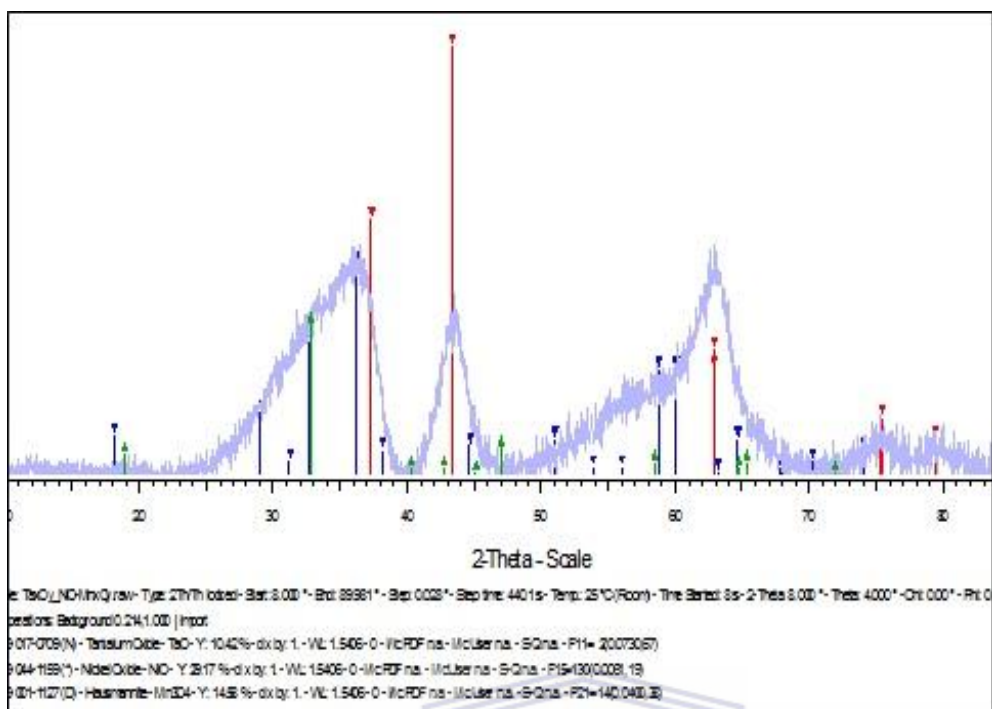
Figure 38. XRD of TaO-NiO-Mn₃O₄.

Chemical synthesis of single, binary and ternary metal oxide nanocrystals using modified sol-gel aqueous or non-aqueous and largely surfactant assisted method has been successful. In the synthesis of such inorganic metal oxide nanocrystals, the precursor compound in bulk solution (i.e. the nickel acetate, the manganese acetate, etc) is decomposed to generate atoms followed by precipitation starting from dissolved atoms as building blocks to form the nanocrystals. The precipitation process basically consists of a nucleation step followed by crystal growth stages. Generally, there are three kinds of nucleation processes: homogeneous nucleation, heterogeneous nucleation, and secondary nucleation. The sol-gel chemical colloidal nanocrystal synthesis of the metal oxide follows the homogeneous nucleation process. Homogeneous nucleation occurs in the absence of a solid interface by combining solute molecules to produce nuclei. It occurs due to the driving force of the thermodynamics because the supersaturated solution is not

92

stable in energy. Seed formation proceeds according to the LaMer model [161], according to which, the concentration of atoms in the crystal nucleation process steadily increases with time as the precursor is decomposed by heating. Colloidal nanocrystal formation comprises the following three steps:

(i)   The atoms start to aggregate into nuclei via self-nucleation as the monomer concentration in the solution is increased to supersaturation levels.

(ii)   Then monomers continuously aggregate on the pre-existing nuclei or seed which leads to gradual decrease in the monomer concentration. As long as the concentration of reactants is kept below the critical level, further nucleation is discouraged.

(iii)   With a continuous supply of atoms via ongoing precursor decomposition, the nuclei will grow into nanocrystals of increasingly larger size until an equilibrium state is reached between the atoms on the surface of the nanocrystal and the atoms in the solution.

The sol-gel chemistry involved in the synthesis of metal oxides is quite complex, on the one hand due to the high reactivity of the metal oxide precursors towards water and the double role of water as ligand and solvent, and, on the other hand, due to the large number of reaction parameters that have to be strictly controlled in order to provide good reproducibility of the synthesis protocol. Such parameters include hydrolysis and condensation, reactivity of the metal oxide precursors, pH, temperature, method of mixing, rate of oxidation, the nature and concentration of anions, etc. Further, the as-synthesized precipitates are generally amorphous and the post-synthetic annealing step required to induce crystallization process prevents

93

subtle control over crystal size, shape and at times the phase. As the temperature is elevated, a gel passes through various phase transitions until at some high temperature, depending on the nature of the gel, the most thermodynamically stable state is achieved. What transition phases appear at specific temperatures is very sensitive to the initial conditions under which the gel was made, such as temperature, pH, and concentrations of reactants. Rare, metastable phases, sometimes difficult to reproduce, have been documented [162]. Failure for this absolute control, and lack of very clear understanding of the process and very thin parameters controlling the precipitation though helpful in improving the engineering of the growth of nanocrystals to the desired size and shape, maybe the reason for formation of nanoparticles of same transition metal oxides in different oxidation states such as Mn_2O_3 in the composite $TaO-Mn_2O_3$, while Mn_3O_4 formed in the synthesis of $TaO-NiO-Mn_3O_4$ composite. Also TaO formed in the synthesis of $TaO-NiO-Mn_3O_4$ and $TaO-Mn_2O_3$ while TaO_2 was formed in the synthesis of TaO_2-NiO and TaO_2 oxides nanoparticles. The different reactivity of metal oxide precursors towards a specific solvent complicates the synthesis of oxides containing two or more metals. The reaction of metal halides with alcohols almost always results in metal oxide nanoparticles with halide impurities. To avoid this contamination synthesis routes based on the reaction of metal acetates, acetylacetonates or alkoxides with alcohols provide a halide-free alternative. Hence, the choice of acetates and alkoxides in this work was preferred.

5.7 Synthesis of sulphonated and the metal oxide doped polyaniline nanocomposites

Doped PANi was prepared by an oxidative dispersion method. PSSA was used as both a polymeric stabilizer and a dopant agent. Aqueous hydrochloric acid (HCl) and aniline were mixed and the reaction mixture was continuously stirred at 0 °C for one hour. In forming the metal oxide nanocomposites with doped PANi, the metal oxide nanoparticles (mono, binary and ternary mixed metal oxides) were weighed and dispersed into a measured volume of HCl and ultra-sonicated for 30 minutes before adding the aniline and the PSSA. A weighed amount of oxidant, ammonium peroxydisulfate ($(NH4)_2S_2O_8$) (APS) was added and the reaction mixture stirred for 24 hours at 0 °C in an ice-bath. The solution gradually darkened and acquired a blue colour over a period of about 20 min and eventually turned into dark green which is a characteristic colour of doped PANi. The resulting dark green dispersions were purified four times by centrifugation, filtered and washed in order to remove oligomers and excess monomers. In these approaches, the monomer is polymerized in the presence of commercially available inorganic acid particles which act as colloidal substrate for the precipitating polymer nuclei leading to the formation of conducting polymer–inorganic oxide composite [163].

The successful synthesis of the novel poly-(4-styrene-sulphonic acid) and tantalum oxide, tantalum oxide-nickel oxide, tantalum oxide-manganese oxide and tantalum oxide-nickel oxide-manganese oxide doped polyaniline nanocomposites were determined and ascertained using FTIR, TEM/HRTEM coupled with EDX. Figures 40, 41 (a)/(b), 43 (a)/(b) and 45 are TEM/HRTEM micrographs of TaO_2-PANi-PSSA, TaO_2-NiO-PANi-PSSA, TaO-Mn_2O_3-PANi-PSSA and TaO-NiO-Mn_3O_4-PANi-PSSA respectively. They

95

all show clustering of metal oxide nanoparticles anchored on nanofibrous polymer network with corresponding EDX spectra (figures 39, 42, 44 and 45 respectively) giving the elemental composition of each composite and informing of the successful synthesis of the nanocomposites. From the spectra, all the elements in each composite were confirmed. It is observed from the spectra of all the samples that sulphur, nitrogen, carbon and oxygen elements are present in all of them. The presence of S, N, C and O in each of the EDX is a signature of successful doping of the polymer with the sulphonic acid group, -SO$_3$H. The presence of respective metals and oxygen in the EDX spectra indicates successful entrapment of the respective metal oxides within the polymeric network. Figures 39, 41 (a) & (b), 43 (a) & (b) and 45 are the HRTEM micrographs of the composites. It is observed from the micrographs that the oxide nanoparticles (black spots) are uniformly dispersed and in some cases agglomerate with dense distribution in the PANi matrix. They show perfect diffraction patterns (as some of the examples displayed shows) with clear atomic fridges oriented in different directions showing that the materials are polycrystals made of different nanocrystallites uniformly distributed and oriented in different planes. This is confirmed from the XRD studies. During the 30 minutes sonication to disperse the composites in ethanol for TEM analysis, the oxide nanoparticles were not detached from the polymer matrix meaning that the interaction between the metal oxide nanoparticles and the polymer is strong suggesting formation of composites.
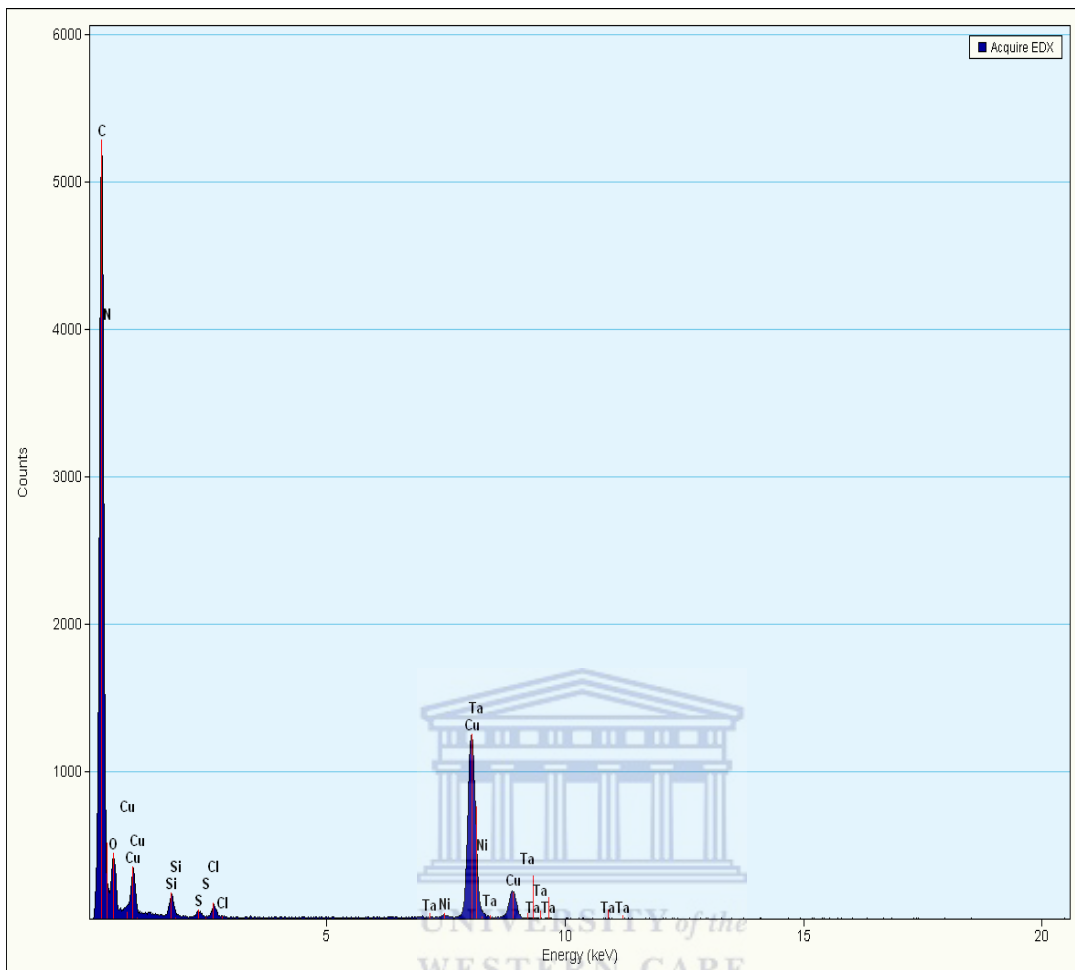
Figure 39. EDX of TaO₂-PANi-PSSA.
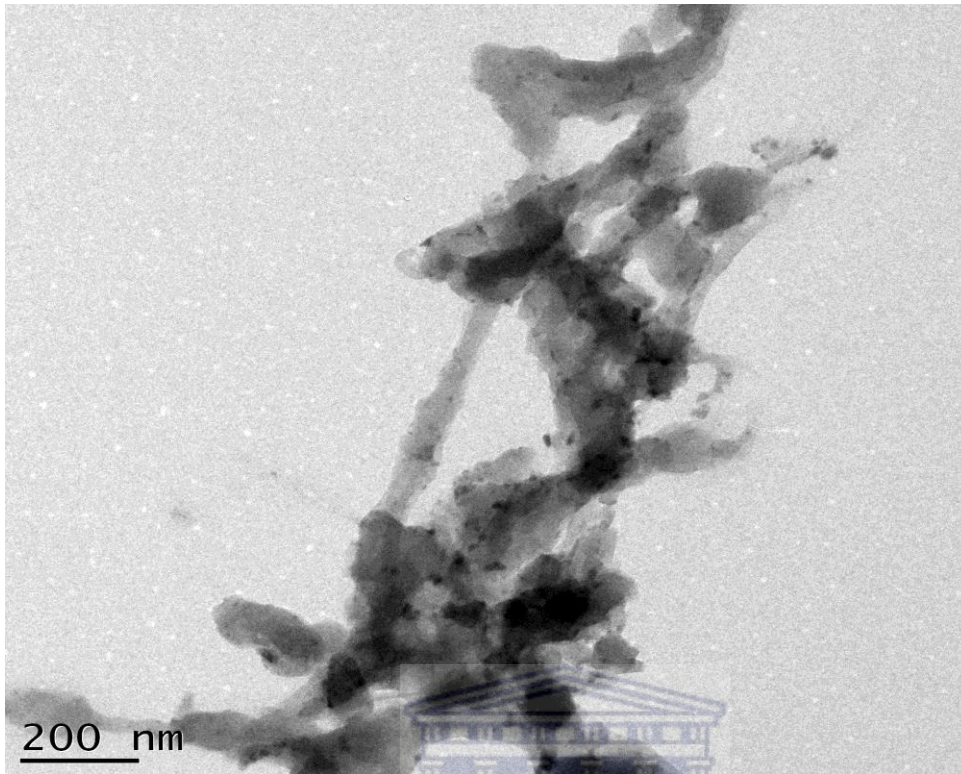
Figure 40. TEM of TaO₂-PANi-PSSA.
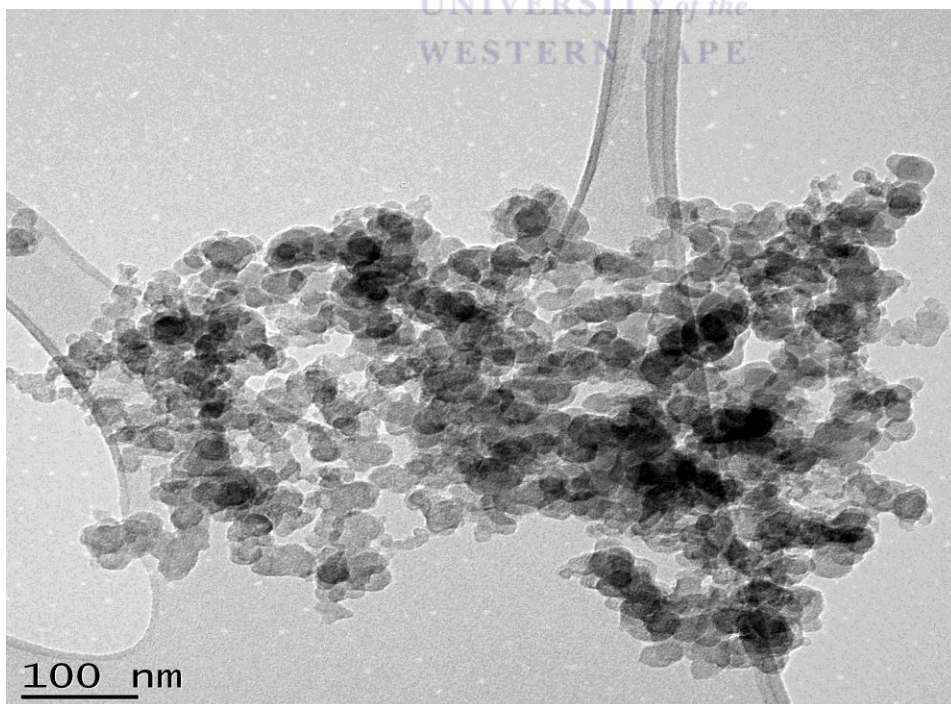
(a)
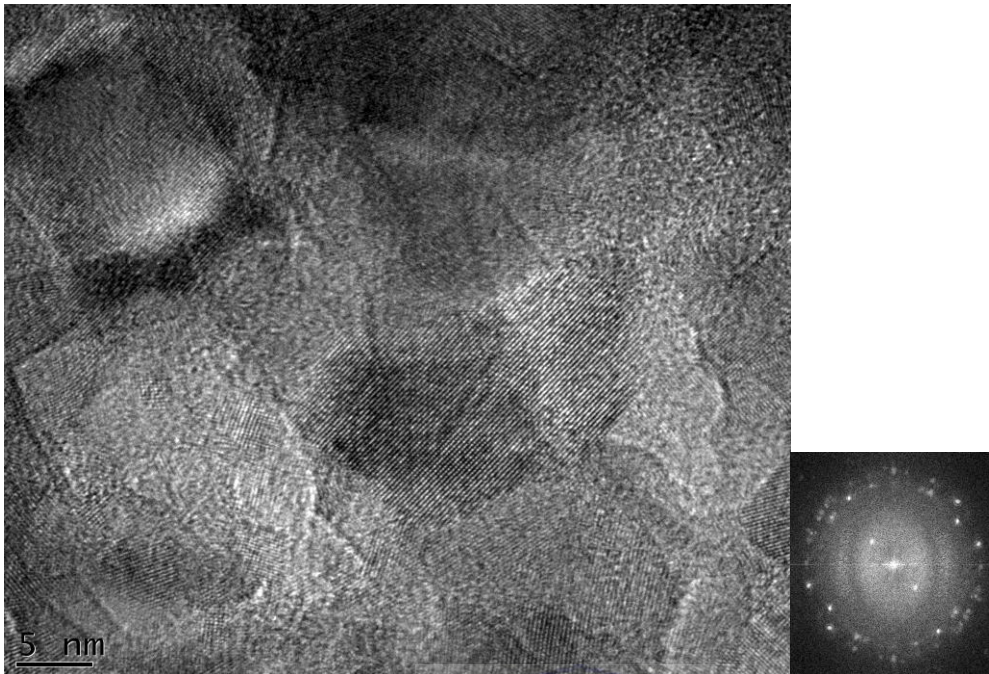
(b)

Figure 41. HRTEM of TaO₂-NiO-PANi-PSSA at a magnification of (a) x 88K and (b) x 410K
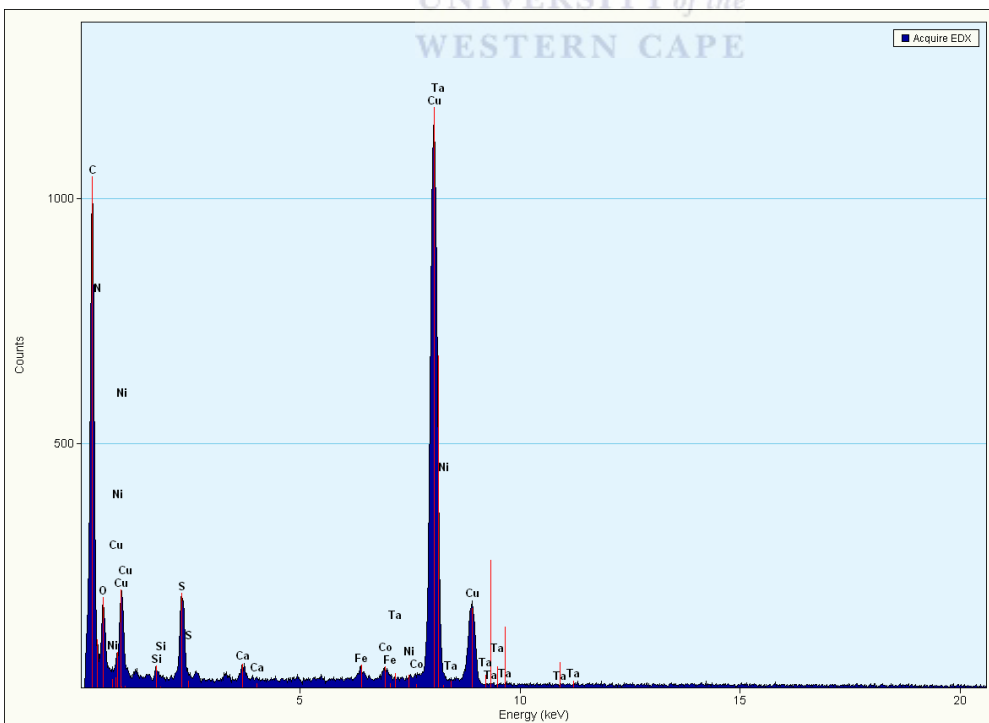
Figure 42. EDX of TaO₂-NiO-PANi-PSSA
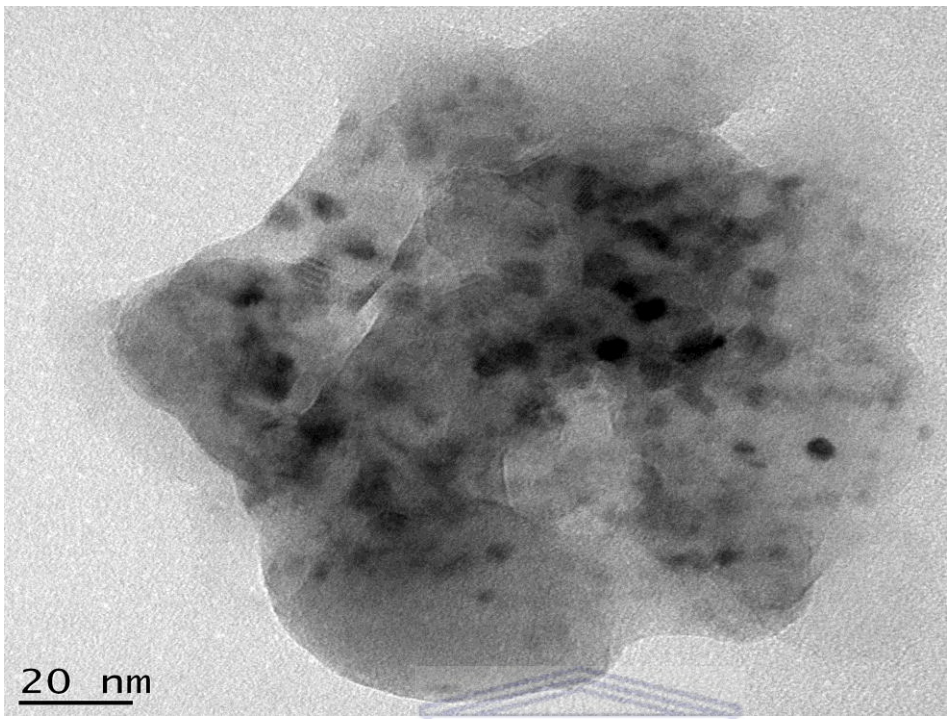
(a)
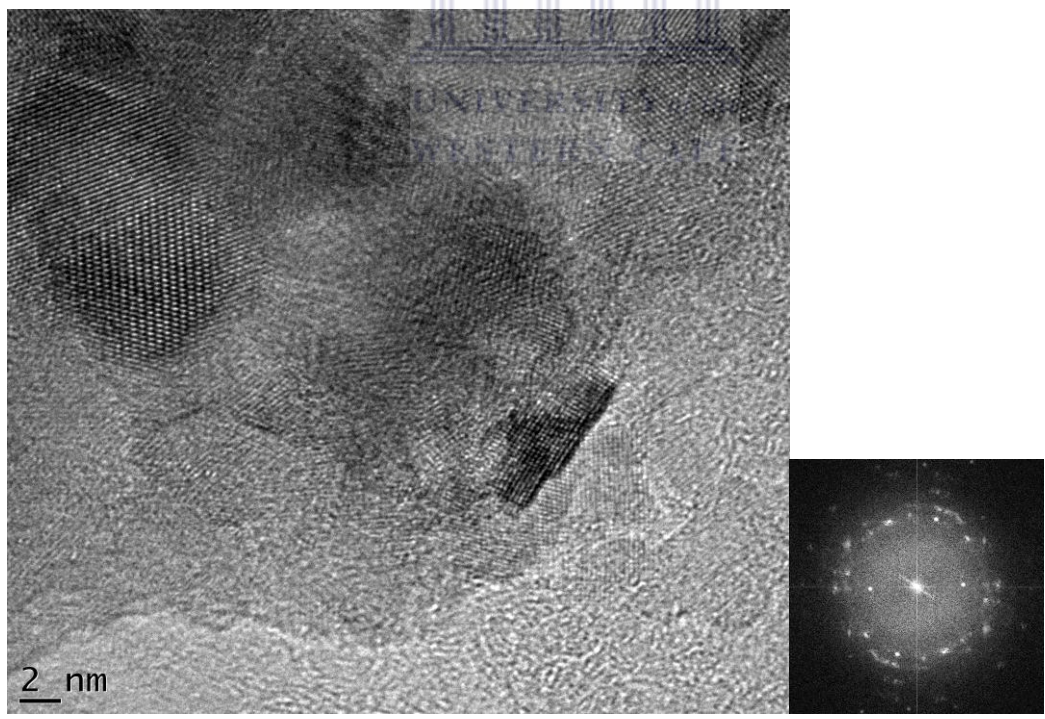
(b)

Figure 43. . HRTEM of TaO-Mn$_2$O$_3$-PANi-PSSA at a magnification of (a) X35 K and (b) X64 K
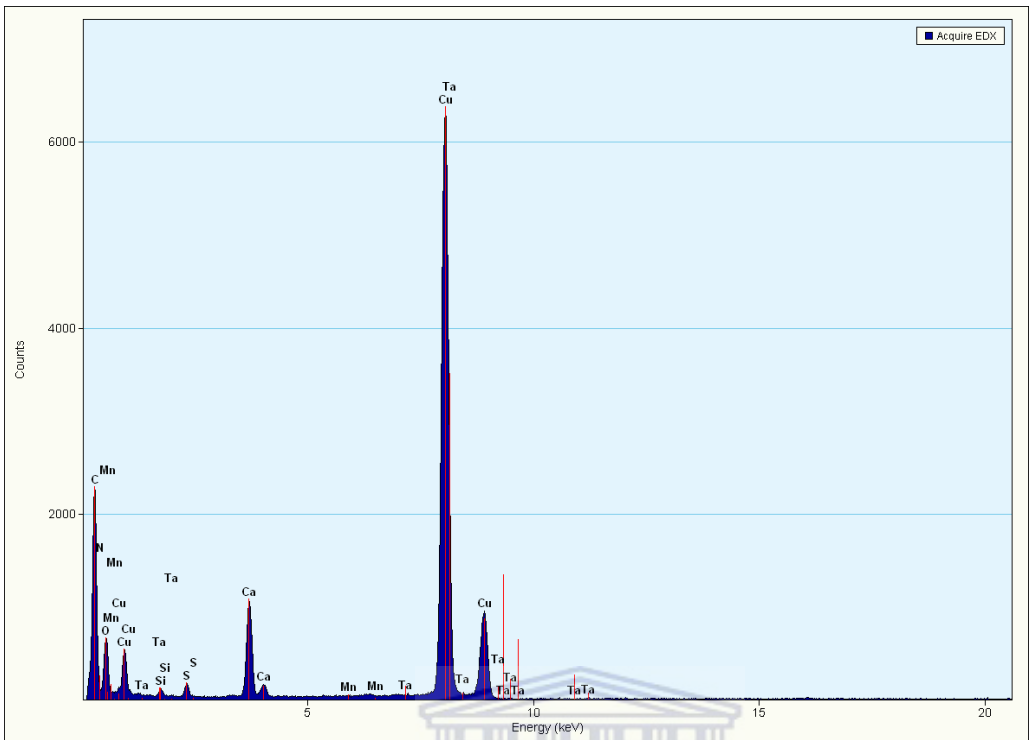
Figure 44. EDX of TaO-Mn₂O₃-PANi-PSSA
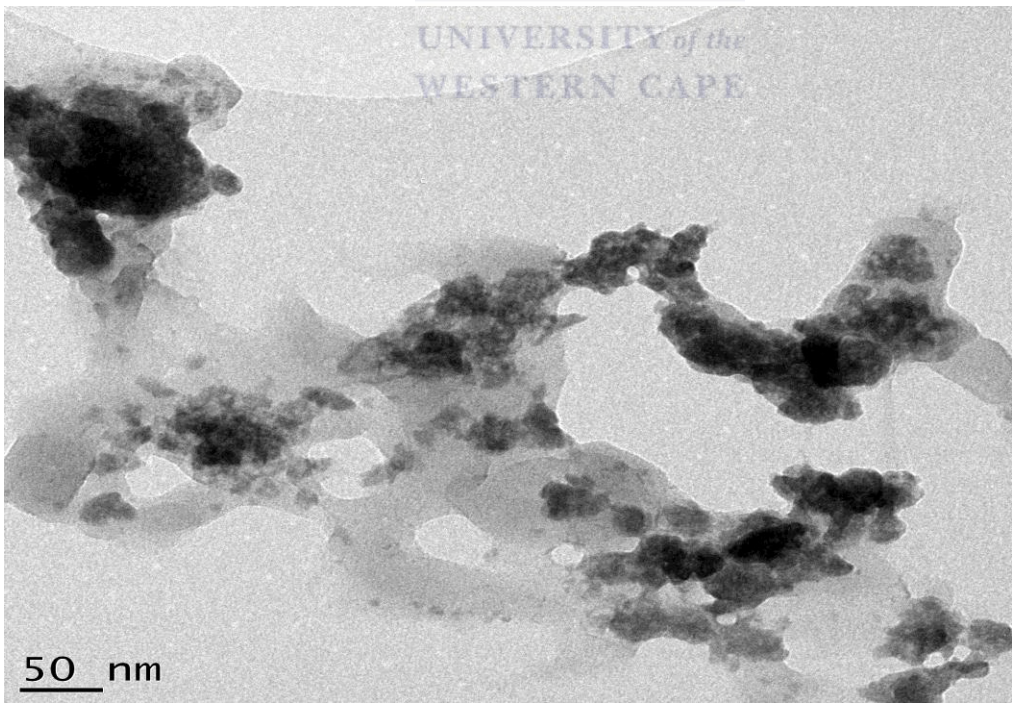
Figure 45. TEM of TaO-NiO-Mn₃O₄-PANi-PSSA

101

5.8 FTIR analysis of the doped PANi nanocomposites

The FTIR spectra for TaO_2-PANi-PSSA, TaO_2-NiO-PANi-PSSA, TaO-Mn_2O_3-PANi-PSSA and TaO-NiO-Mn_3O_4-PANi-PSSA are shown in figure 46. Pure polyaniline has characteristic peaks at 1590, 1494, 1302, 1140, and 820 cm^{-1} with the bands at 1590 and 1494 cm^{-1} being attributed to the C=C and C=N stretching modes of vibration for the quinoid (-N=Q=N- where Q = quinoid ring) and benzenoid units while the bands at 1302 and 1242 cm^{-1} are assigned to the C-N stretching mode of benzenoid units. The band at 1140 cm^{-1} is due to the quinoid unit (-N=Q=N- where Q = quinoid ring) of polyaniline. The band at 820 cm^{-1} is attributed to C-C and C-H stretching for benzenoid unit of polyaniline and band at 681.92 cm^{-1} assigned to out of plane C-H vibration [164-165]. Doping of PANi with poly(4-styrene sulphonic acid) and/or incorporation of the metal oxide nanocomposites leads to shifts of some FTIR peaks in PANi as the results in figure 46 show.
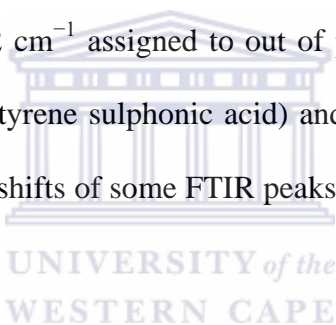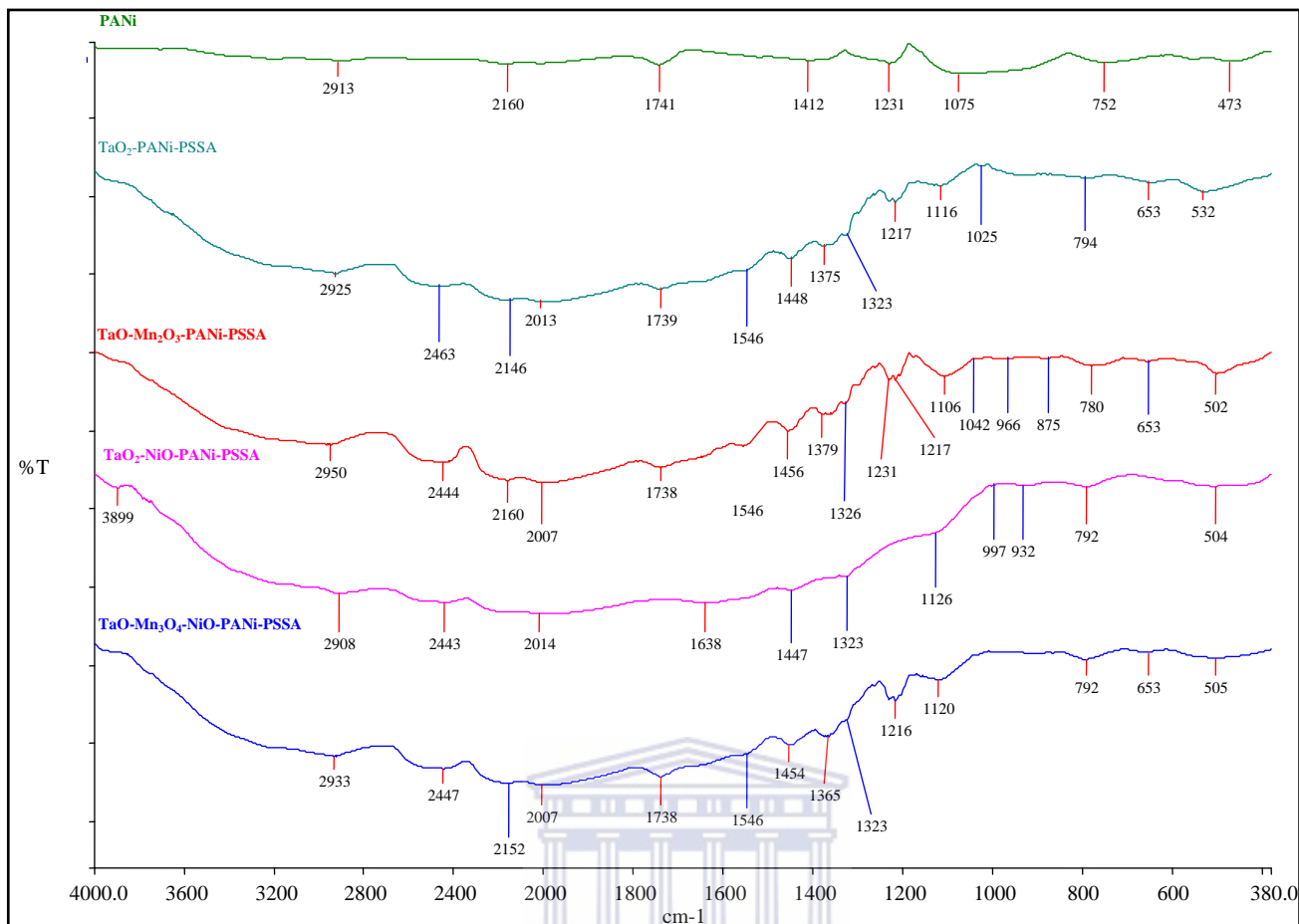
Figure 46. FTIR of PANi based nanocomposites

Transmission maxima at 752 cm^{-1}(for PANi), 794 cm^{-1} (TaO$_2$-PANi-PSSA), 780 cm^{-1} (TaO-Mn$_2$O$_3$-PANi-PSSA), and 792 cm^{-1} (for TaO$_2$-NiO-PANi-PSSA and TaO-NiO-Mn$_3$O$_4$-PANi-PSSA) are consistent with the C-H out-of-plane bending motions of benzenoid rings. The 1375 cm^{-1} (TaO$_2$-PANi-PSSA), 1379 cm^{-1} (TaO$_2$-NiO-PANi-PSSA and TaO-Mn$_2$O$_3$-PANi-PSSA) and 1365 cm^{-1} (TaO-NiO-Mn$_3$O$_4$-PANi-PSSA) corresponds to the C-N stretching of the secondary aromatic amine; 1231 cm^{-1} (PANi), 1217 cm^{-1} and 1323 cm^{-1} (TaO$_2$-PANi-PSSA), 1231 cm^{-1} and 1326 cm^{-1} (TaO-Mn$_2$O$_3$-PANi-PSSA), 1323 cm^{-1} (TaO$_2$-NiO-PANi-PSSA) and 1216 and 1323 cm^{-1} (TaO-NiO-Mn$_3$O$_4$-PANi-PSSA) is associated with the C-H stretching vibration with aromatic conjugation; 1412 cm^{-1} (PANi), 1448 cm^{-1}(TaO$_2$-PANi-PSSA), 1456 cm^{-1} (TaO-Mn$_2$O$_3$-

PANi-PSSA), 1447 cm^{-1} (TaO$_2$-NiO-PANi-PSSA) and 1454 cm^{-1} (TaO-NiO-Mn$_3$O$_4$-PANi-PSSA) are associated with C-C aromatic ring stretching vibrations of the benzenoid diamine unit; 1546 cm^{-1} (TaO$_2$-PANi-PSSA), 1546 cm^{-1} (TaO-Mn$_2$O$_3$-PANi-PSSA & TaO-NiO-Mn$_3$O$_4$-PANi-PSSA) and 1638 cm^{-1} (TaO$_2$-NiO-PANi-PSSA) arises mainly from both the stretching vibrations of N=Q=N and N-B-N rings of the quinoid (Q) and benzoid (B) units. The transmission maxima around the wave numbers 1100 cm^{-1} and 1000 cm^{-1} (varying from one composite to another) are all consistent with the presence of -SO$_3$H group and arises, respectively, from asymmetric and symmetric stretching modes of S-O of the –SO$_2$-O$^-$ group. However, the peaks around 1100 cm^{-1} and observed at wavenumbers 1116 cm^{-1} (TaO$_2$-PANi-PSSA), 1106 cm^{-1} (TaO$_2$-NiO-PANi-PSSA), 1126 cm^{-1} (TaO-Mn$_2$O$_3$-PANi-PSSA) and 1120 cm^{-1} (TaO-NiO-Mn$_3$O$_4$-PANi-PSSA) respectively and absent in doped PANi can also signify dominance of quinodic ring structure and is also a measure of degree of electron delocalization. Any polymer attack occur preferentially on the quinoneimine units due to the higher charge localization on the C=N and C=C bonds present in the monomeric units [166-172]. These FTIR results enhance the EDX results and show successful polymerization and doping of PANi by the PSSA. Differences in the FTIR spectra can be explained on the basis of constrained growth and restricted modes of vibration in PANi grown in the presence of metal oxides. In such a case, the aniline monomer gets adsorbed on the oxide particles, which were dispersed in the reaction mixture before initiation of polymerization by ultrasonication and the polymerization proceeds initially on the surfaces of these oxide particles when (NH$_4$)$_2$S$_2$O$_8$ (ammonium persulphate) is added to the solution. This leads to adhesion of the polymer to the metal oxide nanoparticles and this explains the

constrained growth around these particles and as a result, the characteristic stretching frequencies are shifted towards lower frequency side compared to those of pure PANi. Hence, there is a kind of weak Van der Waals force of attraction between the polymer chain and the oxide nanoparticles [163]. Also, ionic metal oxide nanoparticles and probably some metallic cations which may form during sonication after dissolving of some metal oxide nanoparticles might bind to more than one nitrogen site in a PANI chain or form inter-chain linkage among several adjacent PANI chains by coordination, and both intra-chain and inter-chain connections might lead to a more coil-like conformational change or a more twisted aggregation of PANI chains [173].

5. 9 UV-visible spectroscopy

The electronic absorption spectra of sulphonated PANi-metal oxide composites are given in figure 47.
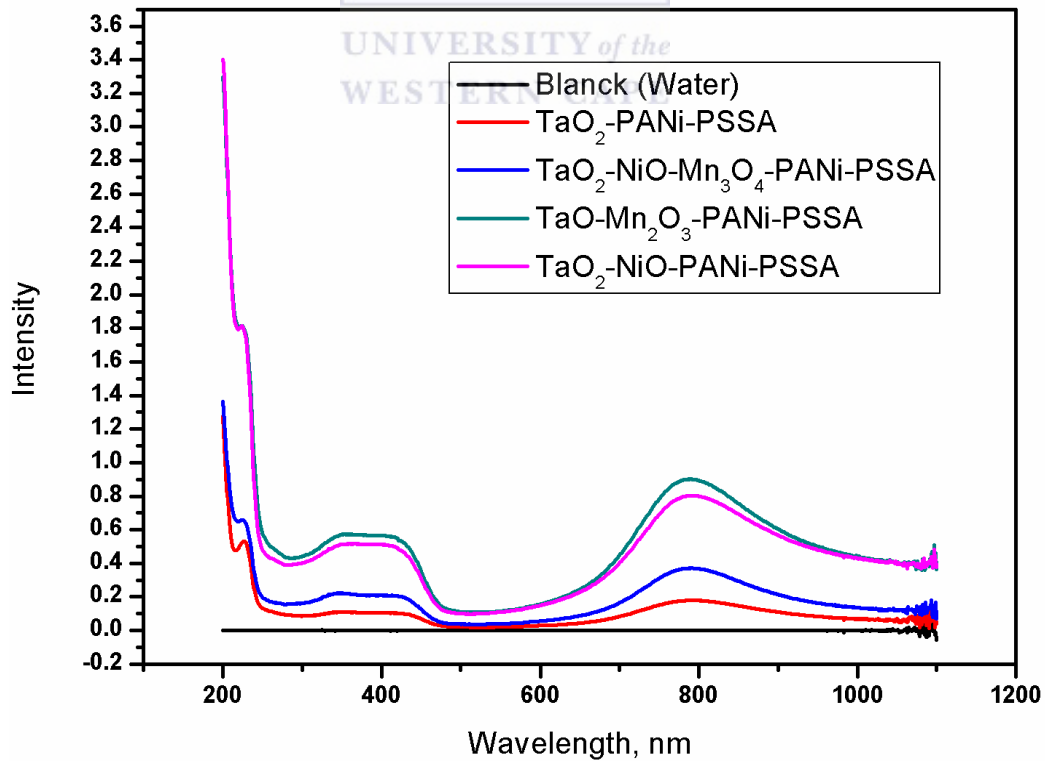
Figure 47. UV-vis spectra of the composites

All the spectra showed three absorption bands. Clearly, the prepared composites not only can strongly absorb the UV light but also can absorb the visible light. Peaks of the composite solutions appeared at about 320 nm which can be asigned to π-π^* transition of the benzenoid ring and at about 430 nm and 850 nm due to polaron-π^* and π-polaron band transitions, respectively. These latter two bands are transitions from a localized benzenoid highest occupied molecular orbital ie a benzenoid to quinoid excitonic transition suggesting that the composites are PANi composites in the PANi doped state, the emeraldine state [170, 174-175]. It is noted that with incorporation of the metal oxides into the PANi matrix, the UV absorption and the absorption around 800 nm is strengthened and slightly blue shifted indicating that there is a strong interaction between polyaniline and the metal oxide nanocystallite dopants. The rationale behind the use of the UV-Vis spectroscopical technique as a spectroscopical signature [176] relies on the fact that polymers doped with long chain organic acids are structurally modulated and their electronic spectra display additional absorption bands associated with the existence of polarons/bipolarons. The latter bands are delocalization charge defects in the polymer whose presence converts the polymer into an intrinsic conductor. It is now known that the electronic spectra of undoped polyanilines (prestine) are basically made up of two absorption bands. A band at 320 nm due to the π-π^* transition of the benzoid rings and another at 600 nm assigned to the π-π^* of the quinonoid structures [177]. In addition to these bands, organic acid doped polyanilines are characterized by additional bands at 420 and 800 nm associated with the polaron/bipolaron states in the polymer. The latter states are new electronic energy levels created within the polymer sub-gap energies during the polymer/dopants interactions.

106

Figures 48 (a)-(d) shows the XRD diffraction patterns for sulphonated and the metal oxide doped PANi composites. The spectra patterns of these composites exhibit three broad peaks at 2-Theta values around 26°, 55° and 80° with a sharp peak appearing at 20° in TaO_2-PANi-PSSA, and TaO-NiO-Mn_3O_4-PANi-PSSA which is diminished in TaO_2-NiO-PANi-PSSA and TaO-Mn_2O_3-PANi-PSSA. The peak is right shifted in TaO_2-NiO-PANi-PSSA.

(a)

(b)

(c)
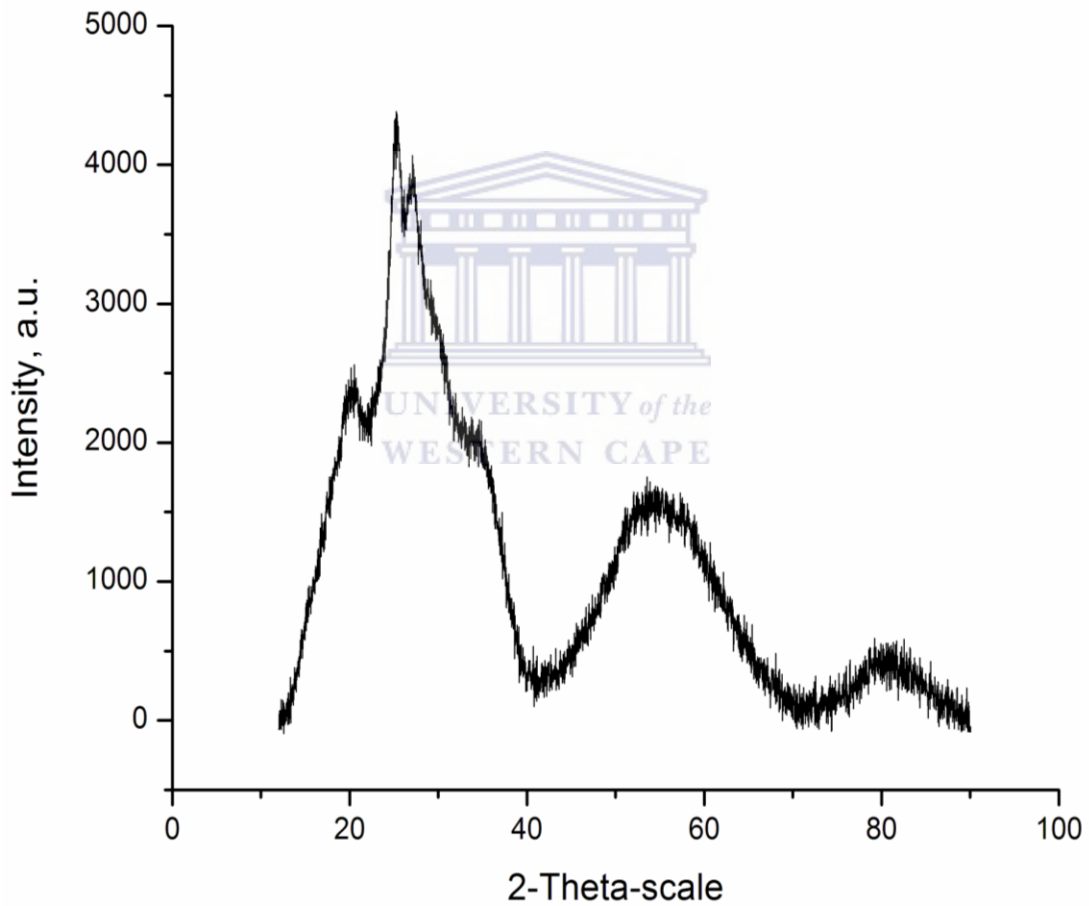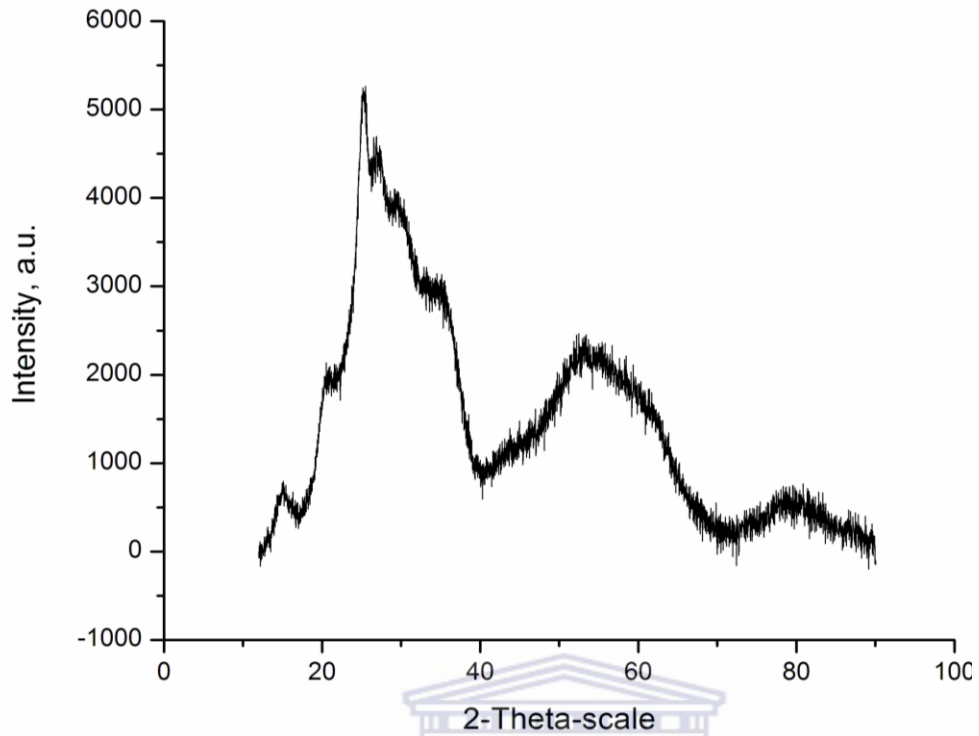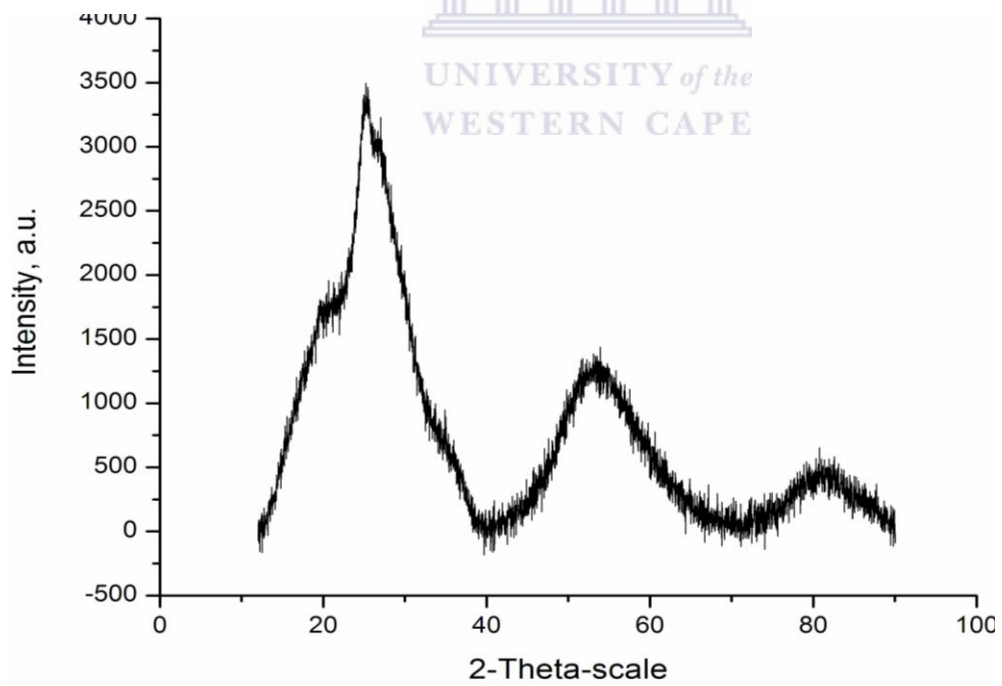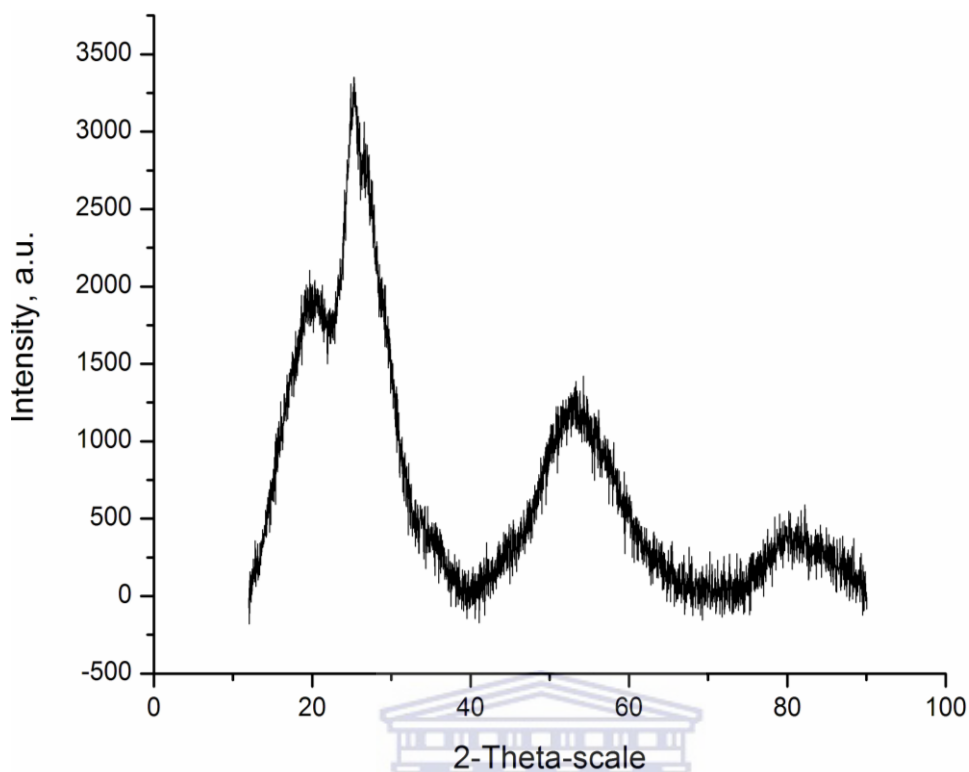
Figure 48. XRD of (a) TaO$_2$-PANi-PSSA, (b) TaO$_2$-NiO-PANi-PSSA, (c) TaO-Mn$_2$O$_3$-PANi-PSSA and (d) TaO-NiO-Mn$_3$O$_4$-PANi-PSSA

The degree of sharpness of this peak indicates that these composites are polycrystalline in nature. The peak centred at 20º may be ascribed to the periodicity parallel to the polymer chain while the other peaks may be caused by the periodicity perpendicular to the polymer chain [169-170]. Characteristic peaks of crystalline PANi appear at about 2-Theta = 20º, 26º and 92º [178-179]. It can be argued that in forming the sulphonated PANi composites with the metal oxides, these characteristic peaks were broadened and shifted in the composites as is evident from the XRD spectra in figures 4(a)-(d). Changes and shifting of peaks suggests that the addition of nanocrystalline metal oxide nanoparticles hampers the crystallization of the polyaniline molecular chain. This

109

happens when the deposited polyaniline is absorbed on the surface of the oxide nanoparticles. The molecular chain of absorbed polyaniline is tethered and the degree of crystallinity decreases [174].

5.10   Scanning electron microscopy (SEM)

SEM images were obtained using HITACHI X-650 Scanning Electron Microscopy with an electron accelerating voltage of 25 KV and a working distance of 15 mm. Figures 49-52 are the SEM images showing the morphological features of the composites.
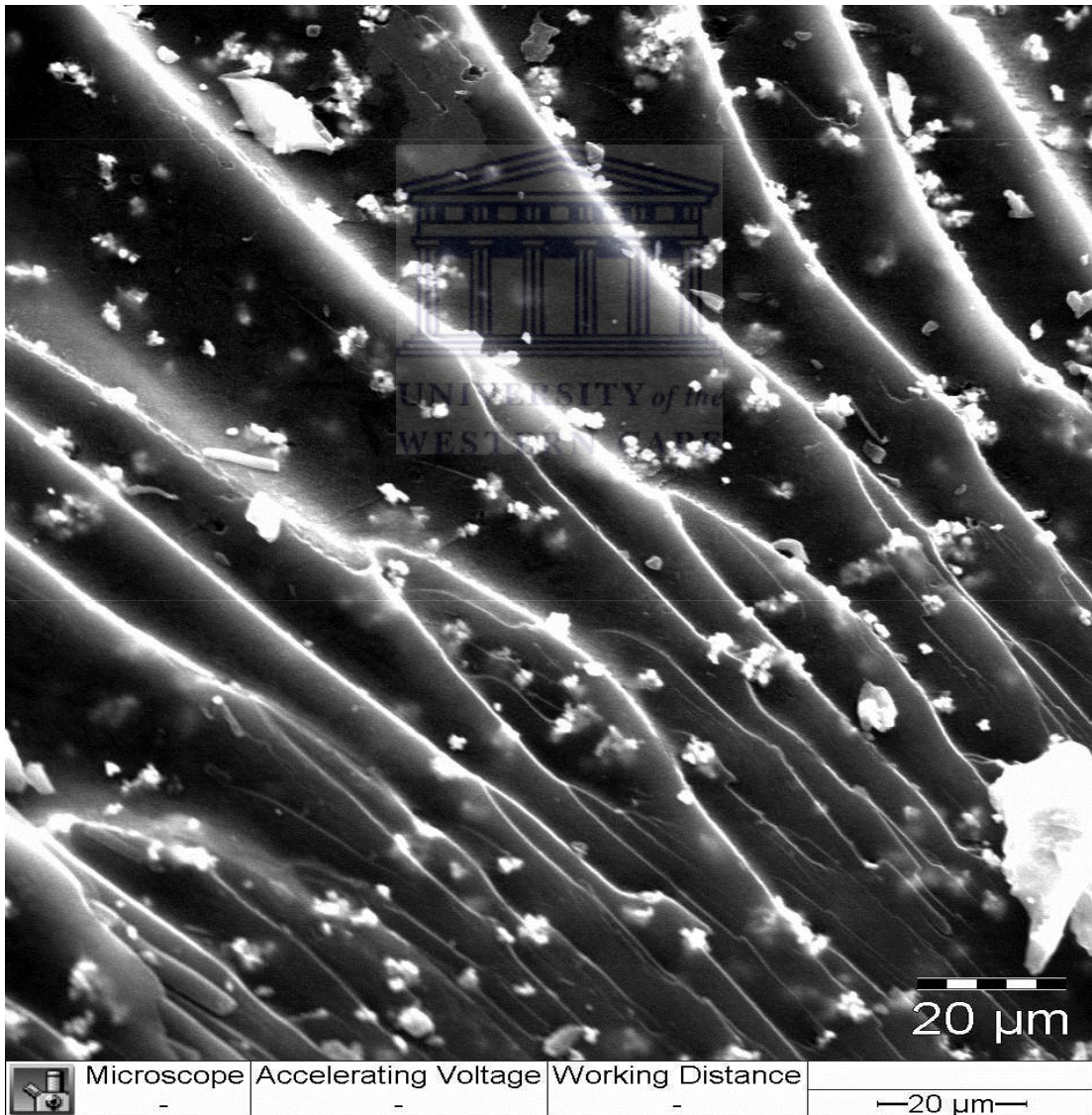
Fig 49. SEM image of Ta$_2$O-PANi-PSSA.
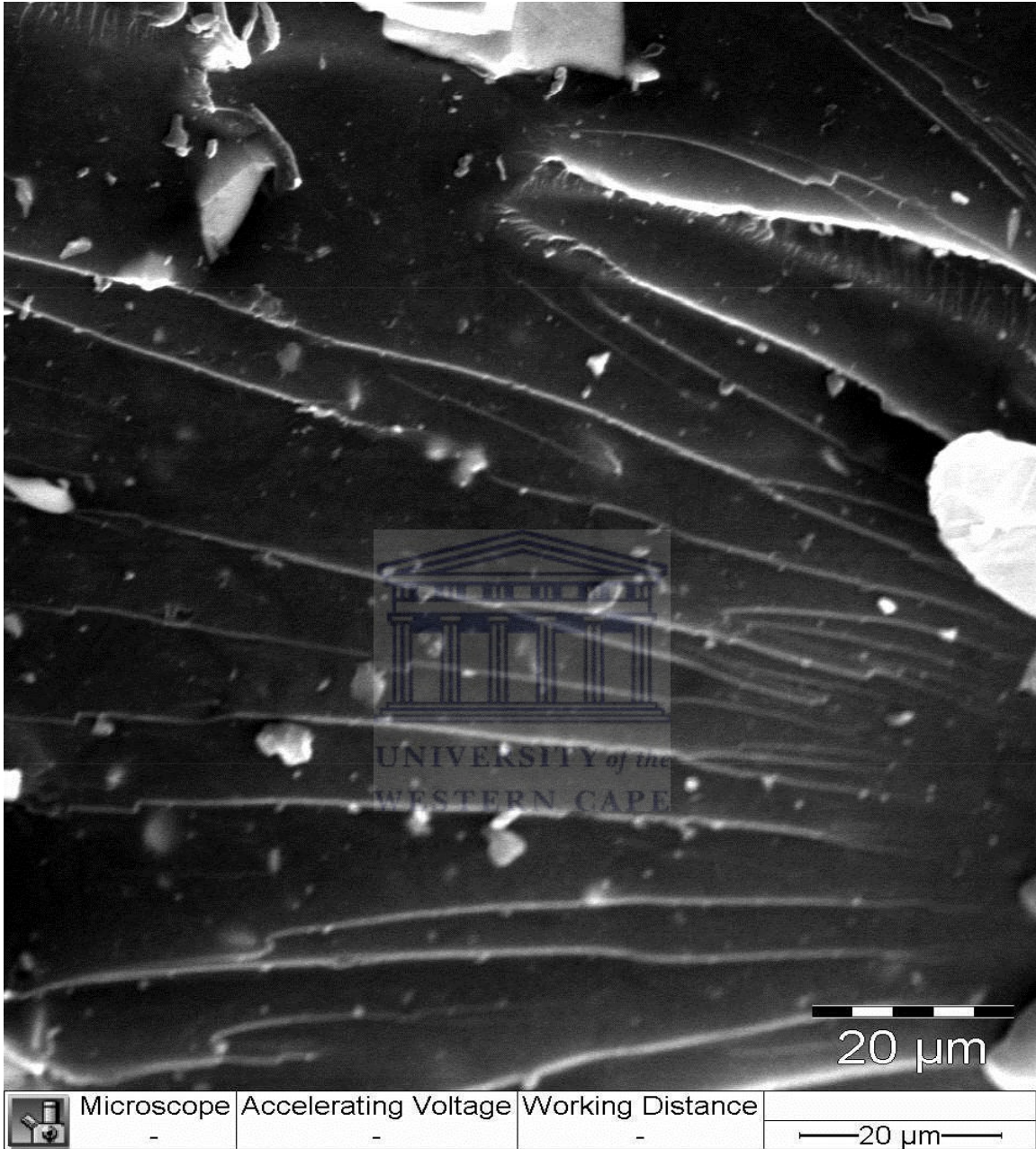
Fig 50. SEM image of Ta$_2$O-NiO-PANi-PSSA

Fig 51. SEM image of TaO-Mn₂O₃-PANi-PSSA
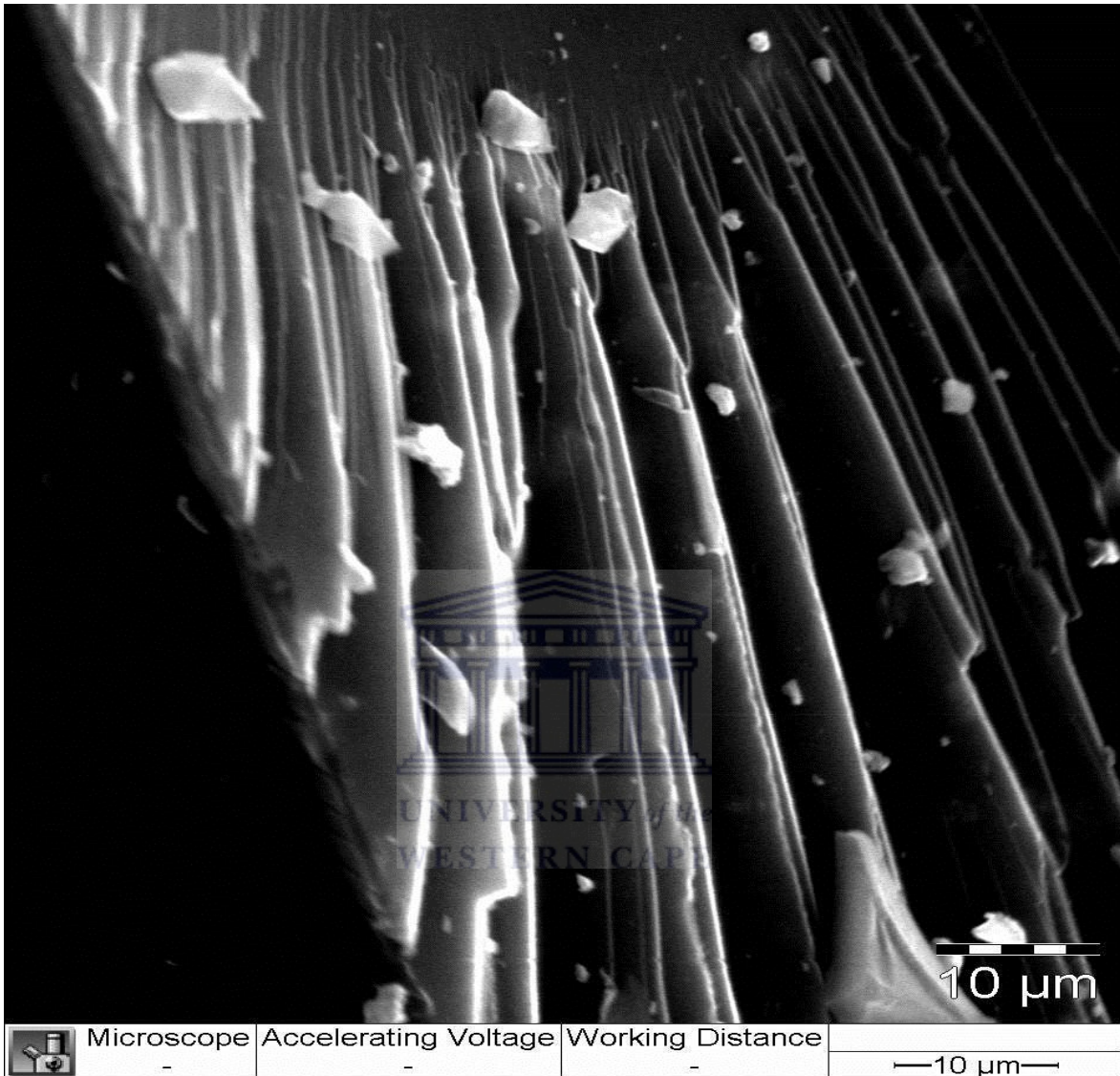
Fig 52. SEM image of TaO-NiO-Mn₃O₄-PANi-PSSA

The composites display unique nanofibre morphologies and the use of a high resolution SEM would be necessary to clearly describe the true morphology. The design and manipulation of morphological microstructure of conducting polymer is one of the most challenging tasks in materials science. It is still difficult to prepare predictable nanostructures based on rational design. It is found that the morphology of PANi nanostructures is strongly

113

affected by the nature, species, and concentration of the dopant, solvent, surfactant, oxidant, and monomer, as well as the various kinds of template and synthesis methods. The ultimate aim in this work was to prepare PANi polymeric nanocomposite materials with high surface area morphology, a characteristic feature and requirement of good electrode materials for electrochemical charge storage. The observed morphology, the nanofibres with redox active transition metal oxide nanoparticles clearly anchored on to the redox active polymer surface, meets this criterion and can serve as good electrode materials and when they are integrated with activated graphitic carbon (see section 4.3.3), their charge storage capacity is enhanced due to an enhanced surface area and functionality.

5.11 Scanning electrochemical microscopy (SECM) analysis of the doped PANi nanocomposites

The SECM370 electrochemical workstation model of SECM utilises a fast and precise, closed loop x, y, z positioning system with nanometer resolution, along with a flexible data acquisition system [180-183]. The SECM bipotentiostat was used to apply a potential to an Ultra-Micro Electrode (UME) immersed in a solution containing a redox active mediator, potassium ferrocyanide ($K_3Fe(CN)_4$), which is an electroactive species. The electrode tip was used to generate, via electrolysis, a reduced or oxidized mediator species. When the electrode tip is far from the substrate surface immersed in the solution, the reaction of the redox active dissolved species at the tip results in a Faradaic current driven by the hemispherical flux of the substrate from the solution to the tip as shown in figure 53. A current response at the tip electrode as the tip is moved closer and closer to the substrate in a solution of $Fe(CN)_6^{4-}$ is generated.

114
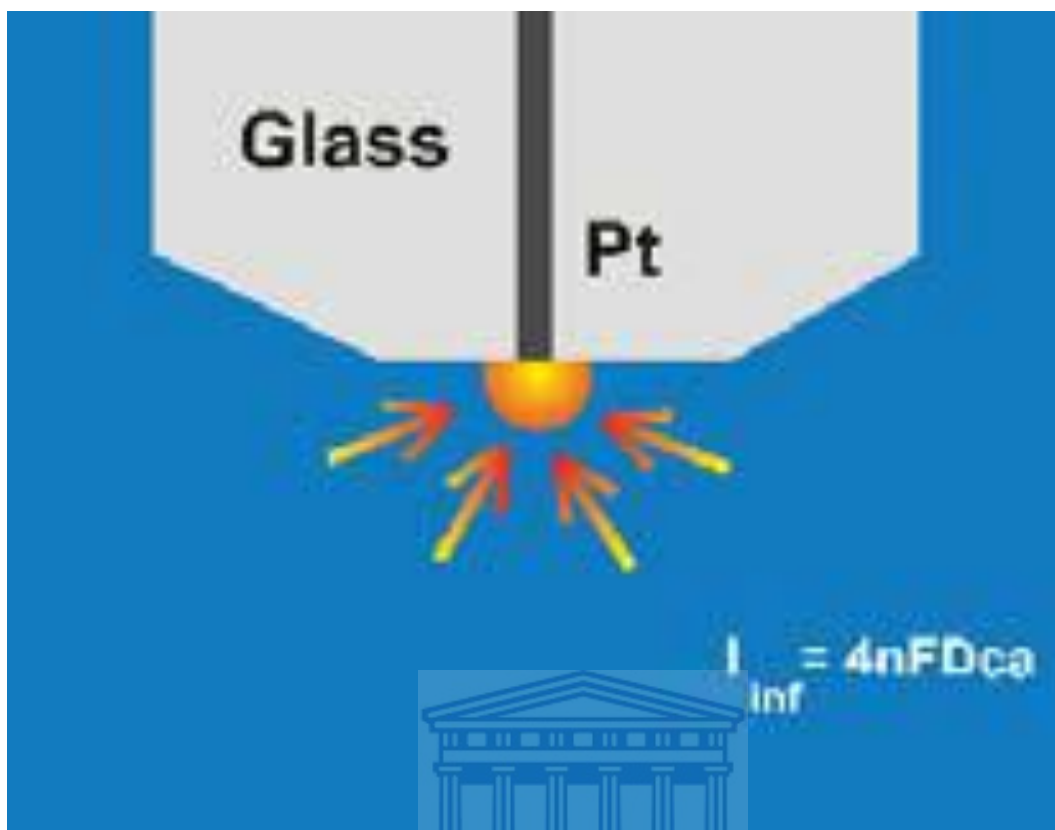
Figure 53. Hemispherical diffusion

The Faradaic current generated was used to study the surface electrical conductivity of the nanocomposite material substrate using the feedback and constant height modes of the SECM. In the constant height mode, a flat surface was assumed all through after a leveling protocol was undertaken at the initial stage of cell assembly. Figures 54, 55, 56, 57 are the SECM z-approach curves for TaO_2-PANi-PSSA, TaO_2-NiO-PANi-PSSA, TaO-Mn_2O_3-PANi-PSSA and TaO-NiO-Mn_3O_4-PANi-PSSA polymeric nanocomposites. Approach curves are plots of tip current versus the distance between the tip and substrate electrode as the tip is advanced toward the substrate in a solution containing a reactant which can be reduced (or oxidized) at the tip and substrate electrodes. The SECM approach experiments were meant to determine whether the materials were electrically

conductive or not. The positive feedback curve profiles obtained for the four composites showed that all the materials are electrically conductive. The mechanism of this conductivity is explained below.
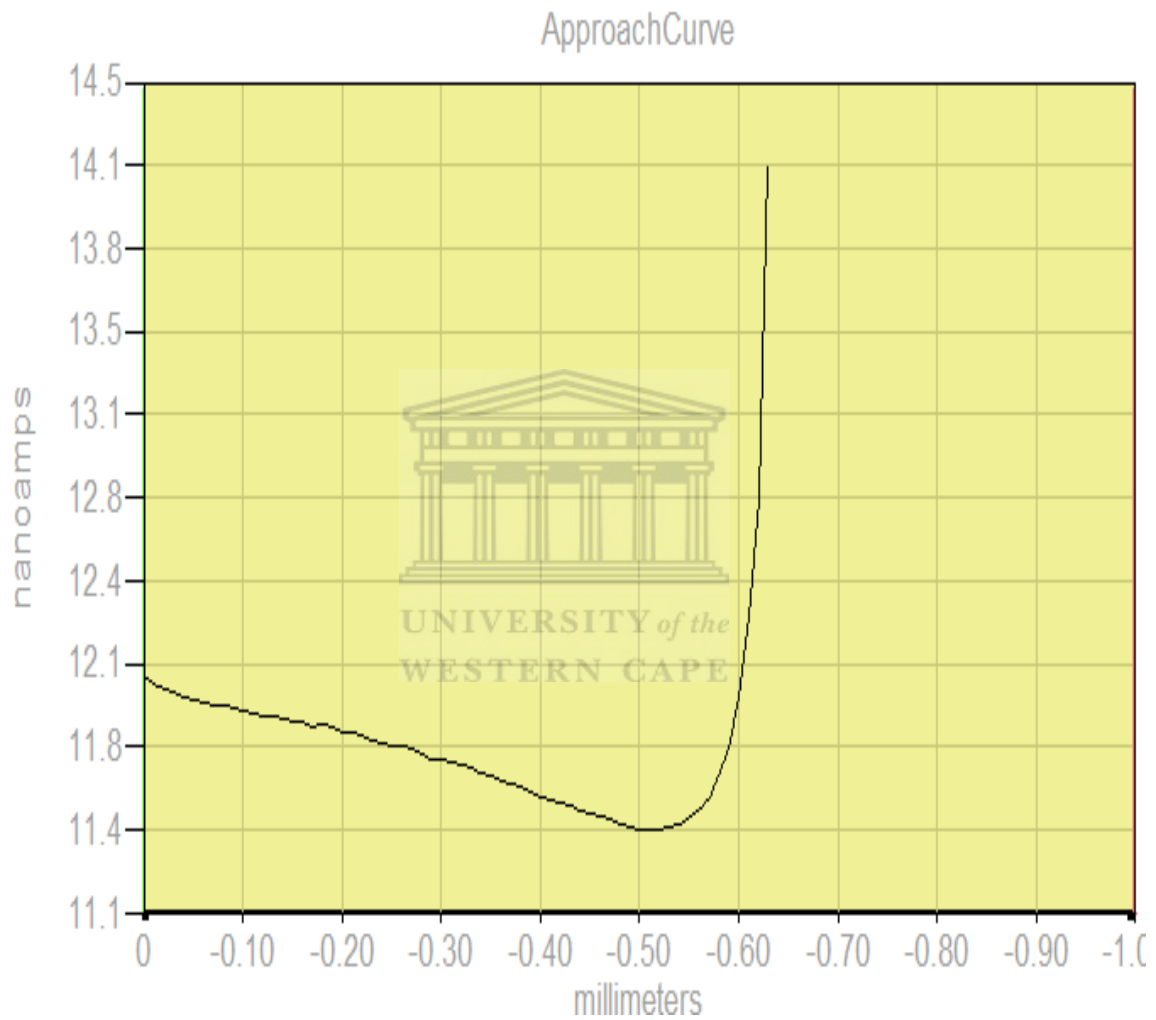
Figure 54. Approach curve for TaO$_2$-PANi-PSSA
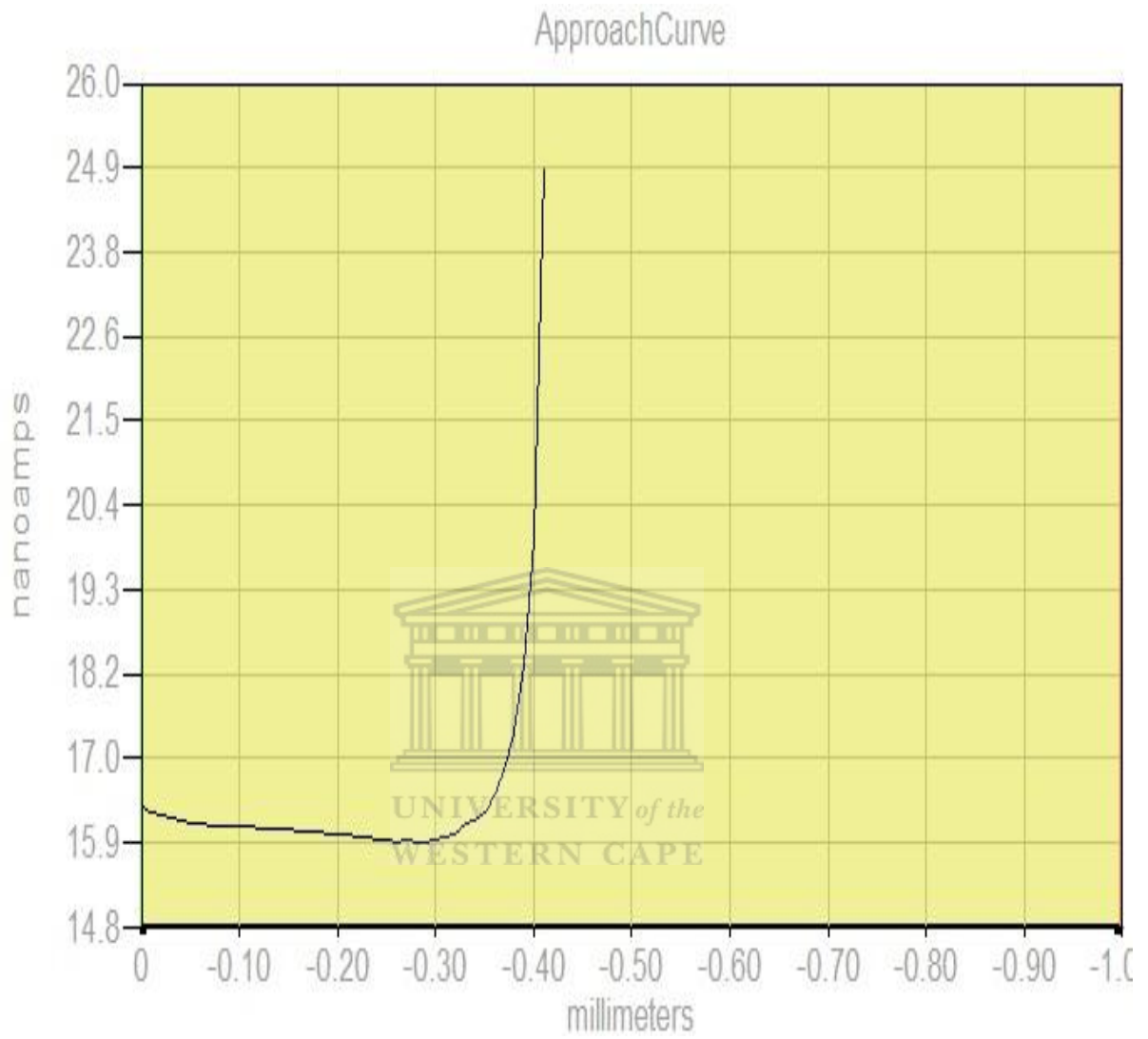
Figure 55. Approach curve for TaO$_2$-NiO-PANi-PSSA
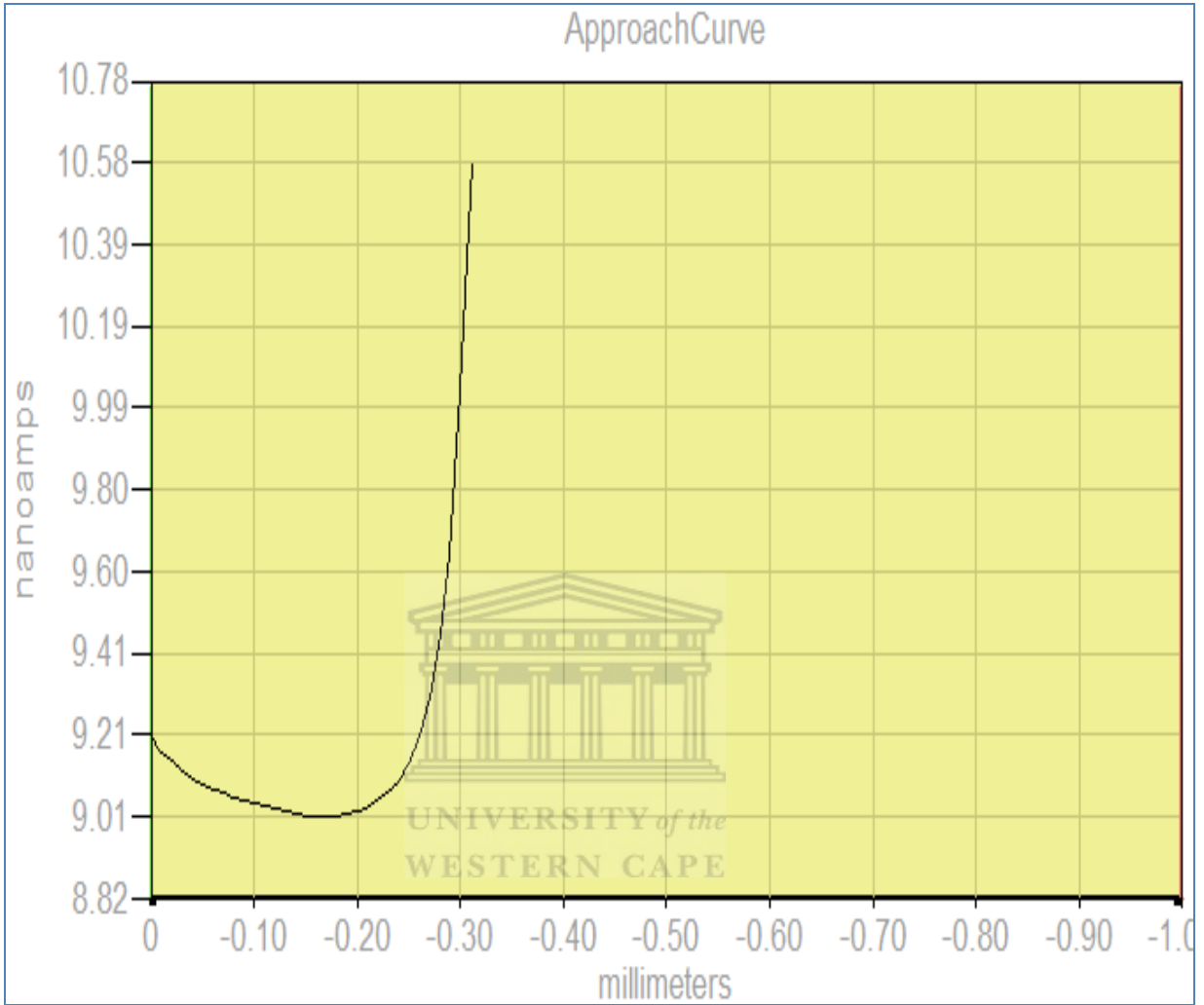
Figure 56. Approach curve for TaO-Mn$_2$O$_3$-PANi-PSSA
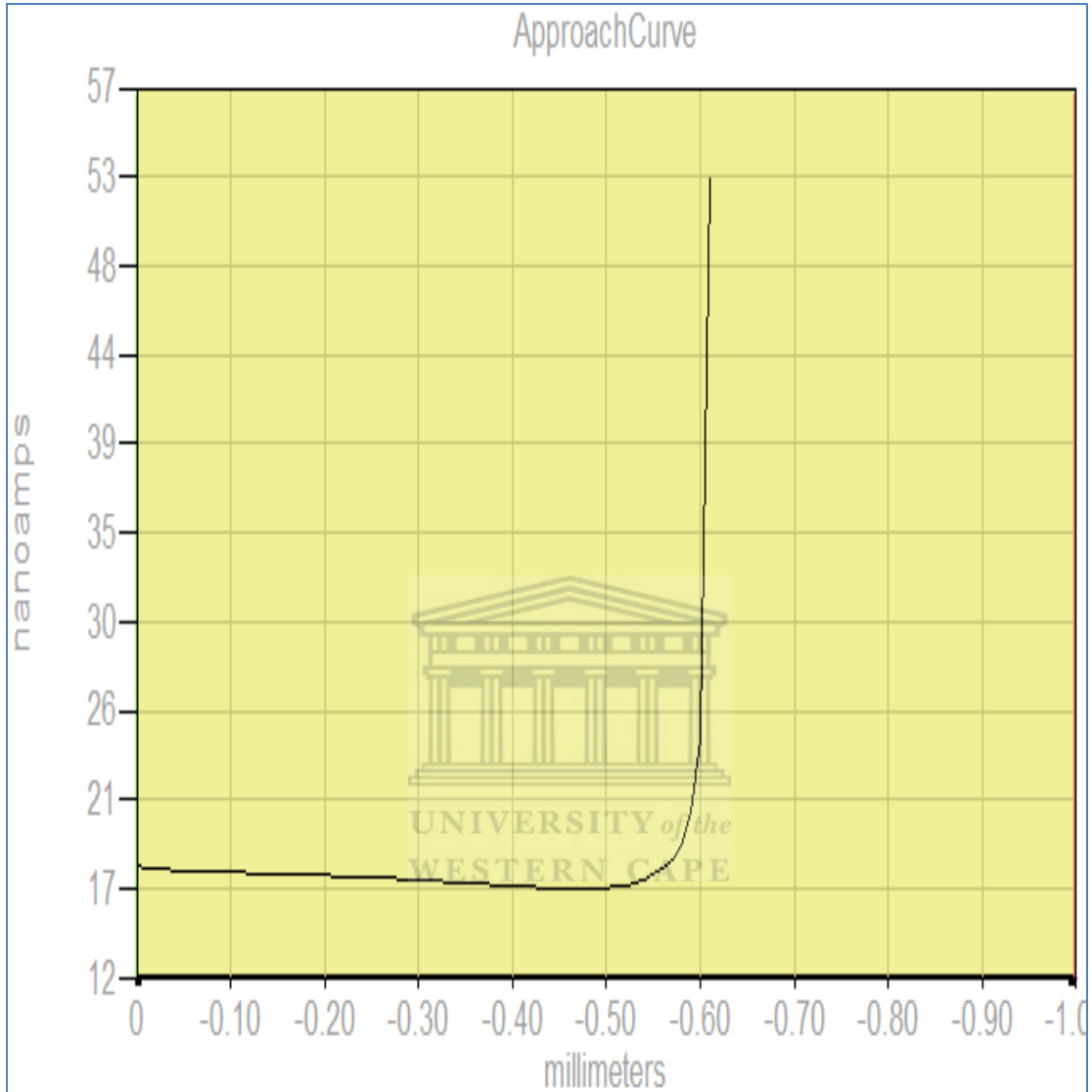
Figure 57. Approach curve of TaO-NiO-Mn₃O₄-PANi-PSSA

Once a sufficiently positive potential was applied to the UME tip, oxidation of Fe^{2+} occurred via the reaction;

$$Fe^{2+} (aq) \rightarrow Fe^{3+}(aq) + e^- \tag{i}$$

The oxidation occurs at a rate governed by diffusion of Fe^{2+} to the UME surface. If the tip is far (i.e. greater than several tip diameters) from the substrate immersed in the electrolyte, a steady state current, i.e. a current at infinite distance from the substrate, flows. This steady-state current ($i_{T,\infty}$) is given by;

$$i_{T,\infty} = 4nFDca \qquad (5.1)$$

Where F is the Faraday constant, n is the number of electrons transferred in reaction (i), D and c are the diffusion coefficient and the bulk concentration of Fe^{2+} respectively and a is the tip radius. When the tip is brought to within a few tip radii of a conductive substrate surface, the Fe^{3+} species diffuses to the substrate where it is reduced back to Fe^{2+} via the reaction;

$$Fe^{3+}(aq) + e^{-} \rightarrow Fe^{2+}(aq) \qquad (ii)$$

The process of equation (ii) produces an additional flux of reduced species to the UME tip making the tip current, i_T, to increase relative to $i_{T,\infty}$, meaning $i_T > i_{T,\infty}$. The shorter the separation distance (d) between the tip and the substrate, the larger the tip current. As $i_T \rightarrow \infty$, d→0. This explains the shape upward trend of the curve and hence the positive feedback (increasing current as the distance of minimum approach decreases) approach curve profiles obtained for the four nanocomposites showing that all of them are electrically conducting materials. A mechanism of the positive feedback mode is illustrated in figure 58.
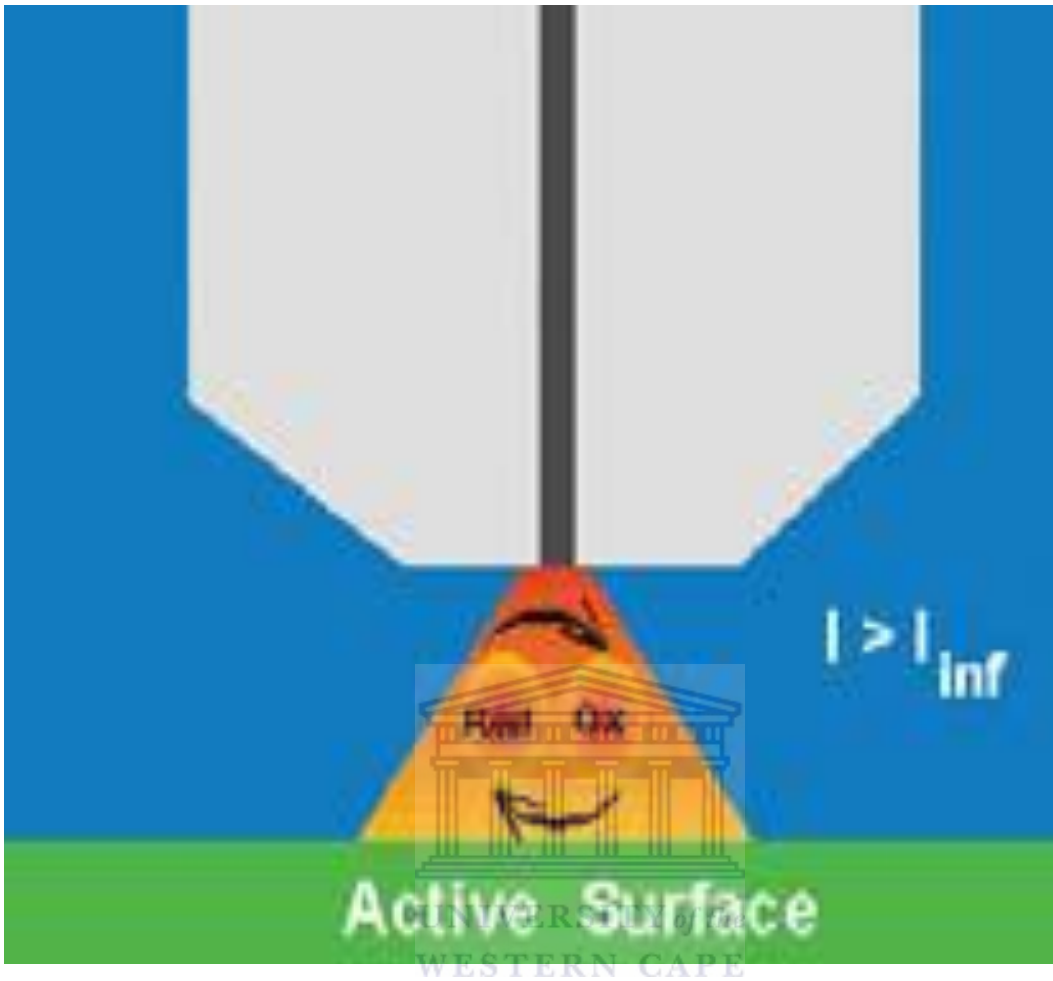
Figure 58. Mechanism of positive feedback

The converse is true for cases of substrates which are inert electrical insulators. The tip-generated oxidized species, O, cannot react at their surfaces. At small d, the insulator blocks the diffusion of species R to the tip surface as illustrated in figure 59.
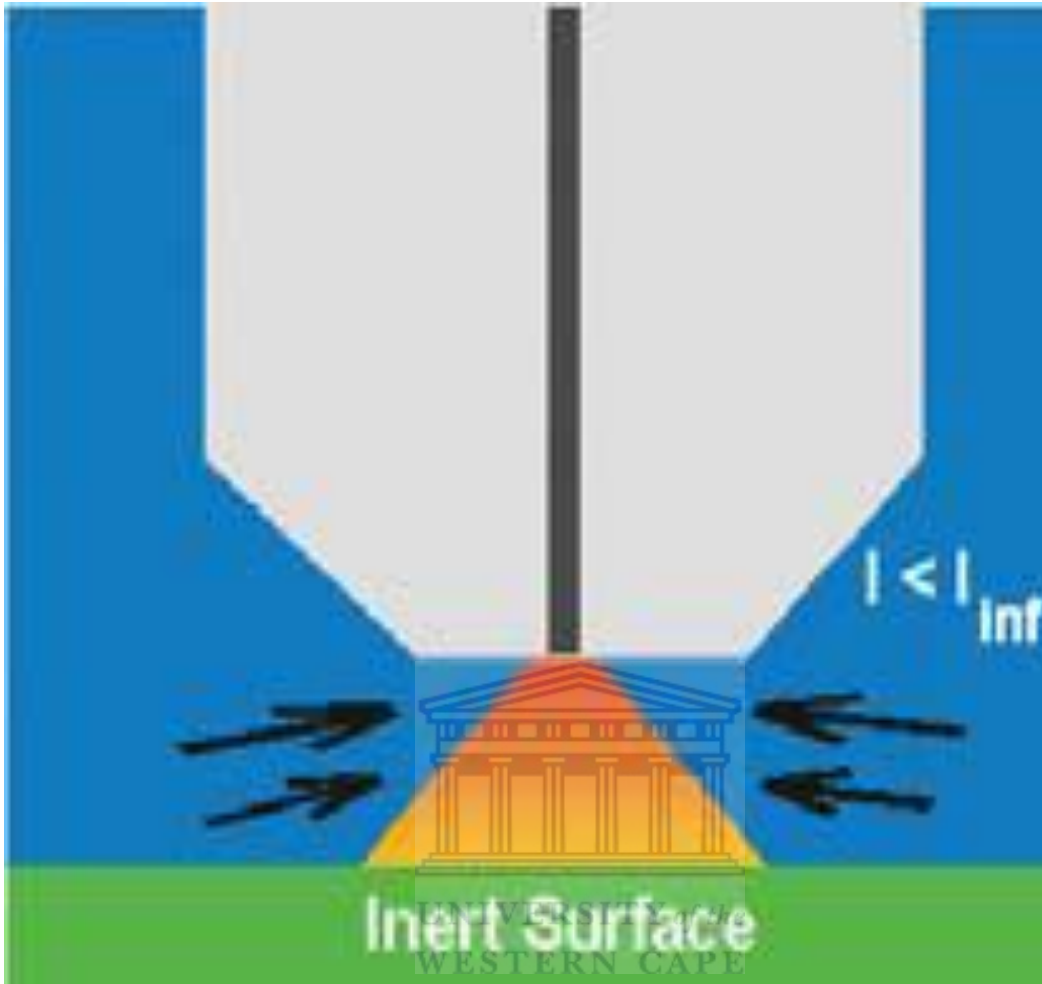
Figure 59. Mechanism of negative feedback

As such, i_T becomes smaller than $i_{T,\infty.}$ The closer the tip to the insulator substrate, the smaller the i_T. i_T approaches zero as d approaches zero. This would result in a downward trend of the curve and hence a negative feedback (decreasing current as the distance of minimum approach decreases) approach curve profile. Overall, the rate of the mediator regeneration at the substrate determines the magnitude of the tip current and conversely the dependence of the measured tip-substrate separation.

Figures 60-62 are the images of the surface redox reactivity of the chemically synthesized sulphonated and transition metal oxide doped polyaniline nanocomposites. The constant height mode of the SECM was used in this investigation to map the redox surface reactivity of the nanocomposites. The chemical images were obtained by rastering the UME tip laterally in the x- and y-directions at a distance d above the geometrically flat substrate surface and monitoring the tip current, i_T, as a function of tip location, within a dimensionally defined surface area.
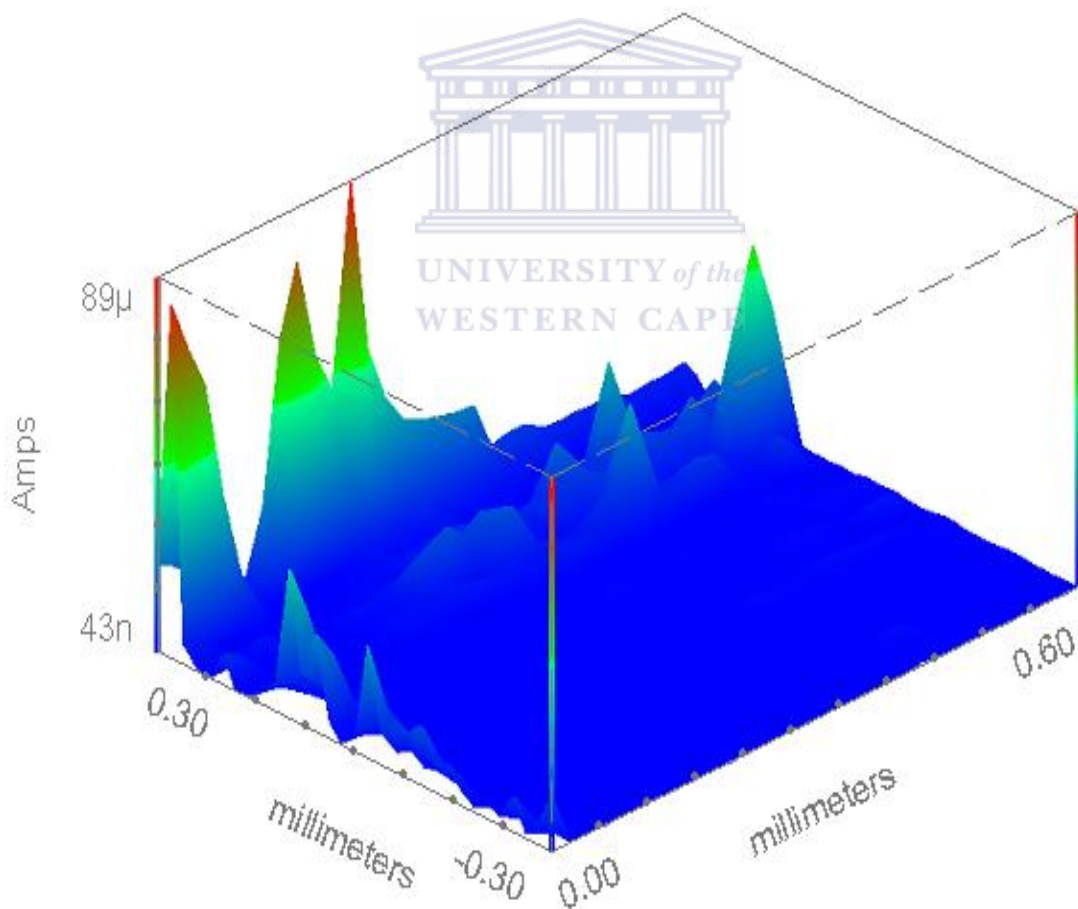
Figure 60. Surface imaging of TaO-Mn$_2$O$_3$-PANi-PSSA
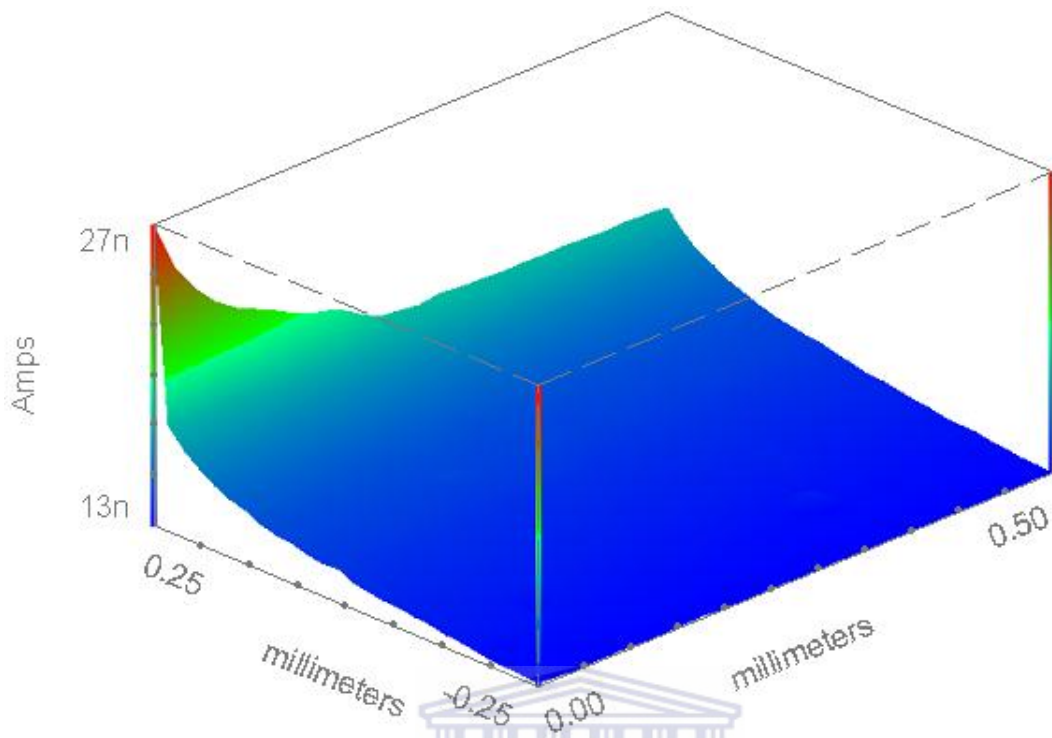
Figure 61. Surface imaging of TaO_2-NiO-PANi-PSSA
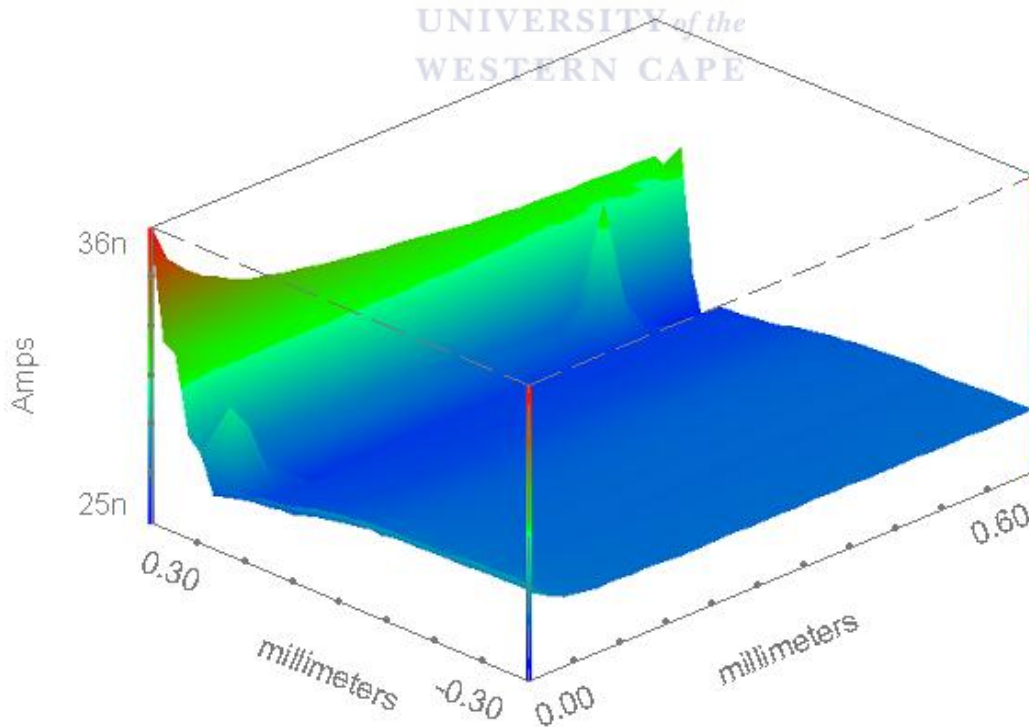
Figure 62. . Surface imaging of TaO-NiO-Mn_3O_4-PANi-PSSA

124

During the rastering, the tip-current changes are observed which are attributed to variations in surface reactivity. The SECM images show that the surface reactivity is not homogenous, especially when materials are compared to one another. The mode can also be used to study and/or map surface topography. The disadvantage of the constant height approach mode in the study of surface reactivity is that in a constant-height experiment, the current may also be a convolution of surface reactions and topography of the sample. Also it only works well with relatively large tip electrodes. When smaller tips are used in trying to achieve higher resolutions, scanning in this mode becomes more difficult and could possibly lead to the tip crashing because of a change of sample height or an increase in surface tilting. The mode is usually suitable for a flat surface or for substrate-generation/tip-collection mode with a probe positioned far from the surface. The constant distance mode is a better alternative for interrogating sample topography and monitoring local electrochemical activity/conductivity in proximity to solid/liquid interfaces. It can protect the tip from crashing at surface protrusions with the distance being adjusted by a feedback loop to the z-piezzo to maintain the distance. The constant current mode whose imaging is straightforward when the substrate surface consists of only insulating or conducting substrate where the tip current is used as a feedback signal is another better alternative.

5.12   Cyclic voltammetry characterization

The oxidative polymerization of aniline and aniline related monomers is a chain reaction whose chain termination step involves the coupling of radical cations to form dimers, oligomers and finally the polymer [184-185]. Figure 63 is the current versus potential cyclic voltammetry responses of the chemically synthesized TaO-NiO-Mn$_3$O$_4$-PANi-PSSA nanocomposite obtained in 1M H$_2$SO$_4$ as the supporting electrolyte at different scan rates.
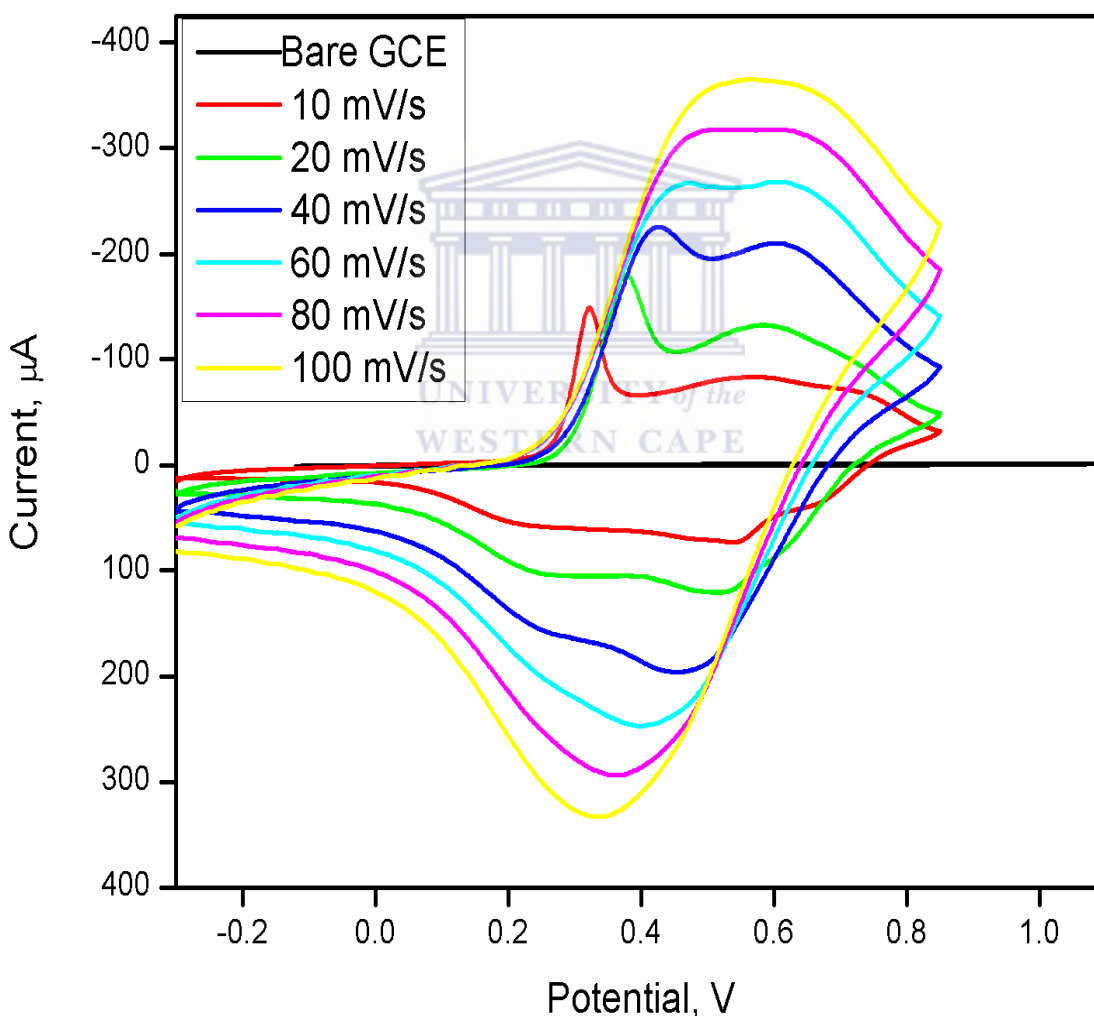
Figure 63. Current Vs potential plots of TaO-NiO-Mn$_3$O$_4$-PANi-PSSA

They exhibit a complex electrochemistry indicating that the composite is electroactive. Electroactive species can be oxidized (ox) or reduced (red) and therefore have the ability to pass on an electron(s) from one species to another thus contributing greatly to pseudocapacitance [186]. In this work, composites of transition metal oxides with PANi doped with PSSA were chemically synthesised. Cyclic voltammetric studies of metal oxide components and the doped polyaniline shows that these components are redox active. Their multiscan CV curves are given in the appendix. The results of these multiscan studies shows polyaniline-based systems have the ability to undergo more than one oxidation or reduction and therefore have multi-redox potentials. Indeed, it has been shown that polyaniline-based systems can exist in three oxidation states, the most reduced polyleucoemeraldine form, the protonated polyemeraldine form (polyemeraldine salt) and the fully oxidized polypernigraniline form [176, 187]. Figure 64 is a cyclic voltammetric cycle of TaO-NiO-Mn$_3$O$_4$-PANi-PSSA at 10 mV/s. It exhibits three characteristic redox couples. This observation was made in all the other composites. At low scan rates, the composites displayed well defined oxidation-reduction responses typical of PANi related

composites.
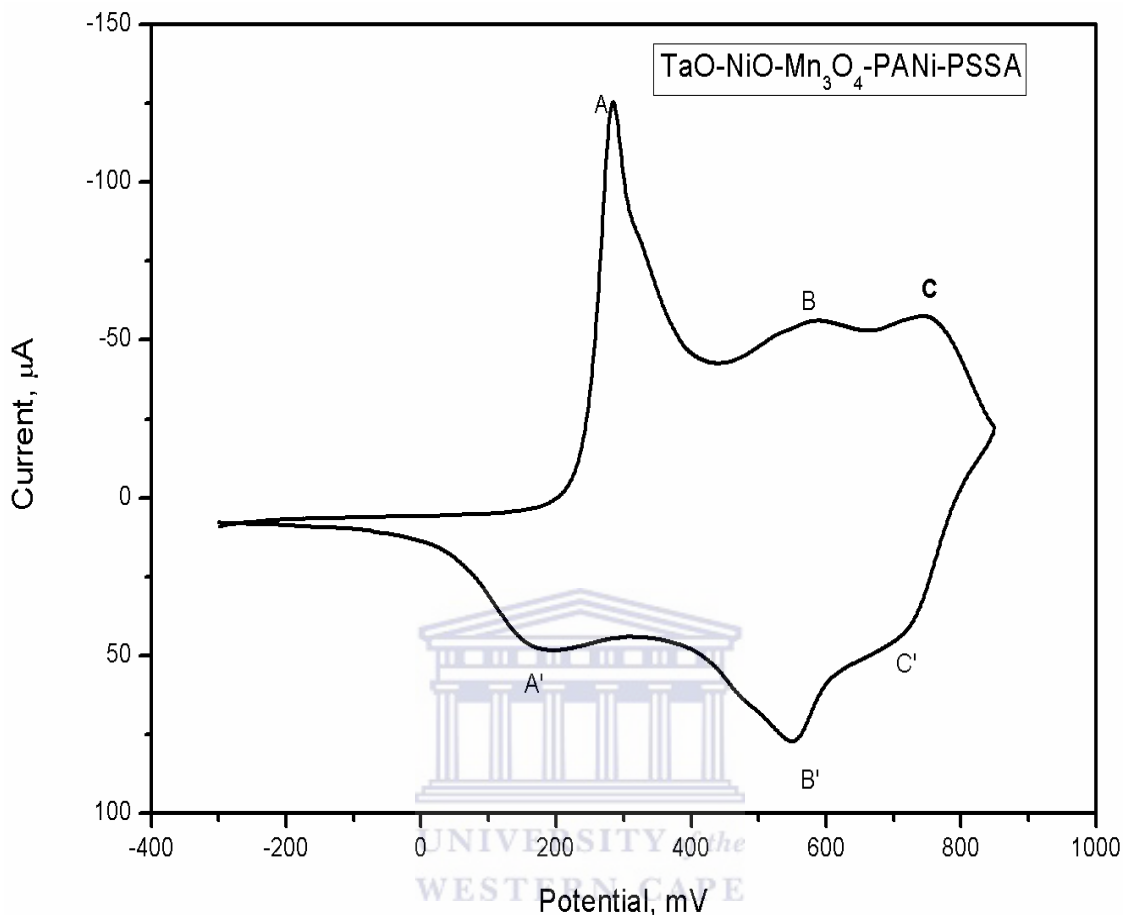
Figure 64. CV of TaO-NiO-Mn$_3$O$_4$-PANi-PSSA at 10 mV/s

The redox couple A/A' could be assigned to the polyleucoemeraldine/polyemeraldine salt transition. The couple at peaks C/C' is the polyemeraldine/polypenigraniline transition [187-188]. The middle redox couple (B/B') can be attributed to the oxidation/reduction of dimers and oligomers entrapped within the polymer matrix [188]. The middle peak/couple in polyaniline-based systems has been assigned to the degradation products of over-oxidized polyaniline [189] or to the quinone/hydroquinone by-products [190-191]. It has also been attributed to defects in the linear structure of the polymer [192]. From figure 63, the middle peak at B merged with the peak at C at higher scan rates

128

during the oxidative cycles as the peak at A shifted inconsistently towards higher potentials. Also during reductive cycles, the merging together of the peaks at C' and A' with the middle peak at B´ with increase in scan rates to form a broad anodic peak centred at the middle of the cyclic voltammetry potential range was accompanied by a shift of the resulting peak towards lower potential values. The shifting of peaks suggests that an irreversible behavior could be taking place during both oxidative and reductive processes while the merging suggests some sluggish electron transfer processes. The behaviour of TaO-NiO-Mn$_3$O$_4$-PANi-PSSA is replicated in TaO$_2$-NiO-PANi-PSSA, TaO-Mn$_2$O$_3$-PANi-PSSA and TaO$_2$-PANi-PSSA as their CVs at different scan rates illustrated in figures 65 (a)-(c) show.

(a)

129
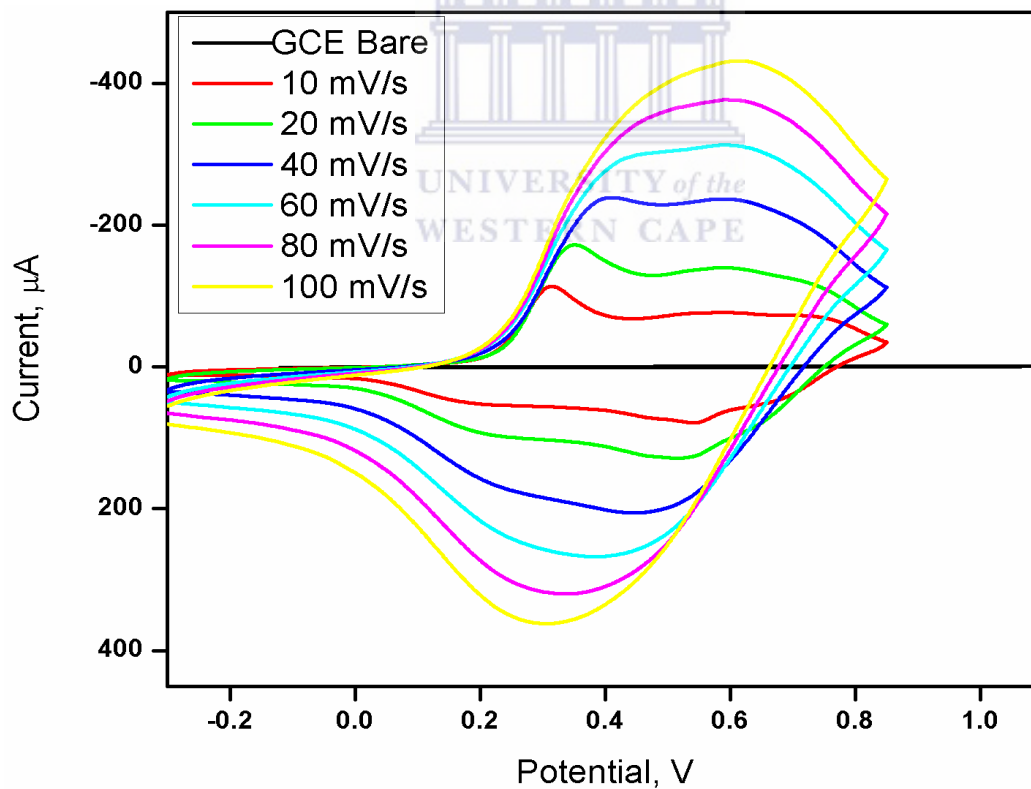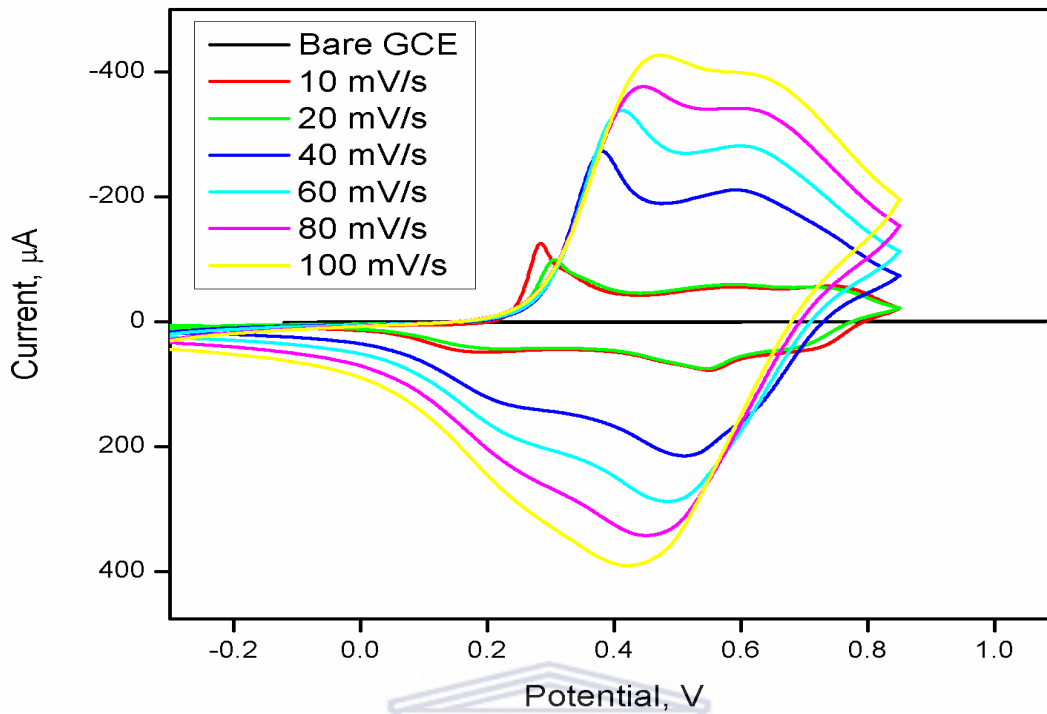
(b)
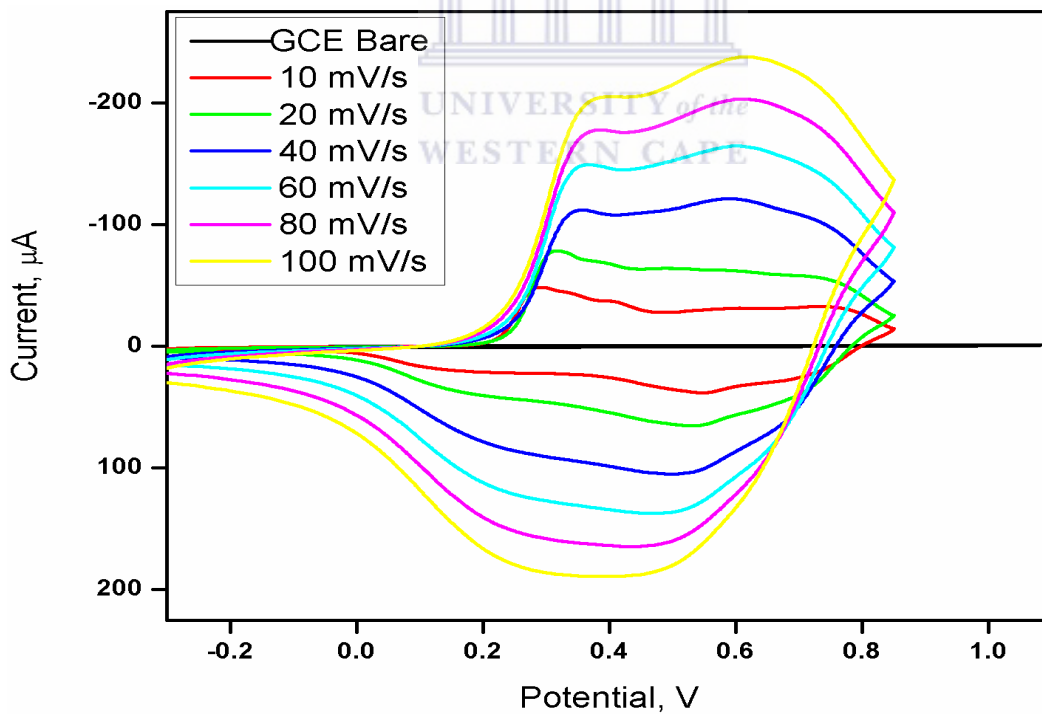
(C)

Figure 65. CV of (a) TaO$_2$-NiO-PANi-PSSA, (b) TaO-Mn$_2$O$_3$-PANi-PSSA, (c)

TaO$_2$-PANi-PSSA at different scan rates

Attempt was made to interrogate the anodic peak at A which appeared consistent. This was done by plotting peak current (i_p) against scan rate. Figure 66 is the i_p versus scan rate graph for TaO-NiO-Mn$_3$O$_4$-PANi-PSSA.
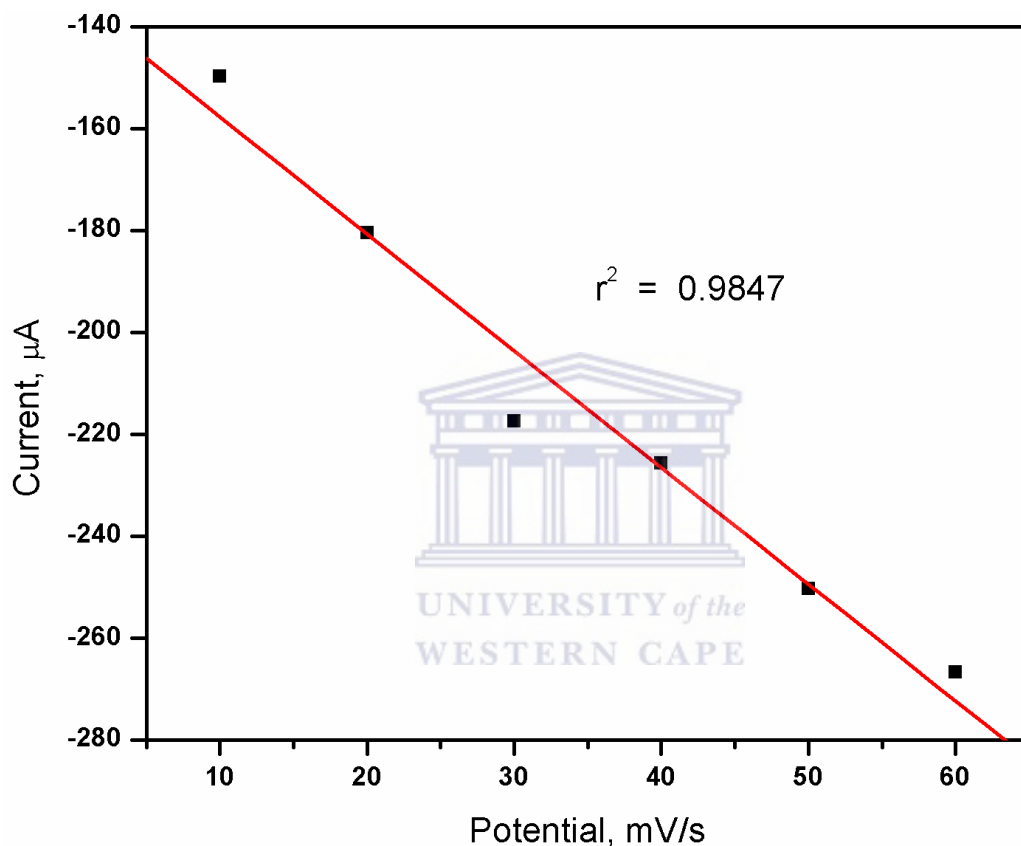
Figure 66. Plot of anodic peak current against scan rate for TaO-NiO-Mn3O4-PANi-PSSA

It can be seen from figure 66 that the anodic peak currents at A´ increased linearly with scan rates, analogous to or suggesting a case of anodic waves originating from the surface confined species. According to Laviron's equation [193-194]

$$I_p = \frac{Wn^2 F^2 A\Gamma \upsilon}{4RT}$$

5.2

131

and

$$Q = nFA\Gamma \hspace{4cm} 5.3$$

From equations 5.2 and 5.3, Laviron's equation can be described as;

$$I_p = \frac{nFQ\upsilon}{4RT} \hspace{4cm} 5.4$$

Where Γ is the active surface coverage of the electrode reaction substance in mol cm^{-2} and A is the electrode area (cm^2), Q the quantity of charge (C) calculated from the anodic peak area of the voltammogram by integration of area under the anodic peak, and n, I_p, F, R and T are the number of electrons transferred across the double layer, the anodic peak current at A´, the Faraday's constant, the gas constant and absolute temperature respectively. From the slopes of I_p versus v plot, n was calculated and gave an insignificantly low value. The number of electrons transferred during the oxidation process at A´ and hence the active surface coverage of the electrode reaction substance of the composite could then not be verified using Laviron's theory. Also, this was found to be the case for the other composites; TaO$_2$-NiO-PANi-PSSA, TaO-Mn$_2$O$_3$-PANi-PSSA and TaO$_2$-PANi-PSSA with TaO$_2$-PANi-PSSA giving a value of 1.56×10^{-7}. Overall, the presence of redox active dopants in the composites whose redox activity occurs at different potentials complicates and distorts known redox peaks of polyaniline.

5.13 Design and characterization of supercapacitors

In the construction of an electrode, an electrode material with a stable structure must be fabricated and is essential to providing repeatable results. An ideal single electrode should be mechanically strong and electrically conductive. Therefore, the nanocomposite material nanoparticles should be bound into stable matrix with minimum non-conductive

polymer binder. A hydrophilic surface is desirable so that aqueous electrolyte can easily penetrate into the pores of the electrode material. A tight contact between the electrode material and the current collector is necessary. Overall, the electrode has to be structurally stable to ensure the repeatability of electrochemical measurements.

5.13.1 Components of electrode materials

The main active electrode materials are the chemically synthesized sulphonated-PANi which is doped with the transition metal oxides TaO_2, TaO_2-NiO, TaO-Mn_2O_3 and TaO-NiO-Mn_3O_4. These are the polymeric nanocomopsite materials which were the focus of this investigation. As a conductive material, activated graphitic carbon was added to increase the conductivity of the electrode material [195-198]. The storage of electric charges in activated carbons is mainly non-Faradaic, and the accumulation of ionic charges occurs on a double layer at the electrode/electrolyte interface. The large specific surface area and the porosity of activated carbons are the basic requirements to achieve the quick formation of a double layer; the capacitive behaviours of activated carbons are influenced by their exposed surface area and pore size distribution. In addition, most of activated carbons have the functional groups containing many heteroatoms (such as oxygen, nitrogen, sulphur, and halogen), due to the residual surface-valence of carbons. The presence of these functionalities gives activated carbons an acid-base character, which enhances their capacitance by the pseudocapacitive effect. Therefore, tailoring porous structure and surface chemistry of activated carbons is very important to improve electrochemical performance of supercapacitors. Also, these various kinds of functional groups, the acidic surface oxides, serve as adsorption sites for polar molecules [199]. This increases surface hydrophilicity and hence wettability. Surface wettability of the

133

electrode material is important for ensuring the entire pores contact electrolyte for charge storage and or redox activity in the event of pseudocapacitance. Due to the non-conductive nature of PTFE binder, the amount of PTFE added should be limited such that it can bind the particles to stabilize the matrix but still leave the electrode material as conductive as possible. The higher the PTFE content, the higher the resistance of the electrode material. The need to minimize the amount of PTFE is therefore clear. 10% wt of the PTFE was found to bind the material appropriately. From literature, any amount between 4% (the lowest amount reported) and 10% wt is said to be appropriate [198, 200-201]. The material of the current collector should be non-corroding in the chosen electrolyte and within the test range of cyclic voltammetry. Nickel mesh is essentially a metal material that cannot store charge, but can be quite resistant to the KOH electrolyte and offers good contact between the active electrode material and the current collector. Otherwise contact resistance greatly affects the performance of an electrochemical capacitor [202-203]. A hydraulic pressure machine was used to apply a pressure of 20 Mpa for 5 minutes to press the active material onto the nickel mesh. Applying pressure improves the contact between electrode material and current collector and consequently decreases the contact resistance. Moreover, the contact resistance takes up a large percentage of the total internal resistance of the cell.

5.13.2 Performance of supercapacitor cell

The two-electrode cell system was used to evaluate the performance of capacitor cell, using the **BST8-3** eight-channel battery tester. The tester, working at the constant current charge/discharge mode, was used to evaluate the parameters cell specific capacitance, specific energy, coulombic efficiency and other parameters like the cell stability.

134

5.13.2.1 Capacitance measurement with constant current charge/ discharge (C/D)

During the test, 0.01 A was used as the average charge/discharge current. The charging and discharging was done within a potential range of 0.0 V to 1.2 V. The choice of the potential range is informed from the choice of the electrolyte. The choice for supercapacitor electrolyte aqueous medium is sulphuric acid (H_2SO_4) or potassium hydroxide (KOH). Their decomposition voltage limit is theoretically 1.23 V or practically, in kinetic terms, between 1.3 V and 1.4 V. However, strong solutions of acid are much more corrosive than strong solutions of KOH, so KOH is preferred. NaOH could also have been used. These hydroxide electrolytes are very soluble in water and because of OH⁻ anion, have very good conductivities. Both the acid and alkaline electrolytes have advantageously high equivalent conductivities in aqueous medium owing to the special mechanism of proton transport (proton hopping) that determines their conductance [2]. Figures 67-70 represent the charge/discharge curves from the asymmetric supercapacitor cell configurations assembled using the composites as cathode material and activated carbon as anode material for the first five cycles for each cell. The different behaviour of the first cycle is always due to the initial starting point. The whole system needs time to reach steady-state behaviour.
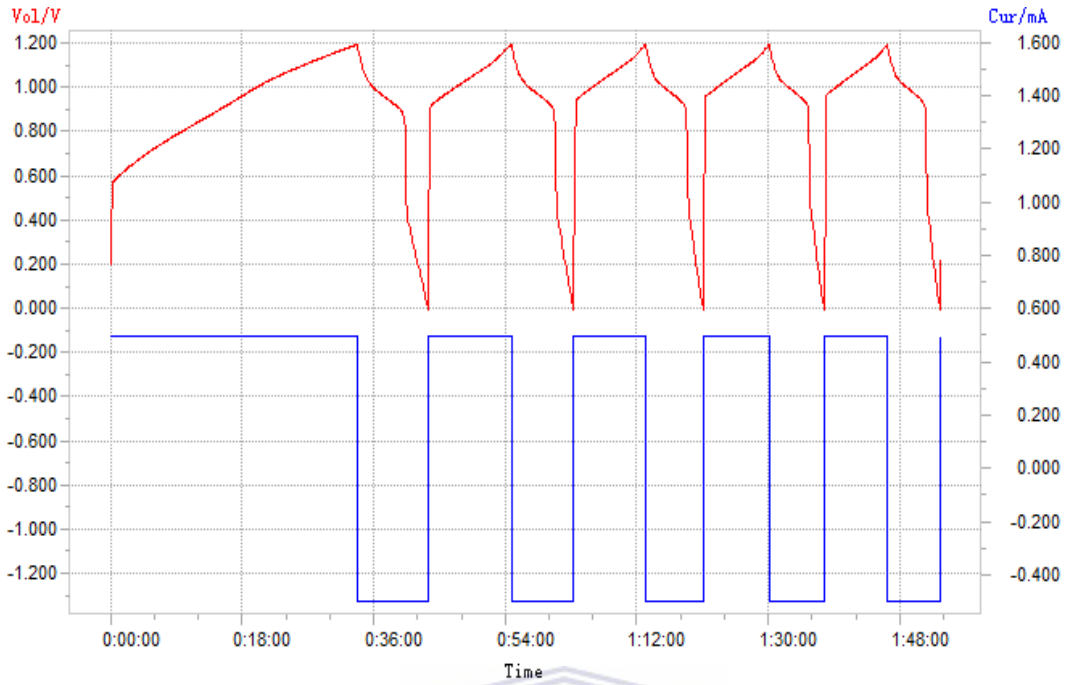
Figure 67. Charge/discharge curves of TaO$_2$-PANi-PSSA (1st five cycles)
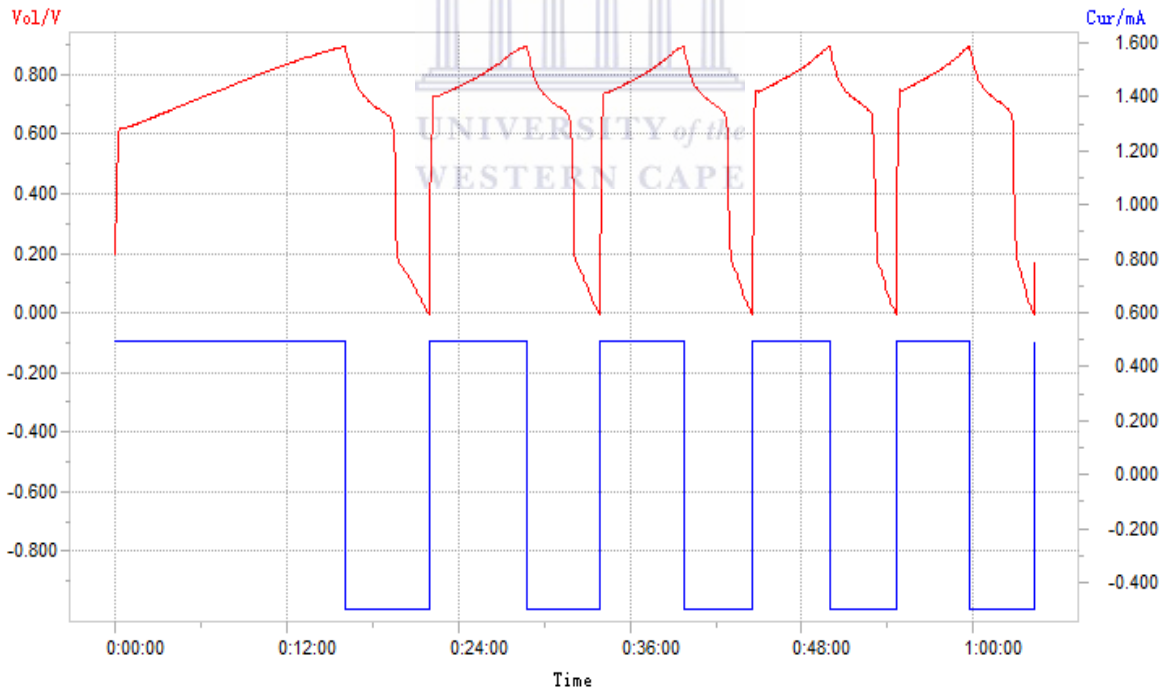
Figure 68. Charge/discharge curves of TaO$_2$-NiO-PANi-PSSA (1st five cycles)
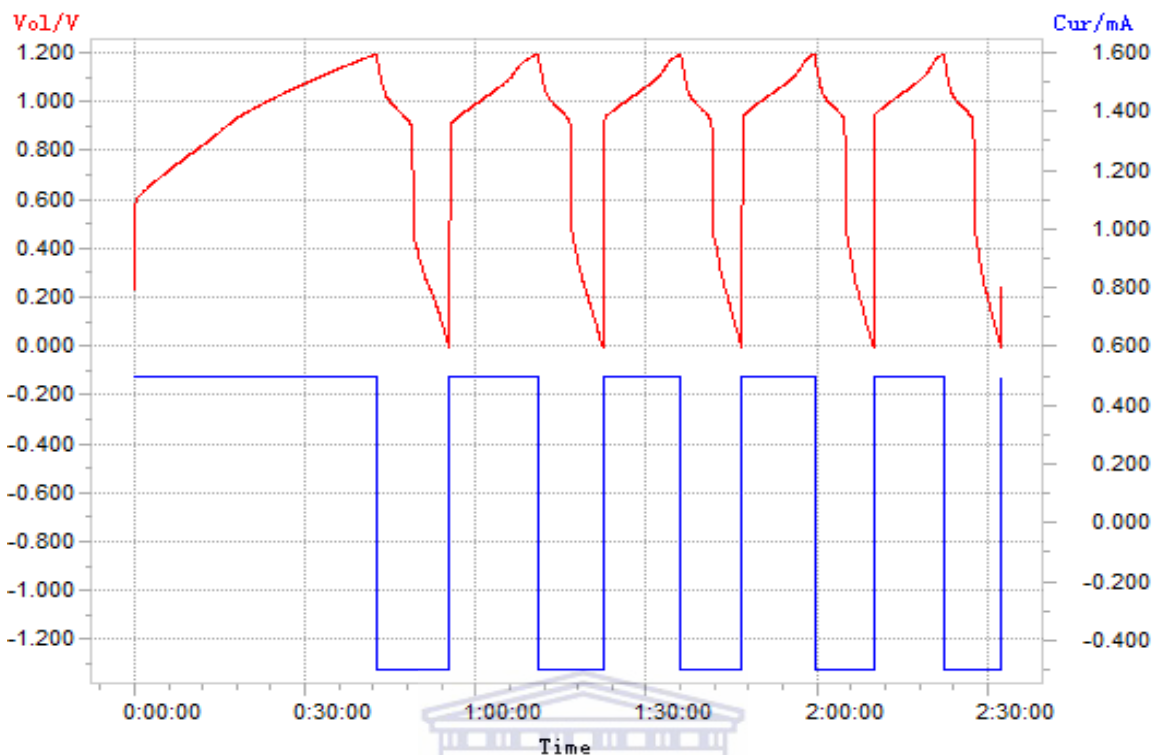
Figure 69. Charge/discharge curves of TaO-Mn₂O₃-PANi-PSSA (1st five cycles)
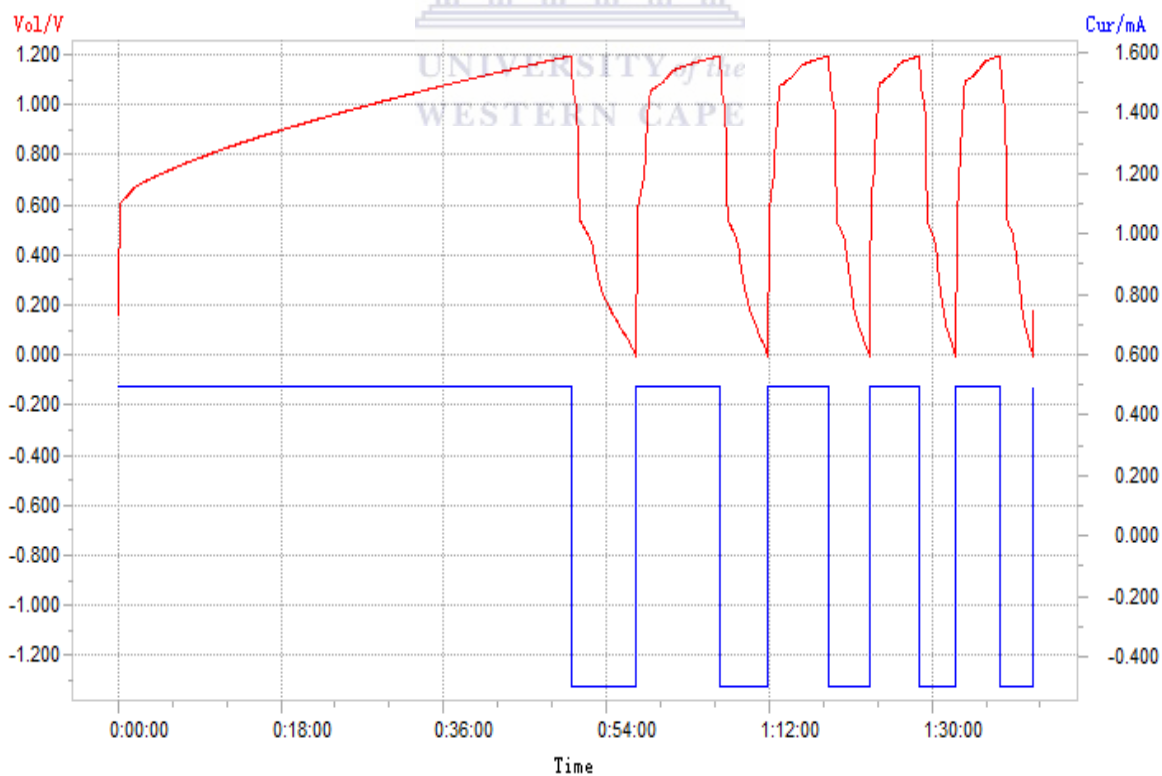
Figure 70. Charge/discharge curves of TaO-NiO-Mn₃O₄-PANi-PSSA (1st five cycles)

The discharge segment of the curves was used to calculate the electrical parameters such as specific capacitance (SC), specific power (SP) and specific energy (SE). These were calculated using the following equations [204-205]:

Specific Capacitance, $SC = \dfrac{I \times t}{V \times m}$ 　　　　　　　　　　6.1

Specific Power, $SP = \dfrac{I \times V}{m}$ 　　　　　　　　　　6.2

Specific Energy, $SE = \dfrac{I \times t \times V}{m}$ 　　　　　　　　　　6.3

In these equations, SC is the specific capacitance in F g^{-1}, SP the specific power in Wg^{-1} and SE is the specific energy in Whg^{-1}. The expressions show the discharge current (I) in amperes, voltage range (V) in volts, discharge time (t) in seconds and mass of the electroactive material (m) in grams.

The coulombic efficiency is calculated using the equation, $\eta = \dfrac{t_D}{t_C} \times 100$ 　　　　6.4

where t_C and t_D represent the time of charging and discharging, respectively. Table 1 shows the values of electrical parameters computed from charge-discharge profiles for the composites using the 3rd discharge cycle.

Table 1. Values of electrical parameters computed from charge-discharge profiles.

Composite	*SC*/Fg^{-1}	*SE*/Whg^{-1}	*SP*/Wg^{-1}	*η*%
TaO$_2$-PANi-PSSA	170.5	245.5	0.50	80.36
TaO$_2$-NiO-PANi-PSSA	166.1	179.4	0.61	83.19
TaO-Mn$_2$O$_3$-PANi-PSSA	248.4	357.7	0.57	81.06
TaO-NiO-Mn$_3$O$_4$-PANi-PSSA	119.6	172.3	0.65	77.97

It can be seen that the charge–discharge profiles deviate from the typical linear variation of voltage with time normally exhibited by an electrochemical double layer capacitors (EDLC). The observed non-linearity could be due to the pseudocapacitance arising out of the redox reactions within the potential range used. The values of specific capacitance obtained are within the capacitance values of good supercapacitors values reported in literature though comparatively, both lower and high specific capacitances have been reported for single electrode materials [4, 68, 206-215]. The values obtained depend on several factors key among which is the method used to determine the specific capacitances. When cyclic voltammetric charge is used specific capacitance values depends on the scan rates and increases with increase in scan rate. When a charge-discharge technique is used like the galvanostatic-potentiostatic, the values reported depend on current densities.

The values reported in literature are therefore unique to the methods used and the conditions of measurements. As such, comparison between values reported by different researchers is difficult. This also applies to the values of specific energy and specific power.

The materials are found to be relatively stable over large number of cylces. From the voltage-time profile for TaO-NiO-Mn$_3$O$_4$-PANi-PSSA shown in figures 71, the potential remains stable over a large number of cylces meaning that the materials does not degrade when cycled many times. They have longer cycle life and therefore a high structural integrity under repeated charging and discharging which is a desirable characteristic of supercapacitor materials. Voltage-time profiles for the other nanocomposites are given in the appendix.
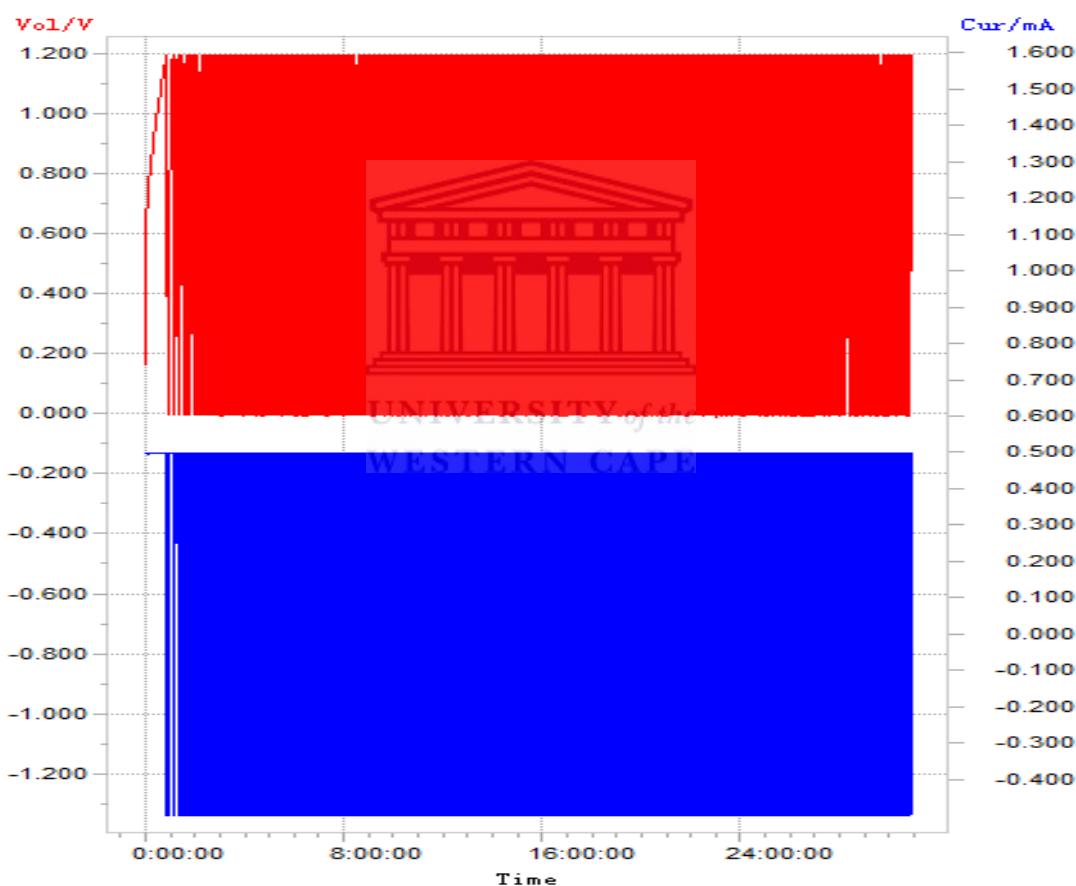
Figure 71. Voltage-time profile for 143 cycles for TaO-NiO-Mn$_3$O$_4$-PANi-PSSA

The coulombic efficiency is quite high and remains high as the materials are cycled over and over again as is illustrated in the coulombic efficiency-number of cycles curve profiles relating coulombic efficiency, charging and discharging at increasing number of

140

cycles (illustrated in figure 72 for TaO$_2$-PANi-PSSA). The curves for the rest of composites are given in the appendix. The efficiency obtained is as high as 81.82% in TaO-Mn$_2$O$_3$-PANi-PSSA through 81.86% in TaO-NiO-Mn$_3$O$_4$-PANi-PSSA, 89.0% in TaO$_2$-PANi-PSSA to 94.85% in TaO$_2$-NiO-PANi-PSSA which is found to have the highest coulombic efficiency and specific power at any cycle. In the figures, the top curve represents efficiency while the bottom two represents charge during the charging (blue) and discharging (green) regimes. The difference between the bottom two represents the inability of the supercapacitor device to discharge or charge leakage through self discharge.
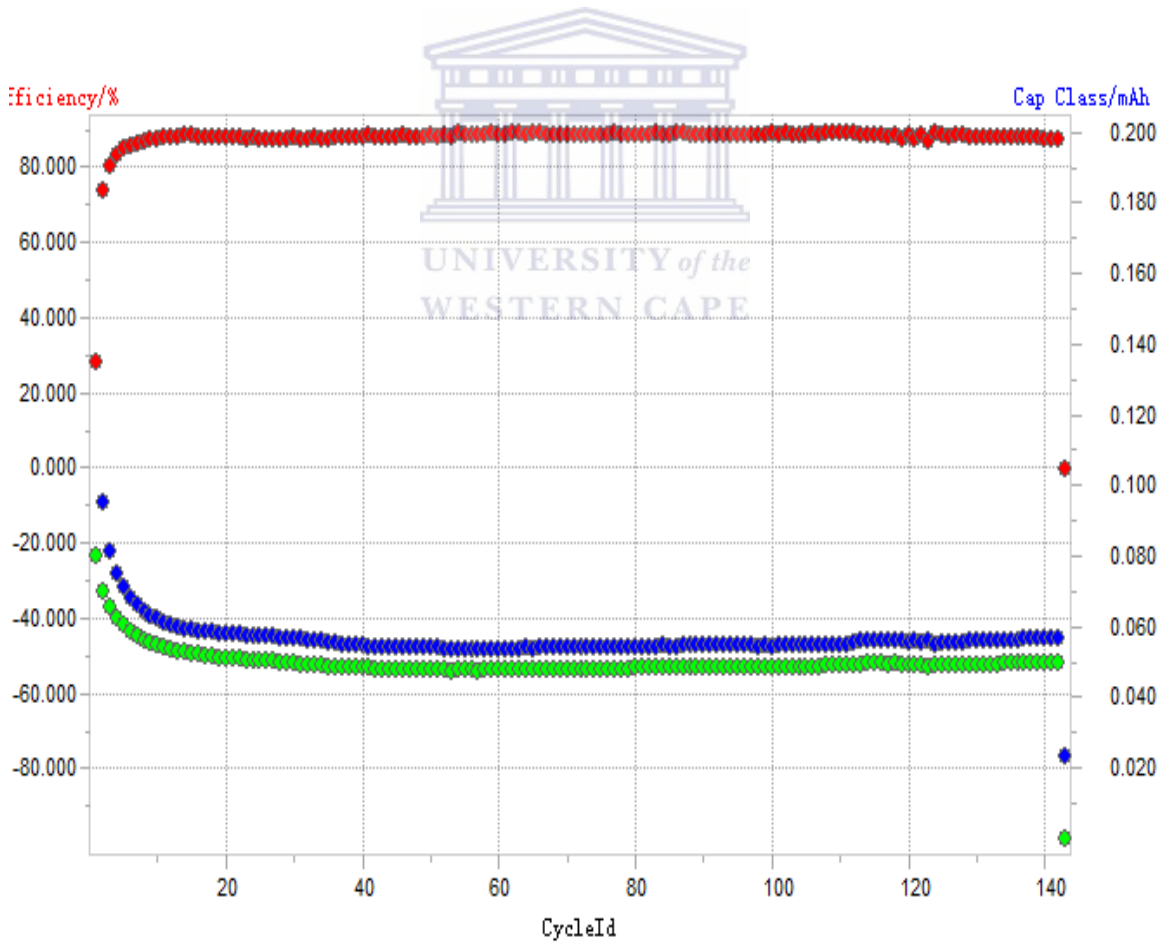
Figure 72. Coulombic efficiency as a function of the number of cycles for TaO$_2$-PANi-PSSA

5.14 Electrochemical impedance spectroscopy (EIS)

For the situation of an electrode in contact with an electrolyte a Randles circuit as is illustrated in figure 73 can be used to model impedance parameters.
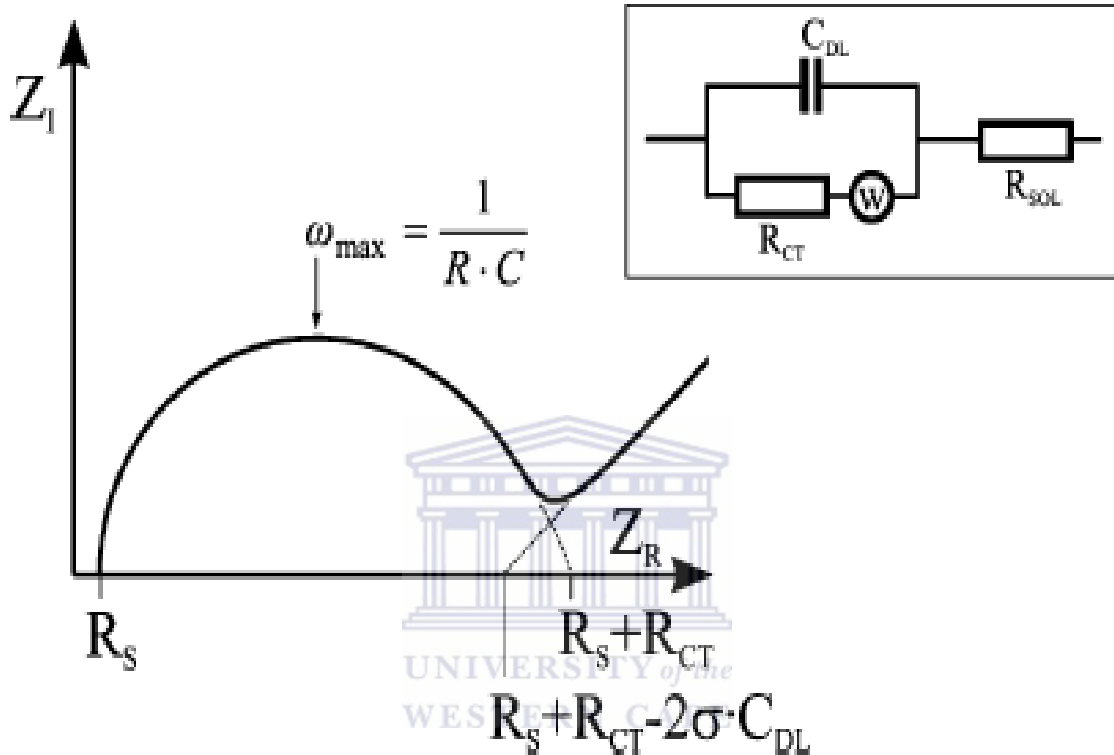
Figure 73. Randles' equivalent circuit for an electrode in contact with an electrolyte and corresponding Nyquest plot [216].

The double-layer capacitance C_{dl} results from charge being stored in the double layer at the interface. The charge transfer resistance R_{CT} refers to resistance to current flow produced by redox reactions at the interface, and the Warburg impedance results from the impedance of the current due to diffusion from the bulk solution to the interface. R_s model the solution resistance afforded by the ion concentration and the cell geometry. R_s and R_{CT} are easily determined from the Nyquist plot. The double layer capacitance can be calculated from the frequency at the maximum of the semicircle ($\omega = 2\pi f = 1/R_{CT}C_{dl}$). The

product of R_{CT} and C_{dl} is often termed the time constant τ of the electrochemical process. The 45° line indicating Warburg-limited behaviour can be extrapolated to the real axis. The intercept is equal to $R_s + R_{CT} - 2\sigma C_{dl}$, from which σ and subsequently diffusion coefficients can be calculated. For analytical applications, however, the equivalent circuit is often simplified by neglecting the Warburg impedance. This can be done by choosing a frequency range where no 45° line is observed in the Nyquist plot and the interfacial or bulk impedance is dominant [214].

In this work, electrochemical impedance spectroscopy measurements were carried out at a dc bias of 1 V with a sinusoidal perturbation signal of 10 mV over the frequency range from 10 kHz to 100 MHz. Figure 74 presents complex-plane impedance plots for the composites. Plots for individual composites used in the fitting are given in the appendix.
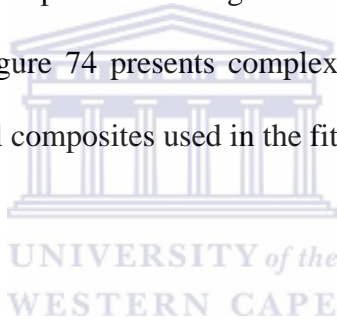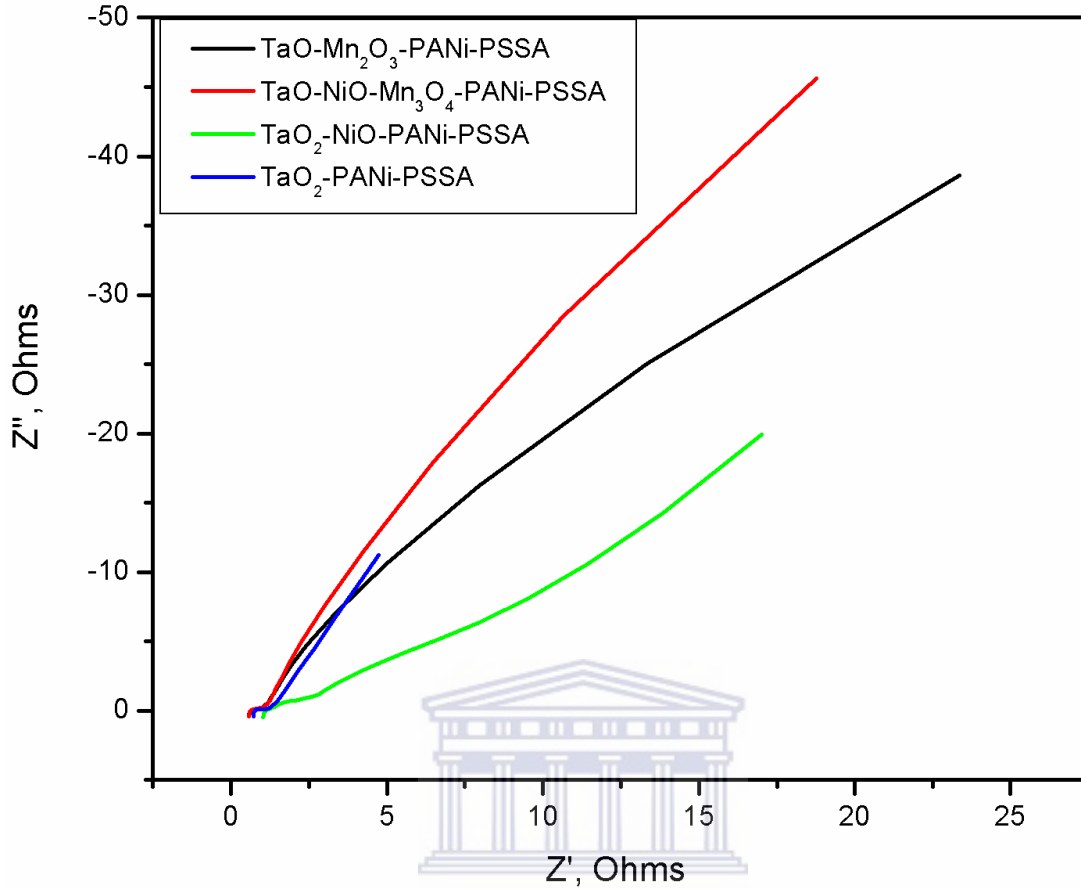
Figure 74. Nyquist plots of the polymer composites.

From the nyquist plots, the imaginary part of the impedances at lower frequencies for all the composites decreases. This is a deviation from an ideal capacitive behaviour of an electrode. An electrical double layer is formed at the interface between an electrode and an electrolyte at a given potential. In the absence of faradaic reactions, smooth and clean surfaces show ideal capacitive behaviour described by the equation;

$$Z_{(\omega)} = \frac{1}{(j_\omega C_d)} \hspace{5cm} 3$$

where the double layer capacitance C_d is independent of frequency. The ideal behavior is represented as a vertical line in the Nyquist plot of impedance [215]. The ac perturbation impedance method is also used to measure the capacitance of electrodes, which is

144

influenced by the frequency, especially for porous electrodes, where almost no current flows down the pore at higher frequencies [216] for ideal capacitors. As is shown in table 2, the values of capacitance are low compared to literature values [217]. The non-ideality or frequency dispersion has been described widely by the constant phase element (CPE) which is an empirical distributed element. The impedance of a CPE is formulated by;

$$Z_{(\omega)} = M_0 (j\omega)^{-\phi} \hspace{4cm} 4$$

Where the CPE exponent ϕ is associated with the degree of non-ideality. When $\phi = 1$ and $M_0 = 1$, equation (4) represents ideal capacitive behavior. Frequency dispersion leads to an inclined line whose phase angle is $-(\pi/2)\phi$ in the Nyquist plot of impedance. The CPE element results from various origins of frequency dispersion; diffusion in a diffusion-limited system, geometric factors, sluggish processes such as adsorption of anions, surface reconstruction and transformation in adlayer, and crystallographic heterogeneity [215]. For the redox active sulphonated and transition metal oxide doped composites studied in this thesis, the integration of the composites with the highly porous activated graphitic carbon increases the porosity of the nanocompsites. In a case like this, of porous and redox active electrodes, geometric factors and faradaic reactions are the most important among the origins of frequency dispersion. The non-ideality due to the geometric factors can be divided into two classes; dispersions in-a-pore and by-pore size distribution (PSD). In-a-pore dispersion occurs since penetration depth of an ac signal into a pore decreases with frequency. Therefore, apparent capacitance or equivalent series resistance changes with frequency even in the porous materials composed entirely of pores with equal dimension. The in-a-pore dispersion occurs at low penetrability (high frequency), giving a phase angle of $\pi/4$. As penetrability increases (or frequency

decreases), impedance approaches the ideal capacitive behavior but is shifted along the abscissa by in-a-pore dispersion part. For non-ideality due to the by-PSD dispersion, penetration depth becomes distributed even at an identical frequency since dimension of each pore determines its own penetration depth. Therefore, the electrochemical behavior of porous materials with PSD shows frequency dispersion different from that predicted by an in-a-pore dispersion even when using the average dimension of pores.

Fitting parameters based on the equivalent circuits are presented in table 2.

Table 2. Results from EIS fitting

Kinetic parameters	TaO_2-PANi-PSSA	TaO-Mn_2O_3-PANi-PSSA	TaO-NiO-Mn_3O_4-PANi-PSSA
C_{dl}(mF)	4.00	4.30	4.98
R_s (Ω)	0.7542	0.0754	0.7769
R_{ct} (Ω)	0.2728	0.9516	0.1589
CPE (nF)	778.8	778.8	778.8
D_w	241	241	445.1
W_{max} (Hz)	915.96	262.72	1263.96
τ (s rad^{-1})	0.00109	0.00381	0.00079

The ideal or non-ideal capacitive behaviour is also reflected in cyclic voltammetry. Ideal double layer capacitance behaviour of an electrode material expresses itself in form of a rectangular shape in a cyclic voltammetric characterization as is illustrated by curve 1 in

figure 75 [217]. The sign of current is instantiously reversed upon reversal of the potential sweep. Any model to study the electrochemical impedance behaviour of the nanocomposites must take into account the complexity of the equivalent circuit for a porous capacitor electrode and whether the electrode utilizes pseudocapacitance [215].
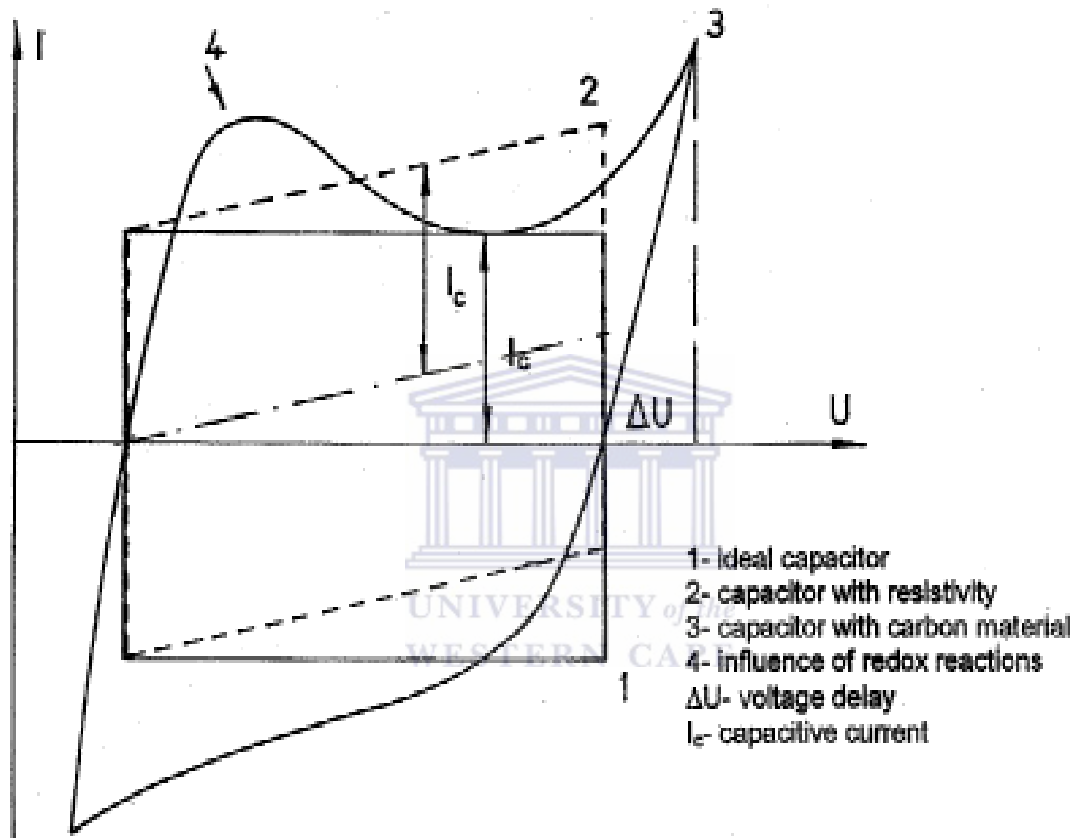
Figure 75. Typical reduction/oxidation voltammetry characteristics of an electrochemical capacitor [217].

In the type of energy storage illustrated by curve 1 in figure 74, the phenomenon is purely electrostatic and current is independent on potential. Electrode materials with pseudocapacitance properties point out a deviation from such a rectangular shape and reversible redox peaks connected with pseudofaradaic reactions are remarkable (see curve 4 in Figure 74). In this case the charge accumulated in the capacitor is strongly

147

dependent on the electrode potential. The observed delay of potential during reversing the potential sweep is connected with a kinetically slow electron transfer process involved during charging the pseudocapacitance [6, 218-219]. This is what is observed in all cases of the polymeric nanocomposites studied in this thesis and illustrated in the rectangularly distorted cyclic voltammetric curves illustrated in figures 63, 65(a)-(b). These composites are made up of porous materials that gives pseudocapacitance properties i.e. poly(4-styrene sulphonic acid) and transition metal oxides doped polyaniline nanocomposites. The metal oxides used and polyaniline polymer exhibit, as is explained elsewhere in this thesis, redox activities.

Chapter 6

Conclusions and recommendations

Novel nanocomposite tantalum (IV) oxide based nickel (II) oxide, manganese (III) oxide and manganese (II, III) oxide poly(4-styrene sulphonic acid) doped polyaniline with nanofibre morphologies were synthesized in this thesis using a combination of sol-gel methods and chemical oxidative polymerization of aniline. Four novel polymeric nanocomposites were the focus of this thesis. These were TaO_2-PANi-PSSA, TaO_2-NiO-PANi-PSSA, TaO-Mn_2O_3-PANi-PSSA and TaO-NiO-Mn_3O_4-PANi-PSSA. These materials were found to be crystalline, conductive and electro-active. On being integrated with activated graphitic carbon they were found to exhibit good supercapacitor material properties with high specific capacitance, long cycle life and good coulombic efficiency. Investigation of commercial supercapacitor cell samples indicates a number of supercapacitors are available in a range of sizes and modular configurations. Some like those from Maxwell boasting of capacitances of few microfarads to as high as 2400 Farads, a value which could be much lower than the values obtained in this work if reported in unit specific capacitance. However, commercial supercapacitors are rated in terms of Farads and this gives a poor comparison to experimental supercapacitor cells which normally are rated in terms of Farads per unit mass or unit surface area. Also the commercial supercapacitors are designed for specific and wide range of applications, including consumer electronics, hybrid cars, and renewable energy sources thus varying in a range of sizes.

As we move forward in developing environmentally friendly low-carbon strategies for alternative energy production technologies and as we focus on problems associated with

sustainable energy solutions, these novel materials need to be looked at keenly as potentially superior materials in the design and production of efficient high capacitance, high energy and high power supercapacitors.

This thesis provided an overview of electrochemical double layer capacitors (EDLC). Scientific background has been covered in order to better understand supercapacitor performance characteristics and armed with a basic understanding of EDLC performance and design issues, it is hoped that one would be better equipped to undertake design tasks and utilise supercapacitors for energy storage. Possible applications of EDLC technology have been described to illustrate to the reader the wide range of possibilities that exist, and may perhaps even encourage the formation of ideas about new ways that supercapacitors could be used effectively. It is apparent that the state of the EDLC as an energy storage solution is still very much in the early stages of development. The physical processes that occur during charge transfer and the implications that they have for EDLC performance are only just being fully understood and quantified.
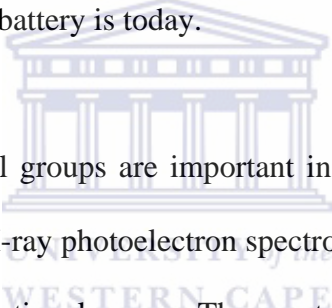
Current cost evaluations usually rule out supercapacitors as a viable alternative to batteries, a mature technology that has been widely available for many decades. Because of the advantages of charging efficiency, long lifetime, fast response, high power density and wide operating temperature range, it might be tempting to try and apply EDLCs to any application that requires energy storage.

The limitations of the current technology must be fully appreciated, however, and it is important to realise that supercapacitors are only useful within a finite range of energy and power requirements. Outside of these boundaries other alternatives are likely to offer better solutions. Nevertheless, commercial EDLC devices have been available for many

years now, and their quantity and performance has been steadily increasing. Both improvements in performance and the demand for better devices support each other in a mutually sustaining cycle. As devices of greater energy density and higher power become available, more new applications are formulated and demand will become greater. Increased levels of interest in the technology then lead to increased research and development efforts, which in turn will result in better devices being manufactured. An established market will make it easier for new companies to enter the arena, and costs will drop as manufacturing quantities and demand both increase. The most important thing to remember about supercapacitor technology is that it is a new and different technology in its own right as is illustrated in the literature review and are, at any rate, a part of the new wave of advanced energy storage devices that will further the push towards greater energy efficiency and more sustainable alternatives. They will be a useful tool with which to engineer highly efficient electrical and electronic systems, and as the state of the technology advances they will become progressively more commonplace.

Research and development efforts into EDLC technology have been steadily gathering momentum since the 1970's. This rate of progress is likely to continue as concerns about energy efficiency and sustainable development increase. The emission-free electric car has long been the dream of many of those concerned about retarding the progress of environmental degradation, and the potential use of EDLCs in EVs continue to draw new attention to the technology. The available energy and power of EDLC devices greatly depends upon the materials used, and significant research is directed at ways of improving the electrode and electrolyte materials. Greater understanding of the charging

151

processes in the electric double-layer would lead to a clear recognition of the crucial factors that must be addressed by electrode and electrolyte materials. New methods of carbon activation and new polymer and metal-oxide materials are continuously being developed, and improved electrolytes will result in increased cell voltages. EDLCs will become a more competitive energy storage option as interest in the technology grows and production levels are increased. Greater availability and more competitive prices combined with improved energy and power performance will lead to widespread adoption of supercapacitors as energy storage devices. While the technology is still in its infancy and is invisible to the public consciousness it is likely that supercapacitors will one day be as ubiquitous as the battery is today.

In this work, surface functional groups are important in introducing pseudocapacitance and improving wettability, so X-ray photoelectron spectroscopy (XPS) need to be used to find out which are the exact functional groups. The exact oxidation states of the transition metal oxides which greatly enhance pseudocapacitance, need to be determined using solid state NMR. BET analysis would be necessary to ascertain the porosity of the materials and synthetic methods optimized to produce morphologies of high surface area. Although electrode material, electrolyte and contact resistance all contribute to internal resistance, contact resistance could be several orders of magnitude higher than the other two factors and therefore adopting and re-thinking of supercapacitor design protocols capable of minimizing contact resistance would be an essential ingredient to the performance of the supacapacitor.

References

1.   http://www.cantecsystems.com/ccrdocs/brief-history.

2.   Conway, B., *Electrochemical Supercapacitors; Scientific Fundamentals and Technological Applications*. 1999, New York: Kluwer Academic/Plenum Publishers.

3.   Lewandowski, A. and M. Galinski, *Practical and theoretical limits for electrochemical double-layer capacitors.* Journal of Power Sources, 2007. 173(2): p. 822-828.

4.   Shukla, A.K., S. Sampath, and K. Vijayamohanan, *Electrochemical supercapacitors: Energy storage beyond batteries.* CURRENT SCIENCE, 2000. 79(12): p. 1656-1661.

5.   Kötz, R. and M. Carlen, *Principles and applications of electrochemical capacitors.* Electrochimica Acta, 2000. 45(15-16): p. 2483-2498.

6.   Frackowiak, E. and F. Béguin, *Carbon materials for the electrochemical storage of energy in capacitors.* Carbon, 2001. 39(6): p. 937-950.

7.   Zhang, Y., H. Feng, X. Wu, L. Wang, A. Zhang, T. Xia, H. Dong, X. Li, and L. Zhang, *Progress of electrochemical capacitor electrode materials: A review.* International Journal of Hydrogen Energy, 2009. 34(11): p. 4889-4899.

8.   Pandolfo, A.G. and A.F. Hollenkamp, *Carbon properties and their role in supercapacitors.* Journal of Power Sources, 2006. 157(1): p. 11-27.

9.   Lewandowski, A. and M. Galinski, *Practical and theorectical limits for electrochemical double-layer capacitors.* J. Power Sources, 2007. 173: p. 822-828.

10.   Shukla, A.K., S. Sampath, and K. Vijayamohana, *Electrochemical supercapacitors: Energy storage beyond batteries.* CURRENT SCIENCE, 2000. 79(12): p. 1656-1661.

11.   Frackowiak, E. and F. Beguin, *Review: Carbon materials for the electrochemical storage of energy in capacitors.* Carbon, 2001. 39: p. 937-950.

12.   Zhang, Y., H. Feng, X. Wu, L. Wang, A. Zhang, T. Xia, H. Dong, and L. zhang, *Progress of electrochemical capacitor electrode materials: A review.* Intern. J. of hydrogen energy 2009. 34: p. 4889-4899.

13.   Padolfo, A.G. and A.F. Hollen Kamp, *Review: Carbon properties and their role in supercapacitors.* J. Power Sources, 2006. 157: p. 11-27.

14.   Kotz, R. and C. M., *Principles and applications of electrochemical capacitors.* Electrochimica Acta, 2000. 45: p. 2483-2498.

15.   Aida, T., K. Yamada, and M. M., *An advanced hybrid electrochemical capacitor that uses a wide potential range at the positive electrode.* Electrochem. Solid-State Lett., 2006. 9: p. A534-6.

16.   Conway, B.E., ed. *Electrochemical supercapacitors*. Scientific Fundamentals and Technology applications. 1999, Kluwer Academic/Plenum Publishers: New York.

17.   Kaempgen, M., C.K. Chan, J. Ma, Y. Cui, and G. Gruner, *Printable Thin Film Supercapacitors Using Single-Walled Carbon Nanotubes.* Nano Letters, 2009. 9(5): p. 1872-1876.

18.   Wei, D., S.J. Wakeham, T.W. Ng, M.J. Thwaites, H. Brown, and P. Beecher, *Transparent, flexible and solid-state supercapacitors based on room temperature ionic liquid gel.* Electrochemistry Communications, 2009. 11(12): p. 2285-2287.

19.   Bradley, K., J.-C.P. Gabriel, and G. Grüner, *Flexible Nanotube Electronics.* Nano Letters, 2003. 3(10): p. 1353-1355.

20.   Dougal, R.A., S. Liu, and R.E. White, *Power and Life Extension of Battery Ultra-capacitor Hybrids.* IEEE Transactions on Components and Packaging Technologies, 2002. 25(1): p. 120 - 131

21.   Jarvis, L.P., T.B. Atwater, and P. J. Cygan, *Fuel cell/electrochemical capacitor hybrid for intermittent high power applications.* Journal of Power Sources, 1999. 79(1): p. 60-63.

22.   Lam, L.T., N.P. Haigh, C.G. Phyland, and A.J. Urban, *Failure mode of valve-regulated lead-acid batteries under high-rate partial-state-of-charge operation.* Journal of Power Sources, 2004. 133(1): p. 126-134.

23.   Sauer, D.U. and J. Garche, *Optimum battery design for applications in photovoltaic systems — theoretical considerations.* Journal of Power Sources, 2001. 95(1-2): p. 130-134.

24.   Dunlop, J. and F. Brian. *Recommendations for maximizing battery life in Photo-voltaic systems: A review of lessons learned. .* in *Proceedings of Forum Solar Energy:The Power to Choose.* 2001 Washington, DC.

25.   Scherson, D.A. and A. Palencsár, *Batteries and Electrochemical Capacitors.* Electrochemical Society Interface, 2006: p. 17-22.

26.   Sparnaay, M.J. and *The electric double layer.* 1 ed. Vol. 4. 1972, Sydney: Pergamon Press (Aust.) Pty. Ltd.

27.   Becker, H.I. and V. Ferry, *Low Voltage Electrolytic Capacitor.* United states patent, 1957. 2800616.

28.   Boos, D.L. and S.D. Argade, *International Seminar on Double Layer Super-capacitors and Similar Energy Storage Devices.* Florida Educational, Seminars, Deerfield Beach, FL, 1991.

29.   Boos, D.L., *Electrolytic capacitor having carbon paste electrodes.* United States patent, 1970. 3536963.

30.   Rightmire, R.A., *Electrical energy storage apparatus, .* United States patent, 1966. 3288641.

31.   Endo, M., T. Takeda, Y.J. Kim, K. Koshiba, and K. Ishii, *High power electric double layer capacitor (EDLC's); from operating principle to pore size control in advanced activated carbons.* Carbon Science, 2001. 1: p. 117-128.

32.   Yoshida, A., K. Imoto, A. Nishino, and H. Yoneda. *An electric doublelayer capacitor with high capacitance and low resistance*. in *41st Electronic Components and Technology Conference*. 1991. Atlanta, GA, USA.

33.   http://www.elna-america.com/company.htm.

34.   Bullard, G.L., H.B. Sierra-Alcazar, H.L. Lee, and J.L. Morris, *Operating principles of the ultracapacitor.* IEEE Transactions on Magnetics, 1988. 25: p. 102-106.

35.   IEA, *International Energy Agency, Report on the first phase of the IEA implementing agreement for hybrid electric vehicle technology and programmes - 1993-1999*. 1999: Paris.

36.   Kaefer, A.E. and M. Gomez-Kaifer, *Supramolecular Electrochemistry*. 1999, New York: Wiley-VCH.

37.   Wang, J., *Analytical Chemistry*. 1994, New York: VCH Publishers Inc.

38.   Sims, M.J., N.V. Rees, E.J.F. Dickinson, and R.G. Compton, *Effects of thin-layer diffusion in the electrochemical detection of nicotine on basal plane pyrolytic graphite (BPPG) electrodes modified with layers of multi-walled carbon nanotubes (MWCNT-BPPG).* Sensors and Actuators B: Chemical, 2010. 144(1): p. 153-158.

39.   De Vitre, R.R., M.L. Tercier, M. Tsacopoulos, and J. Buffle, *Preparation and properties of a mercury-plated iridium-based microelectrode.* Analytica Chimica Acta, 1991. 249(2): p. 419-425.

40.   Dhawan, S.K., D. Kumar, M.K. Ram, S. Chandra, and D.C. Trivedi, *Application of conducting polyaniline as sensor material for ammonia.* Sensors and Actuators B: Chemical, 1997. 40(2-3): p. 99-103.

41.   Tercier-Waeber, M.L., C. Belmont-Hebert, J. Buffle, FGraziottin, G.C. Fiaccabrino, and M. Koudelka-Hep. *A novel probe and microsensors for in situ, continuous, automatic profiling of trace elements in natural waters.* in *IEEE Oceanic Engineering Society OCEANS'98 Conference Proceedings.* 1998.

42.   Tercier-Waeber, M.L., J. Buffle, M. Koudelka-Hep, and F. Graziottin, *Submersible Voltammetric Probes for Real-Time Continuous Monitoring of Trace Elements in Natural Aquatic Systems*, in *Environmental Electrochemistry.* 2002, American Chemical Society. p. 16-39.

43.   Gründig, B., G. Wittstock, U. Rüdel, and B. Strehlitz, *Mediator-modified electrodes for electrocatalytic oxidation of NADH.* Journal of Electroanalytical Chemistry, 1995. 395(1-2): p. 143-157.

44.   Bartlett, P.N., P.R. Birkin, J.H. Wang, F. Palmisano, and G. De Benedetto, *An Enzyme Switch Employing Direct Electrochemical Communication between Horseradish Peroxidase and a Poly(aniline) Film.* Analytical Chemistry, 1998. 70(17): p. 3685-3694.

45.   Trojanowicz, M., A. Lewenstam, T.K.V. Krawczyk, I. Lähdesmäki, and W. Szczepek, *Flow injection amperometric detection of ammonia using a polypyrrole-modified electrode and its application in urea and creatinine biosensors.* Electroanalysis, 1996. 8(3): p. 233-243.

46.   Cosnier, S., M. Stoytcheva, A. Senillou, H. Perrot, R.P.M. Furriel, and F.A. Leone, *A Biotinylated Conducting Polypyrrole for the Spatially Controlled Construction of an Amperometric Biosensor.* Analytical Chemistry, 1999. 71(17): p. 3692-3697.

47.   Evans, S.A.G., J.M. Elliott, L.M. Andrews, P.N. Bartlett, P.J. Doyle, and G. Denuault, *Detection of Hydrogen Peroxide at Mesoporous Platinum Microelectrodes.* Analytical Chemistry, 2002. 74(6): p. 1322-1326.

48.   Imokawa, T., K.-J. Williams, and G. Denuault, *Fabrication and Characterization of Nanostructured Pd Hydride pH Microelectrodes.* Analytical Chemistry, 2005. 78(1): p. 265-271.

49.http:www.standrews.ac.uk/~www_pa/Scots_Guide/info/comp/passive/capacit/dielec/dielec.htm.

50.   Emmenegger, C., P. Mauron, P. Sudan, P. Wenger, V. Hermann, R. Gallay, and A. Züttel, *Investigation of electrochemical double-layer (ECDL) capacitors electrodes based on carbon nanotubes and activated carbon materials.* Journal of Power Sources, 2003. 124(1): p. 321-329.

159

51.   Bard, A. and L. Faulkner, *Electrochemical Methods: Fundamentals and applications*. 2nd ed. 2001, New York: John Wiley and Sons.

52.   Atsushi, N., *Capacitors: operating principles, current market and technical trends.* Journal of Power Sources, 1996. 60(2): p. 137-147.

53.   http://electrochem.cwru.edu/encycl/art-c03-elchem-cap.htm.

54.   Joshi, K.M. and R. Parsons, *The diffuse double layer in mixed electrolytes.* Electrochimica Acta, 1961. 4(2-4): p. 129-140.

55.   http://www.anl.gov/PCS/acsfuel/preprint%20archive/Files/Volumes/Vol11-1.pdf.

56.   Matsumoto, M., *Electrical phenomena at interfaces: fundamentals, measurements, and applications*. 2nd ed. Surfactant science series, ed. H. Ohshima and K. Furusawa. Vol. 76. 1998, New York: Marcel Dekker, Inc.

57.   Andrew, B., *Ultracapacitors: why, how, and where is the technology.* Journal of Power Sources, 2000. 91(1): p. 37-50.

58.   Frackowiak, E., *Supercapacitors based on carbon materials and ionic liquids.* Journal of the Brazilian Chemical Society, 2006. 17: p. 1074-1082.

59.   Frackowiak, E., *Carbon materials for supercapacitor application.* Physical Chemistry Chemical Physics, 2007. 9(15): p. 1774-1785.

60.   Frackowiak, E., S. Gautier, H. Gaucher, S. Bonnamy, and F. Beguin, *Electrochemical storage of lithium in multiwalled carbon nanotubes.* Carbon, 1999. 37(1): p. 61-69.

160

61.   Ni, C., E.K. Sichel, R. Hoch, D. Moy, and H. Tennet, *High power electrochemical capacitors based on carbon nanotube electrodes.* Applied Physics Letters, 1997. 70(11): p. 1480-1482.

62.   Britto, P.J., K.S.V. Santhanam, and P.M. Ajayan, *Carbon nanotube electrode for oxidation of dopamine.* Bioelectrochemistry and Bioenergetics, 1996. 41(1): p. 121-125.

63.   Liu, X., T.A. Huber, M.C. Kopac, and P.G. Pickup, *Ru oxide/carbon nanotube composites for supercapacitors prepared by spontaneous reduction of Ru(VI) and Ru(VII).* Electrochimica Acta, 2009. 54(27): p. 7141-7147.

64.   Gupta, V. and N. Miura, *Polyaniline/single-wall carbon nanotube (PANI/SWCNT) composites for high performance supercapacitors.* Electrochimica Acta, 2006. 52(4): p. 1721-1726.

65.   Zhou, Y.-k., B.-l. He, W.-j. Zhou, J. Huang, X.-h. Li, B. Wu, and H.-l. Li, *Electrochemical capacitance of well-coated single-walled carbon nanotube with polyaniline composites.* Electrochimica Acta, 2004. 49(2): p. 257-262.

66.   Sun, Y., S.R. Wilson, and D.I. Schuster, *High dissolution and strong light emission of carbon nanotubes in aromatic amine solvents.* Journal of the American Chemical Society, 2001. 123(22): p. 5348-9.

67.   Huang, J.-E., X.-H. Li, J.-C. Xu, and H.-L. Li, *Well-dispersed single-walled carbon nanotube/polyaniline composite films.* Carbon, 2003. 41(14): p. 2731-2736.

161

68.   Frackowiak, E., V. Khomenko, K. Jurewicz, K. Lota, and F. Béguin, *Supercapacitors based on conducting polymers/nanotubes composites.* Journal of Power Sources, 2006. 153(2): p. 413-418.

69.   Koysuren, O., C. Du, N. Pan, and G. Bayram, *Preparation and comparison of two electrodes for supercapacitors: Pani/CNT/Ni and Pani/Alizarin-treated nickel.* Journal of Applied Polymer Science, 2009. 113(2): p. 1070-1081.

70.   Rao, C.N.R., K. Biswas, K.S. Subrahmanyam, and A. Govindaraj, *Graphene, the new nanocarbon.* Journal of Materials Chemistry, 2009. 19(17): p. 2457-2469.

71.   Lü, P., Y. Feng, X. Zhang, Y. Li, and W. Feng, *Recent progresses in application of functionalized graphene sheets.* SCIENCE CHINA Technological Sciences, 2010. 53(9): p. 2311-2319.

72.   Novoselov, K.S., D. Jiang, F. Schedin, T.J. Booth, V.V. Khotkevich, S.V. Morozov, and A.K. Geim. *Two-dimensional atomic crystals*. in *Proceedings of the National Academy of Sciences of the United States of America*. 2005.

73.   Luk'yanchuk, I.A. and Y. Kopelevich, *Dirac and Normal Fermions in Graphite and Graphene: Implications of the Quantum Hall Effect.* Physical Review Letters, 2006. 97(25): p. 256801.

74.   Wang, C., D. Li, C.O. Too, and G.G. Wallace, *Electrochemical Properties of Graphene Paper Electrodes Used in Lithium Batteries.* Chemistry of Materials, 2009. 21(13): p. 2604-2606.

75.   Unsworth, J., B.A. Lunn, P.C. Innis, Z. Jin, A. Kaynak, and N.G. Booth, *Technical Review : Conducting Polymer Electronics.* Journal of Intelligent Material Systems and Structures, 1992. 3(3): p. 380-395.

76.   Salaneck, W.R. and J.L. Brédas, *Conjugated polymers.* Solid State Communications, 1994. 92(1-2): p. 31-36.

77.   Shirakawa, H., E.J. Louis, A.G. MacDiarmid, C.K. Chiang, and A.J. Heeger, *Synthesis of electrically conducting organic polymers: halogen derivatives of polyacetylene, (CH).* Journal of the Chemical Society, Chemical Communications, 1977(16): p. 578-580.

78.   Pud, A., N. Ogurtsov, A. Korzhenko, and G. Shapoval, *Some aspects of preparation methods and properties of polyaniline blends and composites with organic polymers.* Progress in Polymer Science, 2003. 28(12): p. 1701-1753.

79.   Bhadra, S., D. Khastgir, N.K. Singha, and J.H. Lee, *Progress in preparation, processing and applications of polyaniline.* Progress in Polymer Science, 2009. 34(8): p. 783-810.

80.   Gospodinova, N. and L. Terlemezyan, *Conducting polymers prepared by oxidative polymerization: polyaniline.* Progress in Polymer Science, 1998. 23(8): p. 1443-1484.

81.   Bernard, M.-C., A. Hugot-Le Goff, and W. Zeng, *Elaboration and study of a PANI/PAMPS/WO3 all solid-state electrochromic device.* Electrochimica Acta, 1998. 44(5): p. 781-796.

82.   Bernard, M.C., S. Joiret, A.H.-L. Goff, and P.D. Long, *Protection of Iron Against Corrosion Using a Polyaniline Layer: II. Spectroscopic Analysis of the Layer Grown in Phosphoric/Metanilic Solution.* Journal of The Electrochemical Society, 2001. 148(8): p. B299-B303.

83.   Schultze, J.W., T. Morgenstern, D. Schattka, and S. Winkels, *Microstructuring of conducting polymers.* Electrochimica Acta, 1999. 44(12): p. 1847-1864.

84.   Mousty, C., A. Lepellec, S. Cosnier, A. Novoa, and R.S. Marks, *Fabrication of organic phase biosensors based on multilayered polyphenol oxidase protected by an alginate coating.* Electrochemistry Communications, 2001. 3(12): p. 727-732.

85.   Cho, M.S., S.Y. Park, J.Y. Hwang, and H.J. Choi, *Synthesis and electrical properties of polymer composites with polyaniline nanoparticles.* Materials Science and Engineering: C, 2004. 24(1-2): p. 15-18.

86.   Roszberg, K., G. Paasch, L. Dunsch, and S. Ludwig, *The influence of porosity and the nature of the charge storage capacitance on the impedance behaviour of electropolymerized polyaniline films.* Journal of Electroanalytical Chemistry, 1998. 443(1): p. 49-62.

87.   Fusalba, F., P. Gouerec, D. Villers, and D. Belanger, *Electrochemical Characterization of Polyaniline in Nonaqueous Electrolyte and Its Evaluation as Electrode Material for Electrochemical Supercapacitors.* Journal of The Electrochemical Society, 2001. 148(1): p. A1-A6.

88. Hu, C.-C. and C.-H. Chu, *Electrochemical and textural characterization of iridium-doped polyaniline films for electrochemical capacitors.* Materials Chemistry and Physics, 2000. 65(3): p. 329-338.

89. Hu, C.-C. and C.-H. Chu, *Electrochemical impedance characterization of polyaniline-coated graphite electrodes for electrochemical capacitors — effects of film coverage/thickness and anions.* Journal of Electroanalytical Chemistry, 2001. 503(1-2): p. 105-116.

90. Mirkin, M.V. and B.R. Horrocks, *Electroanalytical measurements using the scanning electrochemical microscope.* Analytica Chimica Acta, 2000. 406(2): p. 119-146.

91. http://www.chinstruments.com/CHI920C%20SECM.pdf.

92. Allen, J.B., F.F. Fu-Ren, K. Juhyoun, and L. Ovadia, *Scanning Electrochemical Microscopy. Introduction and Principles.* Anal. Chem, 1989. 61: p. 132-138.

93. Martin, D.R. and P.R. Unwin, *Scanning electrochemical microscopy Kinetics of chemical reactions following electron-transfer measured with the substrate-generation-tip-collection mode.* Journal of the Chemical Society, Faraday Transactions, 1998. 94(6): p. 753-759.

94. Chang, W., B.J. Allen, and M.V. Mirkin, *Scanning Electrochemical Microscopy. 31. Application of SECM to the Study of Charge Transfer Processes at the Liquid/Liquid Interface.* The Journal of Physical Chemistry, 1995. 99(43): p. 16033-16042.

95.   Amphlett, J.L. and G. Denuault, *Scanning Electrochemical Microscopy (SECM): An Investigation of the Effects of Tip Geometry on Amperometric Tip Response.* The Journal of Physical Chemistry B, 1998. 102(49): p. 9946-9951.

96.   Pyo, M. and A.J. Bard, *Scanning electrochemical microscopy. 35. Determination of diffusion coefficients and concentrations of Ru(NH3)63+ and methylene blue in polyacrylamide films by chronoamperometry at ultramicrodisk electrodes.* Electrochimica Acta, 1997. 42(20-22): p. 3077-3083.

97.   Shao, Y. and M.V. Mirkin, *Probing Ion Transfer at the Liquid/Liquid Interface by Scanning Electrochemical Microscopy (SECM).* The Journal of Physical Chemistry B, 1998. 102(49): p. 9915-9921.

98.   Švancara, I., K. Vytřas, J. Barek, and J. Zima, *Carbon Paste Electrodes in Modern Electroanalysis.* Critical Reviews in Analytical Chemistry, 2001. 31(4): p. 311-345.

99.   Kalcher, K., *Chemically modified carbon paste electrodes in voltammetric analysis.* Electroanalysis, 1990. 2(6): p. 419-433.

100.   Smith, B.C., *Fourier Transform Infrared Spectroscopy*. 1996, Boca Raton: CRC press Inc. .

101.   http://mmrc.caltech.edu/FTIR/FTIRintro.pdf.

102.   http://labs.ti.bfh.ch/uploads/media/FTIR.pdf.

103.   http://scienceworld.wolfram.com/physics/FourierTransformSpectrometer.html.

104.   http://spectroscopy.lbl.gov/FTIR-Martin/FTIR-Martin.PDF.

105.   Postek, M.T., *Scanning Electron Microscopy-A Students Handbook*. 1980, Ladd Research Industries, Inc.

106.   Goodhew, P.J. and F.J. Humphreys, *Electron microscopy and analysis*. 1988: Taylor & Francis.

107.   http://web.utk.edu/~prack/MSE%20300/SEM.pdf.

108.   http://serc.carleton.edu/research_education/geochemsheets/techniques/SEM.html.

109.   Goldstein, J., *Scanning electron microscopy and x-ray microanalysis*. Vol. 1. 2003, New York: Kluwer Adacemic/Plenum Pulbishers.

110.   Egerton, R.F., *Physical principles of electron microscopy: an introduction to TEM, SEM, and AEM*. 2005, USA: Springer.

111.   http://www.wiley-vch.de/books/sample/3527310525_c01.pdf.

112.   Bragg, W.L. *The Diffraction of Short Electromagnetic Waves by a Crystal*. in *Proceedings of the Cambridge Philosophical Society*. 1913: Cambridge University Press.

113.   www.gamry.com/App_Notes/Index.htm.

114.   Kim, C.H., S.I. Pyun, and J.H. Kim, *An investigation of the capacitance dispersion on the fractal carbon electrode with edge and basal orientations*. Electrochimica Acta, 2003. 48(23): p. 3455-3463.

115.   Nalwa, H.S., *Handbook of Nanostructured Materials and Nanotechnology*, in *Synthesis and Processing Academic Press*. 2000: San Diego.

116.   http://beam.acclab.helsinki.fi/~knordlun/nanotiede/nanosc2bnc.pdf.

117.   Reetz, M.T. and W. Helbig, *Size-Selective Synthesis of Nanostructured Transition Metal Clusters.* Journal of the American Chemical Society, 1994. 116(16): p. 7401-7402.

118.   Aneesh, P.M., K.A. Vanaja, and M.K. Jayaraj. *Synthesis of ZnO nanoparticles by hydrothermal method*. in *Proc. of SPIE*. 2007.

119.   Mazdiyasni, K.S., C.T. Lynch, and J.S. Smith, *Preparation of Ultra-High-Purity Submicron Refractory Oxides.* Journal of the American Ceramic Society, 1965. 48(7): p. 372-375.

120.   Cushing, B.L., V.L. Kolesnichenko, and C.J. O'Connor, *Recent Advances in the Liquid-Phase Syntheses of Inorganic Nanoparticles.* ChemInform, 2004. 35(47): p. no-no.

121.   Rao, C.N.R. and B. Raveau, *Transition metal oxides*. 1995, New York: VCH Publishers Inc.

122.   Schwarz, J.A., C.I. Contescu, and K. Putyera, *Dekker encyclopedia of nanoscience and nanotechnology*. 2004: M. Dekker.

123.   Itoh, H., S. Utamapanya, J.V. Stark, K.J. Klabunde, and J.R. Schlup, *Nanoscale metal oxide particles as chemical reagents. Intrinsic effects of particle size on*

168

hydroxyl content and on reactivity and acid/base properties of ultrafine magnesium oxide. Chemistry of Materials, 1993. 5(1): p. 71-77.

124. Palkar, V.R., *Sol-gel derived nanostructured γ-alumina porous spheres as an adsorbent in liquid chromatography.* Nanostructured Materials, 1999. 11(3): p. 369-374.

125. Interrante, L.V. and M.J. Hampden-Smith, *Chemistry of Advanced Materials: An Overview*. 1998, New York: Wiley-VCH.

126. Gesser, H.D. and P.C. Goswami, *Aerogels and related porous materials.* Chemical Reviews, 1989. 89(4): p. 765-788.

127. Zhang, F.-b., Y.-k. Zhou, and H.-l. Li, *Nanocrystalline NiO as an electrode material for electrochemical capacitor.* Materials Chemistry and Physics, 2004. 83(2-3): p. 260-264.

128. Wang, Y., J. Zhu, X. Yang, L. Lu, and X. Wang, *Preparation of NiO nanoparticles and their catalytic activity in the thermal decomposition of ammonium perchlorate.* Thermochimica Acta, 2005. 437(1-2): p. 106-109.

129. Ghosh, M., K. Biswas, A. Sundaresan, and C.N.R. Rao, *MnO and NiO nanoparticles: synthesis and magnetic properties.* Journal of Materials Chemistry, 2006. 16(1): p. 106-111.

130. Zheng, Y.-z., H.-y. Ding, and M.-l. Zhang, *Preparation and electrochemical properties of nickel oxide as a supercapacitor electrode material.* Materials Research Bulletin, 2009. 44(2): p. 403-407.

131. Sohn, J.R. and J.S. Han, *Physicochemical and catalytic properties of NiO–TiO2 modified with WO3 for ethylene dimerization.* Applied Catalysis A: General, 2006. 298(0): p. 168-176.

132. Wu, Y., Y. He, T. Wu, W. Weng, and H. Wan, *Effect of synthesis method on the physical and catalytic property of nanosized NiO.* Materials Letters, 2007. 61(13): p. 2679-2682.

133. Tiwari, S.D. and K.P. Rajeev, *Magnetic properties of NiO nanoparticles.* Thin Solid Films, 2006. 505(1-2): p. 113-117.

134. Han, D.Y., H.Y. Yang, C.B. Shen, X. Zhou, and F.H. Wang, *Synthesis and size control of NiO nanoparticles by water-in-oil microemulsion.* Powder Technology, 2004. 147(1-3): p. 113-116.

135. Li, X., X. Zhang, Z. Li, and Y. Qian, *Synthesis and characteristics of NiO nanoparticles by thermal decomposition of nickel dimethylglyoximate rods.* Solid State Communications, 2006. 137(11): p. 581-584.

136. Wu, M.-S. and H.-H. Hsieh, *Nickel oxide/hydroxide nanoplatelets synthesized by chemical precipitation for electrochemical capacitors.* Electrochimica Acta, 2008. 53(8): p. 3427-3435.
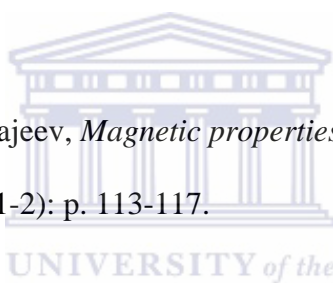
137. Dharmaraj, N., P. Prabu, S. Nagarajan, C.H. Kim, J.H. Park, and H.Y. Kim, *Synthesis of nickel oxide nanoparticles using nickel acetate and poly(vinyl acetate) precursor.* Materials Science and Engineering: B, 2006. 128(1-3): p. 111-114.

138. An, C., R. Wang, S. Wang, and Y. Liu, *A low temperature composite-hydroxide approach to NiO nanocrystals.* Materials Research Bulletin, 2008. 43(10): p. 2563-2568.

139. Waldorf, A.J., J.A. Dobrowolski, B.T. Sullivan, and L.M. Plante, *Optical coatings deposited by reactive ion plating.* Appl. Opt., 1993. 32(28): p. 5583-5593.

140. Duggan, M.J., T. Saito, and T. Niwa, *Ionic conductivity of tantalum oxide by rf sputtering.* Solid State Ionics, 1993. 62(1-2): p. 15-20.

141. Ozer, N. and C.M. Lampert, *Electrochromic characterization of sol–gel deposited coatings.* Solar Energy Materials and Solar Cells, 1998. 54(1-4): p. 147-156.

142. Slade, R.C.T., J. Barker, and T.K. Halstead, *Protonic conduction and diffusion in the hydrous oxides V2O5·nH2O, Nb2O5·nH2O, Ta2O5·nH2O and CeO2·nH2O.* Solid State Ionics, 1987. 24(2): p. 147-153.

143. Lynam, N.R. and A. Agrawal. *Large-Area Chromogenics Materials and Devices for Transmittance Control.* 1990. Bellimgham, Washington: SPIE Press.

144.   Rubio, F., J. Denis, J.M. Albella, and J.M. Martinez-Duart, *Sputtered Ta2O5 antireflection coatings for silicon solar cells.* Thin Solid Films, 1982. 90(4): p. 405-408.

145.   Gu¨rtler, K., K. Bange, W. Wagner, F. Rauch, and H. Hantsche, *Characterization of Ta2O5 layers by electron spectroscopy for chemical analysis rutherford backscattering spectrometry, nuclear reaction analysis and optical methods.* Thin Solid Films, 1989. 175(0): p. 185-189.

146.   Sankur, H.O. and W. Gunning, *Deposition of optical thin films by pulsed laser assisted evaporation.* Appl. Opt., 1989. 28(14): p. 2806-2808.

147.   Lo, G.Q., D.L. Kwong, and S. Lee, *Reliability characteristics of metal oxide semiconductor capacitors with chemical vapor deposited Ta2O5 gate dielectrics.* Appl. Phys. Lett., 1993. 62: p. 97.

148.   Lee, G.H., S.H. Huh, J.W. Jeong, B.J. Choi, S.H. Kim, and H.-C. Ri, *Anomalous Magnetic Properties of MnO Nanoclusters.* Journal of the American Chemical Society, 2002. 124(41): p. 12094-12095.

149.   Park, J., J. Joo, S.G. Kwon, Y. Jang, and T. Hyeon, *Synthesis of Monodisperse Spherical Nanocrystals.* Angewandte Chemie International Edition, 2007. 46(25): p. 4630-4660.

150.   Yin, M. and S. O'Brien, *Synthesis of Monodisperse Nanocrystals of Manganese Oxides.* Journal of the American Chemical Society, 2003. 125(34): p. 10180-10181.

151.   Zhong, X., R. Xie, L. Sun, I. Lieberwirth, and W. Knoll, *Synthesis of Dumbbell-Shaped Manganese Oxide Nanocrystals.* The Journal of Physical Chemistry B, 2005. 110(1): p. 2-4.

152.   Park, J., K. An, Y. Hwang, J.-G. Park, H.-J. Noh, J.-Y. Kim, J.-H. Park, N.-M. Hwang, and T. Hyeon, *Ultra-large-scale syntheses of monodisperse nanocrystals.* Nat Mater, 2004. 3(12): p. 891-895.

153.   Fendler, J.H., *Atomic and molecular clusters in membrane mimetic chemistry.* Chemical Reviews, 1987. 87(5): p. 877-899.

154.   Dixit, S.G., A.R. Mahadeshwar, and S.K. Haram, *Some aspects of the role of surfactants in the formation of nanoparticles.* Colloids and Surfaces A: Physicochemical and Engineering Aspects, 1998. 133(1): p. 69-75.

155.   Moore, W.J., *Seven Solid States: An introduction to the chemistry and physics of solids.* 1967, New York: WA Benjamin INC.

156.   Tao, D. and F. Wei, *New procedure towards size-homogeneous and well-dispersed nickel oxide nanoparticles of 30 nm.* Materials Letters, 2004. 58(25): p. 3226-3228.

157.   Yang, Q., J. Sha, X. Ma, and D. Yang, *Synthesis of NiO nanowires by a sol-gel process.* Materials Letters, 2005. 59(14-15): p. 1967-1970.

158. Li, X., L. Zhou, J. Gao, H. Miao, H. Zhang, and J. Xu, *Synthesis of Mn3O4 nanoparticles and their catalytic applications in hydrocarbon oxidation.* Powder Technology, 2009. 190(3): p. 324-326.

159. Giovannelli, F., T. Chartier, C. Autret-Lambert, F. Delorme, M. Zaghrioui, and A. Seron, *A fast route to obtain manganese spinel nanoparticles by reduction of K-birnessite.* Journal of Solid State Chemistry, 2009. 182(5): p. 1021-1026.

160. Hai-Yan, X., X. SiLe, W. Hao, and Y. Hui, *Characterization of Hausmannite Mn3O4 Thin Films by Chemical Bath Deposition.* Journal of the Electrochemical Society, 2005. 152(12): p. C803-C807.

161. Sugimoto, T., *Monodispersed particles*. 1st ed. 2001, Amsterdam: Elsevier Science B. V.

162. Pierre, A.C., *Introduction to Sol-Gel Processing*. 1998, Boston: Kluwer Academic Publishers.

163. Patil, S., S. Raghavendra, M. Revansiddappa, P. Narsimha, and M. Ambika Prasad, *Synthesis, transport and dielectric properties of polyaniline/Co<sub>3</sub>O<sub>4</sub> composites.* Bulletin of Materials Science, 2007. 30(2): p. 89-92.

164. Dey, A., S. De, A. De, and S.K. De, *Characterization and dielectric properties of polyaniline-TiO2 nanocomposites.* Nanotechnology, 2004. 15: p. 1277-1283.

165. Gupta, K., G. Chakraborty, S. Ghatak, P.C. Jana, A.K. Meikap, and R. Babu, *Synthesis, magnetic, optical, and electrical transport properties of the nanocomposites of polyaniline with some rare earth chlorides.* J. Appl. Phys., 2010. 108(7): p. 073701-10

166. Yelil Arasi, A., J. Juliet Latha Jeyakumari, B. Sundaresan, V. Dhanalakshmi, and R. Anbarasan, *The structural properties of Poly(aniline)—Analysis via FTIR spectroscopy.* Spectrochimica Acta Part A: Molecular and Biomolecular Spectroscopy, 2009. 74(5): p. 1229-1234.

167. Gemeay, A.H., R.G. El-Sharkawy, I.A. Mansour, and A.B. Zaki, *Preparation and characterization of polyaniline/manganese dioxide composites and their catalytic activity.* Journal of Colloid and Interface Science, 2007. 308(2): p. 385-394.

168. Fu, Y., Z. Zhao, J. Liu, K. Li, Q. Xu, and S. Zhang, *Sulfonated polyaniline/vanadate composite as anode material and its electrochemical property in microbial fuel cells on ocean floor.* SCIENCE CHINA Chemistry, 2011. 54(5): p. 844-849.

169. Zhang, Z., Z. Wei, and M. Wan, *Nanostructures of Polyaniline Doped with Inorganic Acids.* Macromolecules, 2002. 35(15): p. 5937-5942.

170. Wang, D., F. Ma, S. Qi, and B. Song, *Synthesis and electromagnetic characterization of polyaniline nanorods using Schiff base through 'seeding' polymerization.* Synthetic Metals, 2010. 160(19-20): p. 2077-2084.

171.   Abdiryim, T., Z. Xiao-Gang, and R. Jamal, *Comparative studies of solid-state synthesized polyaniline doped with inorganic acids.* Materials Chemistry and Physics, 2005. 90(2-3): p. 367-372.

172.   Cataldo, F. and P. Maltese, *Synthesis of alkyl and N-alkyl-substituted polyanilines: A study on their spectral properties and thermal stability.* European Polymer Journal, 2002. 38(9): p. 1791-1803.

173.   Tan, Y., Y. Zhang, and J. Kan, *Synthesis and properties on polyaniline in the presence of nickel chloride.* eXPRESS Polymer Letters, 2009. 3(6): p. 333-339.

174.   Xia, H. and Q. Wang, *Ultrasonic Irradiation: A Novel Approach To Prepare Conductive Polyaniline/Nanocrystalline Titanium Oxide Composites.* Chemistry of Materials, 2002. 14(5): p. 2158-2165.

175.   Lu, F.L., F. Wudl, M. Nowak, and A.J. Heeger, *Phenyl-Capped Octaaniline (COA): An Excellent Model for Polyaniline.* J. Am. Chem. Soc., 1986. 108: p. 8311.

176.   MacDiarmid, A.G., *Nobel Lecture: "Synthetic metals": A novel role for organic polymers.* Reviews of Modern Physics, 2001. 73(3): p. 701-712.

177.   Hino, T., T. Namiki, N. Kuramoto, and *Synthesis and characterization of novel conducting composites of polyaniline prepared in the presence of sodium dodecyl sulphate and several water soluble polymers.* Synthetic Metals, 2006. 156: p. 1327-1332.

178. Wan, M. and J. Li, *Synthesis and electrical–magnetic properties of polyaniline composites.* Journal of Polymer Science Part A: Polymer Chemistry, 1998. 36(15): p. 2799-2805.

179. Wan, M., M. Li, J. Li, and Z. Liu, *Structure and electrical properties of the oriented polyaniline films.* Journal of Applied Polymer Science, 1994. 53(2): p. 131-139.

180. Wipf, D.O., A. Bard, and *Scanning electrochemical Microscopy; VII. Effect of electron-transfer rate at the substrate on the tip feedback current.* J. Electrochem. Soc, 1991. 138(2): p. 469-474.

181. Lu, X., Q. Wang, and X. Liu, *Review: Recent applications of scanning electrochemical microscopy to the study of charge transfer kinetics.* Analytica Chimica Acta, 2007. 601(1): p. 10-25.

182. Jeon, I.C. and F.C. Anson, *Application of scanning electrochemical microscopy to studies of charge propagation within polyelectrolyte coatings on electrodes.* Analytical Chemistry, 1992. 64(18): p. 2021-2028.

183. Mirkin, M.V., W. Nogala, J. Velmurugan, and Y. Wang, *Scanning electrochemical microscopy in the 21st century. Update 1: five years after.* Physical Chemistry Chemical Physics, 2011.

184. Prévost, V., A. Petit, and F. Pla, *Studies on chemical oxidative copolymerization of aniline and o-alkoxysulfonated anilines II. Mechanistic approach and monomer reactivity ratios.* European Polymer Journal, 1999. 35(7): p. 1229-1236.

177

185.   Malinauskas, A., *Chemical deposition of conducting polymers.* Polymer, 2001. 42(9): p. 3957-3972.

186.   Monk, P.M.S., *Fundamentals of electroanalytical chemistry*. 2001, New York: Wiley & Sons.

187.   Lindfors, T. and A. Ivaska, *pH sensitivity of polyaniline and its substituted derivatives.* Journal of Electroanalytical Chemistry, 2002. 531(1): p. 43-52.

188.   Widera, J., W. Grochala, K. Jackowska, and J. Bukowska, *Electrooxidation of O-methoxyaniline as studied by electrochemical and SERS methods.* Synthetic Metals, 1997. 89(1): p. 29-37.

189.   Yue, J., Z.H. Wang, K.R. Cromack, A.J. Epstein, and A.G. MacDiarmid, *Effect of sulfonic acid group on polyaniline backbone.* Journal of the American Chemical Society, 1991. 113(7): p. 2665-2671.

190.   Huang, L.-M., C.-H. Chen, T.-C. Wen, and A. Gopalan, *Effect of secondary dopants on electrochemical and spectroelectrochemical properties of polyaniline.* Electrochimica Acta, 2006. 51(13): p. 2756-2764.

191.   Sivakumar, R. and R. Saraswathi, *Redox properties of poly(N-methylaniline).* Synthetic Metals, 2003. 138(3): p. 381-390.

192.   Valter, B., M.K. Ram, and C. Nicolini, *Synthesis of Multiwalled Carbon Nanotubes and Poly(o-anisidine) Nanocomposite Material: Fabrication and*

178

Characterization of Its Langmuir–Schaefer Films. Langmuir, 2002. 18(5): p. 1535-1541.

193.   Zhang, L., X. Jiang, E. Wang, and S. Dong, *Attachment of gold nanoparticles to glassy carbon electrode and its application for the direct electrochemistry and electrocatalytic behavior of hemoglobin.* Biosensors and Bioelectronics, 2005. 21(2): p. 337-345.

194.   Laviron, E., *The use of linear potential sweep voltammetry and of a.c. voltammetry for the study of the surface electrochemical reaction of strongly adsorbed systems and of redox modified electrodes.* Journal of Electroanalytical Chemistry and Interfacial Electrochemistry, 1979. 100(1-2): p. 263-270.

195.   Panchompoo, J., L. Aldous, and R.G. Compton, *Size-effects in the chemical modification of carbon black nanoparticles with 4-nitroaniline.* New Journal of Chemistry, 2010. 34(11): p. 2643-2653.

196.   Yang, C.-C., S.-T. Hsu, and W.-C. Chien, *All solid-state electric double-layer capacitors based on alkaline polyvinyl alcohol polymer electrolytes.* Journal of Power Sources, 2005. 152(0): p. 303-310.

197.   Li, J., X. Wang, Y. Wang, Q. Huang, C. Dai, S. Gamboa, and P.J. Sebastian, *Structure and electrochemical properties of carbon aerogels synthesized at ambient temperatures as supercapacitors.* Journal of Non-Crystalline Solids, 2008. 354(1): p. 19-24.

198.   Wei, Y.Z., B. Fang, S. Iwasa, and M. Kumagai, *A novel electrode material for electric double-layer capacitors.* Journal of Power Sources, 2005. 141(2): p. 386-391.

199.   Miura, K. and T. Morimoto, *Adsorption sites for water on graphite. 3. Effect of oxidation treatment of sample.* Langmuir, 1986. 2(6): p. 824-828.

200.   Park, J.H., O.O. Park, K.H. Shin, C.S. Jin, and J.H. Kim, *An Electrochemical Capacitor Based on a Ni(OH)[sub 2]/Activated Carbon Composite Electrode.* Electrochemical and Solid-State Letters, 2002. 5(2): p. H7-H10.

201.   Ramani, M., B.S. Haran, R.E. White, B.N. Popov, and L. Arsov, *Studies on activated carbon capacitor materials loaded with different amounts of ruthenium oxide.* Journal of Power Sources, 2001. 93(1-2): p. 209-214.

202.   Hahn, M., M. Bärtsch, B. Schnyder, R. Kötz, M. Carlen, C. Ohler, and D. Evard. *A 24 V BIPOLAR ELECTROCHEMICAL DOUBLE LAYER CAPACITOR BASED ON ACTIVATED GLASSY CARBON*. in *Power Sources for the New Millenium*. 2001. Pennington, NJ: The Electrochemical Society.

203.   Jim P, Z., *Resistance distribution in electrochemical capacitors with a bipolar structure.* Journal of Power Sources, 2004. 137(1): p. 158-162.

204.   Prasad, K.R. and N. Munichandraiah, *Electrochemical Studies of Polyaniline in a Gel Polymer Electrolyte.* Electrochemical and Solid-State Letters, 2002. 5(12): p. A271-A274.

205. Ganesh, V., S. Pitchumani, and V. Lakshminarayanan, *New symmetric and asymmetric supercapacitors based on high surface area porous nickel and activated carbon.* Journal of Power Sources, 2006. 158(2): p. 1523-1532.

206. Gao, B., C.-z. Yuan, L.-h. Su, L. Chen, and X.-g. Zhang, *Nickel oxide coated on ultrasonically pretreated carbon nanotubes for supercapacitor.* Journal of Solid State Electrochemistry, 2009. 13(8): p. 1251-1257.

207. Yuan, C., L. Chen, B. Gao, L. Su, and X. Zhang, *Synthesis and utilization of RuO2[middle dot]xH2O nanodots well dispersed on poly(sodium 4-styrene sulfonate) functionalized multi-walled carbon nanotubes for supercapacitors.* Journal of Materials Chemistry, 2009. 19(2): p. 246-252.

208. Gupta, V. and N. Miura, *High performance electrochemical supercapacitor from electrochemically synthesized nanostructured polyaniline.* Materials Letters, 2006. 60(12): p. 1466-1469.

209. Yuan, C., L. Su, B. Gao, and X. Zhang, *Enhanced electrochemical stability and charge storage of MnO2/carbon nanotubes composite modified by polyaniline coating layer in acidic electrolytes.* Electrochimica Acta, 2008. 53(24): p. 7039-7047.

210. Ko, J., K. Ryu, S. Kim, and K. Kim, *Supercapacitive properties of composite electrodes consisting of polyaniline, carbon nanotube, and RuO<sub>2</sub&gt.* Journal of Applied Electrochemistry, 2009. 39(8): p. 1331-1337.

211.   Srinivasan, V. and J.W. Weidner, *Studies on the Capacitance of Nickel Oxide Films: Effect of Heating Temperature and Electrolyte Concentration.* Journal of The Electrochemical Society, 2000. 147(3): p. 880-885.

212.   Girija, T.C. and M.V. Sangaranarayanan, *Polyaniline-based nickel electrodes for electrochemical supercapacitors—Influence of Triton X-100.* Journal of Power Sources, 2006. 159(2): p. 1519-1526.

213.   Zhang, L.L. and X.S. Zhao, *Carbon-based materials as supercapacitor electrodes.* Chemical Society Reviews, 2009. 38(9): p. 2520-2531.

214.   Lisdat, F. and D. Schäfer, *The use of electrochemical impedance spectroscopy for biosensing.* Analytical and Bioanalytical Chemistry, 2008. 391(5): p. 1555-1567.

215.   Song, H.-K., H.-Y. Hwang, K.-H. Lee, and L.H. Dao, *The effect of pore size distribution on the frequency dispersion of porous electrodes.* Electrochimica Acta, 2000. 45(14): p. 2241-2257.

216.   Arabale, G., D. Wagh, M. Kulkarni, I.S. Mulla, S.P. Vernekar, K. Vijayamohanan, and A.M. Rao, *Enhanced supercapacitance of multiwalled carbon nanotubes functionalized with ruthenium oxide.* Chemical Physics Letters, 2003. 376(1-2): p. 207-213.

217.   Estaline Amitha, F., A. Leela Mohana Reddy, and S. Ramaprabhu, *A non-aqueous electrolyte-based asymmetric supercapacitor with polymer and metal oxide/multiwalled carbon nanotube electrodes.* Journal of Nanoparticle Research, 2009. 11(3): p. 725-729.

218. Conway, B.E., V. Birss, and J. Wojtowicz, *The role and utilization of pseudocapacitance for energy storage by supercapacitors.* Journal of Power Sources, 1997. 66(1-2): p. 1-14.

219. Orazem, M.E., P. Agarwal, and L.H. Garcia-Rubio, *Critical issues associated with interpretation of impedance spectra.* Journal of Electroanalytical Chemistry, 1994. 378(1-2): p. 51-62.
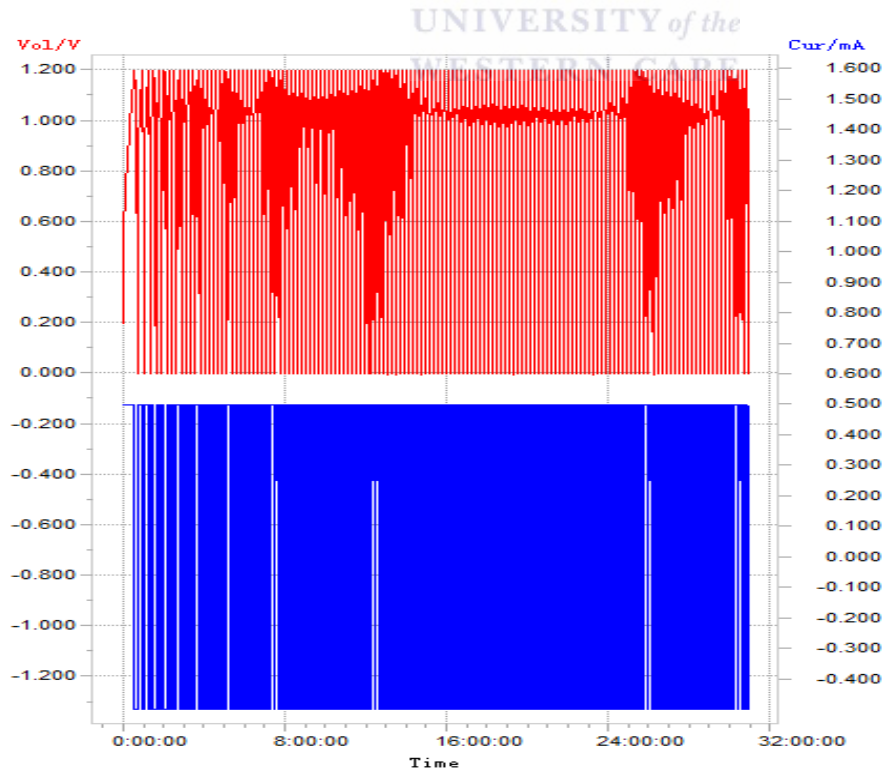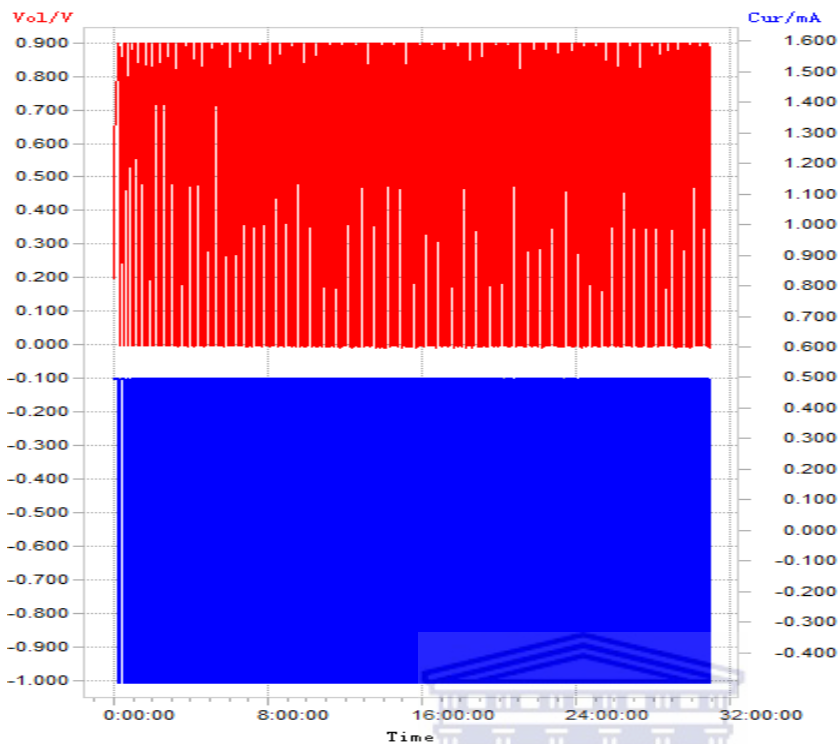
Appendix

1. Charge/discharge voltage-time curve profiles of;
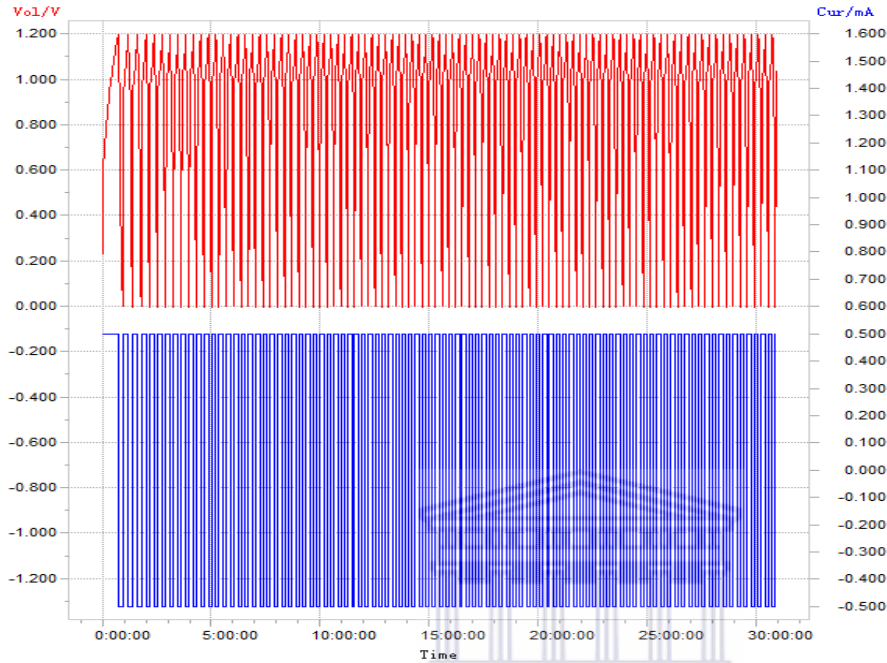
(a) Voltage-time profile for 143 cycles for TaO-Mn$_2$O$_3$-PANi-PSSA
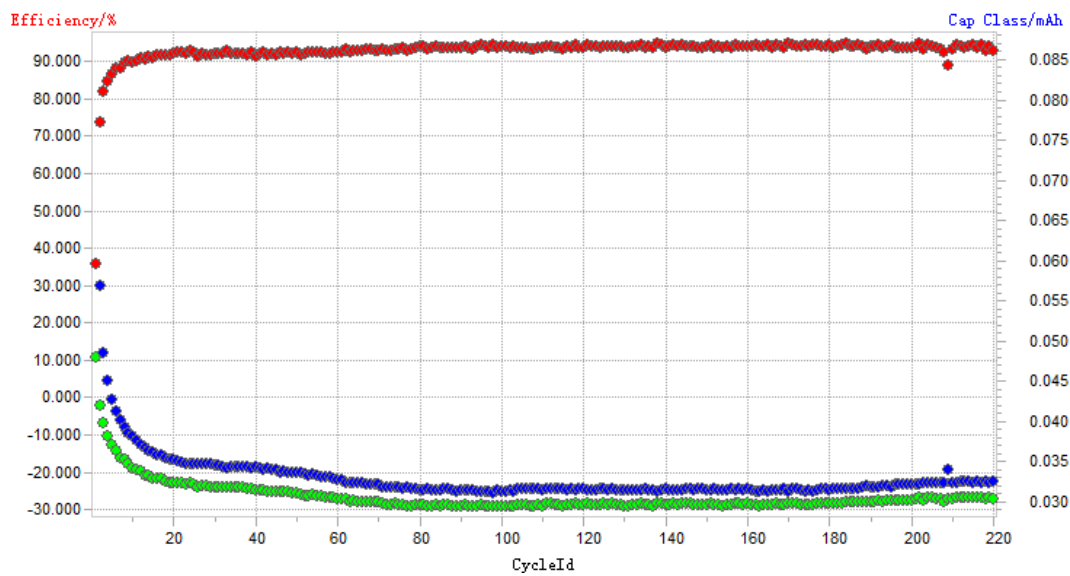

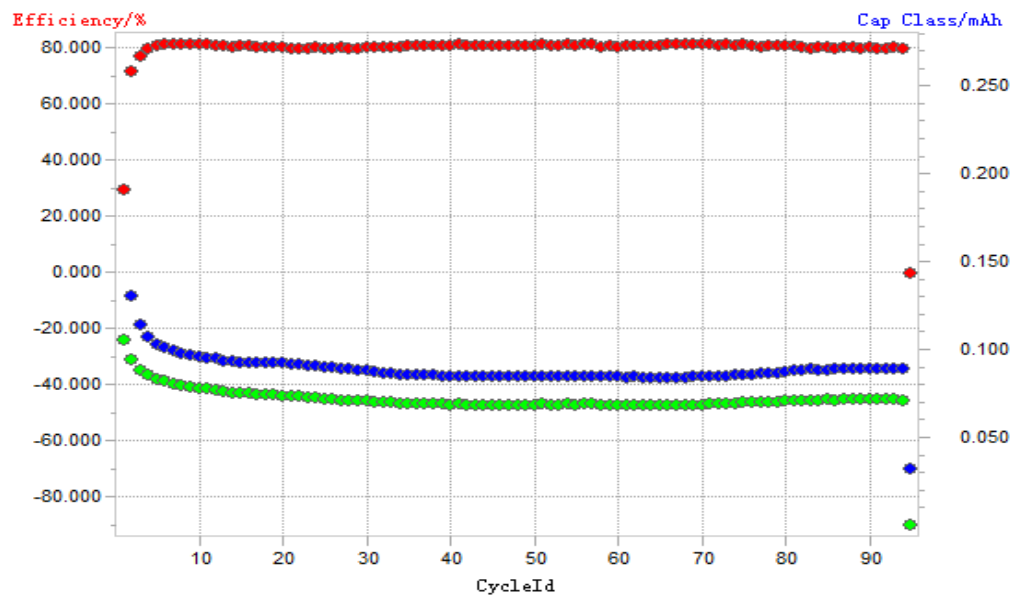**(b) Voltage-time profile for 143 cycles for TaO$_2$-PANi-PSSA**

(c) Voltage-time profile for 241 cycles for TaO$_2$-NiO-PANi-PSSA

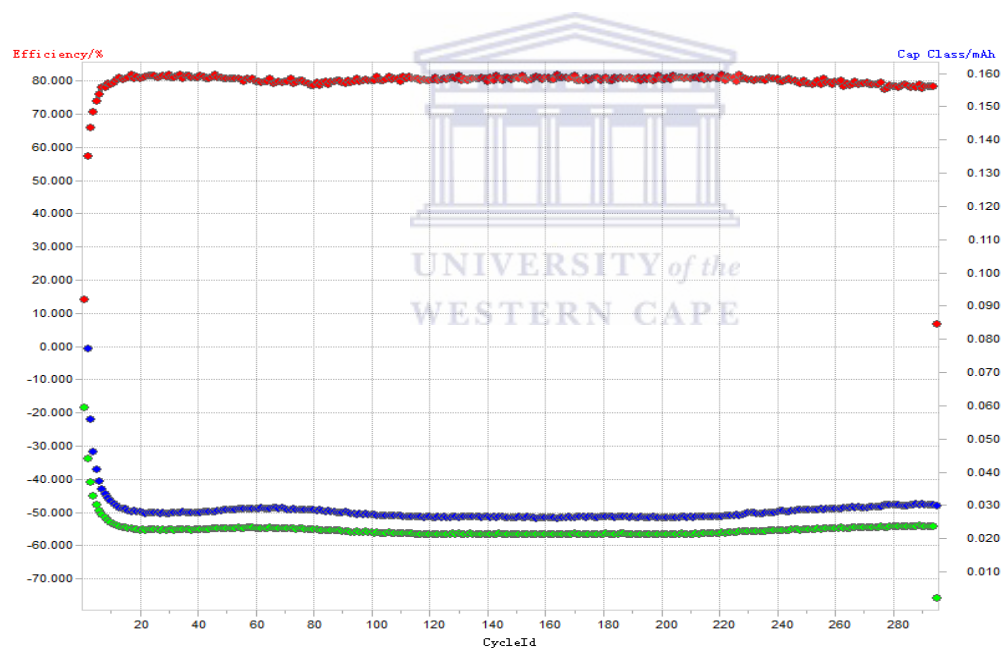**2. Coulombic efficiency as a function of the number of cycles for;**

(a) TaO$_2$-NiO-PANi-PSSA

185

(b) TaO-Mn₂O₃-PANi-PSSA

(c) TaO-NiO-Mn₃O₄-PANi-PSSA

186